



IChF

Institut Chemii Fizycznej PAN

Institute of Physical Chemistry  
Polish Academy of Sciences  
Kasprzaka 44/52  
01-224 Warsaw, Poland

## Ph.D. Thesis

# *Carbazole and acrylate molecularly imprinted polymers and their application as recognition units in electrochemical chemosensors for selective determination of chosen drug substances*

Jyoti

Supervisor: Prof. Włodzimierz Kutner, Ph.D., D.Sc.

Auxiliary supervisor: Krzysztof Noworyta, Ph.D.

The thesis was prepared within the International Doctoral Studies in Chemistry  
at the Institute of Physical Chemistry, Polish Academy of Sciences, Warsaw, Poland

Warsaw, January 2022



*Always in my thought*



WWW.PHDCOMICS.COM

JORGE CHAM © 2014



## **Declaration of originality**

I declare that the research included within this thesis was carried out by myself or with support by others included in acknowledgments.

I state that I have exercised care to ensure that the work is original and contains no previously published material or written by another person, except where citations have been made in the text. The content provided here does not violate any copyrights to the best of my knowledge. I accept that the Polish Academy of Sciences has the right to use plagiarism detection software to ensure the thesis's legitimacy.

I certify that no part of my thesis has been or will be submitted for obtaining a degree or diploma by the Institute of Physical Chemistry, Polish Academy of Science, or any other educational institution.

This thesis's copyright rests with the author, and no information derived from it may be published without the author's consent.

Warsaw, 07 January 2022

Signature



## Acknowledgements

The successful completion of the present Ph.D. thesis would have been impossible without several people's contributions, support, and encouragement. I owe acknowledgments to all of them.

First, I would like to sincerely thank my supervisors, Prof. Włodzimierz Kutner and Dr. Krzysztof Noworyta, for giving me this opportunity to work under their guidance. Particularly, I am grateful to Prof. Kutner for his endless effort in supervising and encouraging me to find my limits and critically analyze my results. His guidance and support were instrumental in shaping my research work and improving me throughout my Ph.D. studies. Undoubtedly, his valuable suggestions and advice have helped me become a better researcher and writer. Moreover, I would like to thank Dr. Krzysztof Noworyta for his valuable suggestions, fruitful discussions, and AFM data analysis. I am grateful to Prof. Paweł Kulesza, Prof. Patrizia Mussini, and Prof. Małgorzata Zagórska for accepting invitations to review my thesis. Furthermore, I am extremely thankful to all our scientific collaborators for their valuable inputs over the years.

In particular, I appreciate the help of the following researchers.

Dr. Teresa Żołek and Prof. Dorota Maciejewska of the Department of Organic Chemistry, the Medical University of Warsaw, for molecular mechanics, molecular dynamics, and DFT calculations and results interpretation.

For his guidance through pharmaceutical substances, Prof. Andrej Kutner of the Department of Bioanalysis and Drug Analysis, the Medical University of Warsaw.

For validating drugs by HPLC, Dr. Edyta Gilant of the Łukasiewicz Research Network – Industrial Chemistry Institute, Warsaw, Poland.

Dr. Piotr Rudzki for friendly discussions related to the research project.

Dr. Renata Rybakiewicz-Sekita of the Faculty of Mathematics and Natural Sciences. School of Sciences, Cardinal Stefan Wyszyński University in Warsaw, for guiding me through the syntheses of carbazole compounds.

Moreover, I would like to thank the following colleagues for other collaborations established during my Ph.D. studies.

Dr. Carlo Gonzato and Prof. Karsten Haupt for enriching my research ideas with their knowledge, and Franck Merlier for HPLC analysis, all of the Université de Technologie de Compiègne, CNRS Laboratory for Enzyme and Cell Engineering, Compiègne, France.

Dr. Evgenia Dmitrieva of the Nanoscale Chemistry and Spectroelectrochemistry group, Department of Electrochemistry and Conducting Polymers of the Leibniz Institute for Solid State and Materials Research, Dresden, Germany, and Dr. Sandra Pluczyk-Małek of the

Department of Physical chemistry and Technology of Polymers, Faculty of Chemistry, Faculty of Chemistry, Silesian University of Technology, Poland for performing the UV-vis-NIR/EPR measurements and data analysis that led to completing our two research projects.

Dr. Piotr Bernatowicz and Dr. Tomasz Ratajczyk of IPC PAS, for the NMR spectral analysis. Special thanks are due to Dr. Paweł Borowicz for performing PM-IMRAS measurements, Dr. Maciej Cieplak for teaching me the HPLC analysis, and Dr. Piyush Sindhu Sharma for his guidance during all these years.

My heartiest thanks to my small "family" of Alcina, Rashmi, Neha, Viki, Swaraj, and Nabila at IPC PAS for providing the much-needed distraction from my Ph.D. life. For being good listeners and friends through good and bad times. Life wouldn't have been the same without you all!

My deepest and sincere gratitude goes to all the people who were always there for me. I am forever indebted to my parents, Diwan Singh and Savita Devi, for their love, patience, and confidence in me. You have supported me through everything and always given me the freedom and facilities to choose my path and realize my potential. Words aren't enough to express my gratefulness. Without you, I wouldn't be what I am today. Special thanks to my brother and sister, Nitesh Kumar and Printa Yadav, for their unwavering faith in me, a constant source of motivation.

A heartfelt thanks to Piyush Yadav for his continuous support, patience, and understanding.

Finally, I'd like to thank my inner self for keeping me motivated to pursue what I've always loved.

Besides, I am grateful to the IPC PAS for funding, including the Erasmus+ EU grant and the mobility grant for my short research visit in Compiegne, and Prof. Maciej Wojtkowski of IPC PAS for funding my short research visit to Dresden.

# 1. Funding

- 1.1 The Polish National Science Center (NCN) through grant no. UMO-2015/19/B/ST4/03743 to Dr. Eng. Krzysztof Noworyta.
- 1.2 Mobility grant of the Institute of Physical Chemistry, Polish Academy of Sciences (IPC PAS), and EU Erasmus+ to Jyoti.
- 1.3 The CREAtion grant of the Department of Physical Chemistry of Biological SysTEms of IPC PAS [CREATE] no. 666295-CREATE--H2020-WIDESPREAD-2014-2015/H2020-WIDESPREAD-2014-2 to Prof. Maciej Wojtkowski financially supported my short research visits.



## 2. List of publications

### 2.1 Publications included in the thesis

- 2.1.1 **Jyoti**, Carlo Gonzato, Teresa Żołek, Dorota Maciejewska, Andrzej Kutner, Franck Merlier, Karsten Haupt, Piyush Sindhu Sharma, Krzysztof Noworyta, and Włodzimierz Kutner, "Molecularly imprinted polymer nanoparticles-based electrochemical chemosensors for selective determination of cilostazol and its pharmacologically active primary metabolite in human plasma," *Biosens. Bioelectron.* **2021**, 193, 113542. (IF = 10.62)  
<https://doi.org/10.1016/j.bios.2021.113542>
- 2.1.2 **Jyoti**, Renata Rybakiewicz-Sekita, Teresa Żołek, Dorota Maciejewska, Edyta Gilant, Katarzyna Buś-Kwaśnik, Andrzej Kutner, Krzysztof R. Noworyta, and Włodzimierz Kutner, "Cilostazol-imprinted polymer film-coated electrode as an electrochemical chemosensor for selective determination of cilostazol and its active primary metabolite," *J. Mat. Chem. B*, **2022**, (IF = 6.33)  
<https://doi.org/10.1039/D1TB02186A>
- 2.1.3 **Jyoti**, Teresa Żołek, Dorota Maciejewska, Edyta Gilant, Elzbieta Gniazdowska, Andrzej Kutner, Krzysztof R. Noworyta, and Włodzimierz Kutner, "Polytyramine film-coated single-wall carbon nanotube electrochemical chemosensor with molecularly imprinted polymer nanoparticles for duloxetine selective determination in human plasma," **2021**, submitted.
- 2.1.4 **Jyoti**, Evgenia Dmitrieva, Teresa Żołek, Dorota Maciejewska, Włodzimierz Kutner, Krzysztof R. Noworyta, "An insight into the polymerization mechanism of selected carbazole derivatives - Why does it not always lead to polymer formation?" **2021**, submitted.
- 2.1.5 **Jyoti**, Sandra Pluczyk-Małek, Renata Rybakiewicz-Sekita, and Włodzimierz Kutner, "Synthesis, electrochemical, and EPR/UV-vis-NIR spectroelectrochemical studies of two *N*-substituted 3,6-dithienylcarbazole derivatives", in preparation.

## 2.2 Publications not included in the thesis

Co-authorship of publications under preparation

- 2.2.1 Paulina Materska-Wilczyńska, **Jyoti**, Renata Rybakiewicz-Sekita, Teresa Żołek, Dorota Maciejewska, Paweł Borowicz, Włodzimierz Kutner, Krzysztof R. Noworyta, "Determination of Imatinib Anticancer Drug Using a Chemosensor with Carbazole-based Molecularly Imprinted Polymer Film as the Recognition Unit," in preparation.
- 2.2.2 Valerii Malyshev, Anna Kidakova, Alcina Sudagar, **Jyoti**, Renata Rybakiewicz-Sekita, Paweł Borowicz, Włodzimierz Kutner, Vitali Syritski, Krzysztof R. Noworyta, "Selective sarcosine determination using molecular imprinting in combination with impedimetric and electrochemical generation-collection transductions," in preparation.
- 2.2.3 Paulina Materska-Wilczyńska, Aleksandra Kalinowska, **Jyoti**, Renata Rybakiewicz-Sekita, Teresa Żołek, Dorota Maciejewska, Edyta Gilant, Andrzej Kutner, Włodzimierz Kutner, Krzysztof R. Noworyta. "Impedimetric chemosensor for sunitinib determination in body fluids with polycarbazole-based molecularly imprinted recognition layer," in preparation.

### 3. List of patent applications

- 3.1 Gajda M., Cieplak M., Rybakiewicz, R., Noworyta, K., Kutner W., Kutner A., Rudzki, P., Gilant, E., Żołek T., Maciejewska D., Materska-Wilczyńska, P., **Jyoti**, Polish Patent Appl. No. P.432365, 22 Dec 2019, „Polimer molekularnie wdrukowany tworzący warstwę rozpoznającą arypiprazol, sposób wytworzenia warstwy tego polimeru, jej zastosowanie do budowy czujników chemicznych do oznaczania arypiprazolu oraz kwas 4-[3,6-di(tiofen-2-yl)-9H-karbazol-9-il]benzoesowy, sposób jego otrzymania i zastosowanie w syntezie polimeru molekularnie wdrukowanego arypiprazolem” (“A molecularly imprinted polymer forming an aripiprazole recognition layer, a method for producing this polymer layer, its use in the construction of chemical sensors for the determination of aripiprazole and 4-[3,6-di (thiophen-2-yl)-9H-carbazol-9-yl] benzoic acid, the method of its preparation and the use in the synthesis of a polymer molecularly imprinted with aripiprazole”). (This work received *ERiNET Innovatorenpreis Special Award* in Nuremberg, Germany, 2018.)
- 3.2 **Jyoti**, Rybakiewicz-Sekita, R., Żołek T., Maciejewska D., Kutner, A., Noworyta, K. R., Kutner, W., Polish Patent Appl. No. P.438383, 8 July 2021, „Warstwa rozpoznająca przewodzącego polimeru, sposób otrzymania warstwy, zastosowanie czujnika elektrochemicznego zawierającego warstwę do rozpoznawania inhibitora agregacji płytek krwi i jego metabolitu” (“Conductive polymer recognition layer, method of preparing the layer, and its application as an electrochemical sensor in recognizing a platelet aggregation inhibitor and its metabolite”).
- 3.3 **Jyoti**, Żołek, T., Maciejewska, D., Kutner A., Noworyta, K., Kutner, W., Polish Patent Appl. No. P.438951, 15 Sep 2021, „Nanokompozytowa warstwa rozpoznająca, sposób otrzymywania nanokompozytowej warstwy rozpoznającej, zastosowanie nanokompozytowej warstwy rozpoznającej w czujniku elektrochemicznym do selektywnego rozpoznawania i wykrywania antydepresanta nowej generacji w ludzkim osoczu” (“Nanocomposite recognition layer, a method of preparing a nanocomposite recognition layer, and its application in the electrochemical sensor for the selective recognition and detection of a new generation antidepressant in human plasma”).

## 4. Active participation at international conferences

### 4.1 Oral presentations

- 4.1.1 **Jyoti**, Krzysztof R. Noworyta, Renata Rybakiewicz, Teresa Zolek, Dorota Maciejewska, and Włodzimierz Kutner, "Synthesis and characterization of carbazole derivatives as new functional monomers for molecularly imprinted polymers (MIPs)," The YoungChem 2018, Bydgoszcz, Poland. (*Audience award for the best presentation.*)
- 4.1.2 **Jyoti**, Carlo Gonzato, Franck Merlier, Karsten Haupt, Paweł Borowicz, Włodzimierz Kutner, Krzysztof Noworyta, "Fabrication of the Electrochemical Cilostazol Chemosensor with Molecularly Imprinted Polymer Nanoparticles as the Recognition Unit," The 71<sup>st</sup> Annual Meeting of the International Society of Electrochemistry (ISE), 31<sup>st</sup> August - 4<sup>th</sup> September 2020, Belgrade, Serbia.
- 4.1.3 **Jyoti**, Carlo Gonzato, Frank Merlier, Karsten Haupt, Piyush Sindhu Sharma, Włodzimierz Kutner, Krzysztof Noworyta, "Molecularly imprinted polymer nanoparticles as the recognition unit of the electrochemical chemosensor for cilostazol," Graduate student symposium on advantageous electrochemistry (GSSAE), 10<sup>th</sup> - 11<sup>th</sup> September 2020, Warsaw, Poland, and the 9<sup>th</sup> Edition of European Young Engineers Conference (EYEC), 19<sup>th</sup> - 21<sup>st</sup> April 2021, Warsaw, Poland.
- 4.1.4 **Jyoti**, Carlo Gonzato, Karsten Haupt, Teresa Żołek, Dorota Maciejewska, Andrzej Kutner, Piyush Sindhu Sharma, Krzysztof Noworyta, and Włodzimierz Kutner, "Acrylate Derivatives Based Molecularly Imprinted Polymer Nanoparticles for the Fabrication of Cilostazol Electrochemical Sensor," The XXVI<sup>th</sup> International Symposium on Bioelectrochemistry and Bioenergetics of the Bioelectrochemical Society, 9<sup>th</sup> - 13<sup>th</sup> May 2021, Cluj-Napoca, Romania.
- 4.1.5 **Jyoti**, Renata Rybakiewicz, Teresa Żołek, Dorota Maciejewska, Andrzej Kutner, Krzysztof Noworyta, and Włodzimierz Kutner, "Carbazole Derivatives Based Molecularly Imprinted Polymer Film for the Fabrication of Cilostazol Electrochemical Chemosensor," The 72<sup>nd</sup> Annual Meeting of the International Society of Electrochemistry (ISE), 29<sup>th</sup> August - 3<sup>rd</sup> September 2021, Jeju Island, Korea.
- 4.1.6 **Jyoti**, Teresa Żołek, Dorota Maciejewska, Andrzej Kutner, Krzysztof R. Noworyta, and Włodzimierz Kutner, "Highly sensitive and selective duloxetine electrochemical chemosensor fabricated using molecularly imprinted polymer nanoparticles," European Materials Research Society (E-MRS), 20<sup>th</sup> - 23<sup>rd</sup> September 2021, Warsaw, Poland.

## 4.2 Poster presentations

- 4.2.1 **Jyoti**, Renata Rybakiewicz, and Włodzimierz Kutner, "Synthesis and characterization of carbazole derivatives as new functional monomers for molecularly imprinted polymers (MIPs)," Microsymposium organized at IPC PAS, 16 – 18 Jan 2018, Warsaw, Poland.
- 4.2.2 **Jyoti**, Renata Rybakiewicz, and Włodzimierz Kutner, "Carbazole functional monomers for molecularly imprinted polymers. Design, synthesis, and characterization," Microsymposium organized at IPC PAS, 15 – 17 Jan 2019, Warsaw, Poland.
- 4.2.3 **Jyoti**, Renata Rybakiewicz, Teresa Zolek, Dorota Maciejewska, Krzysztof R. Noworyta, and Włodzimierz Kutner, "Carbazole functional monomers for molecularly imprinted polymers. Design, synthesis, and characterization," The Chemsession, 8 June 2018, Warsaw, Poland.
- 4.2.4 **Jyoti**, Carlo Gonzato, Renata Rybakiewicz, Frank Merlier, Karsten Haupt, Włodzimierz Kutner, Krzysztof Noworyta, "Molecularly imprinted polymer nanoparticles as the recognition unit in the cilostazol chemosensor," International Conference on Nano Science and Technology (ICONSAT), 5 – 7 March 2020, Kolkata, India.
- 4.2.5 **Jyoti**, Renata Rybakiewicz-Sekita, Evgenia Dmitrieva, Teresa Żołek, Dorota Maciejewska, Włodzimierz Kutner, Krzysztof Noworyta, "Why It Doesn't Always Lead to a Polymer Formation – interesting findings from selected carbazole derivatives," The 6th International Symposium on Surface Imaging/Spectroscopy at the Solid/Liquid Interface (ISSIS), 6 - 9 June 2021, Krakow, Poland.
- 4.2.6 **Jyoti**, Teresa Żołek, Dorota Maciejewska, Andrzej Kutner, Krzysztof Noworyta, and Włodzimierz Kutner, "Highly sensitive and selective duloxetine electrochemical chemosensor fabricated using molecularly imprinted polymer nanoparticles," The European Materials Research Society (E-MRS), 20 - 23 September 2021, Warsaw, Poland.
- 4.2.7 **Jyoti**, Teresa Żołek, Dorota Maciejewska, Andrzej Kutner, Krzysztof Noworyta, and Włodzimierz Kutner, "Molecularly imprinted polymer nanoparticles for selective electrochemical chemosensing of duloxetine - an antidepressant drug" The 10<sup>th</sup> International Workshop on Surface Modification for Chemical and Biochemical Sensing (SMCBS), 5 – 9 November 2021, Warsaw, Poland.

## 5. Short research visits

- 5.1 **Jyoti**, "The EPR-UV-vis-NIR spectroelectrochemistry study of thiophene-appended carbazole compounds" supervised by Dr. Evgenia Dmitrieva at the Leibniz Institute for Solid State and Materials Research, Dresden, Germany, 1 – 31 January 2021.
- 5.2 **Jyoti**, "Preparation of chemosensors for pharmaceuticals using molecularly imprinted polymer nanoparticles" supervised by Prof. Karsten Haupt at the University of Technology of Compiègne, Compiègne, France, 1 March till 3 August 2019.

## 6. Summer schools attended

- 6.1 29<sup>th</sup> Jyväskylä Summer School, University of Jyväskylä, Finland, 5 – 16 August 2019.
- 6.2 European School on Nanosciences and Nanotechnologies, ESONN'21, Grenoble, France, 23 August – 10 September 2021.

## **7. List of abbreviations**

### **A**

AA – acrylamide

ABDV – 2,2'-azobis(2,4-dimethylvaleronitrile)

ACN – acetonitrile

AD – Alzheimer's disease

AFM – atomic force microscopy

AIBN – 2,2'-azobis(2-methylpropionitrile)

AIF – apparent imprinting factor

ASSURED – affordable, sensitive, specific, user-friendly, rapid and robust, equipment-free, and deliverable

### **B**

BIS – *N,N'*- methylenebisacrylamide.

B3LYP – Becke-Lee-Yang-Parr's three-parameter

### **C**

CASTLE - cilostazol: A Study in Long-term Effects

CB – conduction band

CI – capacitive impedimetry

CIL – cilostazol

CL – chemiluminescence

CLM – cross-linking monomer

CNT – carbon nanotube

CE – the counter electrode

CP – conducting polymer

CV – cyclic voltammetry

CVD – cardiovascular disease

### **D**

DCM – dichloromethane

DFT – density functional theory

dhCIL – 3,4-dehydocilostazol  
DMF – *N,N'*-dimethylformamide  
DMSO – dimethyl sulfoxide  
DPV – differential pulse voltammetry  
DUL – duloxetine

## E

EA – ethyl acetate  
ECL – electrochemiluminescence  
EDC – *N*-ethyl-*N'*-(3-(dimethylamino)propyl)carbodiimide  
EPS – electrostatic potential surface  
NHS – *N*-hydroxysuccinimide  
EGDMA – ethylene glycol dimethacrylate  
EG-FET – extended-gate field-effect transistor  
EI – electron impact (ionization)  
EIS – electrochemical impedance spectroscopy  
EPR – electron paramagnetic resonance  
EQCM – electrochemical quartz crystal microbalance  
ESP – electrostatic potential

## F

FM – functional monomer  
f-MWCNTs@AuNP – (functionalized multi-walled carbon nanotubes)@gold nanoparticle  
FQ – fluoroquinolone  
FTIR – Fourier transformed infrared spectroscopy

## G

GO – graphite oxide sheet  
GO<sub>x</sub> – glucose oxidase  
GC-MS – gas chromatography-mass spectroscopy

## H

HCl – hydrochloric acid  
HDRS-17-sum – Hamilton Depression Rating Scale

HPLC – high-performance liquid chromatography

HPMA – *N*-(2-hydroxypropyl) methacrylamide

HOMO – highest occupied molecular orbital

## I

IA – itaconic acid

IC – intermittent claudication

IF – imprinting factor

IF – interferometry

IL – ionic liquid

IR – infrared (spectroscopy)

ITO – indium-tin-oxide (electrode)

IUPAC – International Union of Pure and Applied Chemistry

## L

LAH – lithium aluminium hydride

LC-ESI/MS – liquid chromatography-(electrospray ionization tandem mass spectrometry)

LOD – limit of detection

LOQ – limit of quantification

LSV – linear sweep voltammetry

LUMO – lowest unoccupied molecular orbital

## M

MAA – methacrylic acid

MCI – mild cognitive impairment

MDD – major depressive disorder

MEP – molecular electrostatic potential

MM – molecular mechanics

MD – molecular modeling

MOF – metal-organic framework

MOF@G – metal-organic framework at graphene nanocomposite

MWCNT – multi-walled carbon nanotube

MIP – molecularly imprinted polymer

## **N**

- NE – norepinephrine  
NIP – non-imprinted polymer  
NMR – nuclear magnetic resonance (spectroscopy)  
NP – nanoparticle  
NR – nanorod  
NT – nanotube

## **P**

- PAD – peripheral artery disease  
PANI – polyaniline  
PCM – polarizable continuum model  
PDA – polydopamine  
PDE<sub>3</sub> – phosphodiesterase 3  
PEDOT – poly(3,4-ethylenedioxythiophene)  
PenG – penicillin G  
PGE – pencil graphite electrode  
PM – piezoelectric microgravimetry  
PME – particle mesh Ewald  
PM-IRRAS – polarization-modulation infrared reflection-absorption spectroscopy  
PoC – point-of-care  
PPC – pre-polymerization complex  
PPy – polypyrrole  
PT – polythiophene  
Pty – polytyramine

## **Q**

- QD – quantum dot

## **R**

- RE – reference electrode  
RP-HPLC – reversed-phase high-performance liquid chromatography  
RSD – relative standard deviation

rt – room temperature

## S

S – source

SAM – self-assembled monolayer

SEC – spectroelectrochemistry

SNRI – selective serotonin and norepinephrine reuptake inhibitor

SPE – solid-phase extraction

SPR – surface plasmon resonance

SSRI – selective serotonin reuptake inhibitor

SWCNT – single-walled carbon nanotube

SWV – square wave voltammetry

## T

(TBA)ClO<sub>4</sub> – tetra-*n*-butylammonium perchlorate

(TBA)PF<sub>6</sub> – tetra-*n*-butylammonium hexafluorophosphate

Tc – tetracycline

TD-DFT – time-dependent density functional theory

TLC – thin-layer chromatography

## U

UCNP – upconversion nanoparticle

UV-vis-NIR – ultraviolet-visible-near infrared spectroscopy

UV-vis – ultraviolet-visible (spectroscopy)

## V

VB – valence band

VP – vinyl pyridine

## W

WE – working electrode

## X

XPS – X-ray photoelectron spectroscopy

## 8. List of symbols

### A

$A$  – active electrode surface area,  $\text{cm}^2$

### B

$B$  – magnetic field intensity,  $6.626 \text{ J s}$

$B_0$  – magnetic field magnitude, T

### C

$C_{\text{dl}}$  – electrical double-layer capacitance,  $\mu\text{F}$

$c$  – concentration, M

### D

$D$  – diffusion coefficient,  $\text{cm}^2 \text{ s}^{-1}$

d – doublet

### E

$\Delta E_p$  – pulse amplitude

$\Delta E_t$  – transition energy between two spin states

$E$  – potential, V vs. reference electrode

$E_f$  – final potential, V vs. reference electrode

$E_i$  – initial potential, V vs. reference electrode

$E_{\text{pa}}$  – anodic peak potential, V vs. reference electrode

$E_{\text{pc}}$  – cathodic peak potential, V vs. reference electrode

$E_t$  – potential at the time,  $t$

### F

$F$  – Faraday constant,  $96\,500 \text{ C mol}^{-1}$

$f$  – frequency, Hz

$f_o$  – oscillator strength, dimensionless quantity

### G

$\Delta G$  – Gibbs free energy change,  $\text{kJ mol}^{-1}$

*g* – Landé factor (or *g*-factor), dimensionless quantity

*g<sub>g</sub>* – gravitational acceleration

## **H**

*h* - Planck constant,  $6.63 \times 10^{-34} \text{ J}\cdot\text{Hz}^{-1}$

## **I**

$\Delta I_{\text{normalized DPV}}$  – normalized DPV peak current

$\Delta I_{\text{normalized DPV,max}}$  – maximum value of normalized DPV peak current

*I<sub>p</sub>* – peak current

*I<sub>pa</sub>* – anodic peak current, A

*I<sub>pc</sub>* – cathodic peak current, A

## **J**

*j* – imaginary number,  $j^2 = -1$

## **K**

*K<sub>L</sub>* – Langmuir constant

*K<sub>F</sub>* – Freundlich constant

*K<sub>LF</sub>* – Langmuir-Freundlich constant

## **L**

*L* – light beam path length, cm

## **M**

*m* – multiplet

## **N**

*n<sub>e</sub>* – number of electrons exchanged in the elementary electrode reaction

*n<sub>h</sub>* – homogeneity factor

## **Q**

*q* – charge, C

*q* – quartet

## **R**

$R$  – molar gas constant,  $8.31 \text{ J mol}^{-1}\text{K}^{-1}$

$R_{\text{ct}}$  – charge-transfer resistance,  $\Omega$

$R^2$  – correlation coefficient

$R_{\text{sol}}$  – electrolyte solution resistance,  $\Omega$

$R_s$  – s-polarized light reflectivity

$R_p$  – p-polarized light reflectivity

$R_f$  – retardation factor

## S

$S/N$  – signal-to-noise ratio

s – singlet

## T

$T$  – absolute temperature, K

$t$  – time, s

## V

$\Delta V$  – voltage range, V

$V_0$  – voltage amplitude

$V$  – voltage, V

$V_f$  – final voltage, V

$V_i$  – initial voltage, V

$V_L$  – volume of an electroactive layer,  $\text{m}^3$

$V_m$  – amplitude of sinusoidal voltage, V

$V_R$  – voltage applied to the reference electrode, V

$\nu$  – the resonance frequency of the microwave radiation

$v$  – potential scan rate,  $\text{mV s}^{-1}$

$\nu_m$  – magnetic field frequency, MHz

## Z

$Z$  – impedance,  $\Omega$

$Z_{\text{real}}$  – real component of impedance,  $\Omega$

$Z_{\text{im}}$  – imaginary component of impedance,  $\Omega$

$Z_0$  – impedance associated with the Faradaic process,  $\Omega$

$Z_w$  – Warburg impedance,  $\Omega$

$\alpha$  – selectivity

$\alpha_a$  – charge transfer coefficient of an anodic process

$\alpha_c$  – charge transfer coefficient of a cathodic process

$\lambda$  – wavelength, nm

$\omega$  – angular frequency, rad s<sup>-1</sup>

$\delta$  – chemical shift, ppm

$\mu_B$  – Bohr magneton,  $9.274 \times 10^{-24}$  J T<sup>-1</sup>

$\theta$  – phase angle, degree

$\xi$  – molar absorptivity or extinction coefficient, M<sup>-1</sup> cm<sup>-1</sup>

## Abstract (Eng.)

The thesis combines designing and synthesizing new carbazole functional monomers (FMs) and then using them to devise and fabricate molecularly imprinted polymers (MIPs) based electrochemical chemosensors. With these chemosensors, we have selectively determined chosen pharmaceutical drug substances, cilostazol (CIL) and duloxetine (DUL), of health importance. First, several investigations were conducted to determine the most stable pre-polymerization complexes of the analytes with the designated functional monomers. The Gibbs free energy gains of complex formation were calculated using density functional theory (DFT) with the B3LYP functional and 6-311+G(d,p) basis sets. Moreover, molecular mechanics (MM) and molecular dynamics (MD) were used for modeling molecular cavities formed in MIPs, which helped predict the chemosensor's selectivity. Guided by computer simulations, the most promising MIPs were prepared either by chemical or electrochemical polymerization, with the analytes playing the role of templates. The templates' presence in MIPs, then their extraction from the MIPs was confirmed by HPLC and PM-IRRAS measurements. For analytes determining, different electrochemical transduction techniques were used to reach high sensitivity, detectability, and selectivity. The deposited MIPs nanoparticles were characterized spectroscopically (UV-vis and DLS), electrochemically (CV, DPV, and EIS), and microscopically (AFM and SEM), while MIP films electrochemically (CV and DPV) and microscopically (AFM and SEM). Moreover, recognizing film enforcement with conducting single-walled carbon nanotubes (SWCNTs) scaffolds increased the analytical performance of the chemosensor for DUL. The developed chemosensors' detectability of the analytes in human plasma was higher than the threshold adopted in clinical analysis. The high chemosensors' selectivity allowed discriminating the analytes from their common biological interferences, including structural analogs. Langmuir, Freundlich, and Langmuir-Freundlich isotherms were fitted to DPV sorption data to determine the sorption parameters allowing to elucidate homogeneity or heterogeneity of the imprinted cavities. Furthermore, in-situ EPR/UV-vis-NIR spectroelectrochemistry combined with quantum-chemical calculations helped understand the behavior difference and origins of radical cations' stability in thiophene-appended carbazole polymer films formed during electrochemical doping and de-doping.

## Abstract (Pol.)

Praca łączy projektowanie i syntezę nowych karbazolowych monomerów funkcyjnych, a następnie ich wykorzystanie do opracowania i wytworzenia chemosensorów elektrochemicznych opartych na polimerach wdrukowanych molekularnie (MIP). Za pomocą tych chemosensorów selektywnie oznaczyliśmy wybrane farmaceutyczne substancje lecznicze, cilostazol (CIL) i duloksetynę (DUL). W badaniach wstępnych określiliśmy najtrwalsze pre-polimeryzacyjne kompleksy analitów z tymi monomerami. Zmiany entalpii swobodnej tworzenia kompleksów obliczyliśmy za pomocą teorii funkcjonału gęstości (DFT) z funkcjonałem B3LYP i zbiorami bazowymi 6-311+G(d,p). Ponadto do modelowania struktury wnęk molekularnych wdrukowanych w MIP-y wykorzystaliśmy mechanikę molekularną (MM) i dynamikę molekularną (MD), co pomogło przewidzieć selektywność chemosensorów. Kierując się symulacjami komputerowymi, za pomocą polimeryzacji chemicznej lub elektrochemicznej zsyntetyzowaliśmy najbardziej obiecujące MIP-y, w których anality pełniły rolę szablonów. Obecność szablonów w MIP-ach, a następnie ich brak po ekstrakcji potwierdziliśmy za pomocą pomiarów HPLC i PM-IRRAS. Do oznaczania analitów zastosowaliśmy różne elektrochemiczne techniki przetwarzania sygnału rozpoznawania chemicznego, aby osiągnąć wysoką czułość, wykrywalność i selektywność. Osadzone nanocząstki MIP-ów scharakteryzowaliśmy spektroskopowo (UV-vis i DLS), elektrochemicznie (CV, DPV i EIS) i mikroskopowo (AFM i SEM), natomiast ciągłe warstwy MIPów - elektrochemicznie (CV i DPV) i mikroskopowo (AFM i SEM). Wzmocnienie warstwy rozpoznającej za pomocą rusztowań z jednościeniowych nanorurek węglowych (SWCNT) podwyższyło analityczną sprawność chemosensora do oznaczania DUL. Wykrywalność chemosensorów względem ww. analitów w ludzkim osoczu była wyższa niż ich próg detekcji przyjęty w analizie klinicznej. Wysoka selektywność chemosensorów umożliwiła odróżnienie analitów od typowych biologicznych substancji przeszkadzających w ich oznaczaniu, w tym analogów strukturalnych. Do danych sorpcji DPV dopasowano izotermy Langmuira, Freundlicha i Langmuira-Freundlicha, aby wyznaczyć parametry sorpcji umożliwiające wyjaśnienie jednorodności lub niejednorodności wdrukowanych wnęk. Ponadto spektroelektrochemia EPR/UV-vis-NIR in-situ w połączeniu z obliczeniami kwantowo-chemicznymi pomogła zrozumieć różnicę w zachowaniu i przyczynę trwałości kationów rodnikowych, wytworzonych w polimerowych warstwach karbazolu z dołączonym tiofensem, powstałych podczas elektrochemicznego domieszkowania i od-domieszkowania.

# Table of contents

1. Declaration of originality .....	v
2. Acknowledgements .....	vii
3. Funding .....	ix
4. List of publications .....	x
4.1 Publications included in the thesis.....	x
4.2 Publications not included in the thesis.....	xi
5 . List of patent applications .....	xii
6. Active participation at international conferences .....	xiii
6.1 Oral presentations .....	xiii
6.2 Poster presentations .....	xiv
7. Short research visits .....	xv
8. Summer schools attended .....	xv
9. List of abbreviations .....	xvi
10. List of symbols .....	xxi
11. Abstarct (Eng.).....	xxiv
12. Abstarct (Pol.).....	xxv
Chapter 1 .....	1
1. Introduction .....	1
1.1 Background .....	1
1.2 State-of-art .....	3
1.3 Literature review and research goals for the analyte targets .....	31
1.4 Research objectives .....	36
Chapter 2 Experimental Section .....	38
2.1 Chemicals and materials .....	38
2.2 Procedures .....	43
2.3 Experimental techniques and instrumentation .....	56
Chapter 3 .....	80
An insight into the polymerization mechanism of selected carbazole derivatives - Why does it not always lead to polymer formation? .....	80

3.1 Introduction .....	82
3.2 Experimental procedures .....	82
3.3 Result and discussion .....	84
3.4 Conclusions .....	106
Chapter 4 .....	108
4.1 Molecularly imprinted polymer nanoparticles-based electrochemical chemosensors for selective determination of cilostazol and its pharmacologically active primary metabolite in human plasma .....	108
4.1.1 Introduction .....	110
4.1.2 Experimental and procedures .....	111
4.1.3 Results and discussion .....	112
4.1.4 Summary and conclusions .....	128
4.1.5 Future prospective .....	128
4.2 Cilostazol-imprinted polymer film-coated electrode as an electrochemical chemosensor for selective determination of cilostazol and its active primary metabolite .....	129
4.2.1 Introduction .....	131
4.2.2 Experimental and procedures .....	131
4.2.3 Results and discussion .....	133
4.2.4 Conclusions .....	146
Chapter 5 .....	147
Polytyramine film-coated single-walled carbon nanotube electrochemical chemosensor with molecularly imprinted polymer nanoparticles for duloxetine selective determination in human plasma .....	147
5.1 Introduction .....	149
5.2 Experimental section and procedures .....	149
5.3 Results and discussion .....	150
5.4 Conclusions .....	165
Chapter 6 .....	167
Research summary and future perspectives .....	167
Appendix .....	170
References .....	178





# Chapter 1

## 1. Introduction

The present chapter provides the main characteristics of literature studies required to comprehend the experiments described in the thesis results and conclusions. The chapter's first section covers the significance and necessity of quantifying drug substances to monitor the world's rising population health. Next, the chemosensor and point-of-care systems are briefly explained. Then, the state-of-art section describes molecularly imprinted polymers (MIPs) syntheses, types, and applications. This latter section is crucial. It presents significant improvements that have been made so far in the field. The final section focuses on a critical evaluation of the literature describing strategies for cilostazol (CIL) and duloxetine (DUL) drugs quantification. This section provides an overview of the field's status quo and the issues it faces. The final part of the Introduction describes the research objectives.

### 1.1 Background

#### 1.1.1 The importance of health monitoring

The rapidly increasing human population has led to the surging growth of healthcare, hence the pharmaceutical industry and new biomedical issues.<sup>1</sup> In recent years, we have witnessed an enormous boom in drug production, quality control, and delivery. Moreover, consumers spend billions of dollars annually on detecting and quantifying analytes in clinical settings, e.g., routine blood testing; still, drug overdosing and personalized health monitoring remain a concern.<sup>2</sup> For instance, in 2019, according to National Center for Health Statistics, 70,630 deaths were recorded from the toxic effects of a drug overdose in the United States,<sup>3</sup> which was by 4.8% higher than in 2018. In Scotland, 49% of the drug treatment-seeking population had experienced a drug overdose.<sup>4</sup> It is estimated that at least 8238 overdose deaths occurred in the European Union in 2017.<sup>5</sup> Drug overdose deaths remain a persistent and urgent public health problem worldwide.<sup>6,7</sup> Furthermore, timely health monitoring can decrease human suffering and medical costs, particularly the early diseases diagnoses, leading to improved alternatives for the patient's medical treatment. Therefore, there is an urgent need for sensitive, selective, portable, and cost-effective techniques for drug quantification in patients from the

point of view of personalized drug dosage.<sup>8</sup> But the main challenge of medical clinics and pharmaceutical institutions is the large-scale quantification of the drugs, i.e., in a large number of samples. Until now, many drug quantification methods use such analytical techniques as high-performance liquid chromatography (HPLC), (liquid chromatography)-(electrospray ionization tandem mass spectrometry) (HPLC-ESI/MS/MS), and gas chromatography-mass spectrometry (GC-MS). However, the instruments used to execute these techniques are expensive, require high-grade solvents, sophisticated handling, trained personnel to operate them, and determinations are time-consuming. Therefore, cheaper and easier-to-use alternatives are explored. One is developing determination methods using chemical or biochemical sensors (chemo- and biosensors).

### **1.1.2 What are chemo and bio-sensors?**

A chemosensor, also known as a molecular sensor or probe, is a molecular or supramolecular-based measurement device that can transform the act of analyte recognition into a readable signal.<sup>9</sup> On the other hand, a biosensor is an analytical device that uses biochemical reactions, mediated by isolated enzymes, immune systems, tissues, organelles, or whole cells, to detect and determine chemical compounds, usually via generating electrical, thermal, or optical signals.<sup>10</sup> The chemo- and biosensors are generally composed of two integrated units, vis., the receptor or recognition, and transduction unit.

Chemosensors can be categorized based on their receptors working principle as affinity and catalytic chemosensors. They can also be divided based on signal-transducing, including electrochemical,<sup>11-13</sup> capacitive,<sup>14</sup> calorimetric,<sup>15</sup> fluorometric,<sup>16</sup> piezoelectric,<sup>17</sup> optical,<sup>18</sup> and piezoresistive<sup>19</sup> sensors. Chemosensors are easy to prepare, have a low limit of detection (LOD) and quantification (LOQ), are generally stable, and are reusable or disposable. Moreover, they can detect and quantify ions, small molecules, biomolecules, including proteins, peptides, nucleic acids, and even whole microorganisms, like bacteria, etc. Therefore, the number of chemosensors has over the past decade rapidly grown and made to provide non-invasive monitoring and real-time information acquiring of, e.g., a patient's health status in daily life.

### **1.1.3 Point-of-care (PoC) systems**

Point-of-care (PoC) devices serve diagnostics that can readily be used in hospitals, airports, and, remarkably, patients at homes due to providing an adequate LOD, easy use, cost-effectiveness, and rapid response.<sup>20–22</sup> For the last decade, there has been a tremendous improvement in developing PoC systems to overcome several problems, including long awaiting the determination results and handling sophisticated instruments used in the traditional clinical analysis.<sup>22</sup> The ASSURED principle is assumed for PoC devices, which stands for affordable, sensitive, specific, user-friendly, rapid and robust, equipment-free, and deliverable to end-user operations.<sup>23</sup> PoC systems have made the patients' lives easier, especially in the diagnosis based on the determination of biomolecular compounds.<sup>24,25</sup>

## **1.2 State-of-art**

### **1.2.1 Molecularly imprinted polymers (MIPs)**

A molecularly imprinted polymer (MIP) is an artificial receptor made by imprinting a template molecule in a polymer matrix. It works based on the so-called “lock and key” principle.<sup>26,27</sup> Simply, molecular imprinting (Scheme 1-1) involves the formation of a pre-polymerization complex of functional monomers (FMs) with the target analyte in a solution, which serves as the template at this first imprinting stage. Then, this complex is polymerized, often in the presence of a cross-linking monomer (CLM), to assure appropriate robustness, rigidity, and permeability of the resulting MIP. Next, the template is removed from the MIP via, e.g., solvent extraction, thus vacating imprinted molecular cavities. The size and shape of these cavities and the orientation of their recognizing sites complement the size, shape, and orientation of binding sites of the template molecule.<sup>27,28</sup> For compatibility of the molecular cavity and the analyte molecule, the template often used in the first stage of MIP preparation is either the analyte itself or its close structural analog. Based on the binding mode used to prepare the pre-polymerization complex, the imprinting can be classified into three categories, i.e., covalent, semi-covalent,<sup>29</sup> and non-covalent imprinting.<sup>30</sup> Molecular imprinting in polymers leads, among others, to synthetic receptors of selectivity nearly as high as that of their biological counterparts.

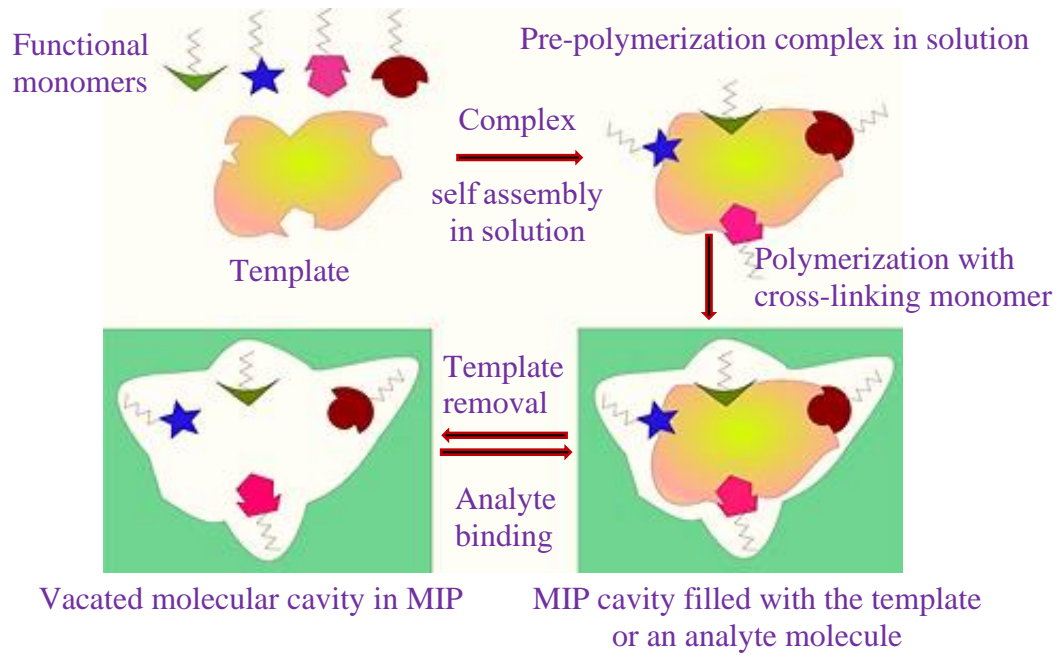
Covalent imprinting involves a molecular imprinting strategy whereby covalent bonds are formed between the template molecule and one or more FM molecules to form a “template–monomer” pre-polymerization complex by a chemical step independent of polymer formation.<sup>31</sup> This imprinting is particularly useful in the case of compounds with no functionalities. The most common way of covalent imprinting involves reversible condensation reactions forming boronate ester, ketal/acetal, and Schiff's base in the complex. The main advantage of covalent imprinting consists in strict control of stoichiometry of the template molecule binding with FMs molecules resulting in the homogenous molecular cavities formation in the polymer and, therefore, limited non-specific binding. Moreover, the strength of the covalent bond is independent of the dielectric properties of the medium. However, covalent imprinting has its drawbacks; for example, the formed complexes are very sensitive to the water presence, preventing the use of emulsion and suspension polymerization methods and harrowing template extraction.

Another approach to MIP preparation involves using FMs that can form a covalent complex with the templates on the one hand and are capable of non-covalent interaction with the analyte after polymerization and template removal on the other. This approach, referred to as semi-covalent imprinting, was introduced by Whitcombe in 1995.<sup>32</sup> Most often, this imprinting involves the formation of ester bonds. Then, these bonds yield free carboxyl groups in the polymer cavities that can bind the analyte through hydrogen bonds. Moreover, this procedure can be used to generate cavities featuring recognition sites interacting with the analyte that contains other than the carboxyl group, e.g., the hydroxyl or amine group. This imprinting, similarly to covalent imprinting, allows forming of homogenous molecular cavities.

Non-covalent imprinting is the most commonly used imprinting procedure. It allows for a straightforward pre-polymerization complex formation via weak electrostatic interactions, including hydrogen bonds, van der Waals forces, and hydrophobic interactions. Its main advantage is the ease of subsequent template removal from the MIP. Moreover, it requires much less chemistry than the pre-synthesis of covalent adducts.

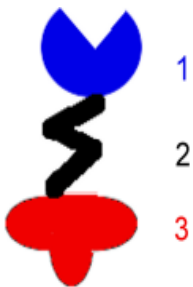
Over the years, the MIPs preparation field has enormously expanded due to the freedom of computer-aided molecular designing of monomers and polymers, giving artificial receptors a significant advantage over those natural. Their frameworks are not restricted to mostly

proteins, unlike natural receptors. Different molecular skeletons, e.g., long carbon chains, fused aromatic rings, etc., can enhance MIPs' stability, flexibility, durability, etc. Moreover, MIPs can feature recognizing sites not encountered in nature. Furthermore, if necessary, by using appropriate functionalities, the stimuli-activated polymers can be prepared that are triggered by photoirradiation, abrupt change of the pH, electric or magnetic field, and others.



**Scheme 1-1.** A scheme of consecutive steps of a molecularly imprinted polymer (MIP) preparation.

MIP designing needs the selection of proper FMs. The FMs are compounds that hold different functionalities. These functional groups or sites are capable of analyte binding. Often, they are called recognizing moieties interacting with the template molecule. Moreover, the FMs contain a polymerizing moiety. Sometimes, according to the need, a spacer between the polymerizing and recognizing moieties is introduced to create molecular cavities of pre-defined properties (Scheme 1-2). The purpose of the polymerizing moiety is to form a polymer while the functionalities interact with template molecules effectively.



**Scheme 1-2.** A schematic view of a functional monomer molecule featuring three different parts of (1) the recognizing moiety, (2) the spacer, and (3) the polymerizing moiety.

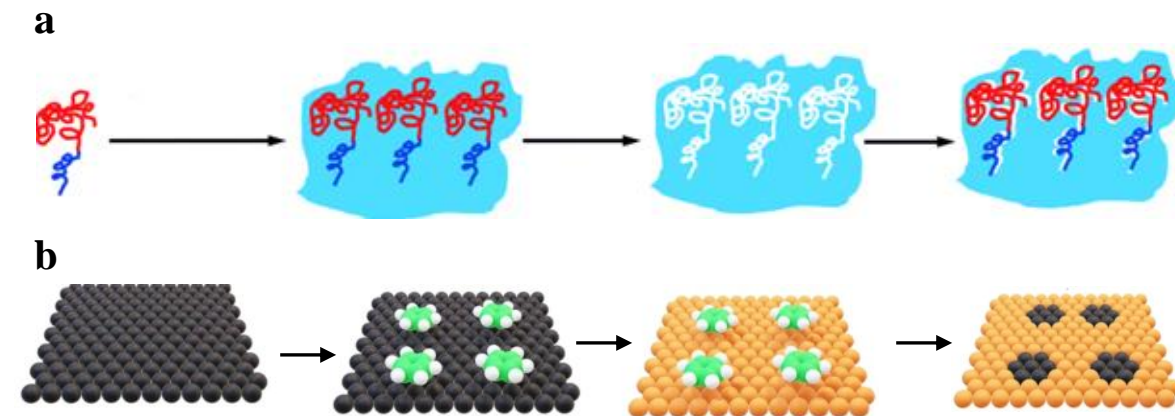
Molecular imprinting in polymers is versatile.<sup>33,34</sup> It opens doors to many applications, including purification and separation,<sup>35–39</sup> drug delivery,<sup>40,41</sup> chemosensing,<sup>28,42</sup> catalysis,<sup>43</sup> diagnosis,<sup>44,45</sup> and analyte determination<sup>46–48</sup> to name a few. The latter has already been employed to determine a broad assortment of target analytes ranging from small-molecule compounds (e.g., amino acids and sugars) to macromolecular compounds (e.g., peptides, proteins, nucleic acids, etc.), cells, and even whole microorganisms.<sup>40,49,50</sup> Several reports claim MIPs as alternatives to antibodies.<sup>50–52</sup> The most impressive advantage of MIPs is their physical and chemical resistance, straightforward preparation, and easy coupling to different substrates or integration with various chemosensor transducers. Recently, MIPs have been applied in PoC devices.<sup>53,54</sup>

MIPs first emerged in 1981 thanks to K. Mosbach and B. Sellergren.<sup>55,56</sup> They focused on using non-covalent interactions between the host and the target, leading to bulk polymers.<sup>27</sup> Typically, bulk polymerization requires a template, different monomers, and a suitable initiator to form a highly cross-linked monolith rigid type polymer matrix (Scheme 1-3a). Therefore, its cavities accessibility is low. The polymerization is followed by grinding and sieving, which is time-consuming and causes the loss of a substantial amount of the MIP material. This rigid and condensed monolith structure hinders the complete removal of the template, and some trapped “dead” sites in the imprinted polymer are left. Moreover, the bulk MIP grinding yields non-uniform particles where the binding sites are heterogeneously distributed. MIPs prepared via traditional bulk polymerization are heterogeneous. Their mass transfer and recognizing ability are relatively low.<sup>57,58</sup> For overcoming these limitations, MIPs nanoparticles (nanoMIPs) were devised.<sup>50,59</sup> They can be prepared by various chemical polymerization

methods, including solid-phase extraction, precipitation, dispersion, emulsion, and suspension polymerization.

Surface imprinting has attained enormous attention in improving MIP performance because it eliminates the difficulty of limited mass transfer and template removal encountered in the standard molecular imprinting procedure. This advancement is highly valuable if imprinting macromolecules, where diffusion limitation is a key issue (Scheme 1-3b).

NanoMIPs have attracted much attention because of their advantageously high surface-to-volume ratio, providing high cavities accessibility for target molecules and significantly enhancing the recognizing ability and kinetics. However, this ability relies on the precise parameters selection that influence the imprinting. Several vital issues, including selecting FMs<sup>60-62</sup> and CLMs,<sup>63</sup> porogenic solvents,<sup>64</sup> initiators,<sup>65</sup> polymerization procedures,<sup>66</sup> polymerization time,<sup>67</sup> and polymerization temperature,<sup>67</sup> influence the imprinting.



**Scheme 1-3.** An illustration of two main strategies for macromolecule imprinting (a) “bulk” imprinting and (b) “surface” imprinting (adapted from<sup>68,69</sup>).

A wide range of different FMs, varying from those capable of forming non-conducting, e.g., acrylic and silane polymers, and self-assembled monolayers (SAMs) to conducting-polymer-forming FMs, were used for preparing MIP-based recognition units of chemosensors. MIP formats with relatively high recognizing properties expect an enhancement in the performance and suit the desirable final application, such as beads, films, or nanoparticles.

Fortunately, advances in software development and an increase in computational computer capacity have enabled the application of molecular simulations based on mathematical modeling. Various modeling methods, including molecular mechanics (MM) and molecular

dynamics (MD), semi-empirical, as well as density functional theory (DFT) “ab initio” have been introduced to select functional monomers and estimate their recognizing modes. As a result, researchers can now estimate the Gibbs free energy gains due to pre-polymerization complex formation using various methods. The DFT-based approach at various approximation levels and basis sets has been extensively explored due to this method's high accuracy and low computation cost. A higher negative gain in this energy indicates a higher possibility of stable complex formation. However, some investigations suggest that an MIP chemosensor can be insensitive to the analyte even though the DFT calculation result was promising. A possible reason for that could be a very high negative gain in Gibbs free energy, indicating a firm contact between the analyte molecule and the recognizing sites of the polymer cavity preventing facile analyte extraction.<sup>70</sup> With this preliminary screening step, the strongest binding functional monomers can be identified and hence advantageously used for imprinting a particular target analyte. This first modeling step of MIP preparation saves money for chemicals and time for laboratory imprinting tries and errors. Moreover, modeling the MIP cavity interactions with the analyte and interference molecules is possible. These results can help in cross-validating the experimental analysis with simulations' results.

The MIP selectivity and sensitivity play an essential role in MIP-based chemosensor preparation. Moreover, the undesired non-specific binding of the analyte in the MIP, i.e., outside the imprinted cavities, is a crucial factor. Therefore, an essential measure of the imprinting efficiency of the MIP is its imprinting factor, *IF* (Equation 1-1). The higher the *IF*, the higher is the binding capacity and eventually low non-specific binding. Moreover, the MIP recognizing mechanism of analyte molecules is mainly associated with the degree of spatial structure matching of recognizing sites and the analyte molecule. In other words, the MIP selectivity (Equation 1-2) depends on the efficiency of binding between the template and monomer molecules and the shape and rigidity of the template and the cavity.

$$\text{Imprinting factor (IF)} = \frac{\text{Fraction of analyte bound to the MIP}}{\text{Fraction of analyte bound to the NIP}} \quad (\text{Equation 1-1})$$

$$\text{Selectivity factor } (\alpha) = \frac{\text{Slope of the calibration plot for the analyte}}{\text{Slope of the calibration plot for the interference}} \quad (\text{Equation 1-2})$$

### **1.2.2 Molecularly imprinted polymers for sensing drug substances**

MIPs are widely used in chemosensing, but their use is not restricted to electrochemical sensing.<sup>71</sup> Other transductions are also employed to devise handy and simple-to-use chemosensors (Table 1-1). In recent years, the number of research papers on chemosensors using MIP recognition has enormously increased,<sup>72</sup> and acrylic-based monomers accounted for more than half of all contributions, outnumbering (conducting polymer)-forming FMs (Figure 1-1). Notably, there has been considerable development in MIP-based optical sensors with luminescence transduction; however, electrochemiluminescence MIP chemosensors share only a small part.

Similarly, when it comes to "electrochemical sensors," a comparable survey indicates a more significant contribution of acrylic-based MIPs.<sup>73</sup> Because no direct channel for electron transfer from the recognizing sites of molecularly imprinted cavities to the electrode surface exists, it appeared impossible to manufacture an electrochemical sensor using the acrylic-based MIPs. Incorporating these non-conducting recognition units in films with conducting scaffolds, notably carbon allotropes, helped overcome these challenges. Furthermore, the breakthrough of various transduction methods, such as capacitive impedimetry (CI) and piezoelectric microgravimetry (PM), not requiring any recognition unit to be conductive, has broadened the range of acrylic-based MIPs uses in electrochemical sensors.

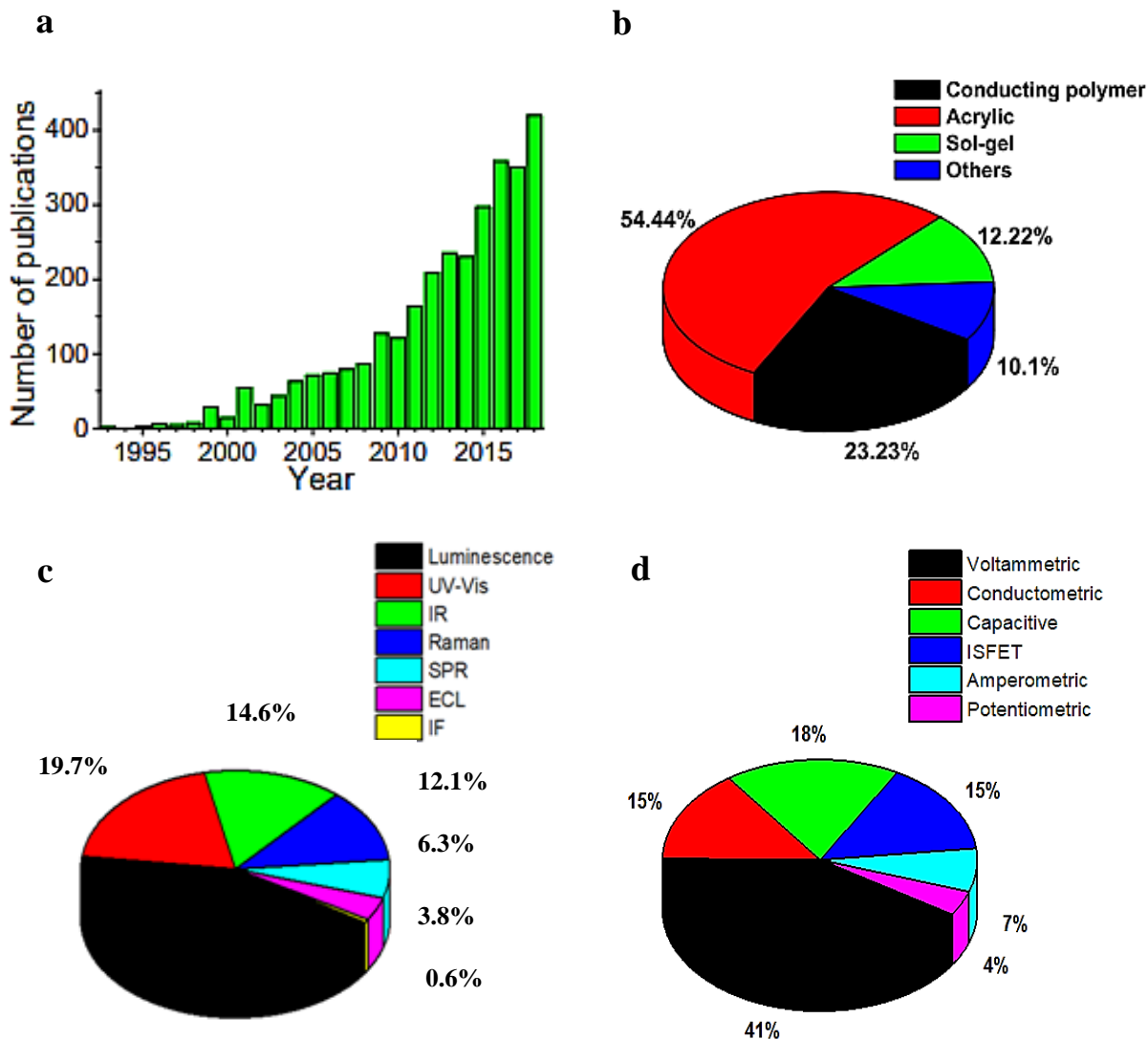


**Figure 1-1.** The number of publications on (a) MIPs used for chemosensor development in 1993–2018. (b) Contribution of different functional monomers to the preparation of all MIP-based chemosensors. (c) Optical transduction used for chemosensors, published in 2018. (d) Distribution of publications on electrochemical chemosensors according to types of transductions. UV-vis - ultraviolet-visible (spectroscopy); SPE - solid-phase extraction; IR - infrared (spectroscopy); SPR - surface plasmon resonance (spectroscopy); ECL - electrochemiluminescence (spectroscopy); IF - interferometry (adapted from<sup>72–74</sup>).

**Table 1-1.** Polymerization methods of MIPs preparation, their advantages and disadvantages, recent representative examples of drug substances determination with different MIP chemosensors, and signal transduction methods.

Polymerization method	Advantages	Disadvantages	Exemplary template drug substance	Transduction method	Ref.
<b>Precipitation polymerization</b>	The most straightforward polymer particle formulation; no stabilizer (surfactant) is required; generally spherical particles; reasonably homogeneous size distribution	Final particle size is highly dependent on component thermodynamics; the need to thermodynamically facilitate precipitation limits monomer-porogen compatibility	Midazolam	Voltammetry	75
			(S)-Propranolol	Spectro-fluorometry	76
			Paracetamol	Fluorescence spectroscopy	77,78
<b>Emulsion polymerization</b>	Better heat control of the process; water-compatible, Regular shape MIP microspheres are obtained	Requires emulsifying surfactant for synthesis	Metronidazole	Fluorescence spectroscopy	79
			Penicillin G (PenG)	Reflectometric interference spectroscopy	80
<b>Suspension polymerization</b>	Synthesis parameters can control particle size; water-compatible process	Requires integrated mechanical mixing for suspension & stabilizing agents	Chlorpromazine	Square wave voltammetry	81
			Ephedrine	Optical	82
<b>Solid-phase polymerization</b>	"Soluble" particles are suitable for in vitro applications. Affinity separation isolates the best-formed receptors, leading to the highest specificity and sensitivity of contemporary MIP formats	Low capacity & yield	Diazepam, nordiazepam, oxazepam, temazepam and nitrazepam	Liquid chromatography-tandem mass spectrometry	83
<b>Core-shell swelling polymerization</b>	Particle size can be controlled; large sizes can be obtained – results in highly uniform material suitable as a column packing media	The time-consuming multiple-step process to grow particles to size; a stabilizer is often necessary	Paracetamol	Differential pulse voltammetry	84
			Diclofenac	Surface plasmon resonance spectroscopy	85
			Capecitabine	Square wave voltammetry	86

<b>Particles embedding in thin polymer layers</b>	Separation of particle and layer synthesis gives more leeway for facile optimization; sub-frit sized particles can be used, and the size effect is minimized	Separation of synthesis steps increases inter-device irregularly	Chlorambucil	Voltammetry	<sup>87</sup>
			Timolol	Square wave voltammetry	<sup>88</sup>
			Sertraline	Differential pulse voltammetry	<sup>89</sup>
<b>Thin polymer films, layers, and membranes</b>	Highly suitable for specific sensor applications; greatest level of interface between transducer and MIP; individual properties can be tuned accordingly	Poor control of layer thickness; susceptible to the "gate effect."	Acetaminophen	Voltammetry	<sup>90</sup>
			Paracetamol	Amperometry	<sup>91</sup>
			Dextromethorphan	Potentiometry	<sup>92</sup>
			Doxycycline	Electrochemiluminescence spectroscopy	<sup>93</sup>

### 1.2.3 Acrylate-based molecularly imprinted polymers for sensing drug substances

Acrylates are acrylic acid salts, esters, and conjugate bases. They reveal intriguing bifunctionality, i.e., their vinyl group can be used for polymerization and the carboxyl for carrying various functionalities. Acrylate polymers display various features, including high glass transition temperature,  $T_g$ ,<sup>94</sup> thermal stability,<sup>95</sup> appealing mechanical properties, and transparency,<sup>94,96</sup> allowing for wide use, including MIPs.

In MIPs, the most successful non-covalent imprinting is based on methacrylic acid (MAA), cross-linked with ethylene glycol dimethacrylate (EGDMA) because the MAA carboxyl serves as both hydrogen donor and acceptor.<sup>97</sup> Moreover, MAA can form stable cyclic hydrogen bonds with suitable templates.<sup>98</sup> A library of acrylate-based monomers is used to synthesize MIP-based recognition sites in MIP chemosensors (Figure 1-2).

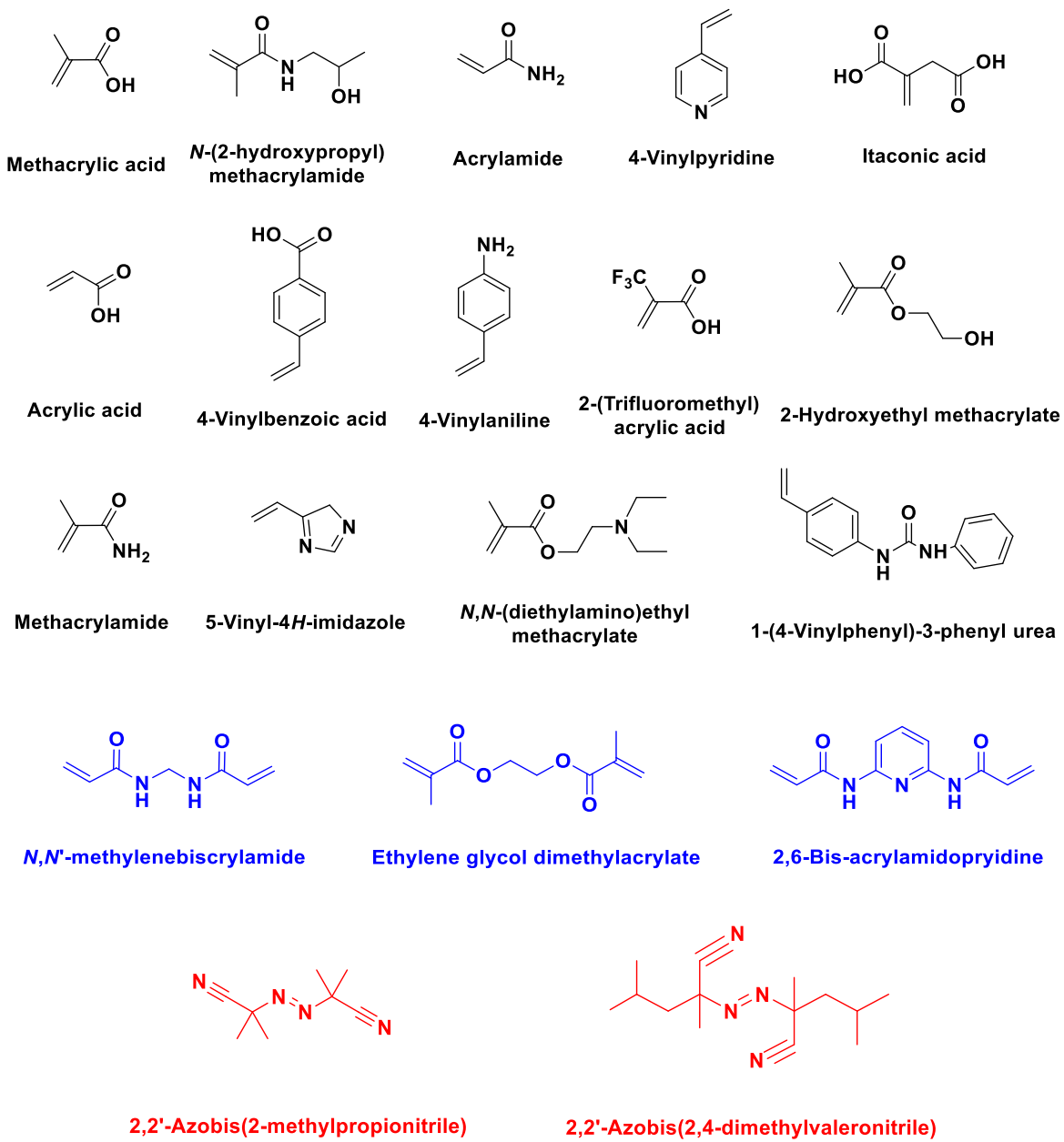


**Figure 1-2.** Structural formulas of commonly used acrylate-based functional monomers, cross-linking monomers, and initiators.

Globular MIP beads are commonly fabricated by heterogeneous polymerization, including emulsion, suspension, dispersion, precipitation polymerization,<sup>99</sup> and solid-phase syntheses.<sup>100</sup> For direct application in chemosensors, MIPs in the particles form are unsuitable. Therefore, some initial chemosensor preparations were attempted by directly immobilizing fine MIP particles on different transducers' surfaces. One exciting method of quantifying the non-electroactive antibiotic vancomycin drug<sup>101</sup> was a solid-phase synthesis yielding highly

selective electroactive nanoMIPs. For that, two ferrocene-derivatized monomers, namely vinyl ferrocene and ferrocenyl methyl methacrylate, were exploited. X-ray photoelectron spectroscopy (XPS) verified the content of the ferrocene probe by estimating the population of ferrocene moieties in the nanoparticle structure. The nanoMIPs were anchored to a Nafion<sup>TM</sup> film modified electrode by direct self-assembly. That enabled indirect electrochemical vancomycin determination by the change in redox behavior of the ferrocene probe upon chemosensor exposure to vancomycin. A linear dynamic vancomycin concentration range was 83 to 410  $\mu\text{M}$  with the sensitivity of  $0.146 \mu\text{M}^{-1}$  and high repeatability (relative standard deviation, RSD = 6.7% at  $n = 3$ ), evidencing high chemosensor reliability.

The above techniques have all been adopted, with a high or low success, in MIPs preparing, the most widely used being precipitation polymerization.<sup>102</sup> This polymerization method was developed by the Stöver group in 1993.<sup>103</sup> Generally, precipitation polymerization is a heterogeneous polymerization that commences as a homogeneous reaction in a continuous phase, where the monomer and initiator are soluble in the solvent used. But after initiation, the produced polymer is insoluble and, hence, precipitates. Several strategies of precipitation polymerization, based on conventional free radical polymerization, have so far been elaborated, including traditional thermo-induced precipitation polymerization,<sup>104–108</sup> photoinduced precipitation polymerization,<sup>109</sup> and distillation precipitation polymerization, all leading to homogenous cross-linked globular polymer particles. Ye et al.<sup>110</sup> first applied precipitation polymerization to MIPs preparation by synthesizing MIPs beads in a sub-micrometer size range. This polymerization is relatively facile, resulting in evenly dispersed micro- and nanobeads without additives, including stabilizers, use.<sup>102,111</sup> However, as indicated above, HPLC and GC-MS techniques are usually exploited for analyte quantization because of no reporting units incorporated in acrylate polymers. Therefore, there is a need to prepare a suitable transducer on which these acrylate-imprinted polymers can be immobilized. Remarkably, integrating electrochemical and optical transducers with MIPs leads to a more sensitive chemosensor.

Recently, numerous advancements in transduction units for acrylate-based MIP chemosensors, prepared by precipitation polymerization, have been scrutinized. Because of simplicity and low limits of detection, fluorescence-based determinations have become a popular signaling approach in recent years, spurring the development of different fluorescence-based chemosensing schemes. One involves the luminescent “double recognition” method using an aptamer-MIP, in conjunction with upconversion nanoparticles, UCNPs, ( $\text{NaY}_{0.78}\text{F}_4:\text{Yb}_{0.2},\text{Tm}_{0.02}$ ) to determine the enrofloxacin antibiotic. In this study, aptamers were immobilized on the UCNPs surface, and an aptamer complex with enrofloxacin was formed (Figure 1-3). The proposed sensing method was applied to determine enrofloxacin in different fish samples. Recovery and RSD values, 87.05 to 96.24% and 1.19 to 4.83%, respectively, were high, with the limits of detection and quantification of 0.04 and 0.12 ng/mL, respectively. Moreover, selectivity to fluoroquinolones (FQs) interferences was high.

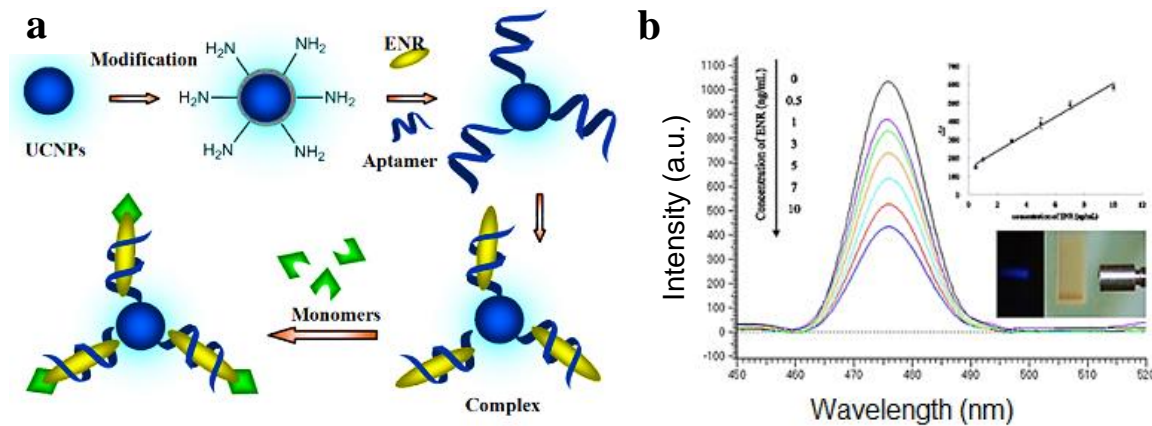


**Figure 1-3.** (a) Schematic representation of the apta-MIP/UCNPs and (b) luminescent spectra of apta-MIP/UCNPs at different enrofloxacin concentrations; UCNPs - upconversion nanoparticle. (adapted from.<sup>112</sup>)

In another research, a one-pot synthesis led to highly efficient, hydrophilic, and fluorescent nanoMIPs (Figure 1-4). An optical chemosensor using these nanoMIPs quantified a tetracycline (Tc) broad-spectrum antibiotic directly in the real, undiluted complex biological serum with the LOD of 0.26  $\mu\text{M}$  and recovery of 98 to 102%. The introduction of hydrophilic polymer brushes and fluorescence labeling onto/into the nanoMIPs significantly improved analyte binding-induced fluorescence quenching properties. However, despite the benefits of

luminescence-based measurements, such as simplicity, low detection limits, etc., there is little research on MIP-based fluorescence sensors for non-fluorescent analytes.

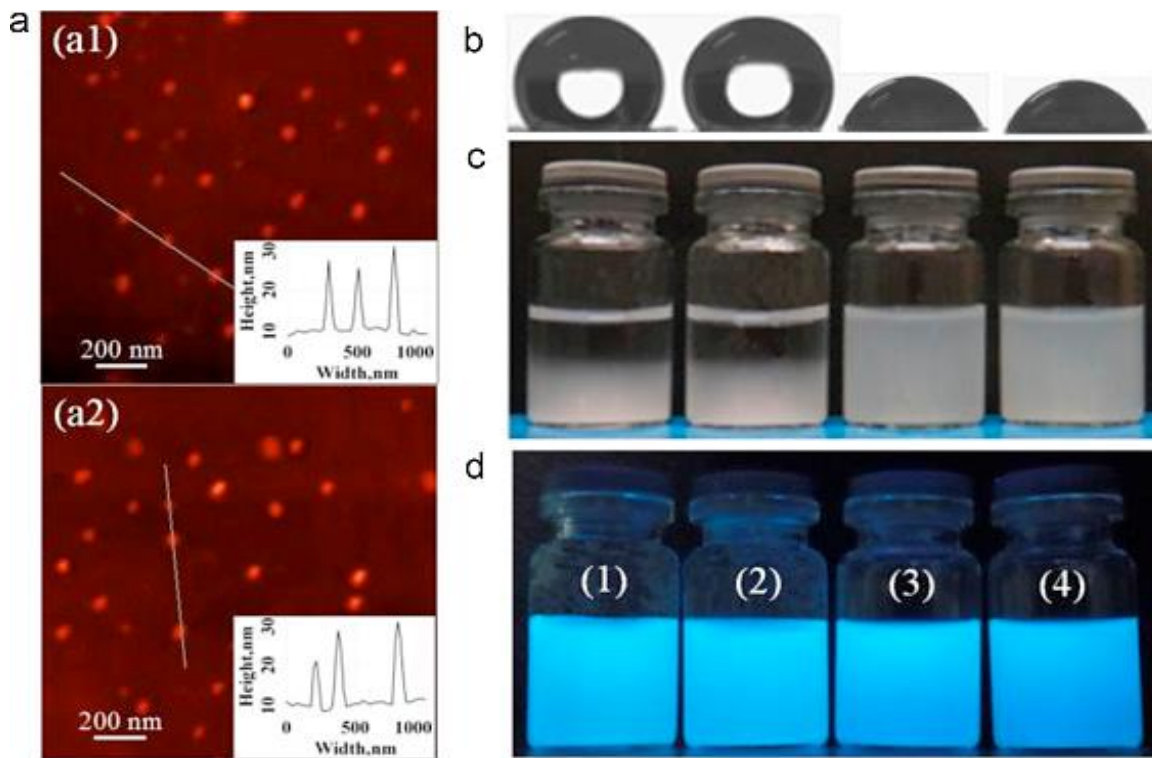


**Figure 1-4.** (a) AFM images of the grafted fluorescent Tc-MIP, (a1) Tc-control polymer, (a2) nanoparticles; inset is a height profile of cross-section (white line). (b-d) Profiles of a water drop on the films of the ungrafted and grafted fluorescent Tc-MIPs/Tc-CPs, (b) their dispersion photographs in pure water (1 mg/mL) at 25 °C after settling down for 1 h (under daylight irradiation), (c) photographs of their homogeneously dispersed samples in water (1 mg/mL) under 365 nm UV light irradiation. (d) The samples from left to right are the ungrafted Tc-MIP (1)/Tc-CP (2) and grafted Tc-MIP (3)/Tc-CP (4) (adapted from<sup>113</sup>); Tc - tetracycline.

Moreover, MIP particles were integrated within, e.g., chitosan,<sup>114,115</sup> polydopamine,<sup>116</sup> or a conducting polymer (CP) film by electropolymerization on an electrode surface.<sup>42,117</sup> This integration led to immediate signaling by the actuator upon any event of binding of an analyte molecule. Noticeably, these attempts were considered to be the preliminary steps for the fabrication of real electrochemical chemosensors.

#### 1.2.4 Electrosynthesized MIP-based sensors

An interesting approach in which electrochemistry meets imprinting technology has led to designing composite sensing materials based on the entrapment of chemically prepared MIP particles into the electropolymerized films. The electrochemical characteristics of the target analyte often guide the measurement techniques selection. According to the analytical signal output, the measurement is the potential (V) in potentiometry, the current (A) in voltammetry and amperometry, the resistance ( $\Omega$ ) in impedance, and the conductivity (S) in the conductance technique. The current generated in amperometry or voltammetry can be used to quantify electroactive substances; however, non-electroactive targets may alter the MIP film's conductivity and or porosity. This alteration could indirectly be regulated and monitored using CV, conductometry, or electrochemical impedance spectroscopy (EIS) with an external redox probe. Redox probes, including hexacyanoferrate(III), hexaammineruthenium(II), or ferrocene, are most commonly used with MIPs for indirect determinations because of their fast charge transfer at several chemically modified and or unmodified transducers. Figure 1-5 demonstrates the general concept of direct and indirect transduction systems involving the MIP.

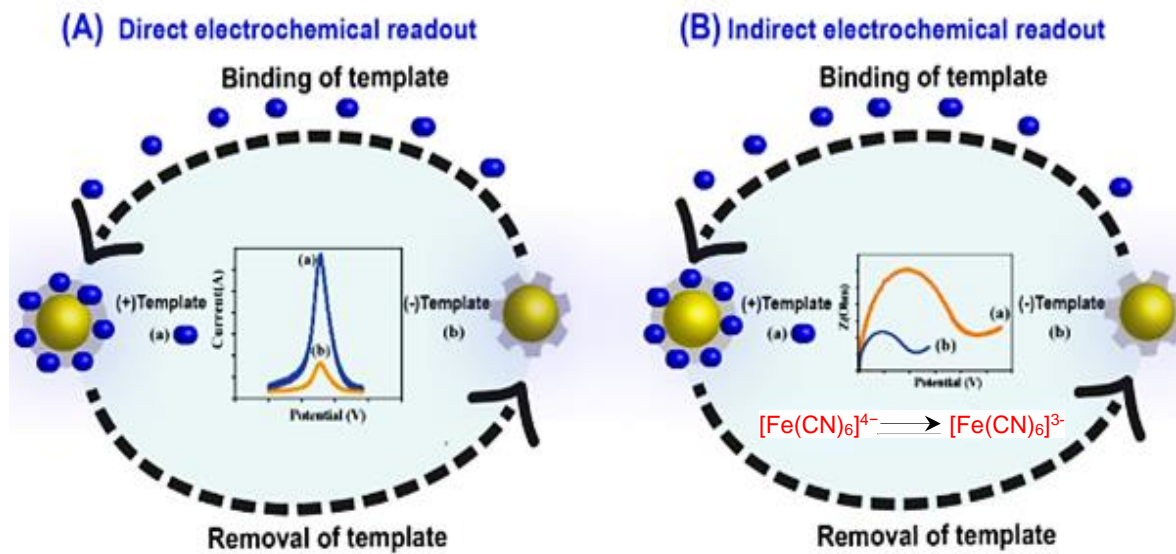


**Figure 1-5.** Graphical sketch of generic (A) direct and (B) indirect electrochemical measurements combined with MIPs (adapted from<sup>118</sup>).

Hutchins and Bachas described the first example of apparent coupling the molecular imprinting technology and electrochemical polymer synthesis.<sup>119</sup> They developed a potentiometric nitrate sensor by “electrochemically mediated molecular imprinting,” i.e., by electro-synthesizing polypyrrole (PPy) in a NaNO<sub>3</sub> aqueous solution. However, the nitrate template was not deliberately removed from the prepared nitrate-doped PPy before the sensing tests, as is now usually done in each MIP using the procedure of sensing. They showed how electrochemical factors might affect selective nitrate recognition and reported substantial interference from thiocyanate and hydroxide.

The electrochemical method combined with molecular imprinting is an intriguing option for developing improved sensors for various applications.<sup>120–123</sup> Electrochemical entrapment of chemically synthesized MIPs, compared to all-chemical MIP sensor fabrication, allows for film thickness control via electrochemical conditions and may often be accomplished using aqueous solutions. However, some site heterogeneity, common in MIPs, appears to be addressed nowadays by using novel electropolymerizable monomers with various functional groups.<sup>124</sup> Hybrid techniques are getting popularity as a promising way to create more sophisticated sensitive devices. In this regard, the proper coupling of electrochemical techniques with nanomaterials and/or chemically synthesized MIPs could be critical in developing MIP chemosensors in the future.<sup>120</sup>

#### **1.2.4.1 Polydopamine and polytyramine based molecularly imprinted polymers for sensing**

A comprehensive study revealed polydopamine (PDA) suitability in surface coating for molecular sensing and affinity separation for pharmaceutical studies and clinical applications owing to its peculiar physicochemical properties.<sup>125–127</sup> PDA was first used in MIPs to quantify nicotine. The MIP film formed in an inert environment by potentiodynamic electropolymerization was compact and insulating.<sup>127</sup> Because of its intrinsic spontaneous chemical reactivity toward nucleophiles and the possibility of interference from redox peaks depending on layer thickness and morphology, caution should be taken while designing PDA-based electrochemical sensors.<sup>128</sup>

Tyramine, 4-(2-aminoethyl)phenol, contains amino and phenolic groups in its molecular structure. In an acidic aqueous solution, studies elucidated the polymerization route through the phenolic moiety and protonation of the amino group to produce polytyramine (PTy) film

(Figure 1-6a).<sup>129</sup> Fourier transform infrared (FTIR) spectroscopy and XPS supported the formation of a polymer with a strong polycationic character. This amino group has been attached to organic molecules or biomolecules of interest.<sup>130–132</sup> For instance, this group can covalently bind through a carboxamide or phosphoramidate bond to an oligonucleotide and anchor to the transducer.<sup>133</sup> At even sub-attomolar concentrations, it is also employed for antibody immobilization, and enzyme and antigen detection.<sup>134,135</sup>

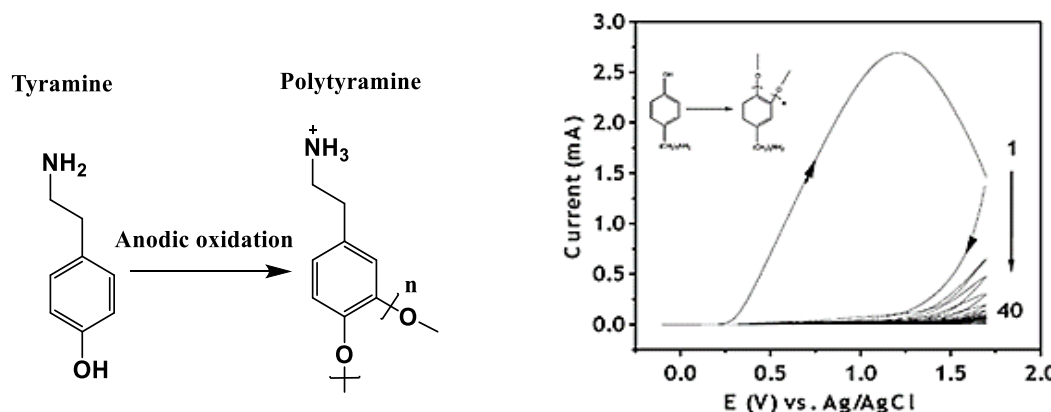


**Figure 1-6.** (a) A reaction scheme of tyramine electropolymerization. (b) Multi-cyclic potentiodynamic curve for electropolymerization of 0.1 M tyramine hydrochloride in 0.3 M NaOH-methanol on the glassy carbon electrode in the -0.10 to +1.70 V vs. Ag/AgCl potential range at 0.5 V s<sup>-1</sup> for 40 cycles (adapted from<sup>136,137</sup>).

The PTy growth is self-limited, resulting in a considerably thinner film than most conducting polymer films. The electro-oxidation of tyramine, a phenol derivative, produces phenoxy radicals, reacting then with tyramine to form a *para*-linked dimer. Further oxidation leads to oligomers, eventually producing a passivating insulating thin film, resulting in its self-limiting property (Figure 1-6b).<sup>138,139</sup> Therefore, substrates and products diffuse more effectively through the PTy films. Moreover, these films are permselective, which helps prevent interfering species from fouling the electrode surface. In effect, fast response and high selectivity can also be expected for the non-conducting PTy films (Figure 1-6b).<sup>140</sup>

Recently, a PTy film was utilized for embedding nanoMIPs.<sup>141,142</sup> To monitor trace amounts of *N*-formyl amphetamine in aqueous samples, a highly sensitive capacitive chemosensor was devised. To do so, the recognition element, i.e., MIP nanoparticles synthesized using thermo- and UV-initiated polymerization, were embedded in the PTy film

deposited on the gold electrode. The linear dynamic concentration range varied from 10 to 250  $\mu\text{M}$  *N*-formyl amphetamine. The LOD was 10  $\mu\text{M}$  in the flowing waterways, such as sewers, springs, rivers, etc., as determined using the capacitive chemosensor. The capacitive signals for the *N*-formyl amphetamine analyte were three times higher than structurally similar compounds. Moreover, the synthesized nanoMIPs were compared to commercially available MIPs to validate the selectivity and selectivity of the chemosensor devised.

#### **1.2.4.2 Carbazole-based molecularly imprinted polymers for sensing drug substances**

Over the last few decades, the conducting polymers (CPs) field has expanded significantly. CPs are classified as intrinsically- and extrinsically-conducting polymers. The former CPs have a solid backbone composed of extensive  $\pi$ -conjugated systems responsible for conductance.<sup>143</sup> The adjacent  $\pi$ -molecular orbitals overlap along the backbone of a conjugated polymer, giving rise to an analogical band structure to inorganic semiconductors. Therefore, CPs are also categorized as organic semiconductors. However, extrinsically-conducting polymers own their conductivity to the presence of an externally added component.

Now, organic semiconductors, a class of materials comprising small organic molecules and polymeric materials, are applied in electronic<sup>144–146</sup> and electrochromic devices,<sup>147</sup> corrosion protection,<sup>148–150</sup> and as recognition materials for chemosensors.<sup>151–153</sup> CPs are in high demand for the latter application because of their advantageous properties, including facile derivatization with various recognition sites, low-temperature manufacturing, and a relatively high electric conductivity. Furthermore, chemical and electrochemical procedures are generally used for their production. Chemical synthesis uses an  $(\text{NH}_4)_2\text{S}_2\text{O}_8$  or  $\text{FeCl}_3$  oxidant to generate CPs in liquids or bulk solids. In contrast, electropolymerization is commonly used to deposit CP films on suitable conducting substrates. The benefits of this process include the ability to control (i) the rate of polymer nucleation and growth by selecting the optimal electropolymerization conditions, (ii) the CP film thickness governed by the amount of charge passed during film deposition, and (iii) the film morphology controlled by the appropriate solvent and supporting electrolyte selection.

CPs are classified as *p*- or *n*-type semiconductors, whether easily oxidized or reduced. Positive charges can be stabilized by *n*-type polymers with electron-rich structures, whereas *p*-type polymers can stabilize negative charges with electron-deficient networks. A CP can be

doped using a suitable potential or an oxidizing or reducing agent. Depending upon the doping, positive or negative radicals or diradicals (polarons or bipolarons) charge carriers are fabricated that can produce electron paramagnetic resonance (EPR) signals due to their spin of  $S = \frac{1}{2}$  or 0, respectively (Figure 1-7b to 7d). These carriers are delocalized over the polymer chains, facilitating electronic conductivity. When a polymer backbone is oxidized,  $\pi$  electrons of this backbone are lost. This loss changes, e.g., the PPy, polyaniline (PANI), poly(3,4-ethylenedioxythiophene) (PEDOT), etc., structures from benzoid to quinoid, generating a radical (polaron) in the backbone. This radical (polaron) creates a localized electronic level within the band structure. Because of the removal of the  $\pi$  electron, this radical (polaron) is then further oxidized to a diradical (bipolaron). This benzoid to quinoid transformation is faster in the case of diradicals (a spinless quantity or bipolarons). If further oxidized, diradical (bipolaron) orbitals overlap again, creating a small band within the main band structure with the lowest energy band gap (Figure 1-7a).<sup>143</sup>

New sub-gap energy states formation and structural changes in a polymer film are reflected in alterations in the ultraviolet-visible (UV-vis), electron paramagnetic resonance, infrared, and Raman spectra. Furthermore, the potential range of CP electroactivity is controlled by its chemical structure, which can be varied by organic synthesis.

So far, different CPs have been investigated for sensing applications. With that regard, polyacetylene,<sup>154–156</sup> PPy,<sup>157</sup> *o*-phenylenediamine,<sup>158</sup> polythiophene (PT),<sup>159</sup> PEDOT,<sup>160–162</sup> polycarbazole,<sup>163–165</sup> and their derivatives are of particular interest. Among them, PPy is one of the most extensively studied CPs. Its monomer is affordable, water-soluble, and readily oxidizable. Furthermore, PPy has several advantages, including environmental stability, redox activity, and the capability to contribute to high electric conductivity. However, the use of PPy in MIPs is limited to water-soluble analytes, and therefore, other polymerizable candidates are explored.

Carbazole and its derivatives are one broad class of heteroaromatic nitrogen compounds with a large-conjugate system, rigid fused rings, intense fluorescence, and excellent electrical and charge transport properties.<sup>166</sup> Their physical and chemical properties can readily and conveniently be altered by functionalizing them with different substituents at (3,6), (2,7), and (1,8) positions, as well as the nitrogen atom position.<sup>167–169</sup> These alterations lead to valuable materials with improved thermal stability, processability, and solubility in organic solvents.

Those materials find their applications in dyes,<sup>170</sup> photoelectrical devices,<sup>171,172</sup> supramolecular recognition materials,<sup>173</sup> sensing materials,<sup>174</sup> and as medicinal agents.<sup>175,176</sup>

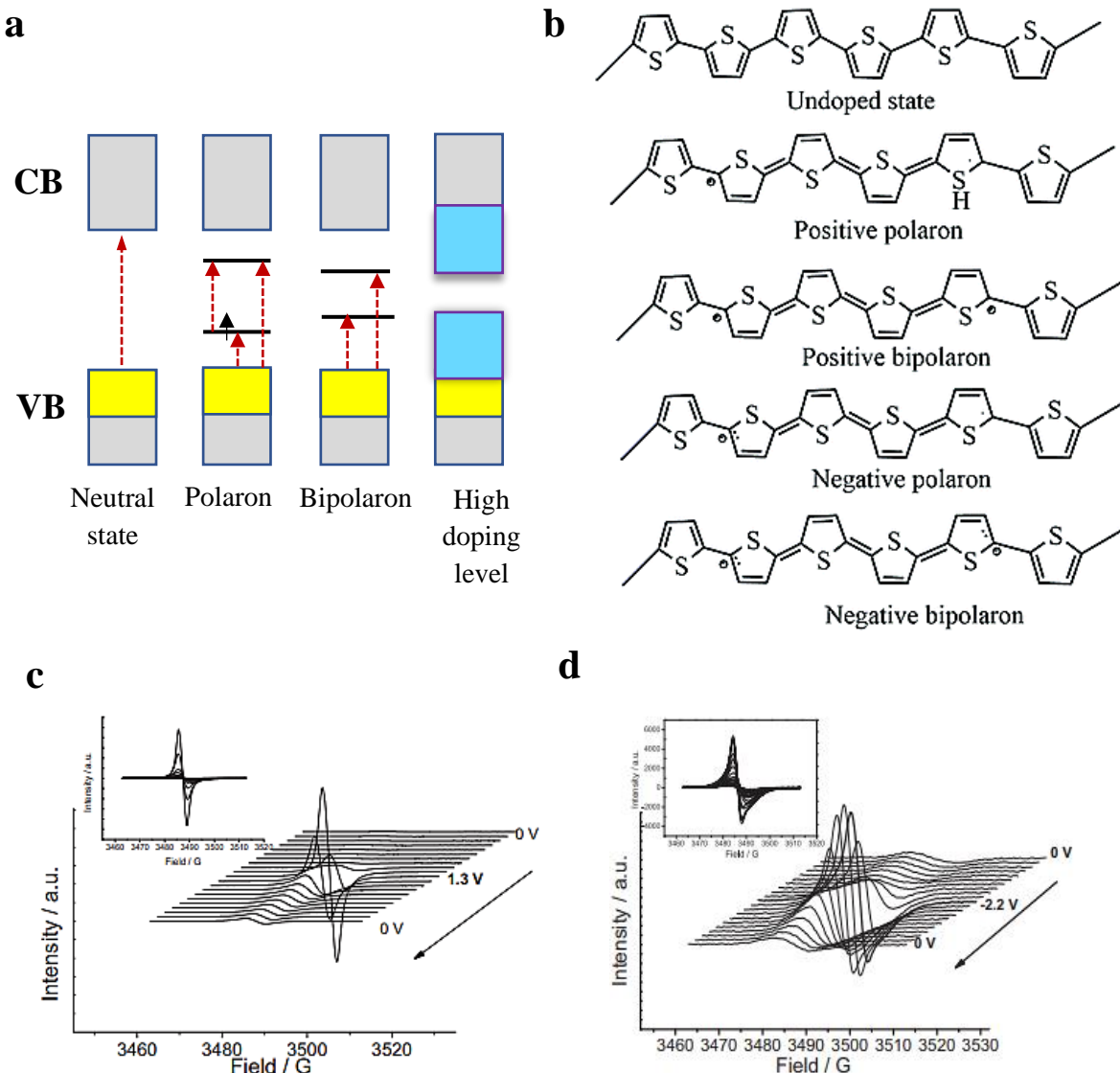


**Figure 1-7.** A general illustration of the (a) electronic bands in the undoped, radical (polaron), diradical (bipolaron), and fully doped states, (b) structural formulas of *p*- and *n*-type doped polythiophene (PT). In situ spectroelectrochemical EPR spectra of poly(2-methoxynaphthalene) during (c) *p*-doping and (d) *n*-doping (adapted from<sup>177,178</sup>).

By electro-oxidation, carbazoles generate polycarbazoles with an oxidation potential lower than their parent monomers. Notably, the number of responses to the "Carbazole" keyword in SciFinder is now ~61253, which is by 3100 more than in the previous 2020 year.

This number is annually increasing substantially, reflecting extensive carbazole use. The long list of associated advantages makes carbazole one of the most suitable candidates for various applications.

- Carbazole monomer derivatization is easy.
- Carbazole monomer derivatization often does not affect its conductivity.
- Carbazole polymers are thermally, chemically, and electrochemically stable.
- Carbazoles can be processed in doped and undoped forms, electro-oxidatively or electro-reductively.
- Carbazole monomer oxidation potential of 1.15 V vs. Ag quasi-reference electrode is lower than that of widely used thiophene monomers.
- Polycarbazoles are readily synthesized by oxidative chemicals or electrochemical polymerization. Moreover, versatile synthetic procedures developed for carbazole derivatives, easy functionalization, and unique, easily tunable electric properties make these polymers attractive for sensing applications.

Like any other electropolymerizable compound, carbazole can be electropolymerized under potentiodynamic, potentiostatic, or galvanostatic conditions. Potentiodynamic electropolymerization is most widely used because it can produce an undoped polycarbazole film whose thickness can readily be adjusted by varying the number of potential scans and/or the potential scan rate.

The electropolymerization mechanism is an essential feature of carbazole molecular electrochemistry (Figure 1-8). A series of electrode and chemical alternating reactions ( $E'C'E''C'''...$ ) begins with the production of oligomers, followed by polymer nucleation and growth, and culminating in fabricating a polymer material. That is, one and two electrons are abstracted per the carbazole and dicarbazole molecule, respectively, during the oxidation. In fact, galvanostatic oxidation usually indicates the transfer of 2.5 to 2.8 electrons because of the possible formation of two products (Figure 1-8b).<sup>179</sup> Dimers or oligomers were postulated to form via intermediates of radical cations at their 3,6 position.<sup>180</sup> Importantly, because the dimer is conjugated more than the monomer, the monomer oxidation requires a higher potential

(1.15 V vs. Ag quasi-reference electrode) than the bicarbazole oxidation (0.90 V vs. Ag quasi-reference electrode).

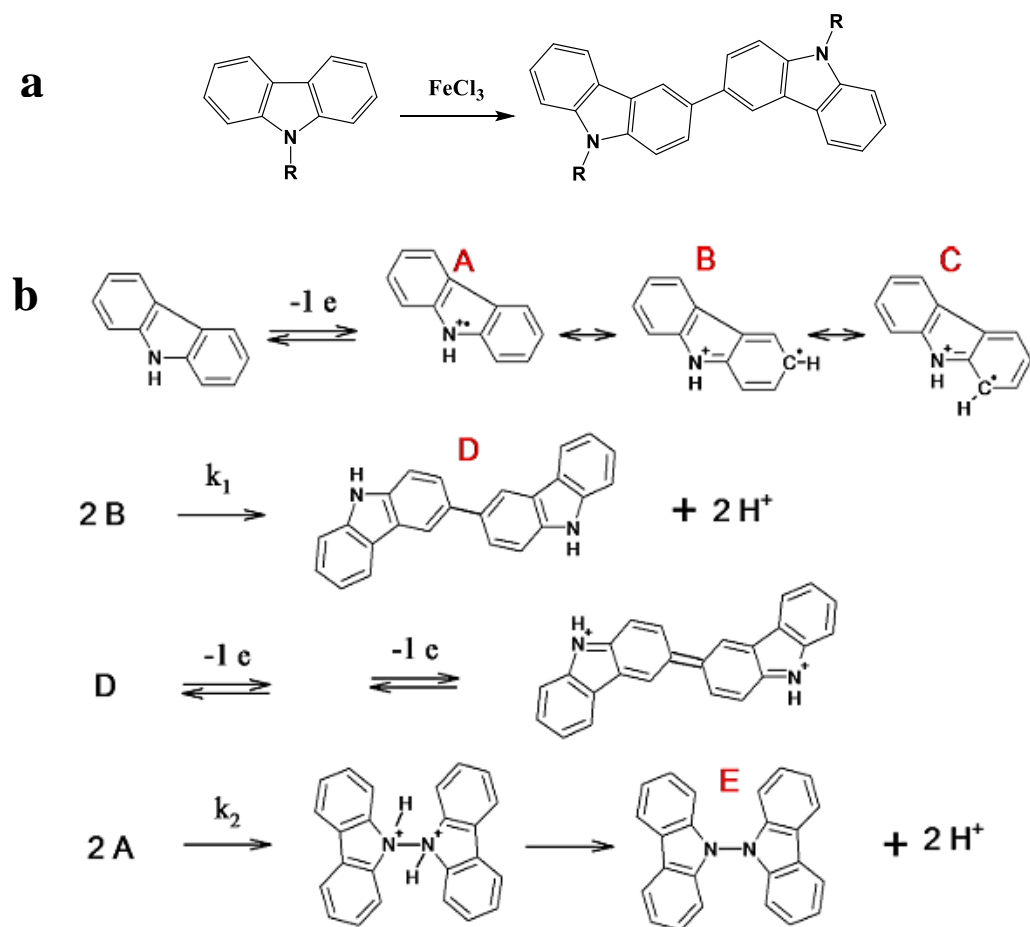


**Figure 1-8.** Reaction mechanism for the (a) chemical and (b) electrochemical oxidation of carbazole (adapted from<sup>181</sup>).

Advantageously, polycarbazoles have been extensively exploited in sensing metals,<sup>182</sup> ions,<sup>183,184</sup> explosives,<sup>185,186</sup> biomolecules,<sup>187</sup> contaminants,<sup>188</sup> and particularly drugs.<sup>189</sup> Another exciting carbazoles' application is their use as functional and cross-linking monomers in MIP syntheses. Due to overall low solubility and structural rigidity, carbazoles contribute to MIPs' appropriateness as imprinted matrices. These features aid in retaining the integrity of the imprinted cavities after template removal.

Over the years, the use of electropolymerizable monomers in molecular imprinting has expanded due to a simple, easily controlled one-step preparation of conductive and non-

conductive polymers (Figure 1-9). The charge passed during the electropolymerization easily controls the thickness of the resultant MIP film. Worth mentioning, the selectivity of acrylate-based MIPs is merely similar to the CP-based MIPs. However, the latter MIPs detectability is higher thanks to analyte preconcentration.

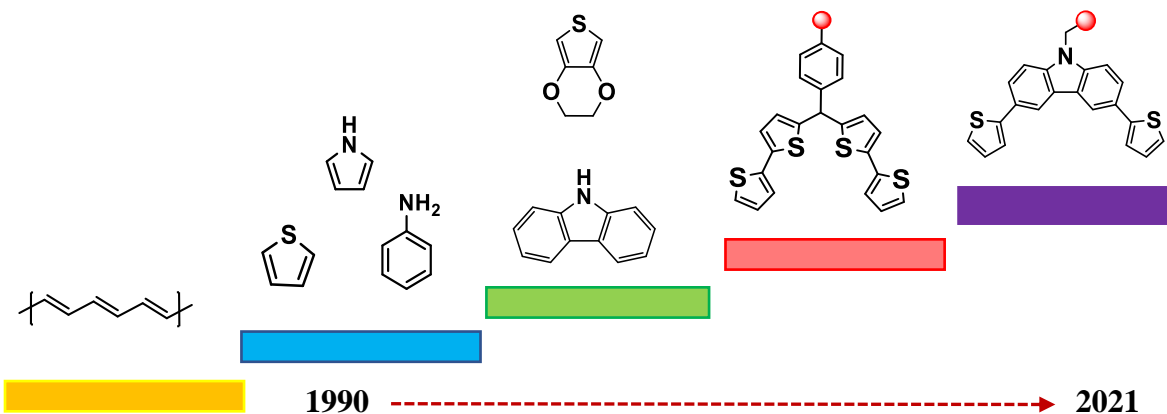


**Figure 1-9.** Progress in functionalized polymers investigated for MIP chemosensor fabrication.

Over a decade ago, a stimulating application of the carbazole derivative was reported.<sup>190</sup> Along with a series of electropolymerizable terthiophenes, that derivative was used to fabricate an MIP for determining naproxen, theophylline, and paracetamol.<sup>190</sup> Bicarbazole monomers substituted with carboxyl (G1CBzCOOH) and hydroxyl (G1CBzOH) functionalities were more effective than their monocarbazole counterpart (G0CBzCOOH) and the bicarbazole amine monomer (G1CBzNH<sub>2</sub>) for imprinting (Figure 1-10). These findings emphasize the importance of cross-linking monomer participation in electropolymerization. In another case, porosity was incurred in the MIP by introducing an ionic liquid (IL) as the porogen instead of a cross-linking monomer.<sup>191</sup>

Recently, an aripiprazole antipsychotic drug was molecularly imprinted using thiophene derivatized carbazole functional and cross-linking monomers.<sup>192</sup> Those new thiophene-carbazole monomers were synthesized to prepare monomers of desirably low oxidation potentials. The atomic force microscopy (AFM) imaging revealed thinning of the MIP film after template removal (Figure 1-11a and 1-11b). The EG-FET chemosensor's linear dynamic concentration range was 30 to 300 pM, with LOD = 22 fM aripiprazole (Figure 1-11c). An

apparent imprinting factor of the MIP equaled  $IF = 4.95$ . The devised chemosensor was highly selective to glucose, urea, and creatinine interferences. Moreover, the chemosensor successfully quantified aripiprazole in human plasma.<sup>192</sup>

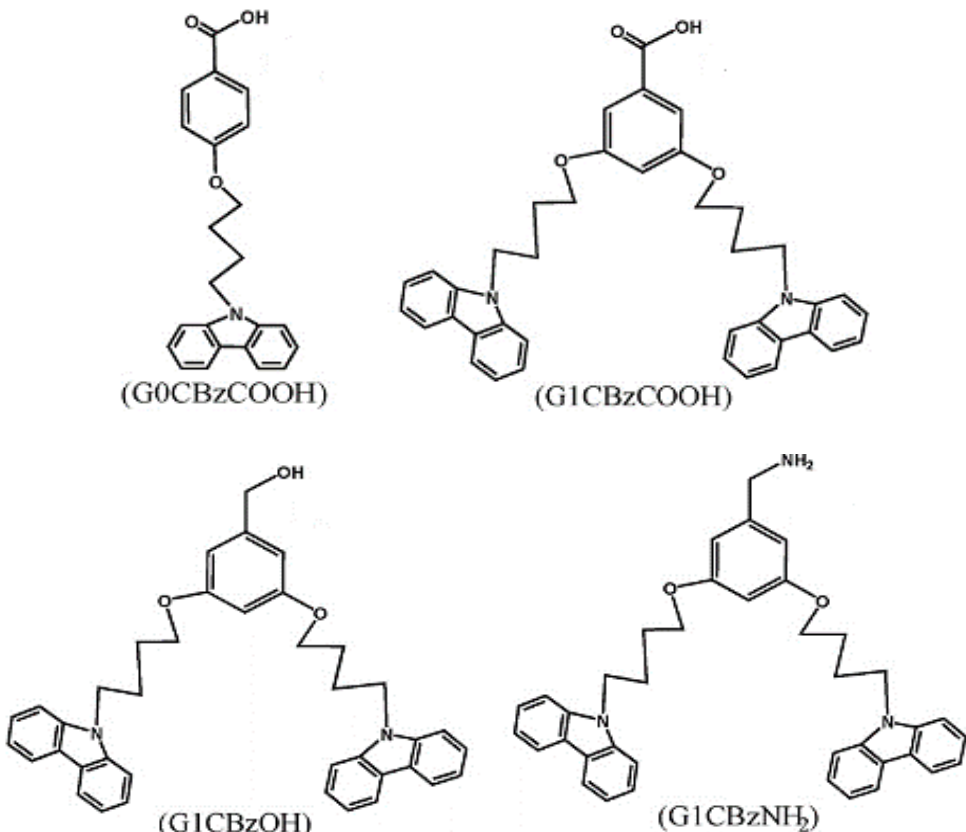


**Figure 1-10.** Structural formulas of carbazole and dicarbazole derivatives (adapted from<sup>190</sup>).

Besides films, carbazole has also been utilized to synthesize water-compatible nanoMIPs for paracetamol sensing. Fluorescence spectroscopy was used for signal transduction in one research, while differential pulse voltammetry (DPV) was in the other. In both cases, a similar procedure was adopted. An amphiphilic copolymer was designed with carbazole, carboxylic acid, and cross-linkable methacrylate groups. As expected, the electrochemical chemosensor sensitivity to paracetamol was superior to other chemosensors.<sup>78,193</sup>

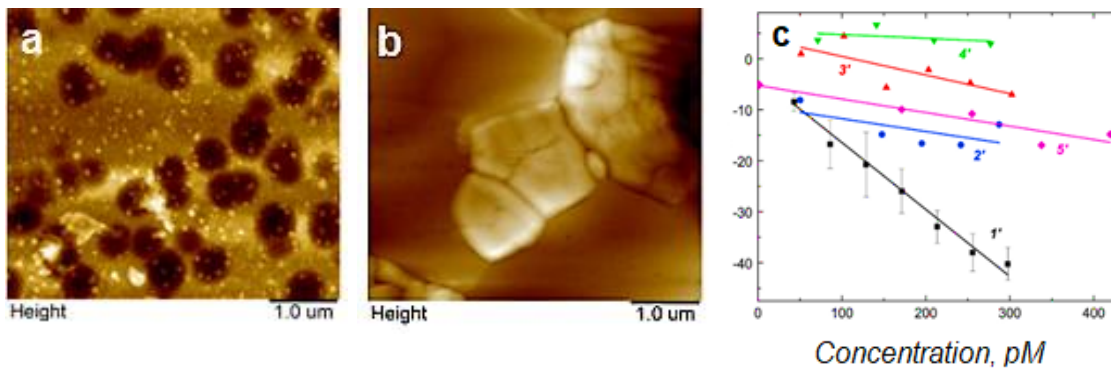


**Figure 1-11.** AFM images of the MIP-ariPIPrazole film (a) after and (b) before aripiprazole extraction in 0.1 M HCl; all films were deposited on Au film-coated glass slides. (c) The EG-FET calibration plots for electrodes coated with the film of (curves 1'-4') MIP-ariPIPrazole and (curve 5') NIP for (curves 1' and 5') aripiprazole, (curve 2') glucose, (curve 3') urea, and (curve 4') creatinine (adapted from<sup>192</sup>).

For bulk MIPs, the residual template left in the polymer matrix slowly leaches out during different steps of polymer operation. This leaching disrupts the solid-phase extraction (SPE) or LC eluate, resulting in systemic inaccuracies in trace analysis. Furthermore, one of the main hurdles to a more extensive MIP deployment as a separation matrix is the possibility of analyte contamination by the residual template during analyte detection.

Unfortunately, confirming a complete template removal from acrylate MIP grains is very difficult. However, that is not the case for conducting MIP films. Commonly used XPS and FTIR spectroscopy confirmed the presence and absence of the template before and after extraction, respectively.

### 1.2.5 Preparation of hybrid composite MIP electrochemical sensor

A three-dimensional nanohybrid electrode architecture provides an increased interfacial communication area by offering highly reactive sites for drug template molecules, thus improving reactivity.<sup>194</sup> The assumption underlying the development of those hybrid systems is that the "templating" will result in affinity and or selectivity higher than those demonstrated by the biomolecule alone.<sup>195</sup> A hybrid composite MIP chemosensor contains a second material. That can be used as either the support or as the transducer. These second materials can be, e.g., metal nanoparticles, quantum dots (QDs), magnetic and non-magnetic metal oxides, optical fibers, etc.<sup>72,196</sup>

Advantageous electrochemical activity, bio-compatibility, rich surface chemistry, and high resistance to bio-fouling made carbon materials, including carbon nanotubes (CNTs), graphene, carbon dots, or nano-diamonds, helpful in building electrochemical chemosensors for determining bio-compounds.<sup>197</sup> Combining these carbon nanomaterials with other materials resulted in MIP mechanical stability, high conductivity, and enhanced signal transduction,<sup>198–200</sup> thus improving MIP chemosensors' sensitivity and detectability.<sup>201</sup> In particular, CNTs, a graphite monolayer rolled up to form a cylinder with a well-ordered arrangement of  $sp^2$  hybridized carbon atoms linked via  $\pi$  bonds, have been extensively exploited in biosensing platforms as an attractive conducting scaffold material.<sup>197,198</sup>

Single-walled carbon nanotubes (SWCNTs) are single-layered seamless cylinders, whereas multi-walled carbon nanotubes (MWCNTs) are composed of two or more single layers of coaxial cylinders interlinked by van der Waals interactions. Furthermore, the surfaces of CNTs may be easily modified in various ways, including covalent and non-covalent functionalization. Introducing various organic functional groups can lead to this functionalization, thus resulting in a high physical sorbing surface area, tunable surface charge, and a supply of protons for chemical ionization.<sup>202</sup>

Several studies used MWCNTs, associated with  $Fe_3O_4$  magnetic nanoparticles,<sup>203</sup> Au nanoparticles,<sup>204</sup> or others,<sup>205</sup> instead of SWCNTs, as the support for MIPs.<sup>206</sup> Those hybrid sensing platforms were built for determining medications, including kanamicin,<sup>207</sup> ciprofloxacin,<sup>208</sup> and ampicillin.<sup>209</sup> Using those materials enhanced the electron transfer, electrocatalytic properties, and sensor sensitivity.

Towards that, an interesting strategy for ketamine determination was proposed. First, in one step, tyramine, the (functionalized multi-walled carbon nanotubes)@gold nanoparticles (f-MWCNTs@AuNPs) nanocomposite, and ketamine were electropolymerized on a pencil graphite electrode (PGE) to prepare the chemosensor. Then, the deposited nanoMIPs, embedded in the PTy film, were characterized microscopically and spectroscopically (Figure 1-12).<sup>210</sup> This nanoMIPs chemosensor revealed two linear dynamic concentration ranges, i.e., from 1 to 50 nM and 50 to 1000 nM ketamine, with LOD = 0.7 nM. Other procedures, where metal-organic framework/graphene nanocomposite (MOFs@G) modified screen-printed electrode was used, showed similar detectability.<sup>211</sup> Both chemosensors demonstrated

excellent stability, high reproducibility and repeatability, and high sensitivity and selectivity towards ketamine.

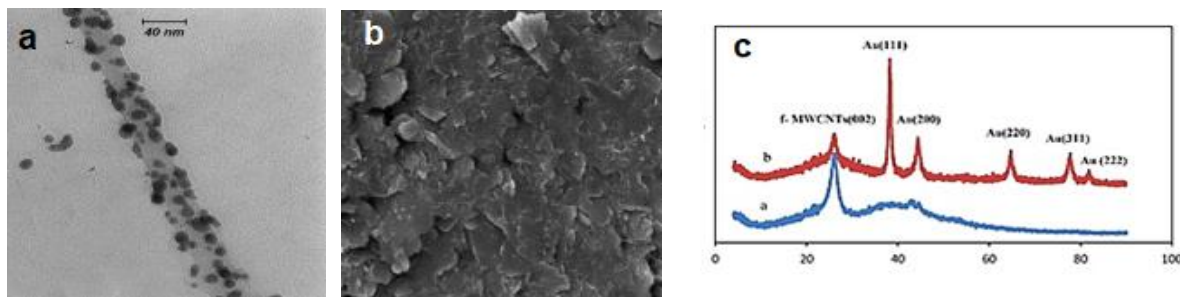
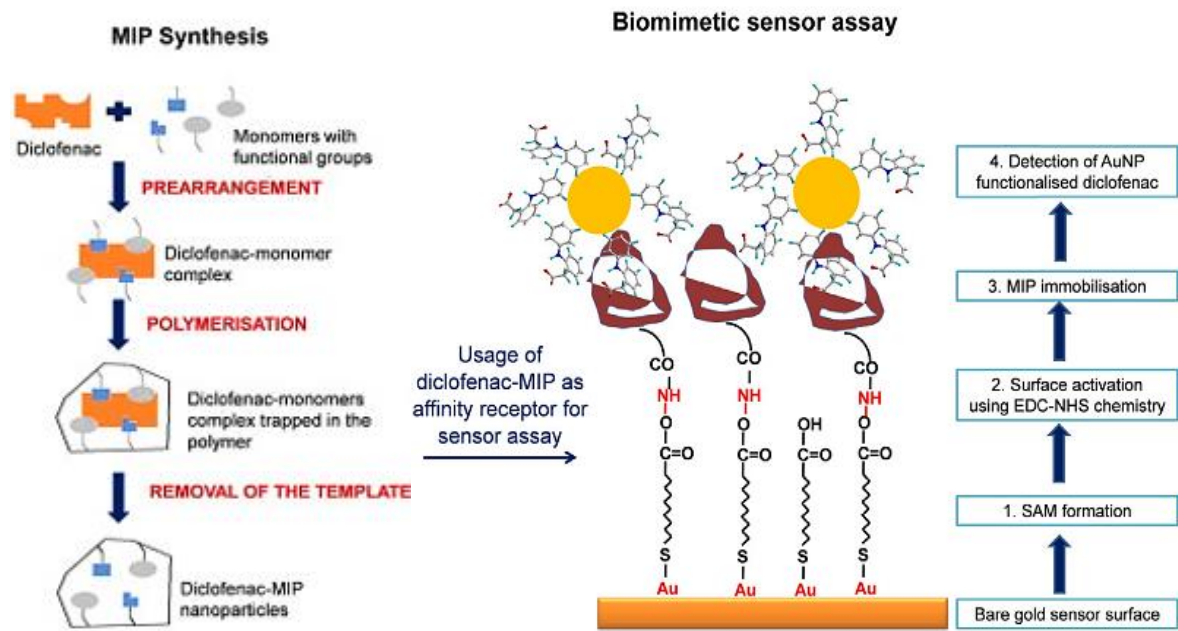


**Figure 1-12.** (a) The transmission electron microscope (TEM) image of the f-MWCNTs@AuNPs nanocomposite, (b) the SEM image of polytyramine/sol-gel/f-MWCNTs@AuNPs MIP/PGE, and (c) XRD patterns of (a) f-MWCNTs and (b) f-MWCNTs@AuNPs nanocomposite; f-MWCNT - functionalized multi-walled carbon nanotube (adapted from<sup>210</sup>).

Furthermore, the electrochemically imprinted chemosensor was successfully applied to determine ketamine in biological samples. A gemcitabine anti-neoplastic drug was imprinted in a microporous metal-organic framework. That was achieved by one-step electropolymerization of aniline moieties of *p*-aminothiophenol gold nanoparticles along with gemcitabine on the surface of the gold electrodes. Intriguingly, no cross-linker was used. Linear sweep voltammetry (LSV) was employed to characterize and investigate the modified electrodes. A calibration plot was constructed for the linear dynamic concentration range of 3.8 fM to 38 nM with LOD = 3 fM gemcitabine.<sup>212</sup>

Various transductions,<sup>213,214</sup> including surface plasmon resonance (SPR) spectroscopy,<sup>85</sup> have been used to devise nanoMIP-based chemosensor for diclofenac, an anti-inflammatory drug. Covalent nanoMIPs immobilization on the surface of the SPR gold chips using *N*-ethyl-*N'*-(3-(dimethylamino)propyl)carbodiimide/*N*-hydroxysuccinimide (EDC/NHS) constructed the chemosensor (Scheme 1-4). The ~132.3 ( $\pm$ 3.2) nm particle size with a 0.1 polydispersity index confirmed the high quality of synthesized nanoMIPs. The diclofenac drug was then successfully determined in the concentration range of 1.24 to 80 ng mL<sup>-1</sup>. The nanoMIP chemosensor surface was regenerated using glycine hydrochloric acid solution, and the kinetic data analysis provided the dissociation constant of  $1.48 \times 10^{-9}$  M. Moreover, the nanoMIPs

affinity to diclofenac was confirmed by passing a diclofenac solution through an SPE nanoMIPs column and analyzing the eluent using LC-MS.



**Scheme 1-4.** Schematic illustration of the fabrication of the chemosensor assay for diclofenac (adapted from<sup>85</sup>).

## 1.3 Literature review and research goals for the analyte targets

Continuing our research on determining pharmaceutical drugs using MIP chemosensors, in the present research, we aimed to fabricate selective MIP chemosensors for CIL and DUL.

### 1.3.1 Cilostazol, CIL

Over the last decades, the number of patients affected by intermittent claudication (IC), an initial symptom of peripheral artery disease (PAD), has increased severely.<sup>215</sup> PAD is a progressive disorder caused by the occlusion of large or medium lower body arteries. Over 200 million people worldwide are afflicted by PAD.<sup>216,217</sup> Moreover, the cardiovascular and diabetic mortality rate increases ~15-fold by IC.<sup>216</sup> Many different drugs are being administered alone or in combinations to cure this disorder. Cilostazol, 6-[4-(1-cyclohexyl-1H-tetrazol-5-yl)butoxy]-3,4-dihydro-2(1H)-quinolinone (CIL) is one of them (Figure 1-13).<sup>218,219</sup>

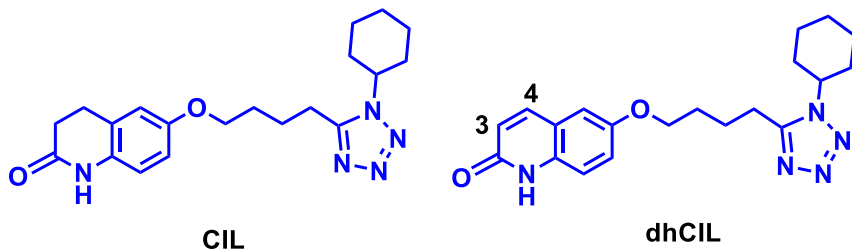
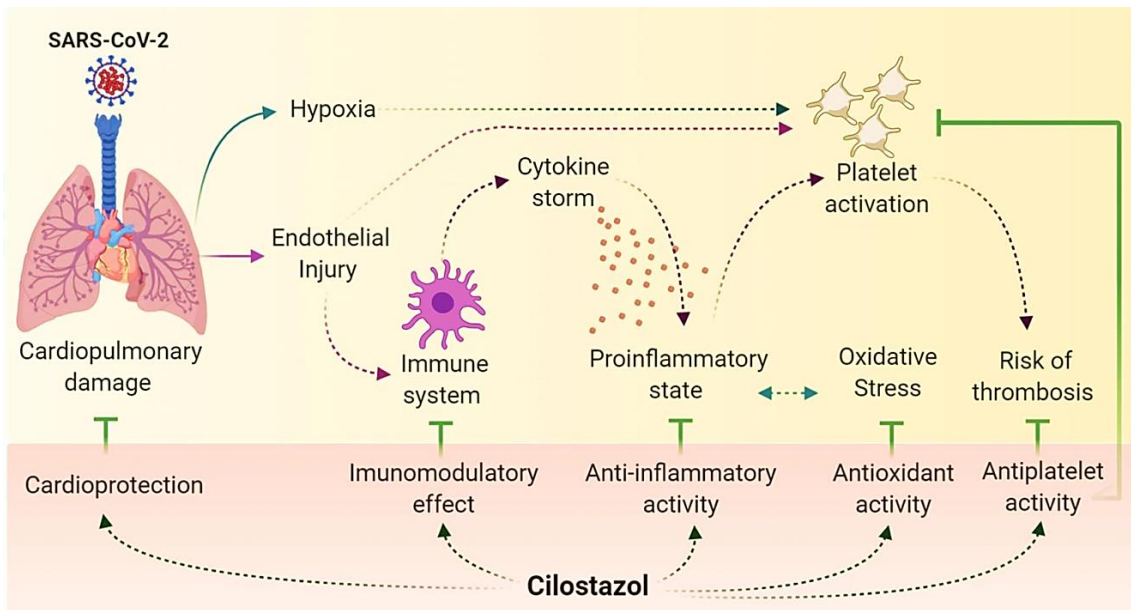


**Figure 1-13.** Structural formulas of cilostazol (CIL) and 3,4-dehydocilostazol (dhCIL).

Cilostazol is an orally administered selective cyclic nucleotide phosphodiesterase 3 (PDE<sub>3</sub>) inhibitor with antiplatelet, vasodilatory, and antimitogenic effects.<sup>220,221</sup> This inhibitor increases 3',5'-cyclic adenosine monophosphate (cAMP) that, in turn, increases protein kinase A in its active form, directly related to inhibition in platelet aggregation and cell proliferation.<sup>222,223</sup>



**Scheme 1-5** Cilostazol uses (adapted from<sup>224</sup>).

Moreover, CIL is helpful for the treatment of the diabetic,<sup>217–219,225</sup> and Alzheimer's patients,<sup>226–230</sup> strokes,<sup>231</sup> and hypertension.<sup>232</sup> A recent study revealed its importance in COVID-19 diagnosis (Scheme 1-5).<sup>224</sup> Currently, CIL is undergoing several clinical trials.<sup>233,234</sup> Furthermore, a CASTLE long-term study (Cilostazol: A Study in Long-term Effects, CASTLE) evaluated CIL efficacy and tolerability in PAD patients. Several small-scale clinical trials were conducted for evaluating the efficacy of CIL in patients with mild cognitive impairment (MCI),<sup>235</sup> Alzheimer's disease (AD), and cardiovascular disease (CVD).<sup>227–229</sup> Moreover, new therapeutic applications of CIL alone or in combination with other drug substances are under extensive clinical development.<sup>236</sup> For examining these effects on a larger scale, randomized placebo-controlled phase II trials are ongoing on patients with MCI and AD.<sup>226</sup> Therefore, a fast and reliable method for the non-invasive CIL determination in large sets of clinical samples is highly demanded. Independent studies revealed that after (50 to 200)-mg dose oral administration of CIL, its concentration in plasma increased to 806 ( $\pm 238$ )  $\mu\text{g/L}$  after 3 h, and then decreased to  $\geq 20 \mu\text{g/L}$  while in the urine samples, the 3,4-dehydrocilostazol (dhCIL) metabolite predominated. Apparently, metabolic rather than urinary excretion is the primary elimination route for CIL.<sup>219</sup> Significantly, dhCIL is five times more potent than its CIL parent drug.<sup>237</sup>

CYP3A4 and CYP2C19, two isoenzymes of the cytochrome P450 system, metabolize CIL to ~11 different metabolites, dhCIL (Figure 1-13) and monohydroxycilostazol (not shown) being primary pharmacologically active metabolites.<sup>237</sup> These metabolites are responsible for inhibitory effects on platelet aggregation.<sup>238</sup> For CIL determination in biological matrices, several analytical procedures were developed, including simultaneous determination of CIL and dhCIL, along with anti-inflammatory drugs.<sup>237,239–241</sup> Nowadays, CIL is determined in human serum using methods mostly involving ESI/MS/MS,<sup>241</sup> HPLC,<sup>242,243</sup> (liquid chromatography)-(electrospray ionization tandem mass spectrometry) (LC-ESI/MS/MS),<sup>239,244</sup> or spectrofluorimetry.<sup>245</sup> Unfortunately, these methods are laborious, time-consuming, and require expensive instrumentation. Moreover, they all need highly skilled operators to perform reliable determinations. Therefore, there is a need for an inexpensive, sensitive, and easy-to-operate sensor for selective CIL and dhCIL determination.

Recently, a very sensitive electrochemical chemosensor for CIL with an  $\alpha$ -vanadium-manganese oxide ( $\alpha$ -MnO<sub>2</sub>-V<sub>2</sub>O<sub>5</sub>) composite nanorods (NRs) recognition unit was prepared. Its linear dynamic concentration range at pH = 7.0 was 0.11 to 100  $\mu$ M with LOD =  $2.48 \times 10^{-8}$  M.<sup>246</sup> However, lack in interferences study like others<sup>247,248</sup> emphasized the need of continuing the research to provide better tools for CIL and dhCIL sensing in human plasma where matrix effect is considerable. Another luminescence-based chemosensor with low LOD was constructed.<sup>249</sup> However, it was devised for CIL determination in pharmaceutical formulations and was not tested in real plasma samples. Therefore, no biological matrix effect was examined.

Chapter 4 reports on two new chemosensors capable of selective CIL sensing in light of these considerations. The chemical recognition units of these chemosensors were (thiophene-appended carbazole)-based conducting MIP film and nanoMIPs, both imprinted with CIL. The signal was transduced with DPV and EIS. The recognition unit adds the desired selectivity to the sensor, whereas DPV provides sensitivity to the combined chemosensor device. Furthermore, no other MIP-based chemosensors for CIL have been described to date.

### 1.3.2 Duloxetine, DUL

Major depressive disorder (MDD) has always been a long-standing global problem, irrespective of the country's health care system.<sup>250,251</sup> Moreover, it increases the risk of suicidal ideation and attempted suicide.<sup>252</sup> Decreased concentrations of neurotransmitters, such as serotonin (5-HT) and norepinephrine (NE), in the central nervous system cause this disorder. Older generation antidepressants, selective serotonin reuptake inhibitors (SSRIs) (Figure 1-14b), have been well exploited, but because of their poor selectivity and considerable side effects, new-generation antidepressants were developed.<sup>253</sup>

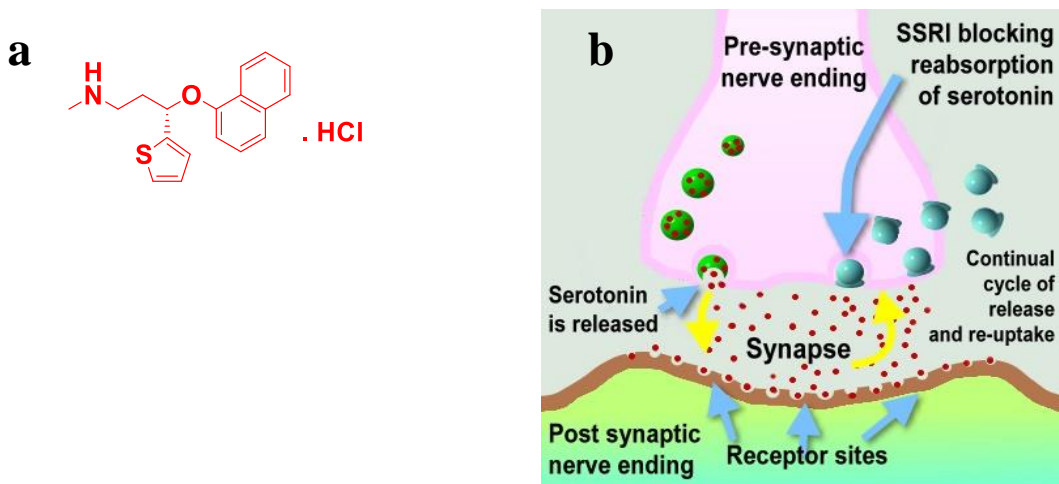


**Figure 1-14.** (a) The structural formula of duloxetine hydrochloride and (b) the selective serotonin reuptake inhibitor (SSRI) mechanism of action (adapted from<sup>254</sup>).

Duloxetine DUL (Figure 1-14a), propanamine, is a selective serotonin-norepinephrine reuptake inhibitor (SNRI), effective in major depressive disorder,<sup>250,252,255</sup> anxiety disorder,<sup>256</sup> and fibromyalgia.<sup>257</sup> Absorption of DUL begins 2 h after oral administration, and the maximum plasma concentration is reached within ~6 h.<sup>256</sup> Several combinations of antidepressants have been tried to treat depressive illness, such as DUL-mirtazapine,<sup>258</sup> DUL-amitriptyline,<sup>259</sup> and venlafaxine.<sup>260</sup> Patient-level post hoc studies revealed no differences between DUL and other SSRIs in the sum score of the Hamilton Depression Rating Scale (HDRS-17-sum) in clinical trials.<sup>261</sup>

**Table 1-2.** Analytical techniques for DUL determination compared with some of those reported earlier, and analytical parameters of these techniques.

Chemosensor composition or determination principle	DUL linear dynamic concentration range	DUL limit of detection (LOD)	Transduction technique	Ref.
<b>Ion-selective membrane electrode on a Cu wire</b>	10 $\mu\text{M}$ – 10 mM	10 $\mu\text{M}$	Potentiometry	<sup>262</sup>
<b>Ion-selective membrane electrode</b>	10 $\mu\text{M}$ – 10 mM	6.31 $\mu\text{M}$	Potentiometry	<sup>263</sup>
<b>Carbon paste electrode</b>	0.2 – 5.0 $\mu\text{M}$ 0.07 – 1.0 $\mu\text{M}$	6.0 nM (LSV) 21 nM (SWV)	Voltammetry (LSV, SWV)	<sup>264</sup>
<b>Multiwall-carbon nanotubes modified carbon paste electrode</b>	3.0 $\mu\text{M}$ – 0.2 mM	0.4 $\mu\text{M}$	Voltammetry (CV, SWV)	<sup>265</sup>
<b>Screen-printed disposable electrode</b>	1.0 $\mu\text{M}$ – 10 mM	0.5 $\mu\text{M}$	Potentiometry	<sup>266</sup>
-	59 nM – 1.19 $\mu\text{M}$	8.9 nM	Spectrofluorimetry	<sup>267</sup>

LOD – limit of detection, LSV – linear sweep voltammetry, SWV – square wave voltammetry, CV – cyclic voltammetry.

Analytical methods using HPLC<sup>268–272</sup> and spectrofluorimetry<sup>273,274</sup> are sensitive in determining DUL. However, their lengthy analysis time, relatively low user-friendliness, and expensive instrumentation open doors for other more straightforward procedures. There is a continuous trend in looking for methods, which are simple, easy to develop, highly selective, sensitive, and reconstructable. Analytical parameters of some of the techniques previously reported for DUL determination are compared in Table 1-2. Given this, the molecular imprinting in polymer technique could be beneficial.

Chapter 5 describes a newly devised MIP nanohybrid chemosensor for DUL. For that, we first prepared nanoMIPs imprinted with DUL and then embedded them, along with SWCNTs serving as electronic bridges and scaffolds, in a PTy film. This procedure allowed increasing the chemosensor signal significantly. Therefore, selective determining DUL in human plasma became possible.

## 1.4 Research objectives

Many financial investments are made to develop simple, highly effective, low-cost sensing methods and sensitive, selective, durable, and reusable tools every year. The pharmaceutical institutions' main challenge is quantifying the drugs in a large number of samples. Some studies suggest using analytical procedures relying on HPLC and MS techniques for drug quantization. However, these methods reveal significant deficiencies, including expensive instrumentation, long drug determination time, and large volumes of high-purity organic solvents. Besides, the main disadvantages of these methods from the patient standpoint are their limited accessibility and rather difficult practical use. Many research types have been accomplished to produce cheaper sensing alternatives, one of which is chemosensor preparation. However, initially devised chemosensors suffered from many deficiencies, requiring further improvement.

Therefore, the current project's overall objective was to design, fabricate, characterize, and validate chemosensors for selective drug determination in human plasma. Two drug substances, CIL and DUL, were chosen as templates for designing three different artificial recognizing systems to complete the research goals. CIL is an antiplatelet agent treating intermittent claudication, whereas DUL is a selective serotonin and norepinephrine reuptake inhibitor (SNRI) that cures fibromyalgia, depressive disorder, and other diseases. Thus, their determination in body fluids is vital from the personalized drug dosage point of view. Keeping that in mind, we devised sensitive and selective chemosensors using molecularly imprinted polymers as recognition units. We envisioned our chemosensors' potential application as point-of-care user-friendly tools to tackle daily quantifying the drugs in clinical and pharmaceutical practice.

Moreover, we synthesized new carbazole derivatives capable of electrochemical polymerization to achieve those goals. Furthermore, we attempted to understand some fundamental issues related to the mechanism of electropolymerization of some of the monomers. Therefore, the research described in the thesis can significantly contribute to early clinical diagnosis and, in consequence, will help save human lives.

After this survey, the “Experimental section” part will be provided in Chapter 2, including a description of chemicals and materials used (Chapter 2.1), “Procedure of monomers syntheses” (Chapter 2.2), and “Experimental techniques and instrumentation” (Chapter 2.3).

Chapter 3 explains why some carbazole derivatives form polymer films during oxidative electropolymerization while others do not despite being both electrochemically active. We thoroughly studied the selected monomers' electro-oxidation spectroelectrochemically using UV-vis-NIR and EPR spectroscopy and CV simultaneously to unravel the reasons for this unusual behavior. Comparative spectroelectrochemical studies of the monomers undergoing electropolymerization and those undergoing only electrochemical oxidation allowed rationalizing the behavior observed.

Chapter 4 discusses the methods developed for CIL and its primary metabolite selective determining in real human plasma samples. To this end, we have attempted to come up with two approaches. (i) In one, we developed CIL-imprinted MIP nanoparticles and devised a method of their immobilization on the electrode surface to fabricate chemosensors. (ii) In another approach, we tested direct electrochemical deposition of polycarbazole MIP films and their use as chemosensor recognition units.

The CNTs/nanoMIPs hybrid recognition unit fabrication in the chemosensor for DUL sensing in human plasma samples is described in Chapter 5. This chemosensor was cross-validation with HPLC-UV. Electrochemical transduction based on the indirect approach using redox probe was used in all developed chemosensors.

Finally, an Appendix characterizes electrochemical, spectroscopic, and SEM properties of the polymer films of two new thiophene-appended carbazole monomers synthesized within the project. Moreover, it contains information on theoretical electronic absorption spectra of CNZ1 and FM2 monomers and their dimers in acetonitrile calculated at the TD-DFT level of theory. A procedure to prepare CIL-spiked artificial serum is also mentioned.

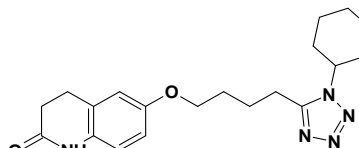
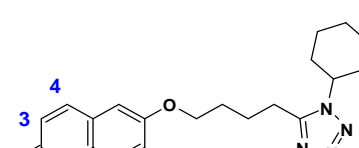
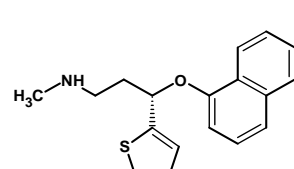
# Chapter 2

## Experimental Section

The present section describes chemicals and materials and provides the main characteristics of the experimental techniques, instrumentation, and procedures used in the present research.

### 2.1 Chemicals and materials

Table 2.1.1 Templates/analytes

No.	Name (CAS)	Structural formula	Source
1.	Cilostazol, CIL (73963-72-1)		MedChemExpress
2.	3,4-Dehydrocilostazol, dhCIL (73963-62-9)		Toronto Research Chemicals, Canada
3.	Duloxetine, DUL		Synthesized at the Łukasiewicz Research Network- Pharmaceutical Research Institute, Warsaw, Poland

**Table 2.1.2 Cross-linking monomers (CLMs)**

No.	Name (CAS)	Structural formula	Source
1.	Ethylene glycol dimethylacrylate, EGDMA (97-90-5)		Sigma-Aldrich
2.	<i>N,N'</i> -methylenebisacrylamide, BIS (110-26-9)		Sigma-Aldrich
3.	4-Bis(3,6-di(thiophen-2-yl)-9H-carbazole-9-yl)benzene, CLM		Synthesized elsewhere

**Table 2.1.3 Functional monomers (FMs)**

No.	Name (CAS)	Structural formula	Source
1.	Methacrylic acid, MAA (79-41-4)		Sigma-Aldrich
2.	Itaconic acid, IA (97-65-4)		Sigma-Aldrich
3.	4-Vinyl pyridine, 4-VP (100-43-6)		Sigma-Aldrich
4.	Acrylamide, AA (79-06-1)		Sigma-Aldrich
5.	<i>N</i> -(2-hydroxypropyl) methacrylamide, HPMA (21442-01-3)		Sigma-Aldrich
6.	4-[3,6-Di(thiophen-2-yl)-9H- carbazole-9-yl]benzoic acid, <b>FM1</b>		Synthesized herein
7.	9-Benzyl-3,6-di(thiophen-2-yl)-9H-carbazole, <b>FM2</b>		Synthesized herein
8.	9-(Naphthalen-2-yl)-3,6- di(thiophen-2-yl)-9H- carbazole, <b>FM3</b>		Synthesized herein

**Table 2.1.4 Initiators**

No.	Name (CAS)	Structural formula	Source
1.	2,2'-Azobis(2,4-dimethylvaleronitrile), ABDV (4419-11-8)		DuPont Chemicals
2.	2,2'-Azobis(2-methylpropionitrile), AIBN (78-67-1)		Sigma-Aldrich

**Table 2.1.5 Interferences**

No.	Name (CAS)	Structural formula	Source
1.	$\beta$ -D(+) Glucose (492-61-5)		Sigma-Aldrich
2.	Cholesterol (57-88-5)		Sigma-Aldrich
3.	Urea (57-13-6)		Sigma-Aldrich
4.	Creatinine (60-27-5)		Sigma-Aldrich
5.	Dehydroaripiprazole-d8 (129722-25-4)		Toronto Research Chemicals, Canada

## Solvents

- Anhydrous acetonitrile, CAS No. 75-05-8, Sigma-Aldrich
- Octanenitrile, CAS No. 124-12-9, Sigma-Aldrich
- Anhydrous dichloromethane, DCM, 98 %, CAS No. 75-09-2, Sigma-Aldrich

## Other chemicals

- Ferrocene, 98%, CAS No. 102-54-5, Sigma-Aldrich
- Tetrabutylammonium perchlorate, ≥99%, (TBA)ClO<sub>4</sub>, CAS No. 1923-70-2, Sigma-Aldrich
- Glacial acetic acid, Sigma-Aldrich
- Sodium hydroxide, NaOH, CAS No. 1310-73-2, 99%, Chempur
- Tyramine form Sigma-Aldrich
- Single-walled carbon nanotubes SWCNT (outer diameter < 2 nm, length 1 - 5 μm), SES Research (Houston TX, USA)
- Potassium hexacyanoferrate(III), K<sub>3</sub>Fe(CN)<sub>6</sub>, Sigma-Aldrich
- Potassium hexacyanoferrate(II), K<sub>4</sub>Fe(CN)<sub>6</sub>, Chempur
- Monopotassium phosphate (analytical grade), KH<sub>2</sub>PO<sub>4</sub>, POCH
- Disodium phosphate (analytical grade), Na<sub>2</sub>HPO<sub>4</sub>, POCH

All reagents and solvents were of analytical grade, unless stated otherwise, and used as received except for 4-VP, purified by distillation under decreased pressure before use.

## 2.2 Procedures

### 2.2.1 Monomers syntheses and their purification methods

Herein, a library of fifteen electroactive carbazole derivative monomers was prepared (Figure 2-3). Among those, three monomers were thiophene-appended carbazoles substituted with naphthalene and benzyl substituents and functionalized with benzoic acid groups at the *N* position. Syntheses of carbazole monomers, vis., 9-(naphthalen-2-yl)-9*H*-carbazole CNZ1,<sup>173</sup> *N*-benzyl-9*H*-carbazole CNZ2,<sup>275</sup> 9-(4-phenylbutyl)-9*H*-carbazole CNZ3,<sup>276</sup> 9-phenyl-9*H*-carbazole CNZ4,<sup>173</sup> 4-(9*H*-carbazol-9-yl)benzoic acid CNZ5,<sup>277</sup> *N*-benzoyl carbazole CNZ6,<sup>278,279</sup> 9-(4-methoxyphenyl)-9*H*-carbazole CNZ7,<sup>280</sup> methyl 4-(9*H*-carbazol-9-yl)benzoate CNZ8,<sup>280</sup> 9-(4-nitrophenyl)-9*H*-carbazole CNZ9,<sup>281</sup> 4-(9*H*-carbazol-9-yl)aniline CNZ10,<sup>279</sup> 9-(naphthalen-1-yl)-9*H*-carbazole CNZ11,<sup>282</sup> and 2BrCNZ1<sup>282</sup> were accomplished as per the literature. The Ullmann coupling reaction was performed using the already known procedure to synthesize the cross-linking monomer, 1,4-di(9*H*-carbazol-9-yl)benzene CLM2.<sup>283–285</sup> Moreover, three new functional monomers with thiophene moieties, 3,6-attached to carbazole, were synthesized and characterized. The syntheses were performed through a multi-step process involving Ullmann coupling and a Suzuki-Miyaura reaction.

The nuclear magnetic resonance (NMR) spectra were recorded at room temperature with BRUKER AVANCE II (300 or 500 MHz <sup>1</sup>H, 100 MHz <sup>13</sup>C) for each synthesized compound. Chemical shift,  $\delta$ , values were reported in ppm relative to that of Me<sub>4</sub>Si ( $\delta$  0.00), D<sub>2</sub>O ( $\delta$  4.79), CDCl<sub>3</sub> ( $\delta$  7.26), DMSO-d<sub>6</sub> ( $\delta$  2.5) for <sup>1</sup>H, and CDCl<sub>3</sub> ( $\delta$  77.00) and DMSO-d<sub>6</sub> ( $\delta$  39.52) for <sup>13</sup>C. The following symbols were used to indicate signal multiplicity: s – singlet, d – doublet, q – quartet, and m – multiplet.

#### 2.2.1.1 Thin-layer chromatography (TLC)

Thin-layer chromatography (TLC) is used to separate non-volatile mixtures. It also monitors the reaction progress, identifies compounds in the studied mixture, and determines the product purity.<sup>286</sup> A thin glass or plastic plate coated with a thin layer of a gel of aluminum oxide or silica acts as the stationary phase, while the mobile phase is a solvent solution chosen according to the properties of the components in the mixture. The principle of TLC is the distribution of a compound between the stationary phase and a liquid mobile phase, i.e., eluting solvent, that

is moving over the stationary phase (Figure 2-1). A small amount of a product mixture is placed immediately above the bottom of the TLC plate as a starting point. For instance, if a normal-phase silica gel is used as the stationary phase, it can be considered polar. Given two compounds that differ in polarity, the more polar compound more strongly interacts with the silica and is, therefore, more capable of dispelling the mobile phase from the binding places.

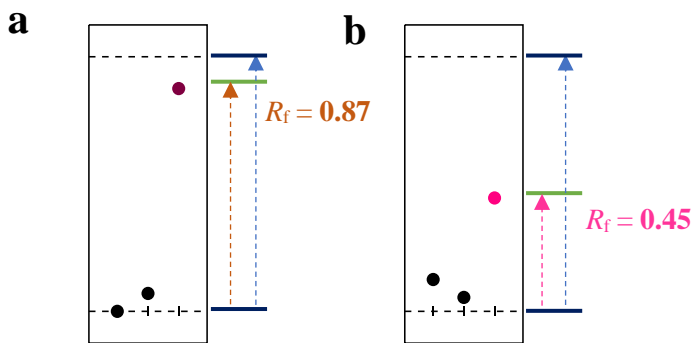


**Figure 2-1.** Development of TLC plates with compounds of (a) low (b) high retardation factor,  $R_f$ .

**Retardation factor  $R_f$ .** The retardation factor,  $R_f$ , defines the position of an individual compound on a TLC plate. It is expressed as a decimal fraction (Equation 2-1). In general, the  $R_f$  of a substance whose structure resembles the stationary phase is low (Figure 2-1a), while that similar to the mobile phase is high (Figure 2-1b).

$$R_f = \frac{\text{Distance traveled by the compound from the starting spot}}{\text{Distance travelled by the solvent from the starting spot}} \quad (\text{Equation 2-1})$$

### 2.2.1.2 Column chromatography

Column chromatography, known as liquid chromatography (LC), is a simple and popular separation and purification technique. Both solid and liquid samples can be separated and purified by LC. An LC column consists of a stationary solid phase that sorbs and separates the compounds passing through it with the help of a liquid mobile phase. Compounds get retained and then eluted according to their chemical nature. Various stationary phases, including silica, alumina, calcium phosphate, calcium carbonate, starch, magnesia, and solvent solutions of different compositions based on the nature of compounds separated and isolated, are used in

LC. The method optimizing is an essential task in separating different compounds in extracts. In LC, a cylindrical glass tube, plugged at the bottom by a piece of glass wool or porous disc, is filled with a slurry of stationary phase particles and a suitable solvent. Samples to be separated are mixed with silica, loaded on the top of the column, and allowed to move with the solvent. Compounds are retained at different column regions according to their polarity differences and eluted with solvents of suitable polarity. The compound of higher retention ability will remain at the top, and that with the lower will appear at the bottom. By the mobile phase addition at the top, compounds get retained and then pass through the column; this process is called elution. A schematic diagram of the LC column is shown in Figure 2-2.<sup>287</sup> All compounds mentioned in this thesis were purified using LC.

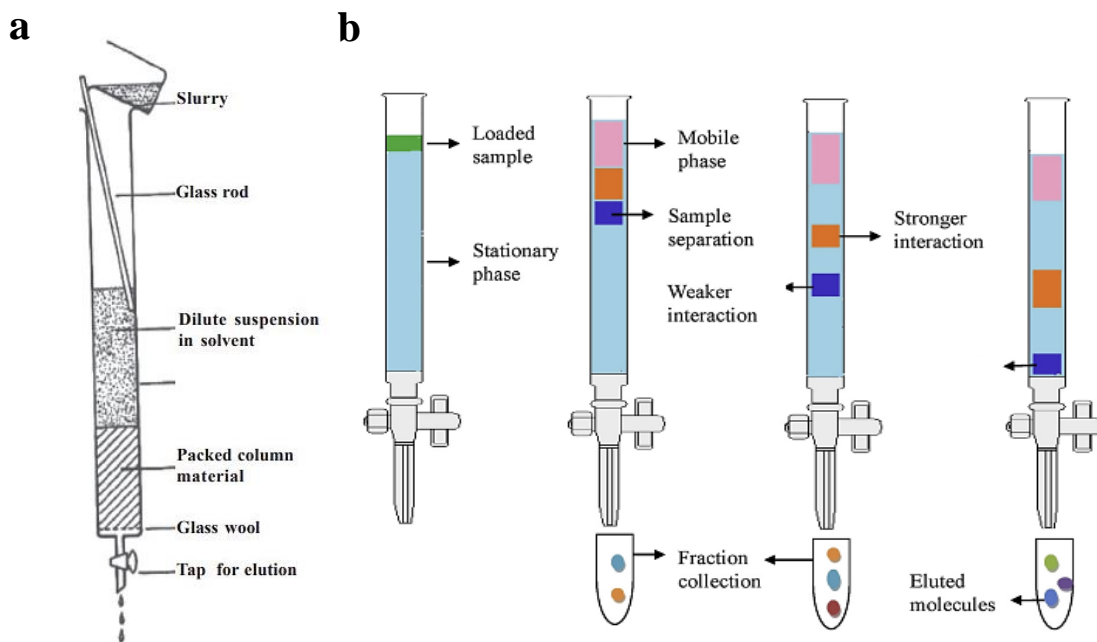
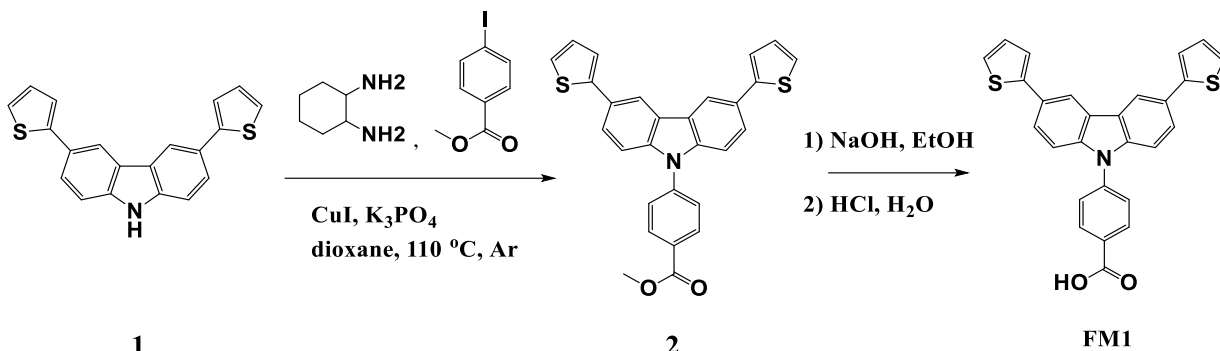


**Figure 2-2.** Liquid chromatography, LC, fundamentals. (a) Packing an LC column with the stationary phase. (b) Compound purification by separation via elution with a mobile phase (adapted from<sup>287,288</sup>).

### 2.2.1.3 General syntheses procedure for thiophene appended carbazole functional monomers



**Scheme 2-1.** The synthetic route of 4-[3,6-di(thiophen-2-yl)-9H-carbazole-9-yl]benzoic acid, **FM1**.

The general procedure for the **FM1** synthesis is presented in Scheme 2-1 and can be found elsewhere.<sup>192</sup> Briefly, to prepare **2**, 4-iodobenzoic acid methyl ester (684 mg, 2.0 mmol), and **1** (650 mg, 2.5 mmol) were dissolved in anhydrous dioxane (15 mL) in a 100-mL three-necked round-bottom flask. Next, CuI (40 mg, 0.2 mmol), K<sub>3</sub>PO<sub>4</sub> (964 mg, 4.5 mmol), and 1,2-diaminocyclohexane (0.2 mmol) were added. Then, the reaction mixture was stirred for 12 h at 110 °C under an inert gas atmosphere. After cooling to room temperature, the mixture was poured into distilled water (50 mL). The resultant solution was three times extracted with dichloromethane, DCM (30 mL). Finally, the organic phase was collected, dried with MgSO<sub>4</sub>, and then the solvent was evaporated under decreased pressure. The crude product was purified by LC using ethyl acetate : hexane (1 : 1, v/v) with 1 vol% of triethylamine as the eluent. (610 mg, 64.2% yield).

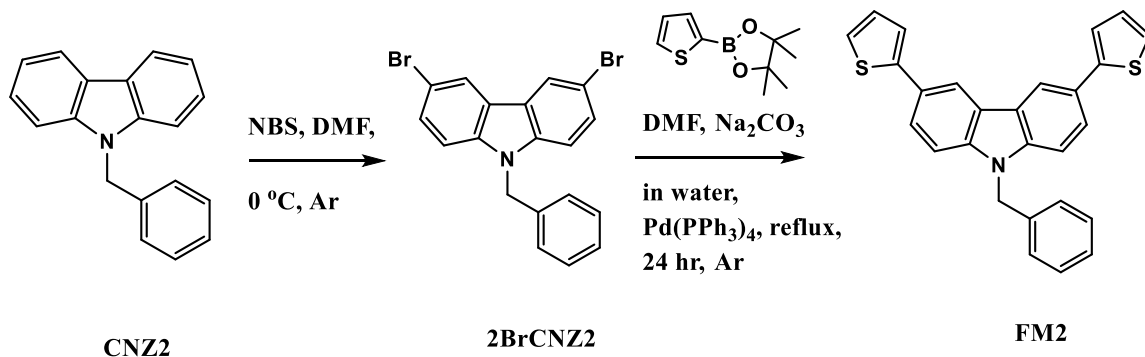
*4-[3,6-di(thiophen-2-yl)-9H-carbazole-9-yl]benzoic acid **FM1**.* Methyl ester **2** (600 mg, 1.2 mmol) was hydrolyzed in a mixture of MeOH (1 mL) and 1.0 M NaOH (0.4 mL). The reaction mixture was refluxed for 10 h. After cooling to room temperature then pouring into distilled water (10 mL), the mixture was acidified with 1.0 M HCl (40 mL), resulting in solid precipitation. The precipitate was filtered off, then washed with water, and then dried in a desiccator. The crude product was purified by LC on a silica gel using ethyl acetate : hexane (1 : 1, v/v) as the eluent. The product was obtained as a yellowish solid (yield 455 mg, 77.5%). The monomer and its polymer

are electrochemically, spectroscopically, and microscopically characterized in Appendix.

**<sup>1</sup>H NMR** (500 MHz, DMSO,  $\delta$  ppm) : 13.09 (s, 1H), 8.72 (d,  $J$  = 1.3 Hz, 2H), 8.25 (d,  $J$  = 8.5 Hz, 2H), 7.83 (d,  $J$  = 8.5 Hz, 2H), 7.78 (dd,  $J$  = 8.6, 1.7 Hz, 2H), 7.60 (d,  $J$  = 2.7 Hz, 2H), 7.53 (dd,  $J$  = 13.3, 5.2 Hz, 4H), 7.18 (dd,  $J$  = 5.0, 3.6 Hz, 2H).

**<sup>13</sup>C NMR** (DMSO, 100 MHz,  $\delta$  ppm): 185.5; 163.2; 161.4; 157.5; 150.4; 147.9; 144.1; 139.8; 128.2; 127.9; 124.5; 123.5; 122.7; 119.1; 110.3.

**IR** ( $\text{cm}^{-1}$ ): 3106, 3067, 1691, 1600, 1483, 1472, 1413, 1363, 1283, 1226, 1166, 800, 685.



**Scheme 2-2.** Synthetic route for 4-[3,6-bis(thiophen-2-yl)-9H-carbazol-9-yl]-benzyl, **FM2**.

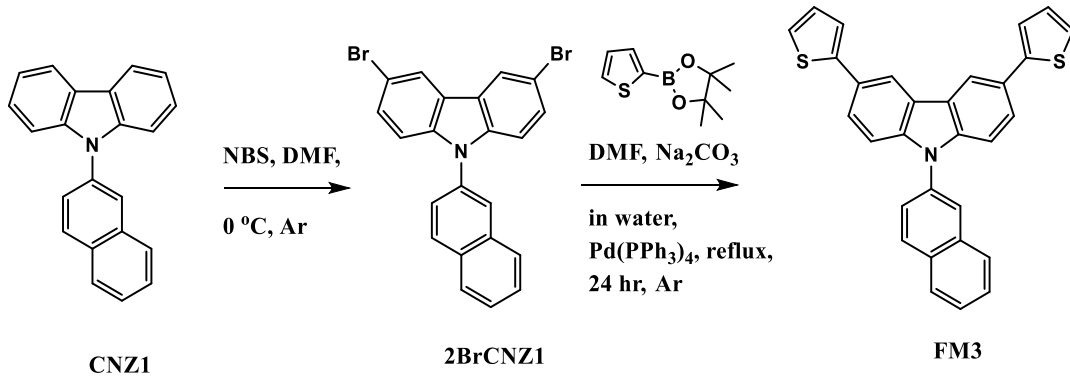
For 9-benzyl-3,6-dibromo-9H-carbazole (2BrCNZ2), first, CNZ2 (500 mg, 1.9 mmol) was added to anhydrous DMF (15 mL) at room temperature while stirring. The resulting mixture was stirred at room temperature for another 15 minutes. *N*-bromosuccinimide (765 g, 4.3 mmol) in anhydrous DMF (10 mL) was added dropwise to the mixture at 0 °C in an inert atmosphere. The resulting solution was allowed to reach room temperature and continued stirring overnight. This solution was poured into ice water. The milky white precipitate formed was filtered and dissolved in DCM and then was dried with anhydrous MgSO<sub>4</sub>. After solvent evaporating, the product was purified by LC on a silica gel column with the ethyl acetate : hexane (70 : 30, v/v) eluent. The product was obtained as an off-white solid (yield 210 mg, 29%).

**<sup>1</sup>H NMR** (CDCl<sub>3</sub>, 300 MHz,  $\delta$  ppm): 8.18 (d,  $J$  = 1.5 Hz, 2H), 7.54 (d,  $J$  = 1.9 Hz, 1H), 7.51 (d,  $J$  = 1.9 Hz, 1H), 7.28 – 7.23 (m, 4H), 7.22 (s, 1H), 7.09 – 7.04 (m, 2H), 5.47 (s, 2H).

4-[3,6-Bis(thiophen-2-yl)-9*H*-carbazol-9-yl]-benzyl **FM2** was prepared by reacting 9-benzyl-3,6-dibromo-9*H*-carbazole (0.120 g, 0.29 mmol), thiophene-2-boronic acid pinacol ester (0.152 g, 0.72 mmol), Pd(PPh<sub>3</sub>)<sub>4</sub> (0.017 g, 0.014 mmol), aqueous Na<sub>2</sub>CO<sub>3</sub> (2.0 M, 5 mL), DMF (30 mL) were mixed in a round bottom flask (Scheme 2-2). The mixture was deaerated, then refluxed for 48 h under an argon atmosphere. After cooling, abundant water was added, then the mixture was extracted three times with DCM. Next, the organic phase was dried with MgSO<sub>4</sub>. After solvent evaporating, the product was purified by LC on a silica gel column with the DCM : hexane (1 : 9, v/v) eluent. A yellowish powder was obtained (yield 83 mg, 68.03%). Electrochemical, spectral, and microscopic features of the monomer and its polymer are described in Appendix.

**<sup>1</sup>H NMR** (CDCl<sub>3</sub>, 300 MHz,  $\delta$  ppm): 8.37 (s, 2H), 7.72 (d,  $J$  = 1.8 Hz, 1H), 7.69 (d,  $J$  = 1.8 Hz, 1H), 7.38 – 7.34 (m, 5H), 7.26 (s, 3H), 7.17 (s, 2H), 7.11 (dd,  $J$  = 5.2, 3.6 Hz, 3H), 5.53 (s, 2H).

**IR** (cm<sup>-1</sup>): 3102, 3068, 3026, 2860, 2930, 1634, 1605, 1480, 1425, 1290, 1205, 1053, 1157, 700, 787.



**Scheme 2-3.** Synthetic route of 3,6-bis(thiophen-2-yl)-9-(4-naphthalen-2-yl)-9*H*-carbazole, FM3.

*3,6-Dibromo-9-(naphthalen-2-yl)-9*H*-carbazole* 2BrCNZ1. First, CNZ1 (1.2 g, 4.09 mmol) was added to anhydrous DMF (15 mL) at room temperature while stirring. The resulting mixture was stirred at room temperature for another 15 minutes. *N*-bromosuccinimide (1.6 g, 9 mmol) in anhydrous DMF (10 mL) was added dropwise to the mixture at 0 °C in an inert atmosphere. The resulting solution was allowed to reach room

temperature and continued stirring overnight. Then this solution was poured into ice water. The milky white precipitate formed was filtered, then dissolved in DCM, and then dried with anhydrous MgSO<sub>4</sub>. The solvent was removed under a high vacuum. A yellowish solid was obtained (yield 1.45 g, 80.5%).

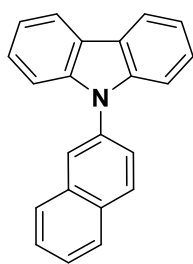
**<sup>1</sup>H NMR** (500 MHz, CDCl<sub>3</sub>,  $\delta$  ppm) : 8.23 – 8.22 (m, 2H), 8.08 (d,  $J$  = 8.5 Hz, 1H), 7.98 (t,  $J$  = 3.1 Hz, 2H), 7.93 – 7.89 (m, 1H), 7.63 – 7.60 (m, 2H), 7.58 (dd,  $J$  = 8.6, 2.1 Hz, 1H), 7.51 (dd,  $J$  = 8.7, 1.9 Hz, 2H), 7.30 (d,  $J$  = 8.7 Hz, 2H).

Preparation of 3,6-bis(thiophen-2-yl)-9-(4-naphthalen-2-yl)-9*H*-carbazole **FM3** followed Scheme 2-3. First, 3,6-dibromo-9-(naphthalen-2-yl)-9*H*-carbazole (1.4 g, 3.1 mmol) was reacted with thiophene-2-boronic acid pinacol (3.0 g, 6.8 mmol), Pd(PPh<sub>3</sub>)<sub>4</sub> (0.23 g, 0.2 mmol), 2.0 M Na<sub>2</sub>CO<sub>3</sub> (5mL), DMF (30 mL) in a round bottom flask. The mixture was deaerated and then refluxed for 48 h under an argon atmosphere. After cooling, abundant water was added, and then the mixture was extracted three times with DCM. The organic phase was dried with MgSO<sub>4</sub>. After solvent evaporating, the product was purified by LC on a silica gel column with the DCM : hexane (1 : 4, v/v) eluent. A light green powder was obtained (yield 1.0 g, 71.42%). Electrochemical, spectral, and microscopic features of the monomer and its polymer are described in Chapter 3.

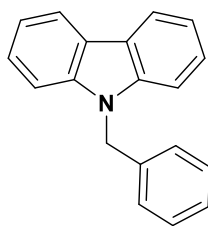
**<sup>1</sup>H NMR** (500 MHz, CDCl<sub>3</sub>,  $\delta$  ppm): 8.42 (d,  $J$  = 1.7 Hz, 2H), 8.09 (d,  $J$  = 8.7 Hz, 1H), 8.05 (d,  $J$  = 1.9 Hz, 1H), 8.02 – 7.97 (m, 1H), 7.93 (dq,  $J$  = 6.8, 3.3 Hz, 1H), 7.71 (t,  $J$  = 2.8 Hz, 1H), 7.69 – 7.65 (m, 2H), 7.63 – 7.59 (m, 2H), 7.45 (d,  $J$  = 8.5 Hz, 2H), 7.39 (dd,  $J$  = 3.5, 1.1 Hz, 2H), 7.29 (dd,  $J$  = 5.1, 1.1 Hz, 2H), 7.15 – 7.11 (m, 2H).

**<sup>13</sup>C NMR** (CDCl<sub>3</sub>, 100 MHz,  $\delta$  ppm): 145.9; 141.6; 135.3; 134.57; 133.1; 130.6; 128.6; 128.5; 128.4; 127.7; 127.5; 127.2; 125.7; 125.5; 124.5; 124.4; 122.9; 118.6; 110.9.

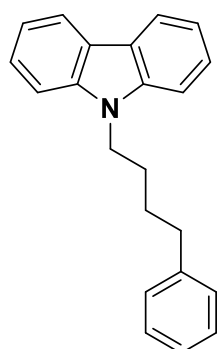
**IR** (cm<sup>-1</sup>): 3111, 3050, 3036, 1626, 1598, 1476, 1423, 1370, 1283, 1222, 1166, 1142, 792, 690.



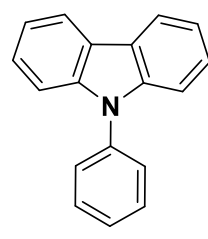
**CNZ1**



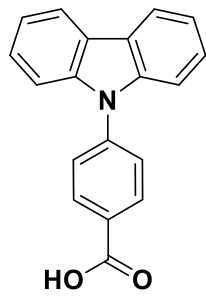
**CNZ2**



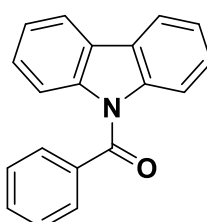
**CNZ3**



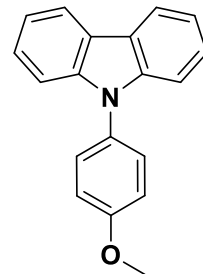
**CNZ4**



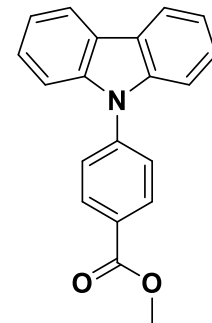
**CNZ5**



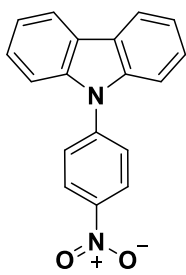
**CNZ6**



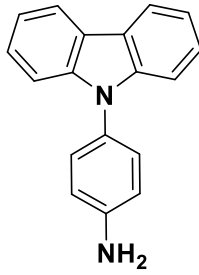
**CNZ7**



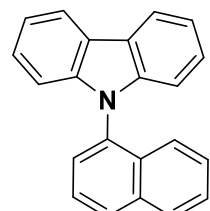
**CNZ8**



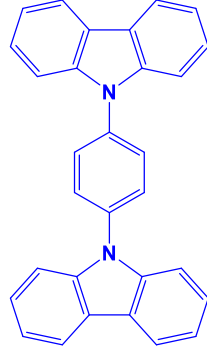
**CNZ9**



**CNZ10**



**CNZ11**



**CLM2**

**Figure 2-3.** Structural formulas of the herein synthesized carbazole monomers.

## **2.2.2 Preparation of molecularly imprinted and non-imprinted polymers**

The following three different MIPs were prepared.

1. **NanoMIP-A** – polymer nanoparticles molecularly imprinted with cilostazol, CIL
2. **MIP-CIL film** – a polymer film molecularly imprinted with cilostazol, CIL
3. **NanoMIP** – polymer nanoparticles molecularly imprinted with duloxetine, DUL

The above MIPs were investigated compared to their respective control non-imprinted polymers (NIPs). NIPs were prepared by deposition from the template-free solutions using the same electropolymerization procedures as those for MIPs.

### **2.2.2.1 Preparation of Au-layered glass slides**

Au-layered glass slides (size  $7 \times 21$  mm) were prepared by evaporating a thin (100 nm) Au layer over a thin (15 nm) Ti underlayer. These slides were used as supports for the deposition of polymer films and then applied for further investigations, i.e., AFM, SEM, and PM-IRRAS studies. Before each film deposition, Au-glass slides were cleaned with the "Piranha" solution for 10 min, then rinsed with Milli Q® water, next with isopropanol, then ultrasonicated in an IS-3R ultrasonic bath (160 W power) of InterSonic, Olsztyn, Poland for 15 min, and finally dried before use. (*Warning. The "Piranha" solution is hazardous if it comes in contact with skin or eyes.*)

### **2.2.2.2 General procedure of polymer preparation and its deposition on electrodes**

A general procedure of preparation of MIP and NIP (Scheme 2-4) was completed in 5 steps.

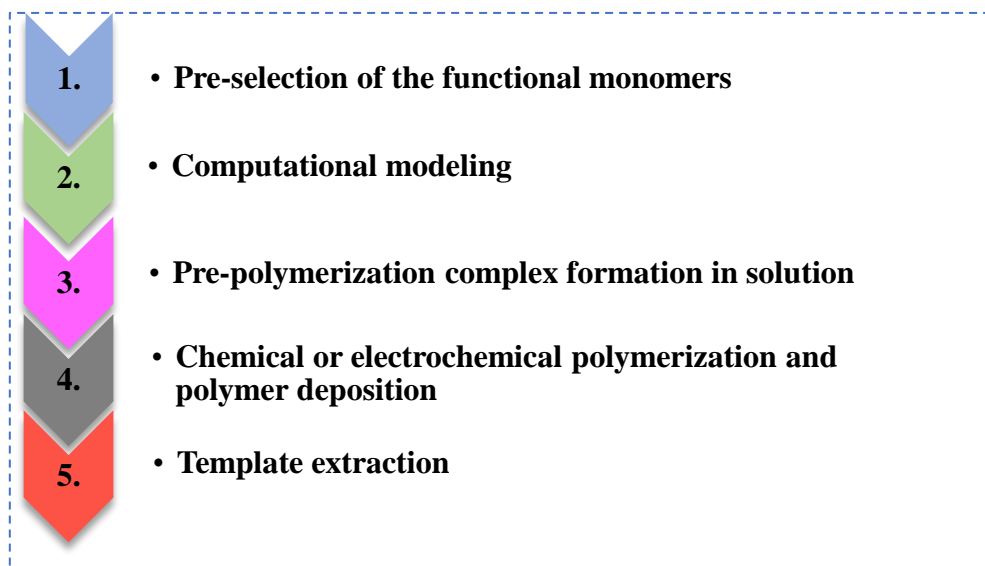
The pre-selection of functional monomers initiated it. This step was completed based on experience, chemical intuition, and a literature survey.

The second step involved computational calculations of stability of the pre-polymerization complex and its structure optimization. For that, structures of a template molecule, functional monomer molecules, and their complexes were optimized separately. Next, Gibbs free energy change ( $\Delta G$ ) corresponding to optimized complex molecules' formation was calculated. The  $\Delta G$  values for complexes of different compositions and stoichiometry were compared to select those most promising for the MIP formation. Therefore, complexes of the most negative  $\Delta G$  values were chosen for the next step.

The functional monomers, selected by computational calculations, were dissolved in a suitable solvent solution with the template and cross-linking monomers to form a pre-polymerization complex in the solution spontaneously.

In the fourth step, these complexes were polymerized under potentiodynamic conditions or by using thermal initiators, and the resulting polymer nanoparticles or films were deposited on the electrodes' surface (i.e., 2-mm Au-glass slides, 0.75-mm diameter Pt disk electrode) in the supporting electrolyte solution. The potentiodynamic technique used allowed for controlling the roughness and thickness of the MIPs deposited. After the deposition, the fabricated sensors were rinsed with abundant solvent to remove excess of the supporting electrolyte and non-polymerized monomers.

The fifth step involved template extraction. This step was dependent on the type of analyte-polymer interactions. It led to emptying molecular cavities imprinted in the MIPs. The deposited-on electrodes, MIP films constituted recognition units of chemical sensors; they were ready in this form for analyte selective detection and determination.



**Scheme 2-4.** Flow chart of consecutive steps of a general MIP film preparation procedure.

### **2.2.2.3 Preparation of polymer nanoparticles molecularly imprinted with cilostazol, CIL**

For nanoMIPs preparation, a mixture of CIL (0.2 mmol), MAA (1.6 mmol), EGDMA (5 mmol), and ABDV (0.04 mmol) was dissolved in acetonitrile (15 mL) in a glass vial sealed with a silicone septum. The (functional monomer)-to-template molar ratio used was excessive, equaling 8 : 1, to drive the self-assembly complexation equilibrium toward forming a pre-polymerization complex. The resulting complex solution was deoxygenated with a nitrogen purge for 15 min on ice. The polymerization was allowed to proceed overnight at 40 °C and then ceased by exposure to air. Subsequently, precipitated nanoMIPs were collected by centrifugation, then triply rinsed, under agitation, at 60 °C with the methanol : (acetic acid) (9 : 1, *v/v*) solution, followed by double rinsing with the ethanol : (acetic acid) (9 : 1, *v/v*) solution, afterward double rinsing with ethanol, and then one rinsing with methanol. Finally, the nanoMIPs were dried overnight (16 h) under decreased pressure (3 mbar) at room temperature (~25 °C). Control, non-imprinted polymer nanoparticles, nanoNIPs, were synthesized the same way, except for the absence of CIL. Moreover, three other nanoMIPs and their corresponding nanoNIPs were prepared using 4-VP and IA functional monomers in either acetonitrile or octanenitrile solvent (15 mL).

### **2.2.2.4 Synthesizing and depositing the CIL-imprinted MIP film**

Under potentiodynamic conditions, the MIP was synthesized and simultaneously deposited as a thin film on the electrode surface. A DCM solution of 0.1 mM CIL template, 0.3 mM FM1 functional monomer, 0.3 mM CLM cross-linking monomer, and 0.1 M (TBA)ClO<sub>4</sub> supporting electrolyte was used for this electropolymerization. Two potential cycles between 0 and 1.0 V vs. Ag quasi-reference electrode were performed at a 100-mV s<sup>-1</sup> scan rate. After that, the electrode was twice rinsed with DCM. Finally, CIL was extracted from the MIP film with 10 mM NaOH for 30 min. The NIP films were deposited without the CIL template and treated similarly to the MIP films. Polymer films were deposited on Pt disk electrodes of 0.75 mm in diameter or Au film-layered glass slides. Before electropolymerization, Pt electrodes were cleaned with the "Piranha" solution. Then, these electrodes' surface was matted by wiping them with sandpaper of the grain size of 1000.

### **2.2.2.5 Preparation of DUL-imprinted polymer nanoparticles via precipitation polymerization**

For the nanoMIPs preparation, a mixture of DUL (0.1 mmol), MAA (0.5 mmol), EGDMA (2 mmol), and AIBN (0.02 mmol) was prepared. A five-fold molar excess of the MAA functional monomer to the DUL template was used to increase the chance of creating a sufficient number of responsive imprinted cavities in the resulting nanoMIP. All the components were dissolved in a 15-mL sample of anhydrous chloroform in a glass vial fitted with an airtight septum. Afterward, the resulting solution was deoxygenated by purging nitrogen for 15 min on ice. Polymerization was performed overnight at 65 °C in an oil bath. After polymerization, NPs were collected by centrifugation.

Non-imprinted polymer NPs, nanoNIPs, were synthesized as described above, except using a DUL analyte. DUL was removed from nanoMIPs by batch solvent extraction with methanol which was 10% in acetic acid (*v/v*), then ethanol which was 10% in acetic acid (*v/v*), next twice with ethanol, followed by one round of methanol until no template peak was detected in the extracting solvent solution in HPLC.<sup>289</sup> Subsequently, nanoMIPs were dried in a vacuum overnight.

### **2.2.2.6 NanoMIPs and nanoNIPs immobilizing in polytyramine films on electrodes**

CIL-imprinted nanoMIPs or nanoNIPs (0.250 mg each) were suspended in 10 mM tyramine in 25 mM H<sub>2</sub>SO<sub>4</sub> (0.250 mL). The resulting suspension was ultrasonicated for 5 min. For the NPs sedimentation, a 2-mm diameter Au disk electrode was fixed upside down, then a 1-mL pipette tip with a cut-off end was mounted on its top. Next, this tip was filled with the suspension to allow NPs sedimentation for 3 h (Figure 2-4). On this electrode surface, subsequently, a polytyramine film was potentiodynamically deposited using 15 potential cycles between 0 to 1.50 V vs. Ag quasi-reference electrode at a 50-mV s<sup>-1</sup> potential scan rate for the NPs embedding in this film.<sup>142</sup> Afterward, the electrode was rinsed with 25 mM H<sub>2</sub>SO<sub>4</sub> then acetonitrile to remove residual unreacted monomers. The same procedure was followed to immobilize the nanoMIPs on Au-layered glass slides for SEM and AFM imaging. This slide was then mounted in the homemade Teflon™ electrochemical cell with a 2-mm diameter O-ring.

Similarly, DUL-imprinted nanoMIPs and nanoNIPs were immobilized on SWCNTs, deposited on the gold disk electrode by potentiodynamic electropolymerization of tyramine. That way, they were integrated with the resulting thin polytyramine film via matrix entrapment.<sup>290,291</sup>

For that, SWCNTs (10 mg) were first dispersed in 10 mM tyramine in 25 mM H<sub>2</sub>SO<sub>4</sub> for ~150 min using an ultrasonic homogenizer. Then, following the so-called “one-pot synthesis,” nanoMIPs (0.5 mg) were added to this dispersion (0.5 ml), and then this was ultrasonicated for 5 min. Next, the dispersion was allowed to sediment for ~75 min, followed by tyramine potentiodynamic electropolymerization where the potential was five times cycled between -0.10 and 0.40 V vs. Ag quasi-reference electrode at 50 mV s<sup>-1</sup>. Afterward, the electrode was rinsed with deionized water to remove any residual tyramine monomer, free SWCNTs, and nanoMIPs from the deposited composite film. Before further examining, the film was air-dried. The same procedure was followed to immobilize the nanoMIPs on Au-layered glass slides for SEM and AFM imaging. This slide was then mounted in the homemade Teflon™ electrochemical cell with a 2-mm diameter O-ring.

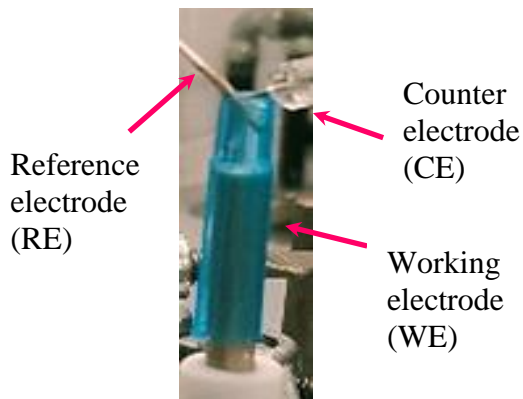


**Figure 2-4.** Photo of a pipette tip (blue) with cut-off end mounted on top of the upside-down fixed Au disk electrode used for sedimenting polymer nanoparticles and SWCNTs and then embedding them in the polytyramine film deposited by electropolymerization on this electrode.

## 2.3 Experimental techniques and instrumentation

### 2.3.1 Computational molecular modeling with molecular mechanics (MM), molecular dynamics (MD), and density functional theory (DFT)

The MIPs structures and interactions were simulated using Discovery Studio 2017R2 BIOVIA software.<sup>292</sup> Molecular structure of all the compounds in solvents was optimized using the DFT method at the B3LYP/6-311+G(d,p) level, implemented in the Gaussian 16 program.<sup>293</sup> The so-called electrostatic potential (ESP) atomic partial charges on the atoms were computed using the Breneman model,<sup>294</sup> reproducing the molecular electrostatic potential (MEP). All molecular structures were visualized using GaussView 5.0 software. Possible interactions of FMs and CLMs with the analytes in the pre-polymerization complexes and with the molecular cavity imprinted in the polymer were examined by MM and MD using the CHARMM force field<sup>295</sup> implemented in the appropriate module of Discovery Studio 2017R2. The particle mesh Ewald (PME) summation technique was implemented to accurately describe electrostatic interactions where all bonds to hydrogen atoms were constrained using the SHAKE algorithm and Leapfrog Verlet integration, allowing the set time step.<sup>296</sup> The solvation effect was considered using PACKMOL software.<sup>297</sup>

The Gibbs free energy change ( $\Delta G_{\text{bind}}$ ) accompanying the polymer matrix binding of the template, analyte, or interference molecules were calculated using Equation 2-2

$$\Delta G_{\text{bind}} = \Delta G_{\text{system}} - \Delta G_{\text{cavity}} - \Delta G_{\text{template/analyte}} \quad (\text{Equation 2-2})$$

where  $\Delta G_{\text{system}}$  is the Gibbs free energy change attributed to the formation of a complex of the imprinted cavity with the template or analyte or interference molecule,  $\Delta G_{\text{cavity}}$  is the Gibbs free energy change accompanying cavity formation, and  $\Delta G_{\text{template/analyte}}$  is the Gibbs free energy change due to the template or analyte, or interference formation.

### 2.3.2 Electroanalytical techniques

An SP-300 potentiostat/galvanostat computerized electrochemical system of Bio-Logic, SAS, controlled by EC-Lab V10.37 software of the same manufacturer, was used for electrochemical measurements. In these measurements, a three-electrode one-compartment V-shaped glass

electrochemical mini-cell was used. A 0.75-mm diameter Pt disk sealed in a soft glass tubing, or a Teflon™ shrouded 2-mm diameter Au disk and Ag and Pt wires served as the working, quasi-reference, and counter electrode, respectively. The mini-cell and electrodes were designed and fabricated in the IPC PAS mechanical shop.

### 2.3.2.1 Cyclic voltammetry (CV)

Cyclic voltammetry, CV is one of the most widely practiced electroanalytical techniques. It is used for simultaneous deposition of an electropolymerizable species and for studying analyte electrochemical properties in solution and adsorbed on the electrode. Generally, a V-shaped glass three-electrode electrochemical mini-cell was used (Figure 2-5), which housed the working, reference, and counter electrodes.

Usually, during CV measurements, the potential is scanned forth and back linearly with time, between the initial ( $E_i$ ) and the final ( $E_f$ ) switching potentials at a constant rate using triangular potential waveform (Figure 2-6a).

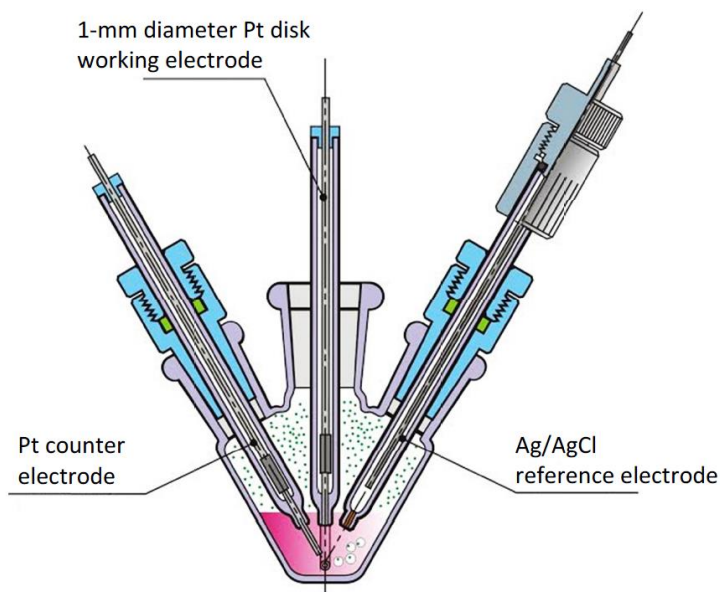


**Figure 2-5.** The cross-section sketch of a three-electrode electrochemical mini-cell setup.

The scanning starts at a slightly negative potential (A) in a typical voltammogram for a one-electron reversible redox process (Figure 2-6b). The current increases as the working electrode potential increases in an anodic scan. Then a current peak is evolved at  $E_{pa}$ , with the

current value of  $I_{pa}$ , indicating that oxidation occurs. Then it decays because of the depletion of the redox species at the electrode surface. A similar process happens during the cathodic scan, and a peak is observed at  $E_{pc}$ , with a corresponding current value of  $I_{pc}$ .

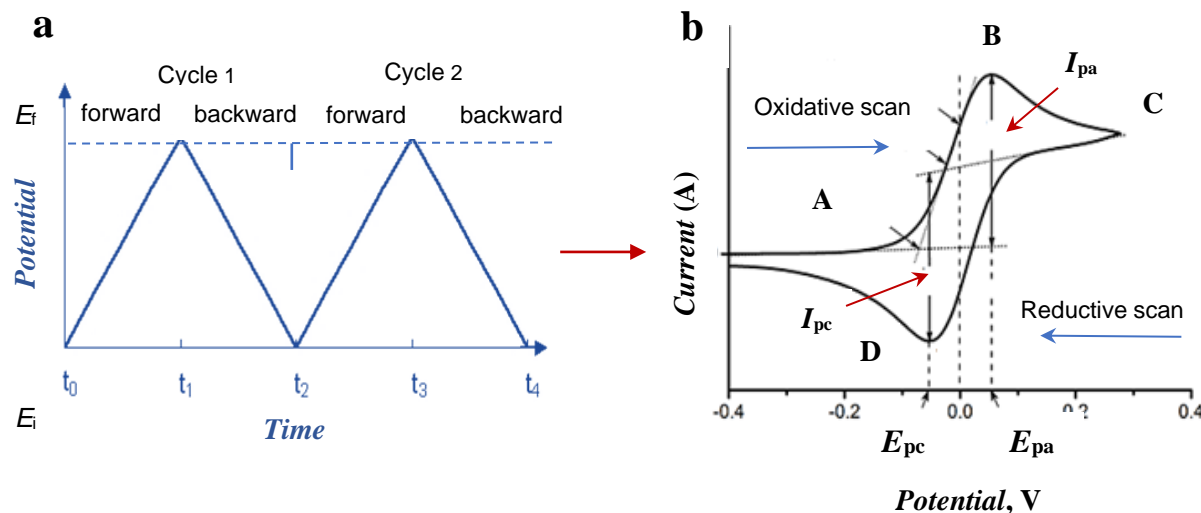


**Figure 2-6.** (a) The cyclic voltammetry (CV) potential-time waveform with switching potentials ( $E_i$  – initial potential,  $E_f$  – final potential) indicated. (b) The cyclic voltammogram for an electrochemically reversible one-electron redox process.  $E_{pa}$  and  $E_{pc}$  stand for the anodic and cathodic peak potential, respectively, while  $I_{pa}$  and  $I_{pc}$  for anodic and cathodic peak current.

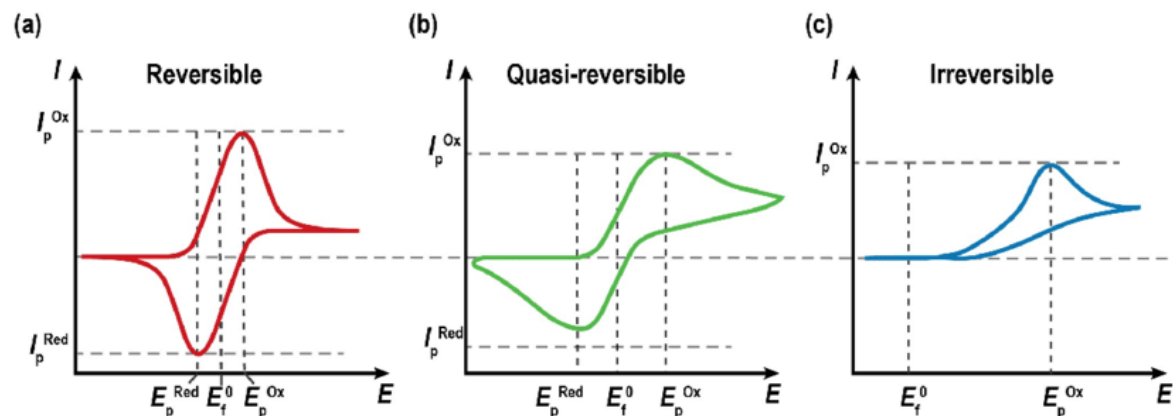


**Figure 2-7.** Cyclic voltammograms of an (a) reversible, (b) quasi-reversible, and (c) irreversible electrode reaction (adapted from <sup>298</sup>).

### 2.3.2.1.1 Nernstian (reversible) redox system

Providing that the charge transfer reaction is reversible, there is no surface interaction between the electrode and the reagents, and that the redox products are stable, the ratio of the anodic-

to-cathodic peak currents,  $I_{pa}/I_{pc} = 1.0$  (Figure 2-7a). Moreover, this system's  $E_{pa}$  and  $E_{pc}$  peak potentials are independent of the potential scan rate and redox substance concentration. The peak potentials' separation is

$$\Delta E_p = E_{pa} - E_{pc} = \frac{0.059}{n_e} V \quad (\text{Equation 2-3})$$

where  $n_e$  is the number of electrons exchanged in the elementary electrode reaction. The peak current,  $I_p$ , for the potential forward sweep in a reversible system at 298 K is expressed by the Randles-Ševčík equation.

$$I_p = (2.69 \times 10^5) n^{3/2} A D^{1/2} v^{1/2} c \quad (\text{Equation 2-4})$$

where  $A$  ( $\text{cm}^2$ ) is the active area of the working electrode, while  $D$  ( $\text{cm}^2 \text{ s}^{-1}$ ),  $v$  ( $\text{V s}^{-1}$ ), and  $c$  ( $\text{M}$ ) are the diffusion coefficient, potential scan rate, and bulk concentration of the electroactive compound, respectively. For a quasi-reversible process, the rate of the electrode process is close to the rate of diffusion (Figure 2-7b). Then, the anodic and cathodic peak potential difference is higher than Equation 2-3 predicts.

### 2.3.2.1.2 Irreversible redox system

For irreversible processes (those with an electron exchange slower than diffusion), the peaks are smaller than reversible and more widely separated. Moreover, the peak potentials depend on the potential scan rate. For irreversible electro-oxidation, the anodic peak current is still proportional to the bulk analyte concentration depending upon the charge transfer coefficient of an anodic process,  $\alpha_a$  (Figure 2-7c).

$$I_{pa} = (2.99 \times 10^5) \alpha_a^{1/2} D^{1/2} A v^{1/2} c \quad (\text{Equation 2-5})$$

In MIPs studies, CV is often applied to deposit a homogenous polymer film<sup>192,299</sup> or immobilize MIP nanoparticles on the electrode surface.<sup>300,301</sup> Moreover, sometimes it is explored as a transduction method.<sup>302</sup>

### 2.3.2.2 Differential pulse voltammetry (DPV)

Differential pulse voltammetry (DPV) is a voltammetric technique that measures the current immediately before each potential change. The accompanying current variation is plotted as a function of the potential applied. Here, potential pulses of small constant amplitude (Figure 2-8) are applied to eliminate background capacity currents and significantly increase the detectability. The pulse height used is 10 to 100 mV and is maintained constant for the base potential.<sup>303</sup>

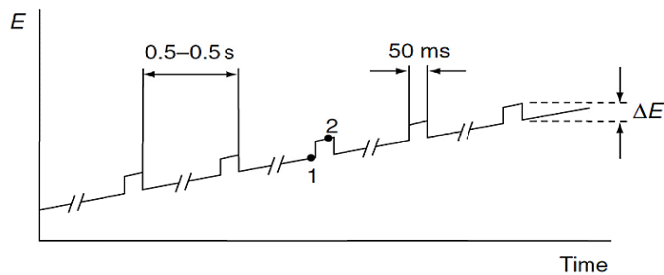


**Figure 2-8.** The potential-time program in DPV.  $\Delta E_p$  is the pulse amplitude, 1 and 2 is the time just before pulse application and at the end of the pulse, at which currents are sampled, respectively (adapted from <sup>303</sup>).

The current difference,  $\delta I = I(t_1) - I(t_2)$ , is recorded versus the potential base ramp, where  $t_1$  is the time just before pulse application, and  $t_2$  is the time just before the end of the pulse (Figure 2-8). The pulse width is selected from the range of 5 to 100 ms. The peak current is proportional to the analyte concentration

$$I_p = \frac{nFAD^{1/2}c}{\sqrt{\pi t_m}} \left( \frac{1-\sigma}{1+\sigma} \right) \quad (\text{Equation 2-6})$$

Where

$$\sigma = \exp \left[ \left( \frac{nF}{RT} \right) \left( \frac{\Delta E}{2} \right) \right] \quad (\text{Equation 2-7})$$

and  $\Delta E_p$  is the pulse amplitude. The peak potential can be identified by

$$E_p = E_{p/2} - \frac{\Delta E_p}{2} \quad (\text{Equation 2-8})$$

Due to high sensitivity, DPV allows for analyte determination at concentrations as low as  $10^{-8}$  M. Hence, DPV is mainly used herein for the batch analysis determinations.

Recently, in MIP studies, the DPV techniques have been extensively used as an indirect proof of template imprinting, then template extracting from MIP molecular cavities, and then analyte determination by exploiting the so-called "gate effect" (Figure 2-9).<sup>304,305</sup>

The "gate effect" involves the change in the redox probe diffusive permeability through the MIP film resulting from interactions of recognizing sites of MIP imprinted cavities with the binding sites of the analyte. This effect is often used for signal transduction. The faradaic current of the redox probe at the MIP film coated electrode is sensitive to the presence of the analyte because analyte binding by the analyte-selective polymer changes the accessibility of the probe to the electrode surface.

### 2.3.2.3 Electrochemical impedance spectroscopy (EIS)

Electrochemical impedance spectroscopy (EIS) is one of the most complex electrochemical techniques. An alternating voltage of a fixed frequency and small amplitude, typically 10 mV, is applied to the working electrode for measuring impedance (Figure 2-10). This voltage is described by Equation 2.9. The EIS results allow determining the polarization resistance (low-frequency region), the solution resistance (high-frequency region), and the double-layer capacitance.<sup>306</sup>

$$E_t = E_0 \sin(\omega t) \quad (\text{Equation 2-9})$$

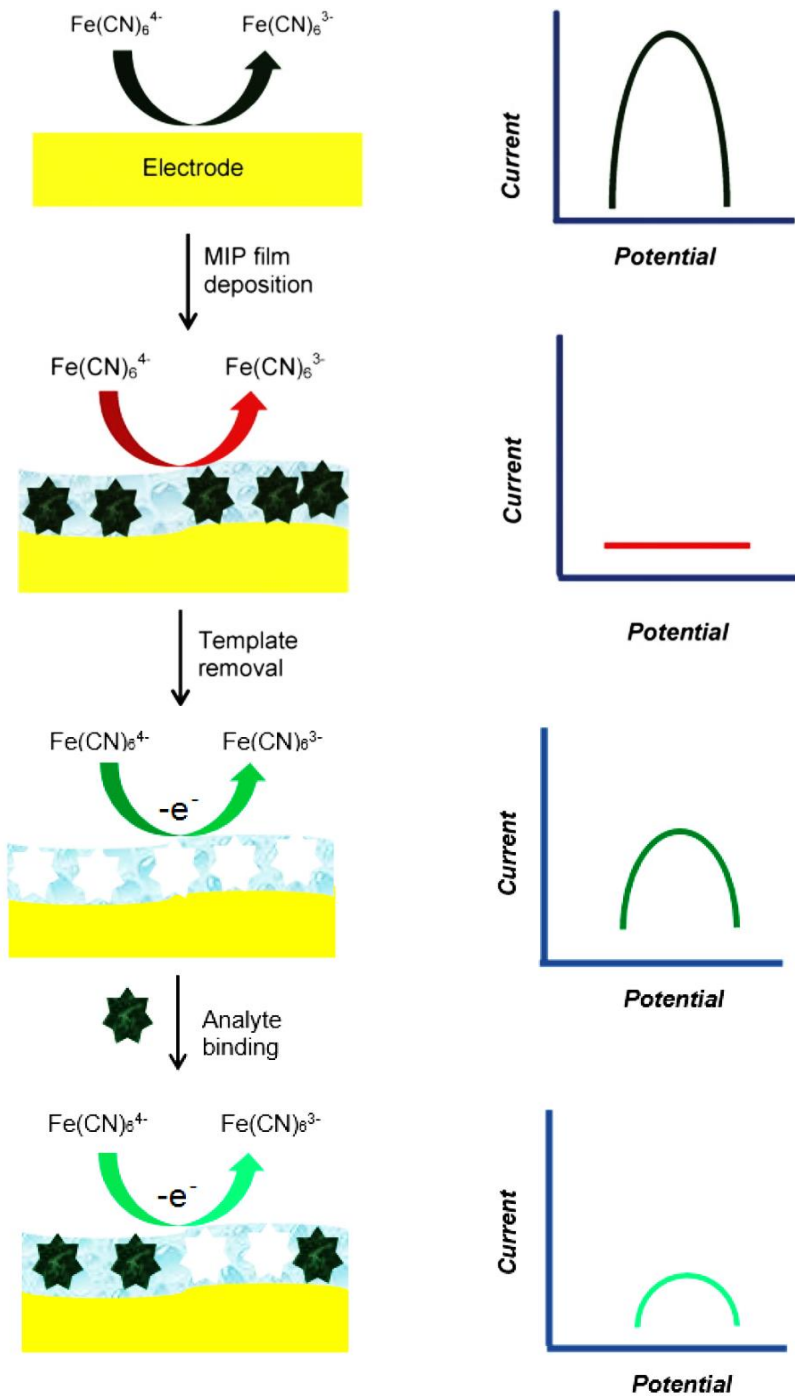


**Figure 2-9.** The DPV manifested "gate effect" exemplified with the  $\text{Fe}(\text{CN})_6^{4-}/\text{Fe}(\text{CN})_6^{3-}$  redox probe. (a) Electrochemical oxidation of the probe on the uncoated electrode and the resulting well-defined DPV peak. (b) Hindering of the  $\text{Fe}(\text{CN})_6^{4-}/\text{Fe}(\text{CN})_6^{3-}$  electrode process after MIP coating and the corresponding DPV response. (c) Enabled diffusion of the probe through the MIP film after template extraction resulting in a DPV peak. (d) Partially blocked diffusive permeability of the probe through the MIP film cavities occupied by the analyte molecules and the corresponding DPV peak of lower intensity (adapted from<sup>307</sup>).

where  $E_t$  is the potential at time  $t$ ,  $V_0$  is the voltage amplitude, and  $\omega = 2\pi f$  is the radial frequency of the alternating voltage of frequency,  $f$ , applied.

In a linear system, the current,  $I_t$ , is phase-shifted by a phase angle  $\varphi$  (Equation 2-10).

$$I_t = I_0 \sin(\omega t + \varphi) \quad (\text{Equation 2-10})$$

where  $I_0$  is a current recorded when the impedance is computed.

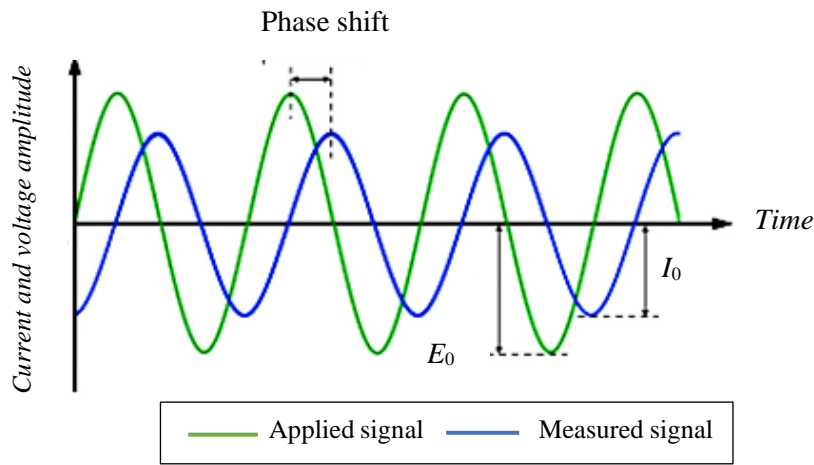


**Figure 2-10.** Current changes incurred by the sinusoidal voltage applied to an ideal capacitor (adapted from<sup>308</sup>).

Finally, the impedance  $Z$  can be calculated for each frequency of an electrochemical cell. For that, Equation 2-11, analogous to Ohm's law, is used.

$$Z = \frac{E_t}{I_t} = \frac{E_0 \sin(\omega t)}{I_0 \sin(\omega t + \varphi)} = Z_0 \frac{\sin(\omega t)}{\sin(\omega t + \varphi)} \quad (\text{Equation 2-11})$$

With Euler's relationship,

$$\exp(j\sigma) = \cos \sigma + j \sin \sigma \quad (\text{Equation 2-12})$$

where  $\sigma$  is a real number and  $j = \sqrt{-1}$  is an imaginary unit, it is possible to express the impedance as a complex function. The potential is then described as

$$E_t = E_0 \exp(j\omega t) \quad (\text{Equation 2-13})$$

and the current response as

$$I_t = I_0 \exp(j\omega t - \sigma) \quad (\text{Equation 2-14})$$

Generally, the complex impedance of an electrode system is given as

$$Z(\omega) = \frac{E}{I} = Z_0 \exp(j\sigma) = Z_0 (\cos \sigma + j \sin \sigma) = Z_{real} - j Z_{im} \quad (\text{Equation 2-15})$$

where  $Z_{real}$  and  $Z_{im}$  are the real and imaginary impedance components, respectively. The impedance at a given  $\omega$  value in the  $-Z_{im}$  against  $Z_{real}$  coordinates is the Nyquist plot (Figure 2-12).

For the impedance measurements of a faradaic system, the (polymer film)-coated electrode in the presence of a redox probe, e.g., the  $[\text{Fe}(\text{CN})_6]^{4-}/[\text{Fe}(\text{CN})_6]^{3-}$  couple, the equivalent electrode circuit adopted is one of the simplest possible models describing processes at the electrochemical interface. It is called the Randles-Ershler equivalent circuit (Figure 2-11).<sup>303</sup>

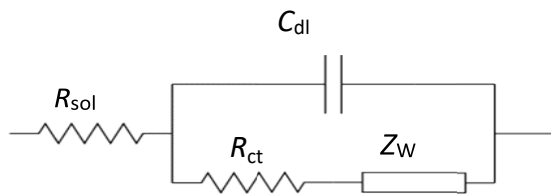


**Figure 2-11.** Representation of the modified Randles-Ershler equivalent electrode circuit of an electrochemical redox system used to fit experimental impedance data.

The total impedance is described by Equation 2.16

$$Z = R_{sol} + \frac{(R_{ct} + Z_w)}{1 + j\omega C_{dl}(R_{ct} + Z_w)} \quad (\text{Equation 2-16})$$

where  $R_{\text{sol}}$  is the electrolyte solution resistance,  $R_{\text{ct}}$  is the charge transfer resistance,  $C_{\text{dl}}$  is double-layer capacitance, and  $Z_w$  is the Warburg impedance representing the mass transfer to the electrode accompanying the redox process.

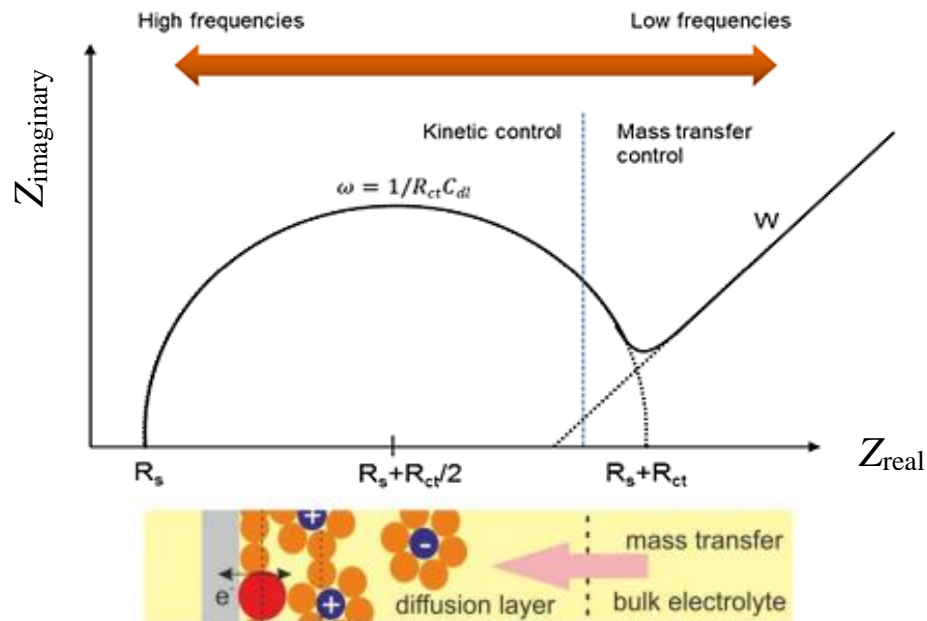


**Figure 2-12.** The Nyquist representation of the impendence data (adapted from<sup>309</sup>).

For the impedance measurements of a non-faradaic system, e.g., a (non-conducting polymer film)-coated electrode in a supporting electrolyte solution, the equivalent circuit applied simplifies to a solution resistance in series with a double-layer capacitance (Figure 2-13). The capacitance and resistance of thin polymer films are negligibly small.



**Figure 2-13.** The equivalent circuit with a non-faradaic electrochemical process for the (non-conducting polymer film)-coated electrode in a supporting electrolyte solution.

### 2.3.3 Other instrumentation

The UV-visible spectra were recorded with a 0.1-nm resolution using a UV 2501-PC recording spectrophotometer of Shimadzu Corp (Tokyo, Japan).

Polymer surfaces were imaged with AFM using a Multimode 8 microscope under the control of a Nanoscope V controller and Multimode v 8.15 software, both of Bruker. An antimony-doped Si tip and cantilevers of 376-kHz resonant frequency and the force constant,  $k = 60 \text{ N m}^{-1}$ , were used for sample imagining with the Tapping Mode<sup>TM</sup>. The MIP and NIP films were deposited on an Au layer with a Ti underlayer ( $7 \times 25$ ) mm<sup>2</sup> coating glass slides using a homemade holder with the Pt plate counter electrode and the Ag wire quasi-reference electrode. For roughness measurements, four points of the sample were imaged at  $(5 \times 5)$   $\mu\text{m}^2$ . Then average roughness was calculated from the results obtained for each image. A single image's roughness calculations were performed using NanoScope Analysis v. 1.2 software from Bruker. For determining average film thickness, some parts of the films were carefully removed in a few different places from the electrode surface, i.e., scratched with a Teflon<sup>TM</sup> spatula under an optical microscope. Subsequently, these scratches were imaged with AFM. Then, the heights of the resulting steps were measured by averaging the number of points on both sides of the step (sufficiently far from its partially detached front). The difference of the average values of points on the step and at its foot determined the height of the step. Finally, step heights measured for different scratches were averaged to get an average film thickness value.

SEM images of polymers deposited on Au-layered glass slides were recorded with Nova NanoSEM 450 microscope of FEI (USA).

Analyte extraction was confirmed with HPLC using an Agilent Infinity 1290 LC system equipped with the DAD detector and the Thermo Hypercyl GOLD C18 (100  $\times$  2.1 mm, 1.9  $\mu\text{m}$ ) column of Thermo Fisher Scientific.

Polarization-modulation infrared reflection-absorption spectroscopy (PM-IRRAS) spectra for the MIP and NIP films were recorded with a Vertex 80v spectrophotometer equipped with the PMA 50 module and controlled with OPUS v. 7.2 software (Bruker) under ambient atmosphere using a liquid-nitrogen cooled B316/6 MCT detector. The 1024 scans with a spectral resolution of  $2 \text{ cm}^{-1}$  were acquired and then averaged for each spectrum.

The DLS measurements were performed using a Zetasizer Nano series (Malvern Instruments, Ltd). Fluorescence data were collected using the FS 900 CDT Spectrofluorimeter (Edinburgh).

In situ EPR and UV-vis-NIR spectroelectrochemical experiments were performed using the optical EPR cavity (ER 4104OR, Bruker, Germany) of the EMX Micro Xband CW spectrometer (Bruker, Germany). UV-vis-NIR spectra were recorded using the Avantes AvaSpec2048x14-USB2 spectrometer with the CCD detector and the AvaSpec-NIR 256-2.2 spectrometer, equipped with the InGaAs detector, and applying AvaSoft 7.5 software. The EPR and the UV-vis-NIR spectrometer were connected to a PG 390 HEKA potentiostat. The PotMaster v2x40 software package (HEKA Electronic, Germany) allowed triggering the experiment. The spectroelectrochemical flat cell with a three-electrode arrangement<sup>310,311</sup> consisting of a laminated indium-tin-oxide ITO film-coated glass slide as the working electrode, a Pt wire as the counter electrode, and an Ag wire coated with AgCl as the quasi-reference electrode was used. Au-microgrid (1024 meshes/cm<sup>2</sup>) was positioned between two pieces of chemically resistant polyester-based lamination foils (DocuSeal, U.S.A.) to create a small, well-defined electrochemically active surface with an insulated electric contact and circular holes providing 0.1-cm<sup>2</sup> free active electrode surface area.

### 2.3.3.1 Spectroscopic techniques

#### 2.3.3.1.1 UV-vis spectroscopy

UV-vis radiation comprises only a small part of the electromagnetic spectrum (Figure 2-14). UV-vis spectroscopy is an analytical technique that measures UV or visible light absorbed by or transmitted through a sample at several discrete wavelengths compared to a reference or blank sample. If light passes through or is reflected from a sample, the amount of light absorbed is the difference between the incident and the transmitted radiation. The amount of light absorbed is expressed as either transmittance

$$\text{Transmittance} = \frac{\text{Intensity of transmitted radiation}}{\text{Intensity of incident radiation}} \quad (\text{Equation 2-17})$$

or absorbance

$$\text{Absorbance} = -\log (\text{Transmittance}) \quad (\text{Equation 2-18})$$

The relationship between absorbance and concentration of an absorbing compound is linear. Lambert-Beer's law describes it with Equation 2.19

$$Absorbance = c \xi L \quad (\text{Equation 2-19})$$

where  $\xi$  is the molar absorptivity or extinction coefficient ( $M^{-1} \text{ cm}^{-1}$ ),  $c$  is the concentration (M), and  $L$  is the light beam path length (cm).

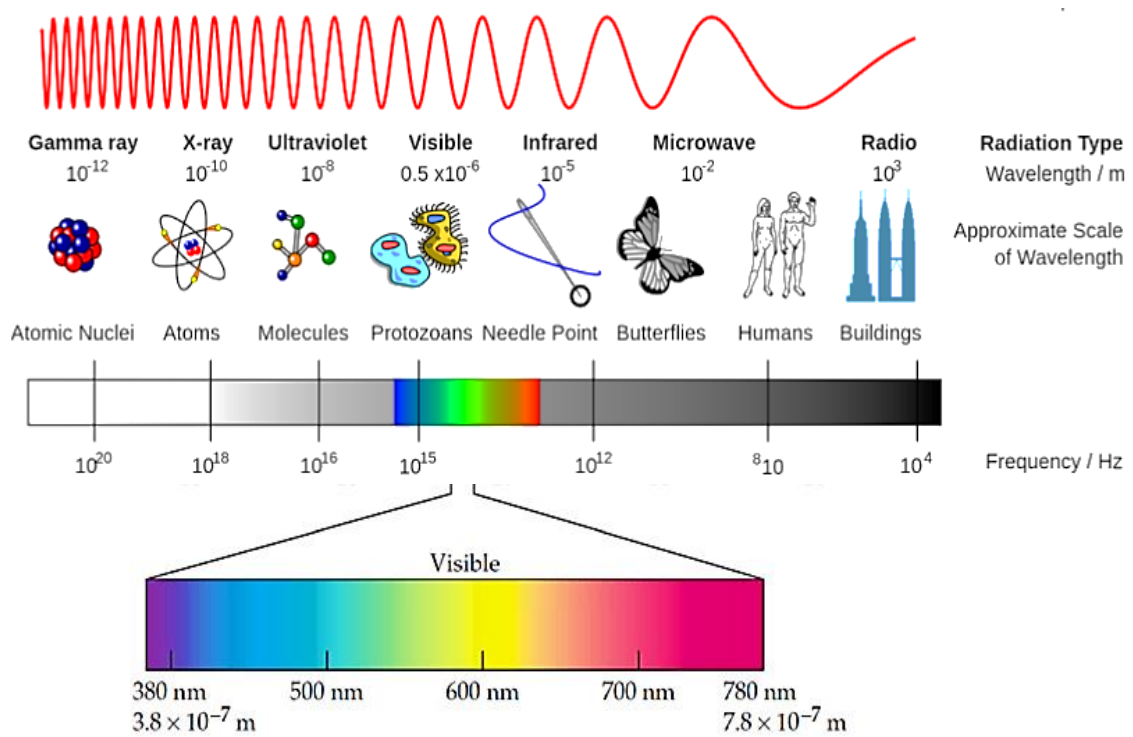


**Figure 2-14.** The electromagnetic spectrum (adapted from<sup>312</sup>).

### 2.3.3.1.2 Fluorescence spectroscopy

Fluorescence spectroscopy is also known as fluorimetry. It is used to analyze sample fluorescence. If molecules of a compound are excited, e.g., with the ultraviolet radiation, its electrons jump to a higher energy vibrational level. Then, within a few nanoseconds, they lose this energy, e.g., via spontaneous light emission, i.e., fluorescence.

First, the initial absorption takes the molecule to an excited electronic state for fluorescence generation. Then, the excited molecule collides with surrounding molecules releasing energy non-radiatively. That way, it steps down the ladder of vibrational levels to

reach the lowest vibrational level of the electronically excited state. The surrounding molecules may not accept more energy needed to lower the molecule state to the ground electronic state. Therefore, this molecule may survive a long time at this electronically excited state until it undergoes spontaneous emission, i.e., fluorescence (Figure 2-15a). The fluorescence frequency is lower than that of the incident radiation because the emissive transition occurs after some vibrational energy dissipation to the surroundings (Figure 2-15b).

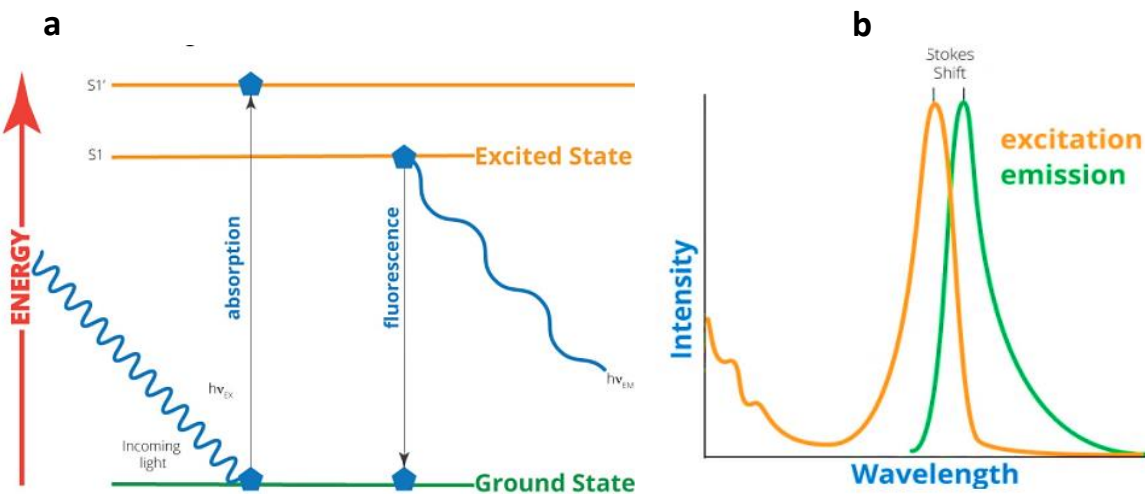


**Figure 2-15.** (a) The Jablonski diagram illustrating the fluorescence radiation. (b) Typical excitation-emission spectra (adapted from<sup>313</sup>).

### 2.3.3.1.3 Infrared (IR) spectroscopy

Infrared (IR) spectroscopy is a powerful non-destructive vibrational spectroscopy technique used, among others, to identify molecular orientation in polymer films, functional groups present in an unknown compound, thus its composition, and detect molecular impurities. In IR spectroscopy, a sample is irradiated with IR light. If the IR radiation frequency matches the frequency of molecular bond vibration, IR light is absorbed, and the bond is vibrating. The IR spectroscopy measures the wavelength and intensity of IR radiation absorbed by a sample. The molecule's vibrational mode's IR absorption probability and frequency depend on molecular bonds strength and polarity. Molecular inter-molecular and intra-molecular interactions influence these properties. Therefore, IR spectroscopy provides structural information about the sample. However, this spectroscopy can detect only IR active molecules, i.e., molecules whose bond vibration is accompanied by a change in the electric

dipole moment.

In organic compounds, bond vibrations usually occur between 4000 and 1500 cm<sup>-1</sup>, mostly being stretching vibrations. They are localized and are characteristic of specific functional groups. At wavenumbers below 1500 cm<sup>-1</sup>, bending vibrations of bonds are involved (Figure 2-16).

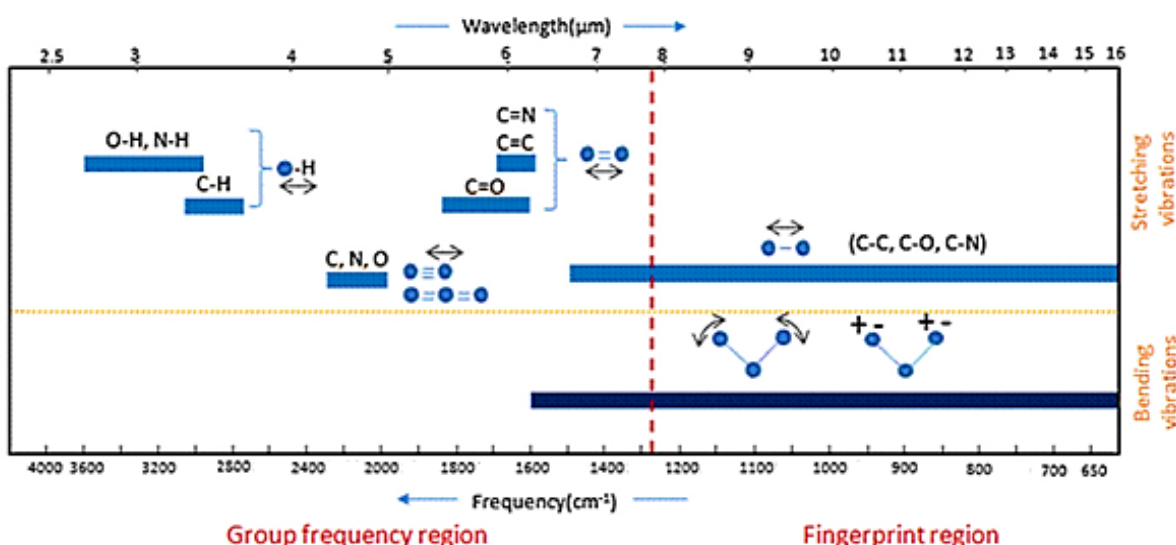


**Figure 2-16.** Group frequency and fingerprint regions of the infrared (IR) spectrum (adapted from<sup>68</sup>).

In polarization-modulation infrared reflection-absorption spectroscopy, PM-IRRAS, incident IR light is modulated in two orthogonal directions, i.e., perpendicular (*p*-polarization) and parallel (*s*-polarization) to the plane of incidence of IR light (Figure 2-17). Surface selection rules dictate that smooth metal surface illumination with the *p*-polarized light at the grazing angle of incidence leads to constructive interference between incident and reflected IR light beams. This interference causes an enhancement of the electric field component perpendicular to the substrate surface. Therefore, the *p*-polarized light ( $R_p$ ) reflectivity is sensitive to the adsorbed molecules with transition dipole moments perpendicular to the substrate surface.<sup>314</sup>

In contrast, illumination under the same conditions using the *s*-polarized light causes a destructive interference between the beams, resulting in the almost complete disappearance of the electric field component parallel to the substrate surface. Therefore, the *s*-polarized light

reflectivity ( $R_s$ ) is insensitive to molecules' functional groups' vibrations parallel to the metal surface. Consequently, it is used to obtain the background spectrum.

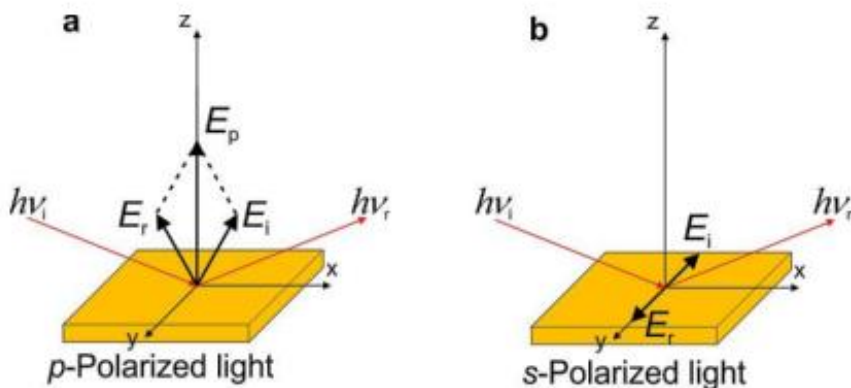


**Figure 2-17.** The surface selection rule of IRRAS. The incident beam,  $h\nu_i$ , (a)  $p$ -polarized or (b)  $s$ -polarized, is reflected from a smooth metal surface, resulting in the electric field enhancing or attenuating, respectively (adapted from<sup>315</sup>).

The reflection-absorption spectrum ( $\Delta R/R$ ) is calculated as follows:

$$\frac{\langle \Delta R \rangle}{\langle R \rangle} = \frac{|(R_p - R_s)|}{\frac{(R_p - R_s)}{2}} \quad (\text{Equation 2-20})$$

The signal from IR absorption by atmospheric water and CO<sub>2</sub> is also removed in this spectrum. PM-IRRAS is very useful for examining irreversibly adsorbed MIP films.

#### 2.3.3.1.4 Spectroelectrochemistry (SEC)

Spectroelectrochemistry (SEC) is a relatively new technique that integrates electrochemistry with spectroscopy characterizing kinetic, thermodynamic, and molecular vibrational processes (Figure 2-18a). SEC has been established as a powerful technique to simultaneously analyze some of the most important aspects of chemistry, viz., the energy and mechanism of a redox reaction and the identities of the participating species. In other words, using this technical combination, both the questions of "how?" and "what?" can be answered.<sup>316,317</sup> Under potential control, spectroscopic information about in situ electrogenerated species can readily be

obtained, including electronic absorption, vibrational modes and frequencies, light emission, and scattering.<sup>317</sup>

As the name suggests, UV-vis-NIR absorption spectroscopy utilizes incident light in the ultraviolet (ca. 200 - 400 nm), visible (ca. 400 – 750 nm), and near-infrared (NIR, ca. 750 – 3000 nm) regions to probe the optical transitions in a material. Since the energy of this range ( $\sim 0.4$  - 6 eV) predominantly excites electrons from  $\pi$ - or non-bonding orbitals to  $\pi^*$  orbitals, this technique is particularly suitable for studying  $\pi$ -conjugated organic molecules and polymers containing  $\pi$ -bonds.

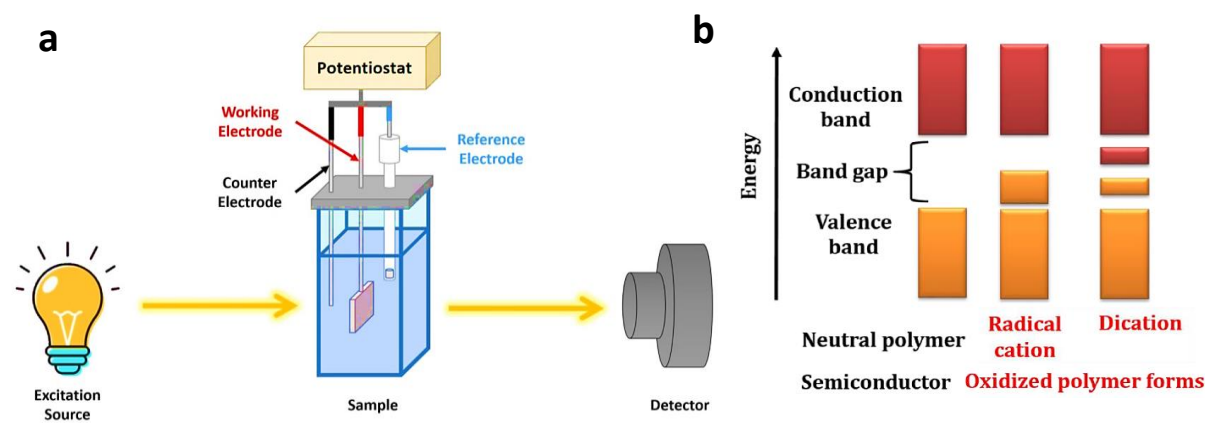


**Figure 2-18.** (a) Schematic diagram of the spectroelectrochemical instrumentation (adapted from<sup>318</sup>) and (b) intermediate energy levels formed within the electronic bandgap region upon polymer oxidation or reduction.

Electron paramagnetic resonance (EPR) spectroscopy detects the presence of unpaired electrons in electroactive polymers formed during charge injection, thus broadening the understanding of electrode processes of the polymer.<sup>319</sup> Each electron has an intrinsic angular momentum (orbital and spin) in addition to its elementary charge. This momentum is associated with the electron spinning around its axis. It can assume two states – parallel or antiparallel to the external magnetic field. In the field absence, these two states energetically degenerate. However, in the field presence, the two states are split into a higher (antiparallel to the magnetic field) and lower (parallel to the magnetic field) energy state. This phenomenon is known as the Zeeman effect. The EPR spectroscopy induces a transition between the two spin states by irradiating the paramagnetic sample with microwaves.<sup>320</sup> The transition energy

$(\Delta E_t)$  between the two spin states, which is also known as the Zeeman splitting energy, is given by Equation 2-21

$$\Delta E = g\mu_B B = h\nu \quad (\text{Equation 2-21})$$

where  $g$  is the Landé factor (or  $g$ -factor),  $\mu_B$  is the Bohr magneton ( $9.274 \times 10^{-24} \text{ J T}^{-1}$ ),  $B$  is the magnetic field intensity applied (that can be measured),  $h$  is the Planck constant ( $6.63 \times 10^{-34} \text{ J}\cdot\text{s}$ ), and  $\nu$  is the resonance frequency of the microwave radiation.

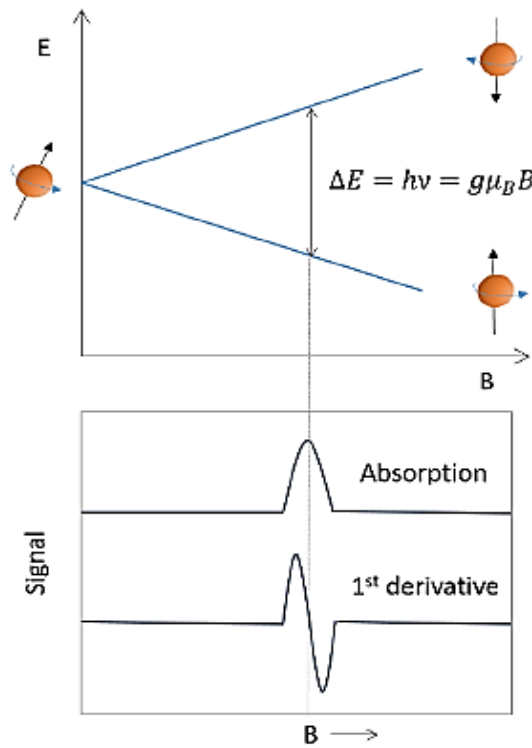


**Figure 2-19.** Schematic illustration of Zeeman splitting of the energy levels of unpaired electrons under an external magnetic field applied. An EPR signal is generated by tuning the incident beam's microwave frequency ( $\nu$ ) and the magnetic field intensity ( $B$ ) to achieve the resonance condition and induce a spin-flip with the absorption of microwaves. Typically, the first derivative of the absorption vs. the magnetic field intensity curve is acquired and reported (adapted from<sup>321</sup>).

The value of  $g$  can then be calculated, as

$$g = \frac{h\nu}{\mu_B B} \quad (\text{Equation 2-22})$$

Since the splitting energy is linearly proportional to the magnetic field intensity, a common way of measuring the EPR spectrum of a sample is by keeping the frequency of the electromagnetic wave constant and scanning the magnetic field intensity. Thus, when the splitting energy at a specific magnetic field matches the irradiation energy, the spin of the unpaired electrons in the sample is flipped, with the accompanying absorption of the photons (Figure 2-19).

The  $g$ -factor of an EPR sample determines the position of the EPR transition in the magnetic field at a given microwave frequency. Equation 2-22 determines  $g$  in an EPR experiment by measuring the field intensity and the resonance frequency. If  $g$  does not equal  $g_e$ , the implication is that the ratio of the unpaired electron's spin magnetic moment to its angular momentum differs from the free-electron value. In solution, due to molecular tumbling,  $g$  is averaged. While for solid-state samples,  $g$  has three components ( $g_x, g_y, g_z$ ) that depend on the molecule's orientation against the magnetic field applied. This anisotropy of the electron Zeeman interaction measures the symmetry of the electronic distribution within the paramagnetic species. Therefore, depending on the symmetry of the electronic distribution,  $g$  can be isotropic ( $g_x = g_y = g_z$ , cubic symmetry), axial ( $g_x = g_y \neq g_z$ , where  $g \perp$  is often used for  $g_x = g_y$  and  $g \parallel$  for  $g_z$ ), or rhombic ( $g_x \neq g_y \neq g_z$ ).

The absorption signal intensity can then quantify the number of unpaired electrons. Moreover, the nature of the species can be investigated because the  $g$ -factor is characteristic of a particular paramagnetic species and its local environment. For example, organic free radicals, with only  $H$ ,  $O$ ,  $C$ , and  $N$  atoms, will have a small contribution from spin-orbit coupling, i.e., with  $g$ -factors very close to the  $g_e$ -factor of free electron (~2.0023) while  $g$  factors of much larger species, e.g., metals, may be significantly different from the  $g_e$ -factor.<sup>322</sup>

Peak-to-peak line-width refers to the horizontal distance between the maximum and the minimum of a first-derivative lineshape of the EPR signal.<sup>323</sup>

#### 2.3.3.1.4.1 In situ EPR-(UV-vis-NIR) spectroelectrochemistry

In the electrode reaction of a neutral organic redox system, the primary cathodic or anodic electron transfer may result in an ion radical. The choice of the spectroscopic technique is the

EPR spectroscopy to detect the resulting paramagnetic structure. However, either a second electron transfer or chemical follow-up reactions of the radicals can result in diamagnetic structures that EPR cannot detect. Therefore, at least one additional in situ spectroscopic technique is required to detect the reaction products and the diamagnetic intermediates. Developing an optical EPR cavity opened the route to a simultaneous application of EPR and UV-vis-NIR spectroscopy in a single in-situ spectroelectrochemical triple technique.<sup>324</sup> That way, both the paramagnetic and diamagnetic structures in electrode reactions can be followed at the same working electrode. Furthermore, this in-situ combination demonstrates it to be a valuable tool for the description of charged states in polymers and oligomers.<sup>325</sup>

#### 2.3.3.1.5 High-performance liquid chromatography (HPLC)

High-performance liquid chromatography (HPLC) is a powerful and versatile chromatographic separation technique used in analytical chemistry to identify, separate, and quantify each mixture component<sup>326,327</sup> (Figure 2-20). It involves the injection of a small volume of a liquid sample into a column filled with porous particles of 3 to 5  $\mu\text{m}$  in diameter called the stationary phase. Individual sample components are moved down the column with a high-pressure mobile phase delivered by a pump. Four major separation modes are most often used for HPLC separations.<sup>326</sup> In a normal phase mode, the column packing is polar (e.g., silica gel, cyanopropyl-bonded, amino-bonded, etc.), but the mobile phase is non-polar (e.g., hexane, isoctane, ethyl acetate, etc.).

However, for our study, reversed-phase HPLC (RP-HPLC) was used. It features non-polar stationary and aqueous-(organic polar solvent) moderately polar mobile phases. One typical stationary phase used is silica surface-modified with  $\text{RMe}_2\text{SiCl}$ , where R is an *n*-alkyl group such as  $\text{C}_{18}\text{H}_{37}$  or  $\text{C}_8\text{H}_{17}$ .<sup>328,329</sup> With these stationary phases, the retention time is longer for less polar eluants, while polar eluants are more readily eluted. Structural properties of the analyte molecule play a vital role in its retention characteristics.<sup>330</sup> Overall, an analyte with a larger hydrophobic surface area (C–H, C–C, and generally non-polar atomic bonds, such as S–S) is retained longer because of non-interacting with an aqueous eluent.

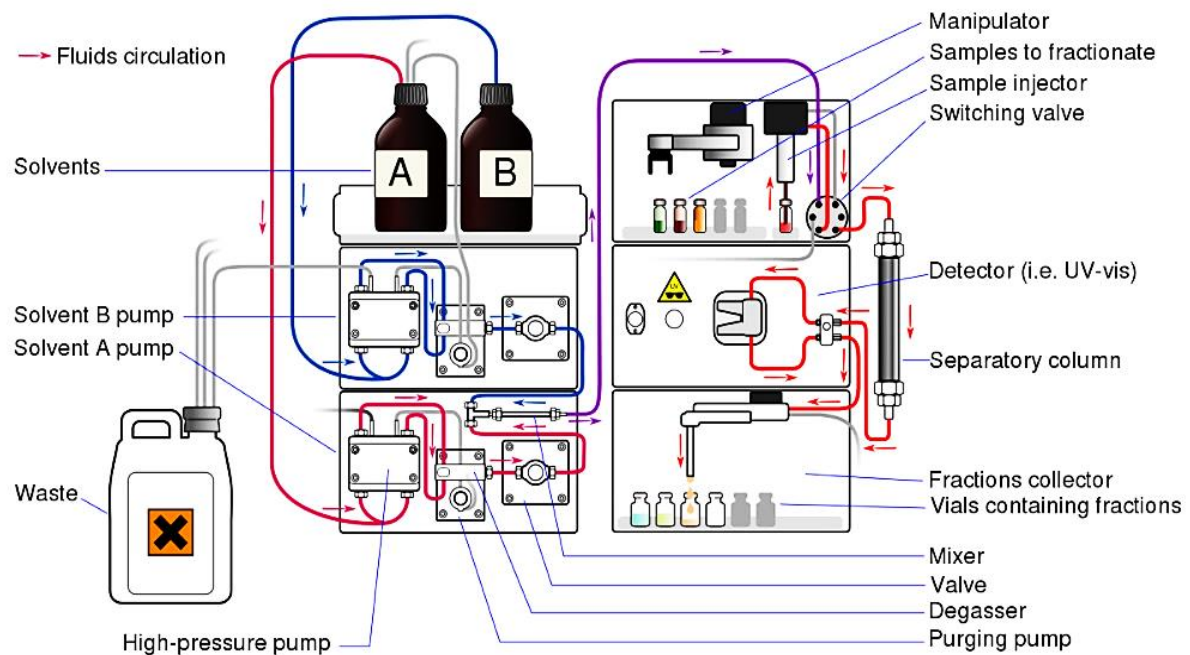


**Figure 2-20.** An HPLC chromatograph flow diagram (adapted from<sup>331</sup>).

### 2.3.3.1.6. Dynamic light scattering (DLS)

Dynamic light scattering (DLS), also known as photon correlation spectroscopy (PCS), is a non-invasive technique to study the diffusion behavior of small particles in dispersion and polymer particles in solution.<sup>332</sup> The diffusion coefficient, and hence the hydrodynamic radii calculated from it, depends on the size and shape of macromolecules. When particles are illuminated with monochromatic and coherent laser light, their scattering intensity fluctuates over time. This fluctuation is caused by the Brownian motion of small particles in the studied suspension. Therefore, the distance between the scatterers in the solution constantly changes with time.

Furthermore, this scattered light then undergoes either constructive or destructive interference by the surrounding particles. Within this intensity fluctuation, information is contained about the time scale of movement of the scatterers. Moreover, DLS measures particle zeta potential (related to the magnitude of the electrical charge at the particle surface) and molecular weight of large polymeric substances dispersed in water.

### 2.3.3.2 Microscopic techniques

#### 2.3.3.2.1 Atomic force microscopy (AFM)

AFM can operate in a contact, semi-contact, or non-contact mode. Herein, topological mapping of the doped and undoped polymer films was accomplished using AFM in a tapping mode (also known as the intermittent mode). Strong repulsive forces (~1 to 10 nN) dominate in this mode. Figure 2-21 shows the basic AFM setup scheme. That consists of a flexible oscillating cantilever with a microscopic tip at one end, scanning the sample's surface and recording the height profile at a nanometer scale. The interactive forces (e.g., van der Waals forces) between the tip and the sample lead to deflections of the tip in case of the contact mode, the tip is in contact with the sample while scanning the sample surface, which is detected by the change in the position of the laser beam on the photodetector. A feedback loop between the photodetector and the cantilever notes the deflection and extension of the cantilever and, accordingly, shifts it up or down such that the initially applied force is maintained, thus mapping the topography of the sample.

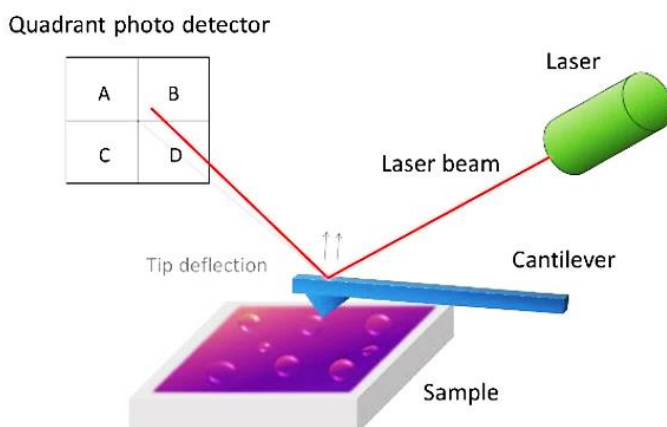


**Figure 2-21.** Illustration of main components and the working principle of atomic force microscopy (AFM).

Similarly, in the semi-contact mode, the cantilever oscillates, and the change in either amplitude, frequency, or phase of the cantilever oscillation can be used as the feedback signal to record the sample topography and control the tip movement. Herein, the oscillating AFM tip is brought close to the sample surface, typically a few to tens of nanometer. At this tip-

sample distance, the main tip-sample interaction forces monitored are weak attractive forces, e.g., van der Waals forces. The semi-contact mode is useful for studying loosely bound molecules. AFM was here used to determine the MIP and NIP film topography and morphology. Non-contact mode is used primarily in studying long-range interactions between the cantilever tip and sample, such as electrostatic or magnetic.

### 2.3.3.2.2 Scanning electron microscopy (SEM)

Scanning electron microscopy (SEM) can deliver high-resolution images of a modified electrode surface in a high vacuum (at least  $10^{-4}$  Pa). A scanning electron beam with energy typically ranging from 0.2 to 40 keV is focused on a spot of the sample with a diameter of a few nm. Electrons penetrate the sample and interact with the atoms to a depth of several micrometers. As measured signals, an SEM microscope produces secondary electrons, reflected or backscattered electrons and photons of various energies, characteristic X-rays, absorbed current, and transmitted electrons. In the SEM, the most significant signals are those of the secondary and backscattered electrons because these vary according to differences in surface topography as the electron beam sweeps across the specimen. Secondary electrons originating from a layer located in a sample, a few nanometers from the surface, are detected, and a two-dimensional image with a lateral resolution of down to 1 nm can be reached (Figure 2-22). This SEM signal is presented as a variation in brightness on the black-and-white display. The ratio of the size of the displayed image to the size of the area scanned on the sample defines the magnification. This magnification can be controlled over a range of ~6 orders of magnitude, namely, from 10 to 3 000 000 times.

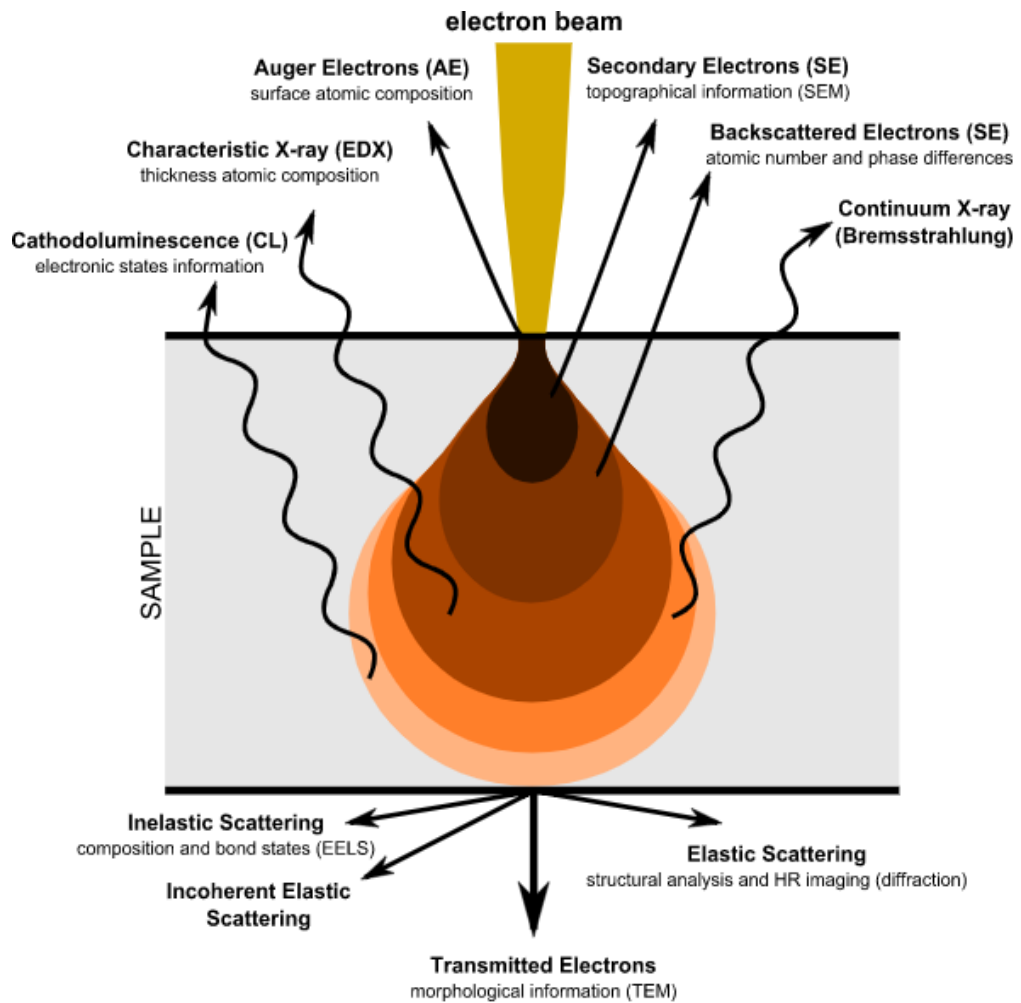


**Figure 2-22.** Illustration of particles generated from electron-matter interaction and their respective information useful for electron microscopes (adapted from<sup>68</sup>).

# Results and discussion

## Chapter 3

### An insight into the polymerization mechanism of selected carbazole derivatives - Why does it not always lead to polymer formation?

The present chapter discusses the research work partially described in a submitted for publication manuscript, authored by *Jyoti, Evgenia Dmitrieva, Teresa Żolek, Dorota Maciejewska, Krzysztof R. Noworyta, and Włodzimierz Kutner*.

#### Abstract

Among numerous carbazole monomers synthesized within this thesis, some show intriguing differences in electrochemical polymerization behavior. Two such carbazole derivatives, namely, 9-(4-naphthalen-2-yl)-9H-carbazole (CNZ1) and 3,6-bis(thiophen-2-yl)-9-(4-naphthalen-2-yl)-9H-carbazole (FM3), were herein studied to a more detail. The main focus of the research was to elucidate the electropolymerization mechanism of both compounds. The monomers were electro-oxidized to form polymer films on electrodes. When CNZ1 and FM3 were electro-oxidized, the overall charge passed amounted 115 and 1500  $\mu$ C, respectively, suggesting the formation of a very thin pCNZ1 film and, in contrast, a thick pFM3 film. The polymers showed reversible electrode behavior. They were characterized by UV-vis-NIR spectroelectrochemistry and electron paramagnetic resonance (EPR) spectroscopy. The UV-vis-NIR absorption intensity for the pCNZ1 film was 10 times lower than for its monomer; however, for pFM3 absorption spectra, no such trend was seen. Furthermore, the EPR signal for CNZ1 was over-modulated to receive a reliable response. The number of radicals formed in pCNZ1 was ~30 times lower than in pFM3. Scanning electron microscopy (SEM) imaging revealed a continuous and spherical structure of pCNZ1 and pFM3 films, respectively. The pFM3 film was porous, beneficially for ion diffusion. UV-vis-NIR and EPR spectroelectrochemistry coupled with quantum-chemical calculations enabled us to explain the differences in the observed behavior. For CNZ1, the radical is delocalized over the whole molecule. That leads to a lower chance of the

radical cation coupling, thus preventing the formation of longer polymeric chains. In contrast, the radical delocalization is much more restricted to the carbazole-thiophene moiety for FM3. Consequently, this leads to the formation of longer polymeric chains.

### 3.1 Introduction

Carbazoles polymerize upon electro-oxidation to form corresponding polycarbazoles with an oxidation potential lower than their parent monomers. Moreover, the oxidation potentials of some non-derivatized carbazole monomers are relatively high, hindering the electropolymerization of these monomers.<sup>333,334</sup> Furthermore, the high potential application causes polymer degradation (overoxidation), slowing the electropolymerization.<sup>335</sup> To overcome this problem, the monomer conjugation is extended to lower the oxidation potential significantly. That is performed by introducing other aromatic moieties in the 3 and 6 positions of the carbazole moiety. A variety of modifications has been studied in this regard.<sup>336–338</sup> Noteworthy, some published research reports state that electro-oxidation of *N*-substituted carbazoles leads to reactive radicals, which form only dimers<sup>181,339</sup> or oligomers.<sup>340,341</sup> However, the substituent influence on the electrode process and radical stability has not been extensively studied yet.

Herein, carbazoles derivatized with the naphthalene moiety at the nitrogen atom, with and without thiophene substituents at 3 and 6 carbon atoms were synthesized, and their electrochemical properties studied. It transpired that the 9-(4-naphthalen-2-yl)-9*H*-carbazole, CNZ1, monomer (Scheme 3-1) did not form stable polymer films upon electro-oxidation while still being electrochemically active. On the other hand, the 3,6-bis(thiophen-2-yl)-9-(4-naphthalen-2-yl)-9*H*-carbazole FM3 monomer containing thiophene moieties (Scheme 3-1) formed readily a conductive polymer upon electro-oxidation. We aimed to understand this behavior difference and origins of the stability of the radical cation formed during the doping and de-doping of CNZ1 and FM3 during electro-oxidation using *in-situ* EPR/UV-vis-NIR spectroelectrochemistry assisted by quantum-chemical calculations.

### 3.2 Experimental procedures

Potentiodynamic measurements were performed at room temperature, 20 ( $\pm 1$ ) °C, using the electrochemical mini cell filled with the 1 mM monomer and 0.1 M (TBA)PF<sub>6</sub> anhydrous acetonitrile solution at a potential scan rate of 50 mV s<sup>-1</sup>. The UV-vis-NIR/EPR experiments were performed using the ITO electrode and the above conditions at a 3.0 or 3.5 mV s<sup>-1</sup> scan rate.

### **3.2.1 3,6-Bis(thiophen-2-yl)-9-(4-naphthalen-2-yl)-9H-carbazole, FM3, monomer synthesizing**

A new electroactive monomer, abbreviated FM3, was synthesized through a multi-step process. First, 9-(naphthalen-2-yl)-9H-carbazole was prepared via Ullmann coupling, widely exploited in literature.<sup>173</sup> Chapter 2 describes the synthesis' details; however, spectral characterization, including normalized UV-vis and fluorescence spectroscopy, are provided herein.

### **3.2.2 Quantum-chemistry calculations**

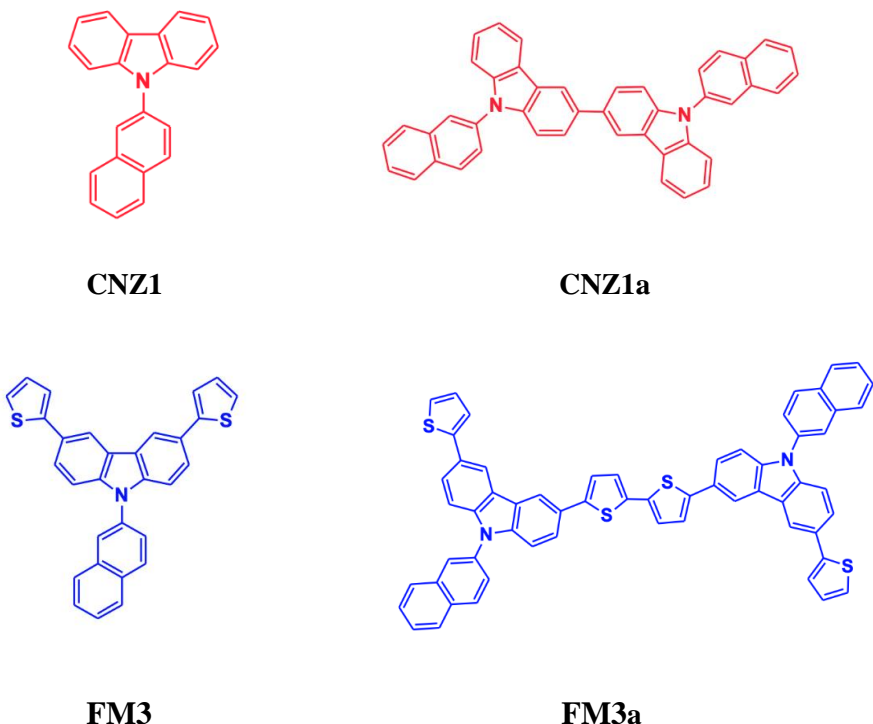
The initial geometry of all compounds was generated using the GaussView 6.0<sup>342</sup> visualization program, while quantum-chemistry calculations were performed using the Gaussian 16W software package. The physicochemical properties of the CNZ1 and FM3 monomers and their CNZ1a FM3a dimers (Scheme 3.1), as well as their radical cations and the dication, were defined using the density functional theory method (DFT) and Becke-Lee-Yang-Parr's three-parameter hybrid functional (B3LYP)<sup>343,344</sup> with the Pople's triple zeta basis set 6-311G(d,p). The solvent effect was considered using the Polarizable Continuum Model (PCM), implemented in Gaussian, which defines the cavities as envelopes of spheres on atoms or atomic groups. Acetonitrile was the porogenic solvent used in all calculations considering the experimental conditions. Vibrational frequency calculations ensured that the obtained structures represented the local minima. All calculations were performed using standard gradient techniques and default convergence criteria. For the optimized geometries, the neutral, radical cation, and dication species, the HOMO and LUMO energy, HOMO-LUMO energy gaps, and total electronic energy values were extracted and analyzed.

Moreover, the following molecular parameters were computed and interpreted to clarify the polymeric potency of the selected CNZ1 and FM3 carbazole derivatives. The unpaired electron spin density distribution for the radical cations and the UV-vis spectra parameters (electronic transitions, vertical excitation energies, absorbance, and oscillator strengths) were calculated using the time-dependent DFT (TD-DFT) methods.<sup>345</sup>

### 3.3 Result and discussion

#### 3.3.1 Experimental spectral characterization of the monomers

As it follows from Figure 3-1, the normalized absorption and emission spectral maxima for CNZ1 in acetonitrile are at  $\lambda_{\text{abs, max}} = 328 \text{ nm}$  and  $342 \text{ nm}$ , and  $\lambda_{\text{em, max}} = 379 \text{ nm}$ , respectively. In contrast, they are at  $\lambda_{\text{abs, max}} = 314 \text{ nm}$ , and  $\lambda_{\text{em, max}} = 387 \text{ nm}$ , and  $408 \text{ nm}$ , respectively, for FM3. Notably, the normalized maximum absorption for CNZ1 is red-shifted compared to FM3, despite the latter's more extended conjugation system.



**Scheme 3-1.** Structural formulas of CNZ1 and FM3 monomers and their CNZ1a and FM3a dimers, respectively.

#### 3.3.2 Simulated absorption spectra and electronic properties

To better understand the nature of the observed spectral changes, the UV-vis-NIR spectra of various forms of monomers and dimers (CNZ1,  $\text{CNZ1}^{+1\bullet}$ ,  $\text{CNZ1}^{+2}$ , and FM3,  $\text{FM3}^{+1\bullet}$ ,  $\text{FM3}^{+2}$ ) in acetonitrile were recorded. The calculated electronic absorptions correspond to transitions from the ground to the first excited state. One-electron excitation from HOMO to LUMO frontier molecular orbitals is mainly described. The theoretically predicted UV-visible-NIR

absorption spectra are visualized in Figures 3-2 and 3-3. The calculated values of the wavelength ( $\lambda$ ), excitation energy, oscillator strength ( $f_o$ ), and electronic transitions are shown in Tables A1 and A2 in Appendix.

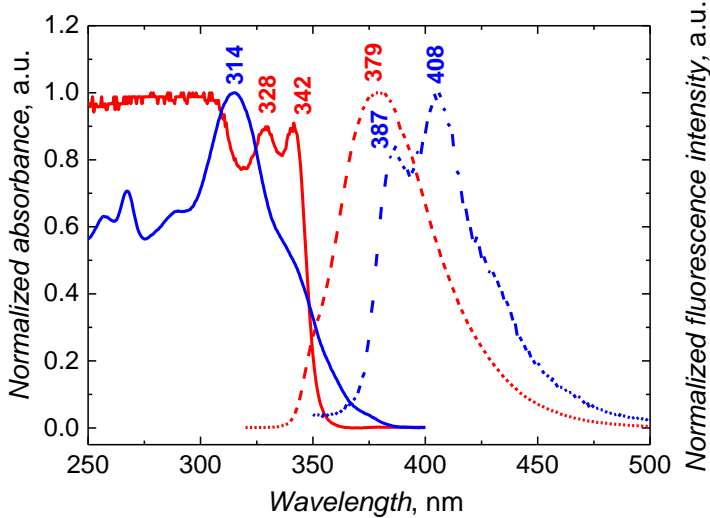


**Figure 3-1.** Normalized absorption and emission spectra of 0.5 mM CNZ1 (red) and FM3 (blue) in acetonitrile.

At 328 and 342 nm, two bands are in the experimental CNZ1 normalized absorption spectrum (Figure 3-1, red spectrum). However, only one band at 314 nm is in the FM3 spectrum (Figure 3-1, blue spectrum). The corresponding calculated absorption bands appear at  $\lambda = 327.2$  nm,  $f_o = 0.049$  and  $\lambda = 354.2$  nm,  $f_o = 0.125$  for CNZ1 (Figure 3-2), and at  $\lambda = 315.2$  nm,  $f_o = 0.060$  for FM3 (Figure 3-2). The HOMO  $\rightarrow$  LUMO+1 (95.6%) electronic excitation contributes to the transition occurring at  $\lambda = 327.2$  nm, while the HOMO  $\rightarrow$  LUMO (95%) excitation corresponds to the band at 354.2 nm, and the HOMO-1  $\rightarrow$  LUMO (88%) excitation corresponds to the band at 315.2 nm (Table A1 in Appendix). Apparently, the experimental and calculational results agree well.

The TD-DFT calculations for the experimental spectra of CNZ1 and FM3 monomers in a neutral state (Figure 3-2 and Table A1) confirm the experimental blue shift of the CNZ1 normalized absorption band compared to FM3. The calculations indicate that the dominant transition for CNZ1 is the direct HOMO-LUMO transition, with LUMO being located on the naphthalene moiety and HOMO on the carbazole unit. On the other hand, the dominant electronic transition for FM3 is the HOMO-LUMO+2 transition, with the HOMO spread quite

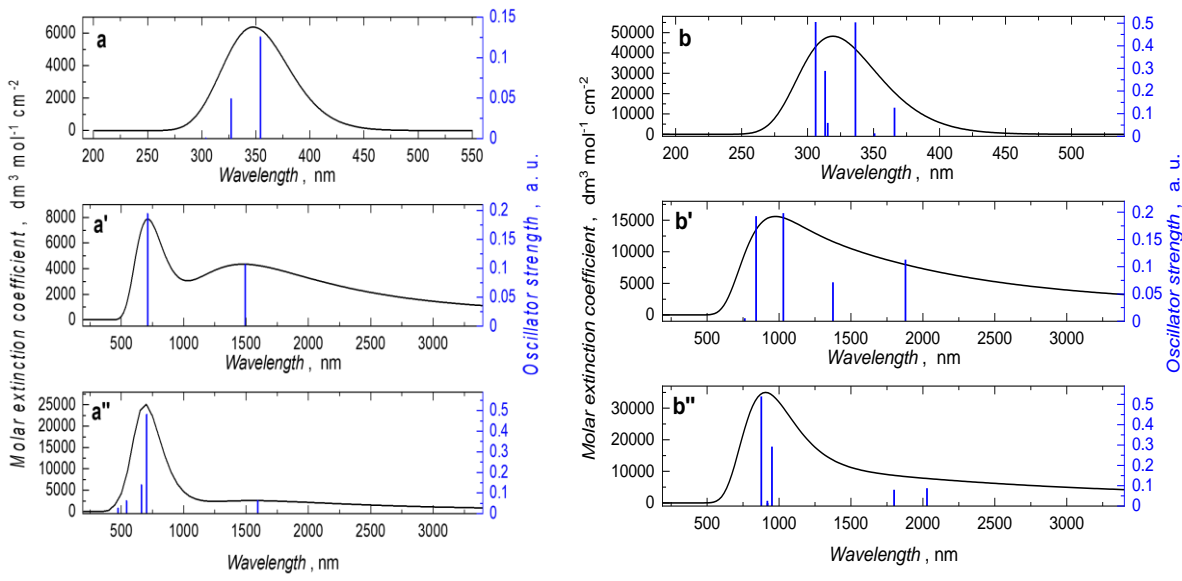


**Figure 3-2.** The TD-DFT 6-311G(d,p) simulated UV-vis spectra of the monomer of (a), (a'), and (a'') CNZ1 as well as (b), (b'), and (b'') FM3 in the form of (a) and (b) neutral molecule, (a') and (b') radical cation, and (a'') and (b'') dication. All spectra were calculated using acetonitrile as the solvent.

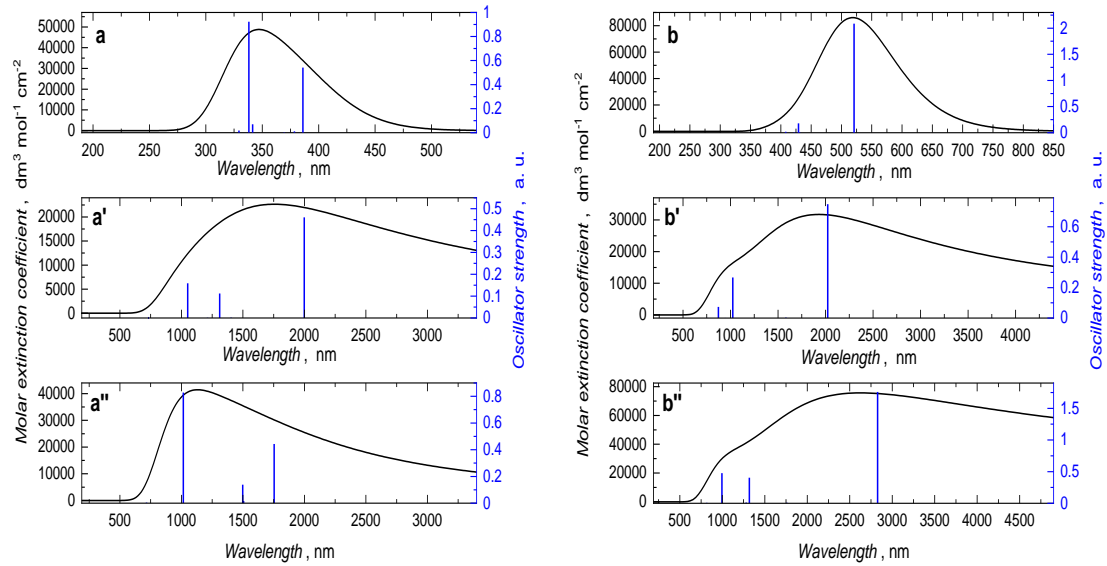


**Figure 3-3.** The TD-DFT 6-311G(d,p) simulated UV-vis spectra of the dimer of (a), (a'), and (a'') CNZ1a as well as (b), (b'), and (b'') FM3a in the form of (a) and (b) neutral molecule, (a') and (b') radical cation and (a'') and (b'') dication. All spectra were calculated using acetonitrile as the solvent.

uniformly over the whole carbazole-thiophene moiety and LUMO+2 more concentrated on the thiophene units. Therefore, the extension of the conjugated system length less influences this transition.

### 3.3.3 Electrochemical characterizing monomers and their polymers

Following the synthesis and chemical characterization, cyclic voltammograms of the carbazole-based monomers, CNZ1 and FM3, were recorded to reveal electrochemical features of both the monomers and their formed polymers. Electropolymerization was carried out for 1 mM monomer in 0.1 M (TBA)PF<sub>6</sub> anhydrous acetonitrile solution under potentiodynamic conditions at a potential scan rate of 50 mV s<sup>-1</sup>.

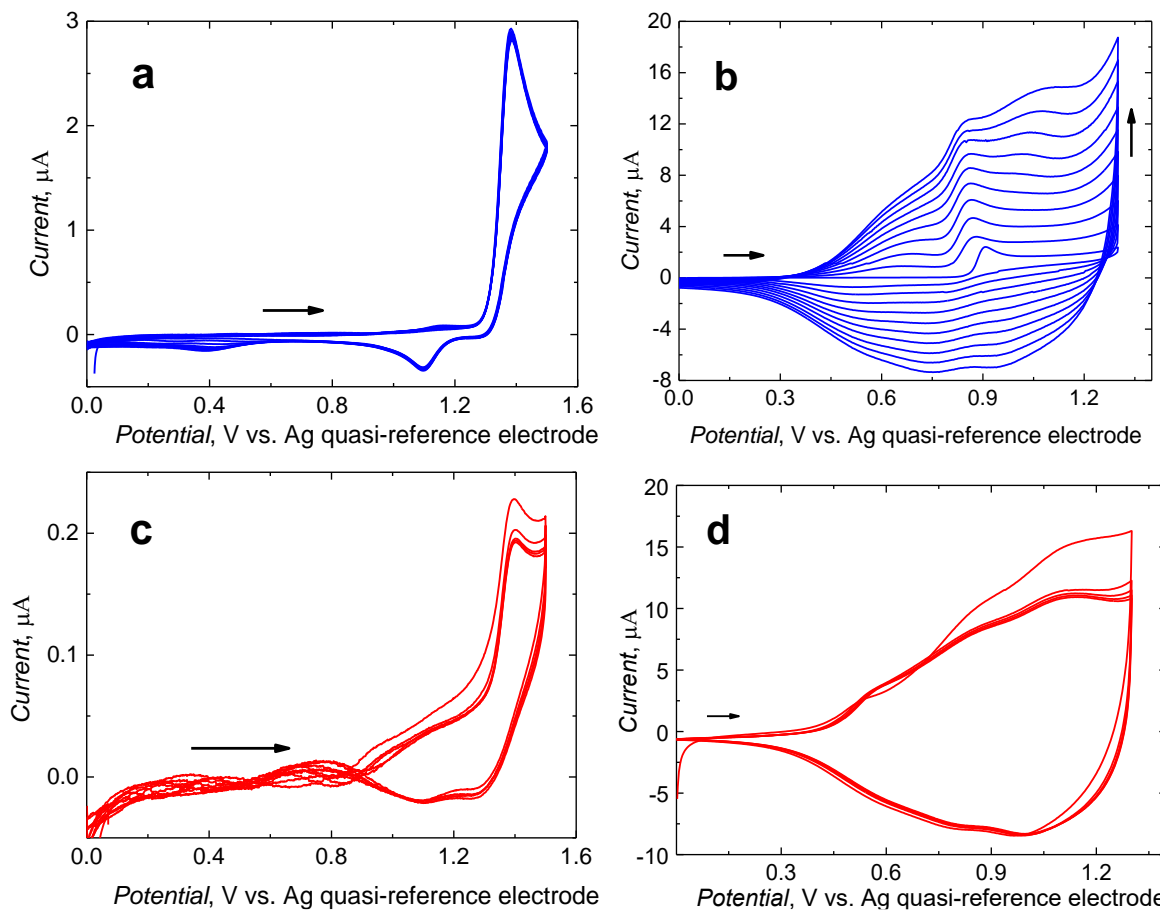


**Figure 3-4.** Multi-cyclic potentiodynamic curves for electropolymerization of (a) 1.0 mM CNZ1 and (b) 1.0 mM FM3, and CV doping and dedoping polymers of (c) CNZ1 and (d) FM3, recorded at the Pt disk electrode in 0.1 M (TBA)PF<sub>6</sub>, in acetonitrile at a 50 mV s<sup>-1</sup> scan rate.

The monomers were used without any additional purification. First, we deposited polymer films on Pt disk electrodes by applying ten potentiodynamic cycles (Figures 3-4a and 3-4b). Both CNZ1 and FM3 showed irreversible anodic peaks at 1.37 and 0.87 V vs. Ag quasi-reference electrode, respectively, during the first anodic scan. In the second cycle, one broad cathodic and one broad anodic peak emerged at potentials between 0.32 and 0.80 V and between 0.45 and 0.80 V, respectively, for FM3. However, for CNZ1, only a small anodic peak grew with the cycle number at 1.15 V vs. Ag quasi-reference electrode. With each consecutive cycle, the FM3 peaks increased, confirming the deposition of a conducting film. In contrast, the CNZ1 peaks raised only marginally.

The calculated HOMOs values (Figure 3-5), related to the first oxidation potentials of the compounds,<sup>346</sup> are -5.64 and -5.23 eV for CNZ1 and FM3, respectively. These values can be recalculated against the ferrocene/ferrocenium (Fc/Fc<sup>+</sup>) redox couple scale by Equation 3-1.<sup>346</sup>

$$E_{\text{HOMO}} [\text{eV}] = -e (E_{\text{ox}} [\text{V}] + 4.71 \text{ V}) \quad (\text{Equation 3-1})$$

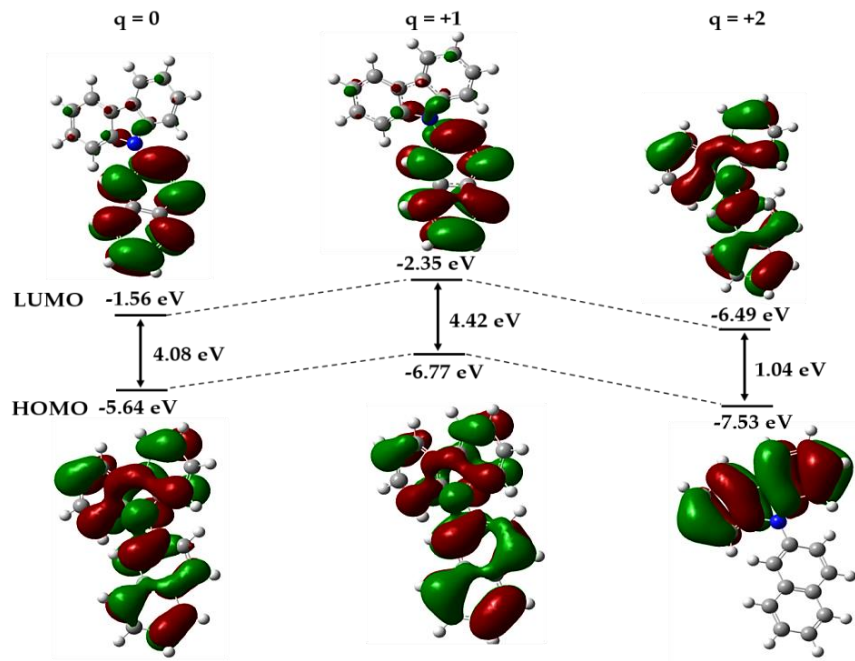
Similarly, the LUMO energy can be related to the first reduction potential by Equation 3-2.

$$E_{\text{LUMO}} [\text{eV}] = -e (E_{\text{red}} [\text{V}] + 4.71 \text{ V}) \quad (\text{Equation 3-2})$$

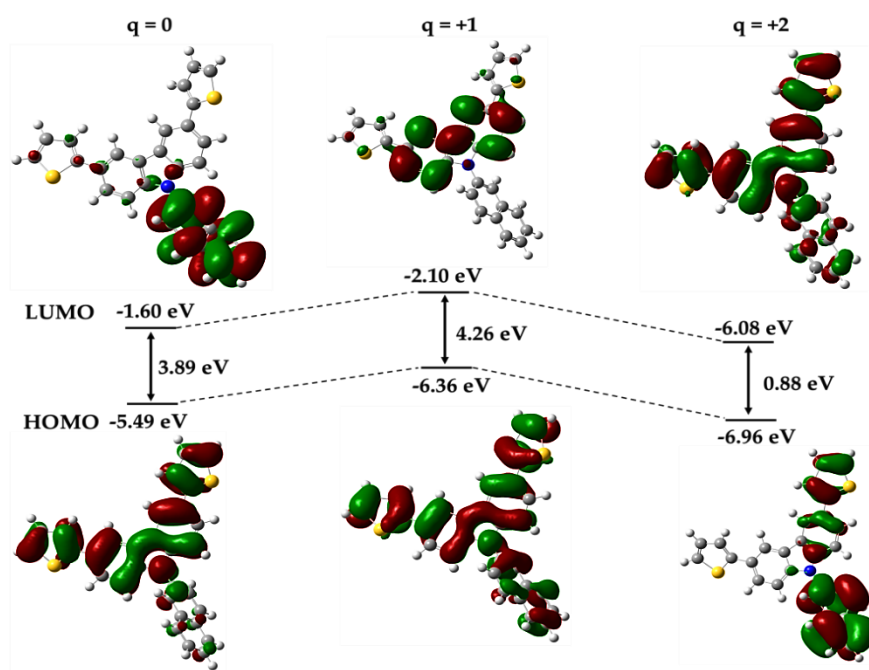
Herein, the Fc/Fc<sup>+</sup> formal redox potential was 0.28 V vs. Ag quasi-reference electrode. Therefore, the calculated oxidation potentials of the CNZ1 and FM3 are 1.21 and 0.80 V vs. Ag quasi-reference electrode, respectively. With the HOMO energy for the irreversible oxidation coinciding with the current onset potential, the calculated values are in good agreement with the experimental values of 1.27 and 0.85 V vs. Ag quasi-reference electrode for CNZ1 and FM3, respectively. For the CNZ1 and FM3 monomer, the LUMO energy was calculated as -1.56 eV and -1.60 eV, corresponding to relatively negative reduction potentials of -2.87 and -2.83 V vs. Ag quasi-reference electrode, respectively. Therefore, the first oxidation potential for the FM3 is by ~0.4 V lower than that of CNZ1. That is in agreement with the experimental values. Noteworthy, the HOMOs for both monomers are highly delocalized and spread over the whole molecule, while LUMOs are localized on the naphthalene moiety (Figure 3-5a and 5b). Hence, the reduction will predominantly involve the

naphthalene moiety while oxidation the carbazole or thietyl-carbazole and naphthalene fragments.

**a**



**b**



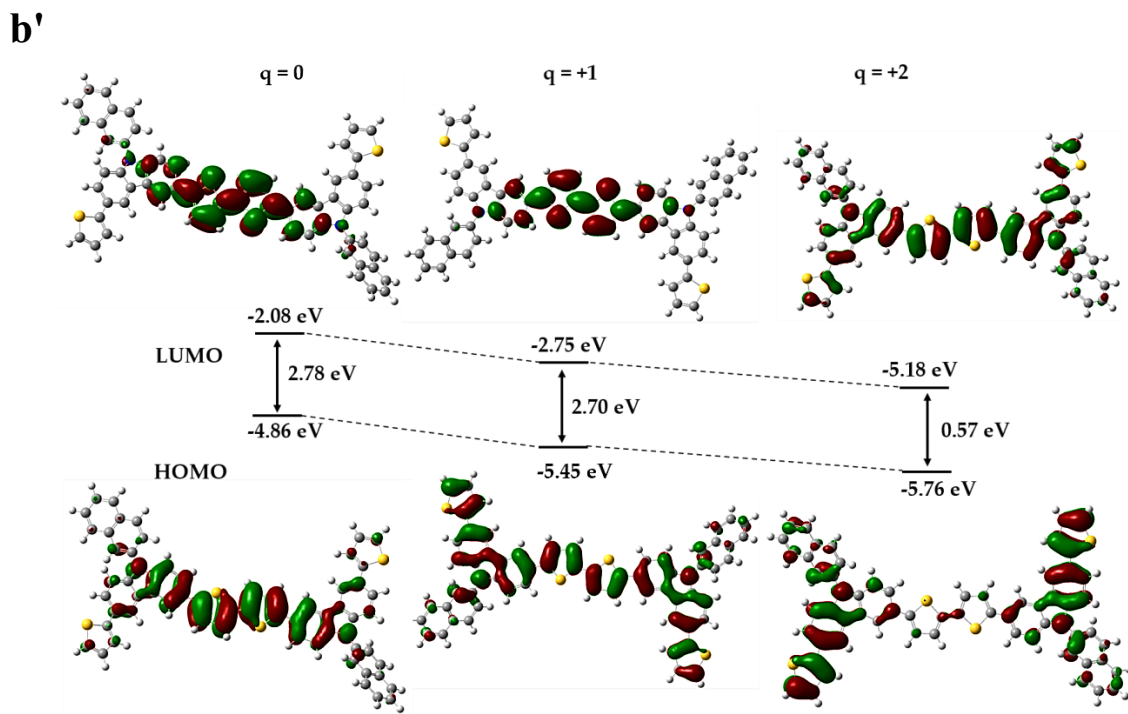
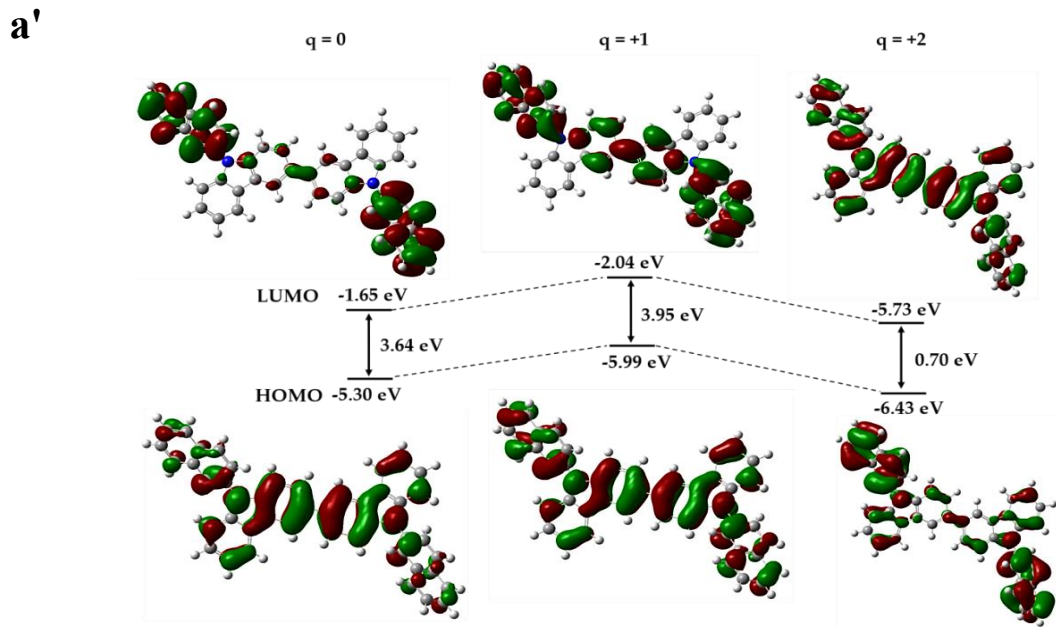


**Figure 3-5.** Frontier molecular orbitals and energy gaps of monomers and dimers, in acetonitrile, of (a) CNZ1, (b) FM3, (a') CNZ1a, and (b') FM3a. (The positive and negative phases are red and green, respectively).

In a monomer-free solution, pFM3 shows broad anodic and cathodic peaks, each composed of three ill-developed overlapping peaks (Figure 3-4d), characteristic of doping and de-doping highly conductive polymers. Three anodic peaks were at 0.57, 0.86, and 1.15 V, and three cathodic peaks at ~0.50, ~0.80, and ~1.00 V. For pCNZ1 (Figure 3-4c), two anodic at ~1.10 and ~1.30 V and two cathodic, one weak at 1.13 and the other well-pronounced at ~1.40 V were present.

Apparently, during CNZ1 monomer oxidation, only a tiny amount of the polymer is formed while significant amounts of dimers and or small oligomers are formed at the electrode vicinity. In contrast, mainly a polymer is formed during FM3a electro-oxidation. The overall charge passed during CNZ1 and FM3 electro-oxidation, being 115 and 1500  $\mu$ C, respectively, supports this inference.

The calculations of the HOMO and LUMO energy levels for the CNZ1a and FM3a dimers (Figure 3-5a' and 5b') confirmed the expected trend of making both energy levels more positive than those of the monomers. In CNZ1a, the HOMO and LUMO energy levels are -5.30 and -1.65 eV, respectively, while for FM3a, the HOMO energy is increased to -4.86 eV, with LUMO energy raised to -2.08 eV. These energy changes translate to less positive oxidation and more positive reduction potentials. Notably, the calculated first oxidation potential of the FM3a dimer is much less positive than that of the CNZ1a dimer. That is understandable given more extensive conjugation in the thiophene-appended carbazole monomer. These calculation results agree with electrochemical studies of the deposited polymers in a monomer-free solution (Figures 3-4c and 3-4d). The onset of the oxidation potential for pFM3 (Figure 3-4d) is ~0.30 V vs. Ag quasi-reference electrode, while for pCNZ1, it can be estimated as ~0.90 V vs. Ag quasi-reference electrode. Interestingly, the experimental oxidation onset potential of pCNZ1 is quite close to the theoretically calculated value for the first oxidation of the CNZ1a dimer (0.87 V vs. Ag quasi-reference electrode). On the other hand, the oxidation onset potential of 0.32 V vs. Ag quasi-reference electrode for pFM3 is by ~100 mV lower than the theoretically calculated potential for FM3a dimer (0.43 V vs. Ag quasi-reference electrode). Most likely, CNZ1 oligomers are relatively short compared to relatively longer polymer chains of FM3.

We performed EPR/UV-vis-NIR spectroelectrochemical experiments, accompanied by extensive quantum-chemistry calculations, for better understanding differences in electropolymerization mechanisms of both monomers.

### 3.3.4 Scanning electron microscopy (SEM) imaging of pCNZ1 and pFM3 films

Scanning electron microscopy imaging revealed morphological features of the pCNZ1 and pFM3 films. The SEM images were taken at two different magnifications, i.e.,  $(2.5 \times 2.5) \mu\text{m}^2$  and  $(10 \times 10) \mu\text{m}^2$  (Figure 3-6). The film is relatively smooth with the undefined pattern for pCNZ1 (Figure 3-6a and 6b). However, the pFM3 film exhibits a globular structure. The higher magnification image indicates increased film porosity, effective for ion diffusion in and out of the film during electrode processes in pFM3

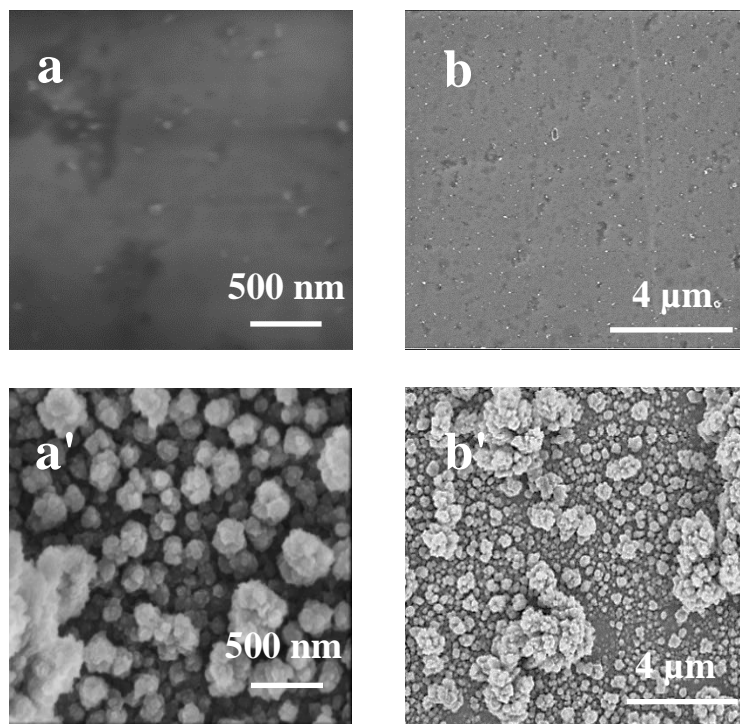


**Figure 3-6.** The (a,a') high- and (b,b') low-magnification SEM images of the (a,b) pCNZ1 and (a',b') pFM3 film on the ITO electrode.

### 3.3.5 UV-vis-NIR spectroelectrochemical examining monomers and polymer films

The UV-vis-NIR spectroelectrochemical technique helps analyze the products of electrochemical reactions. Herein, thin polymer films were potentiodynamically deposited on ITO-layered glass slides under conditions similar to those in Figure 3-4.

Figure 3-7 shows changes in the UV-vis-NIR spectra recorded in the course of potentiodynamic experiments. During initial electro-oxidation of CNZ1, a new well-defined absorption band at 415 nm and a broad band in the 900 to 1200 nm region appear around the monomer oxidation onset (Figure 3-7a). The rather sharp band at 415 nm can be assigned to  $\pi-\pi^*$  transition. CNZ1a dimer calculations confirm that findings as they show that this band is linked to HOMO-LUMO transition (Figure 3-3a and Table A2), which in this case are  $\pi$  and  $\pi^*$  orbitals, respectively. Both transitions would occur in neutral oligomeric species. These bands can be assigned to forming radical cations (polarons). Further potential increase increases intensities of both the band at 415 nm and that between 900 and 1200 nm. Especially, bands centered at  $\sim$ 947 and  $\sim$ 715 nm emerges at the potential of  $\sim$ 1.25 V. In accordance with calculations (Figure 3-3a") this band can be assigned to dications formed during further oxidation of oligomers. Subsequently, the band at 715 nm, at the oxidation potential of the monomer, dominates the spectrum. After electro-reduction, the spectra resemble those of the neutral compounds. That is, no new bands are generated, indicating the electrochemical process reversibility and lack of the following chemical reactions.

The TD-DFT calculated UV-vis-NIR spectra of neutral and positively charged CNZ1 molecules (Figure 3-2a, 2a', 2a" and Table A1) show transitions at 710 and 1494 nm if the radical cation,  $\text{CNZ1}^{+1\bullet}$ , is formed (Figure 3-2a'). That leads to a spectrum with one band at 730 nm and a broad asymmetric band centered at  $\sim$ 1500 nm. Interestingly, the dication formation leads to the appearance of essential transitions at 660 and 704 nm and the suppression of the transition in far NIR (Figure 3-2a"). The spectral shape shows an almost intact band at 730 nm and a suppressed NIR tail. That implies that the experimental band at 715 nm and a broad band between 900 and 1200 nm are associated with radical cations formation during monomer electro-oxidation. However, the band at 415 nm is not considered in the computations, nor is the growth of the narrower band at 947 nm seen in the spectra estimated.

If the formation of the (6-6')-coupled CNZ1a dimer is considered, then spectra of this dimer in the neutral and charged state can be such as those presented in Figures 3-3a, 3a', and 3a'' and Table A2 in Appendix. The neutral dimer exhibits two dominant transitions at 338 and 386 nm, red-shifted compared to the monomer. The CNZ1<sup>+1•</sup> formation leads to relatively strong transitions at 1051 and 1311 nm, while the dication formation - to the transitions at 1016 and 1498 nm. Moreover, both charged CNZ1a forms exhibit dominant transitions in the farther NIR region, i.e., at ~2000 nm.

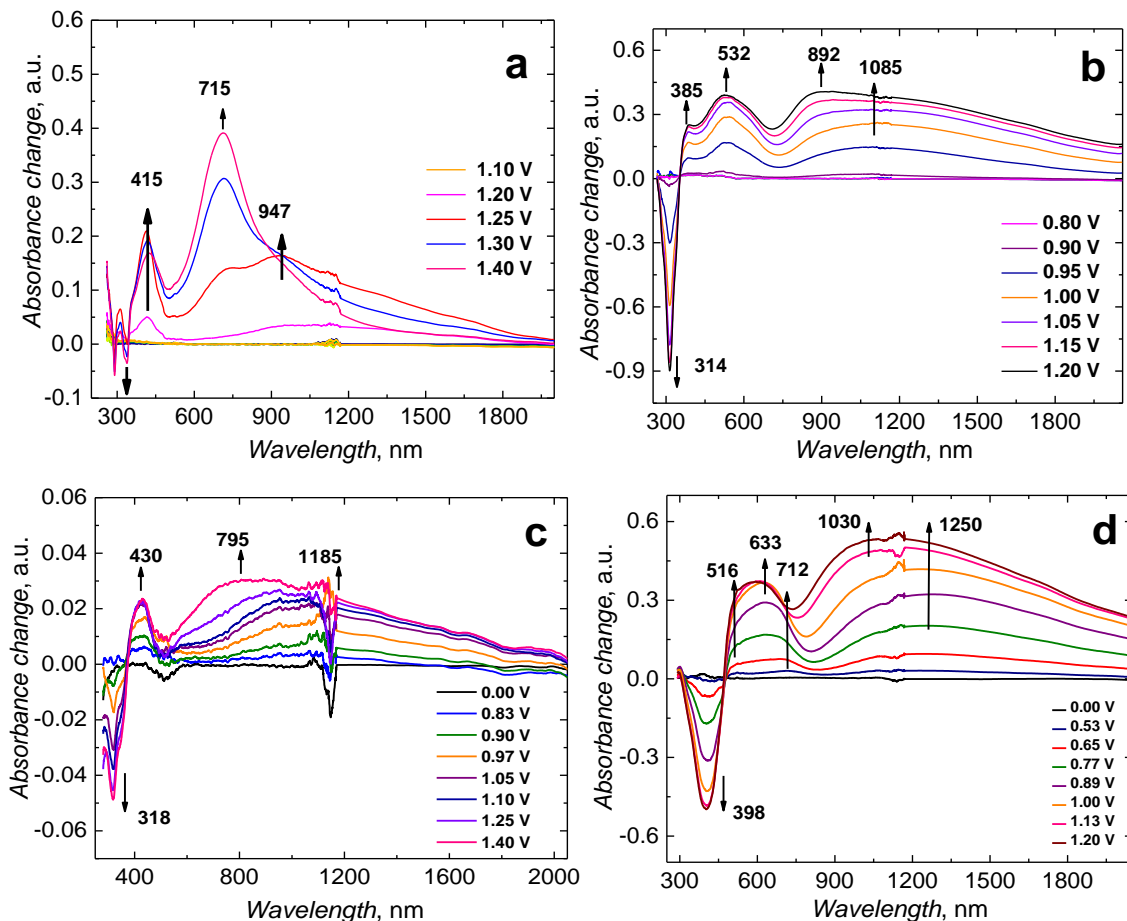


**Figure 3-7.** The UV-vis-NIR spectra evolving during the first scan of electro-oxidation of (a) CNZ1, (b) FM3, (c) pCNZ1, and (d) pFM3, recorded at the ITO electrode vs. Ag/AgCl in 0.1 M (TBA)PF<sub>6</sub>, in acetonitrile, at a 3-mV s<sup>-1</sup> scan rate. Each monomer concentration was 1 mM.

In the oxidized FM3 spectra (Figure 3-7b), the absorption band at 314 nm disappears, and new broad radical cation bands at 385, 512, and 1085 nm are formed. The band at 892 nm is

the most pronounced at a high oxidation potential. All bands intensity increases with the potentiodynamic cycle number (Figure 3-7b). The appearance of broad bands upon oxidation proves polymer film formation on the electrode surface, then the polymer film doping with the formation of radical cation and then dication. The band at 395 nm appears in the spectra of the first-cycle return potential scan. Its intensity further increases with the cycle number. That indicates that the band originates from electronic transition occurring in the neutral conjugated polymer chain.

The TD-DFT calculated UV-vis-NIR spectra of the neutral and charged FM3 monomers (Figure 3-2b, 2b', and 2b" and Table A1 in Appendix) show critical transitions at 306, 313, 336, and 366 nm. Upon oxidation, transitions at 841 and 1030 nm and at 877 and 951 for cation radical and dication, respectively, appear. The FM3 radical cation exhibits transition in far NIR, i.e., at 1878 nm. In this range, the dication shows much weaker transitions at 1800 and 2028 nm.

On the other hand, the calculated spectra of the FM3a dimer (Figure 3-3b, 3b', and 3b" and Table A2 in Appendix) show a transition at 431 nm and a dominant one at 521 nm for the neutral dimer. Dimer oxidation generates transitions at 873 and 1024 nm for the radical cation and 995 and 1317 nm for the dication. Moreover, for both charged forms of the FM3a dimer, intense signals in the far NIR region of 2000 to 3000 nm appear and are the strongest.

Furthermore, pCNZ1 and pFM3 polymers deposited on ITO electrodes were investigated in a monomer-free electrolyte solution (Figures 3-4c and 3-4d, respectively).

During neutral pCNZ1 oxidation, the intensity of the neutral polymer band at 318 nm decreased, and a radical cation new band at 430 nm and in the range of 600 to 2000 nm appeared. However, the absorption signal was weak. These radical cations were further oxidized to dications at higher potentials generating the transition at 795 nm.

During neutral pFM3 oxidation, bands at 516, 712, and 1250 nm emerged while the one at 398 nm decreased. Upon further potential increase, bands at 633 and 1250 nm, ascribed to the radical cation, dominated the spectrum. After reaching 1.00 V, the bands at 560 and 1030 nm became important. Presumably, the radical cations were further oxidized, generating dications responsible for these new bands' emergence. This inference is supported by the FM3a dimer radical cation and dication calculated spectra (Figures 3-3b' and 3-3b", and Table A2 in

Appendix), where the dication formation leads to stronger electronic transition at ~995 nm at the expense of the transition at 1024 nm for the radical cation.

Changes of the absorbance at the wavelength corresponding to characteristic bands observed during CV measurements on the CNZ1 and FM3 monomer solutions (Figure 3-8) offer insight into the origin of these bands. For the CNZ1 monomer, absorbance corresponding to the band at 1000 nm (Figure 3-8a) increases with the onset of the anodic peak recorded in the course of monomer electro-oxidation. During the cathodic scan, the absorbance of this peak decreases. During the first three oxidation-reduction cycles, the absorbance increases then it remains nearly constant. That would indicate that this band is a dicationic electronic transition. The band at 520 nm (Figure 3-8a') has an interesting double-peak shape, with maxima appearing at the potential of ~1.20 V vs. Ag/AgCl during both anodic and cathodic scans. This band has a saddle point at the potential of ~1.40 V. That is consistent with the formation of the radical cation, which is then further oxidized to dication during the anodic scan. The reverse process occurs during the return cathodic scan, i.e., the dication is reduced to the radical cation, then to the neutral monomer. The band's behavior at 308 nm, which is in the range of absorption corresponding to neutral molecule electronic transitions, is somewhat curious (Figure 3-8a''). In the first cycle, absorption slightly increased at the potential scanning started from ~1.20 V. However, in the return scan, the absorption increased below 0.70 V, reaching maximum at ~0.35 V, then slowly decreased through the rest of the cathodic and beginning of the subsequent anodic scan. Then, the absorption abruptly declined from the potential of ~0.80 V during the next cycle. This sequence of events is repeated in consecutive cycles, increasing the maximal absorption in each cycle. Presumably, this behavior indicates the formation of new species following electro-oxidation of the CNZ1 monomer. Typically, oligomer species are formed in the electrode vicinity through radical coupling.

A similar analysis has been performed for the FM3 absorbance during oxidation-reduction cycles (Figure 3-8). In the first cycle, the band at 1126 nm increased when the potential reached ~0.80 V vs. Ag/AgCl, coinciding with the FM3 anodic peak potential (Figure 3-8b''). Then the absorbance reached the maximum at ~1.15 V and then decreased until the potential reached ~0.20 V, which coincides with the end of the cathodic peak of the polymer formed. In subsequent cycles, absorbance at 1126 nm increased at ~0.30 V, which corresponds to the

onset of the polymer oxidation current, then reached the maximum at  $\sim$ 1.19 V and then decreased for the potential reaching  $\sim$ 0.20 V. This sequence was repeated in consecutive cycles, but the absorbance maximum increased until the third cycle and then remained relatively stable. This behavior suggests that the broad band centered at  $\sim$ 1100 nm corresponds to the oxidation of polymer chains, i.e., the formation of radical cations, which are then reduced during the return potential scan.

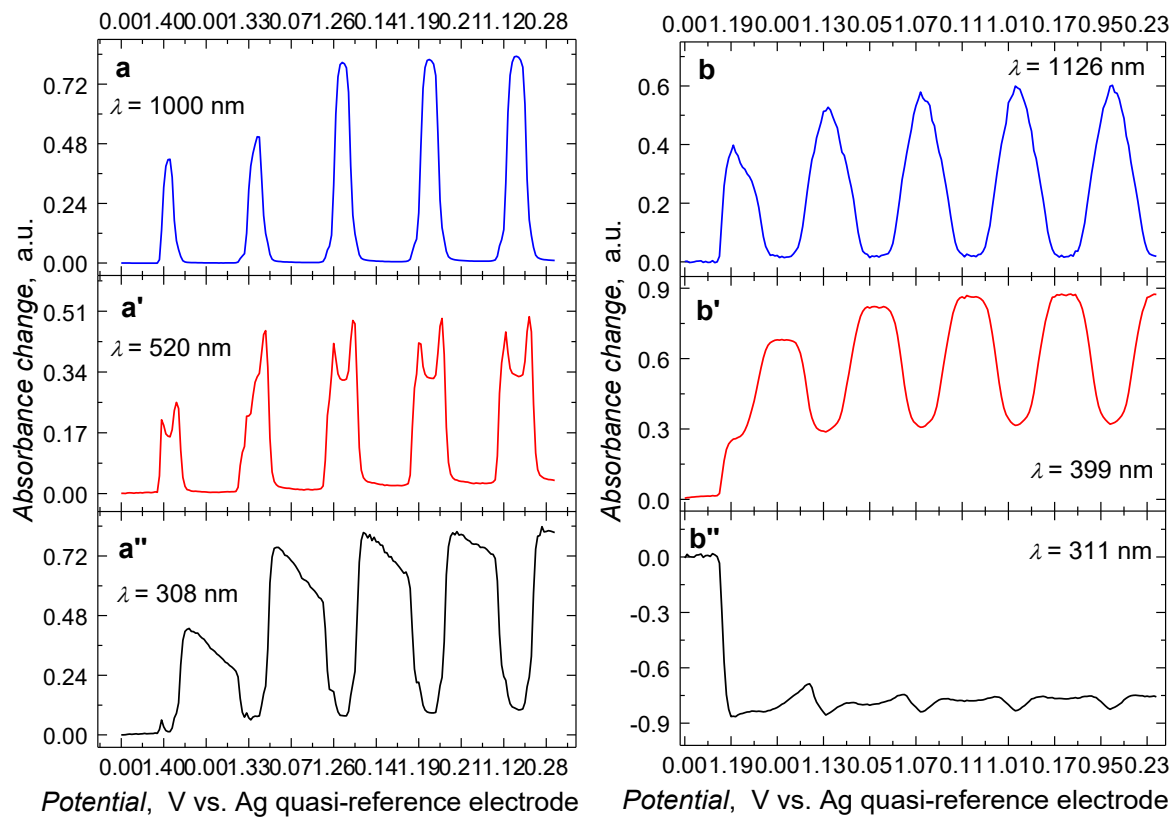


**Figure 3-8.** The absorbance changes, at selected wavelengths, with applied potential recorded during multi-cyclic electro-oxidation of (a), (a'), and (a'') CNZ1 as well as (b), (b'), and (b'') FM3 at the ITO electrode in 0.1 M (TBA)PF<sub>6</sub>, in acetonitrile, at a 3-mV s<sup>-1</sup> scan rate. Each monomer concentration was 1.0 mM.

In the first potential cycle, absorbance at 399 nm increased at  $\sim$ 0.80 V, i.e., where the FM3 monomer is oxidized (Figure 3-8b'). Next, it reached a plateau at  $\sim$ 1.20 V, then increased rapidly during the cathodic scan from  $\sim$ 0.90 V to 0.00 V. Subsequently, it became constant until the potential of  $\sim$ 0.35 V was reached during the next anodic scan. The second increase of the absorbance coincided with the beginning of the reduction of the polymer formed in the

return scan. Afterward, the absorbance decreased and reached a minimum at  $\sim$ 1.20 V. Importantly, the absorbance did not decrease to zero but remained substantial during the oxidation of the pFM3 film formed. This pattern was repeated in consecutive cycles. This behavior is consistent with the conclusion that the band centered at  $\sim$ 400 nm corresponds to the absorption of the neutral polymer. During film doping, radical cations are generated at the expense of the intensity of the neutral polymer band. The effect is opposite during the reduction of the preliminary oxidized polymer film.

The absorption at 311 nm substantially decreased during first oxidation, starting from potential  $\sim$ 0.80 V, then reached negative values (Figure 3-8b). The signal at this wavelength most likely originates from a neutral FM3 monomer present in the solution, which is then oxidized to form a polymer film on the electrode. After reaching the absorbance minimum at 1.20 V, the absorbance slightly increased until attaining the potential of  $\sim$ 0.60 V during the cathodic scan. Then there was a plateau for potentials up to 0.30 V followed by a further absorbance increase until the next anodic scan. This behavior can be associated with partial reduction of the non-polymerized FM3 monomer or its dimer to the neutral form. This redox pattern was repeated in successive potential cycles. That is, the absorbance at 311 nm decreased from the potential of 0.70 V till 1.20 V in the anodic scan, then increased in two steps in the cathodic scan and at the beginning of the following anodic scan until attaining the potential of 0.70 V. However, the absorbance changes in subsequent cycles were much smaller than during the first cycle. That means that the bands are linked to oxidation and reduction of species in solution, most probably FM3 dimers or trimers.

Interestingly, changes of absorbance at 540 nm with potential (not shown) are quite similar to those at 1126 nm except for the formation of the plateau in the potential range of  $\sim$ 1.00 to 0.89 V. It indicates that the band originates from polymer doping and de-doping leading to the formation of radical cations and dications, respectively.

### 3.3.6 EPR spectroelectrochemistry studies

EPR spectroelectrochemical measurements were carried out to gain information on the radical products of electrochemical reactions. For CNZ1, the EPR signal was over-modulated to receive a reliable response for the monomer-containing and monomer-free solutions. For the monomer CNZ1 solution, the EPR signal (Figure 3-9a) in the potential range of 1.25 to 1.30

V vs. Ag/AgCl was broad with the  $g$ -factor of 2.00285 and a linewidth of  $\sim$ 0.80 mT. A narrow signal appeared in subsequent potential cycles with the nearly identical  $g$ -factor of 2.00284. Its intensity increased with the cycle number. The EPR spectra shape indicates the formation of a relatively delocalized radical interacting with numerous nuclei even during the first potential cycle. The delocalization increased in subsequent potential cycles.

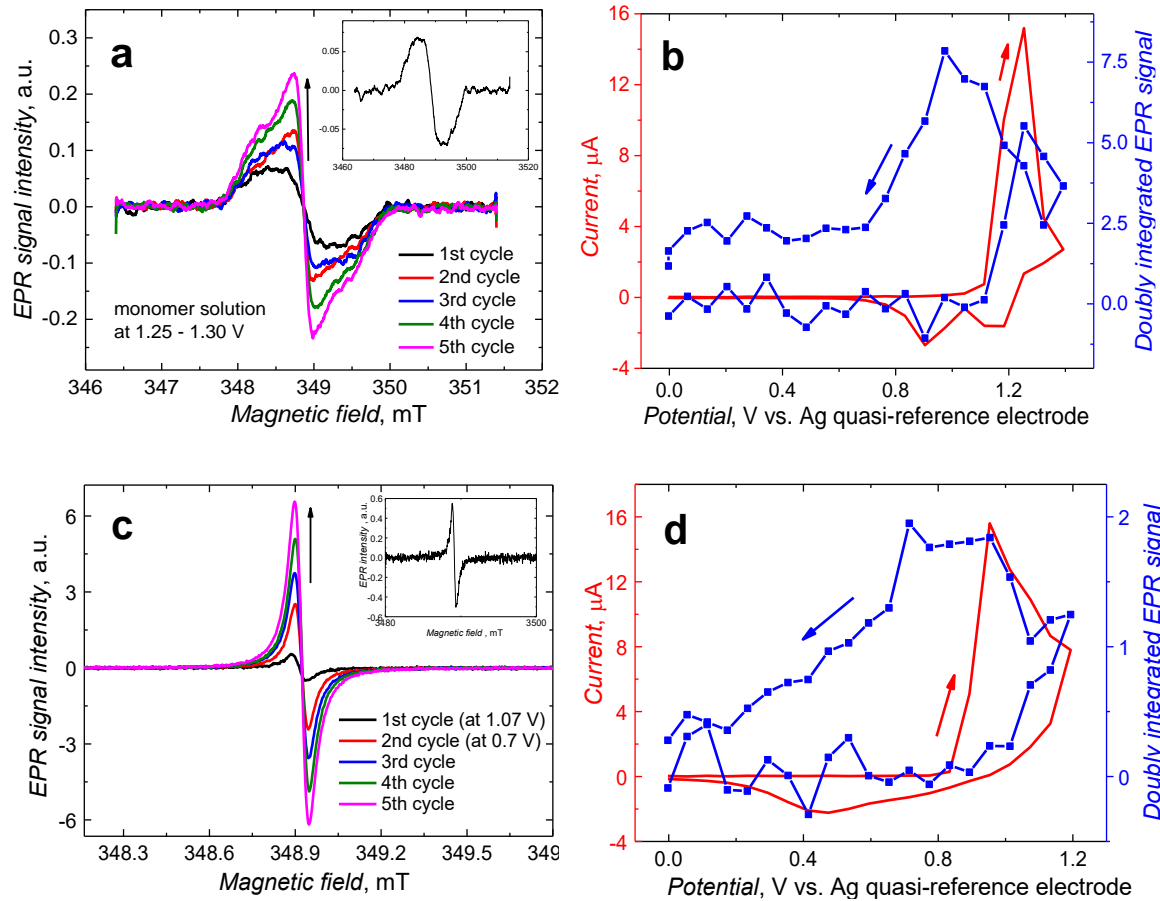


**Figure 3-9.** (a) The EPR signal for 1.0 mM CNZ1 monomer measured at the monomer anodic peak potential of 1.30 V; inset is the EPR signal for the CNZ1 monomer. (b) The (blue) curve of spin concentration change vs. potential during oxidation and then reduction of CNZ1, compared with the (red) CV curve. (c) The EPR signal for 1.0 mM FM3 measured at the monomer anodic peak potential of 1.07 V; inset is the EPR signal for the FM3 monomer. (d) The (blue) curve of spin concentration change vs. potential during oxidation and then reduction of FM3, compared with (red) the CV curve.

However, the measured  $g$ -factor was consistent with radicals interacting with highly electronegative atoms (here, presumably, nitrogen atoms or carbon atoms neighboring nitrogen atoms) or extended conjugated systems, e.g., naphthalene.<sup>347–349</sup> The EPR signal double

integration resulted in the potential dependence of the total spin concentration. For CNZ1, the number of spins remained zero until the potential of 1.10 V vs. Ag/AgCl was reached (Figure 3-9b). When the potential attained the range of the carbazole oxidation, i.e., exceeded 1.10 V vs. Ag/AgCl, the spin concentration commenced increasing till the potential of 1.25 V was reached and then decreased. During the return scan, the spin concentration still decreased to the potential of ~1.30 V and then increased to 0.90 V. When the potential became lower than 0.90 V, the spin concentration decreased once again. This effect originates from radical-cation-bearing species generated in the potential range of 1.10 to 1.25 V, then the simultaneously formed bipolaronic species with paired spins. In the return potential scan, the radical cation formation became dominant in the range of 1.30 to 0.90 V. Finally, reduction of the formed compounds leads to the formation of neutral molecules. However, the total spin number does not return to zero. That is typical for organic polymers and is known as residual spins. Therefore, the oxidation product formed remained partially oxidized.

On the other hand, for the FM3 monomer solution, a well-defined EPR signal appeared at 1.07 V vs. Ag/AgCl in the first anodic scan and at 0.70 V vs. Ag/AgCl in subsequent cycles (Figures 3-9c and 3-9d). The *g*-factor of the signal is 2.00258, which is lower than for CNZ1. Moreover, for FM3, the EPR signal shape points to delocalization of the radical even during the first potential cycle. The *g*-factor value indicates that the radical is less coupled with nitrogen atoms and more with the carbon and sulfur atoms.<sup>348–350</sup> The signal intensity increased with the cycle number, and there was no broad signal (Figure 3-9c). The *g*-factor slightly decreased in subsequent cycles to 2.00252, indicating higher radical delocalization in the polymer chains formed. The EPR signal double integration resulted in the total spin concentration dependence on the potential (Figure 3-9d). Here, this concentration increased at potentials exceeding 0.80 V during the oxidation and until the potential of 0.70 V was reached during the reduction. The spin concentration decreased gradually, with the potential decrease to 0.00 V. Significantly, there was no apparent drop in the spin number at potentials exceeding the anodic peak potential, indicating the less effective dication formation.

During CV studies of pCNZ1 in a monomer-free solution, a weak EPR signal appeared at 1.20 V vs. Ag/AgCl with the *g*-factor of 2.00285. This value is the same as that determined for polymer deposition, as well as the linewidth of 0.14 mT (Figure 3-10a). The linewidth lower than that measured for pCNZ1 deposition indicates higher electron delocalization in the

polymer chains. However, the unchanged *g*-factor indicates that the radical coupling to carbazole and naphthalene carbon atoms remained largely intact. Moreover, the EPR double integral vs. potential curve follows the trend of the cyclic voltammogram (Figure 3-10b). This result is consistent with electro-oxidational depositing a thin polymer or oligomer film on the electrode.

For the pFM3 film in the monomer-free solution, a clear and strong EPR signal is seen (Figure 3-10c). A high-spin concentration signal is accumulated at the experiment initiation, typically for electropolymerized conjugated polymers, indicating that not all cation radicals are reduced to the neutral form during polymer electrodeposition. The relative number of spins remained almost constant until the potential of 0.50 V vs. Ag/AgCl was attained (Figures 3-10c and 3-10d). When the potential reached the region of the carbazole-thiophene oxidation, i.e., above 0.70 V vs. Ag/AgCl, the spin concentration commenced increasing, manifested as an increase in the intensity of the EPR signal. This intensity increased until the potential of ~0.80 V, indicating radical cation formation. Moreover, ill-resolved anodic and cathodic peaks appeared in the cyclic voltammogram during the oxidation and reduction of the polymer (Figure 3-10d). At the potentials exceeding 0.80 V, the spin concentration decreased slightly, causing signal broadening. The partial formation of the spin-less dication explains this effect (Figures 3-10c and 3-10d).

The EPR signal and the spin number increased during the polymer reduction until ca. 0.70 V and then gradually decreased. However, both EPR signal and spin number (Figure 3-10d) did not disappear entirely after the reduction indicating non-complete polymer reduction. A more detailed analysis of the *g*-factor and EPR linewidth evolution with the potential applied is shown in Figure 3-10e. In the organic radicals, it is not easy to specify the *g*-factor values because of their narrow range, i.e., between 2.00 – 2.01, which is close to the free-electron value of 2.0023.<sup>351</sup> Apparently, the residual spins originating from electropolymerization were located mainly on carbon atoms, presumably on the thiophene ring, in the form of polarons as indicated by the initial *g*-factor value of 2.00218.<sup>335,352</sup> The *g*-factor value increase accompanies the oxidation of the polymer, first to 2.00221 and then to 2.00229. This behavior is unexpected, as the formation of polaron states leads to a decrease in the *g*-value, and the formation of bipolarons is linked with a *g*-factor increase.<sup>353</sup>

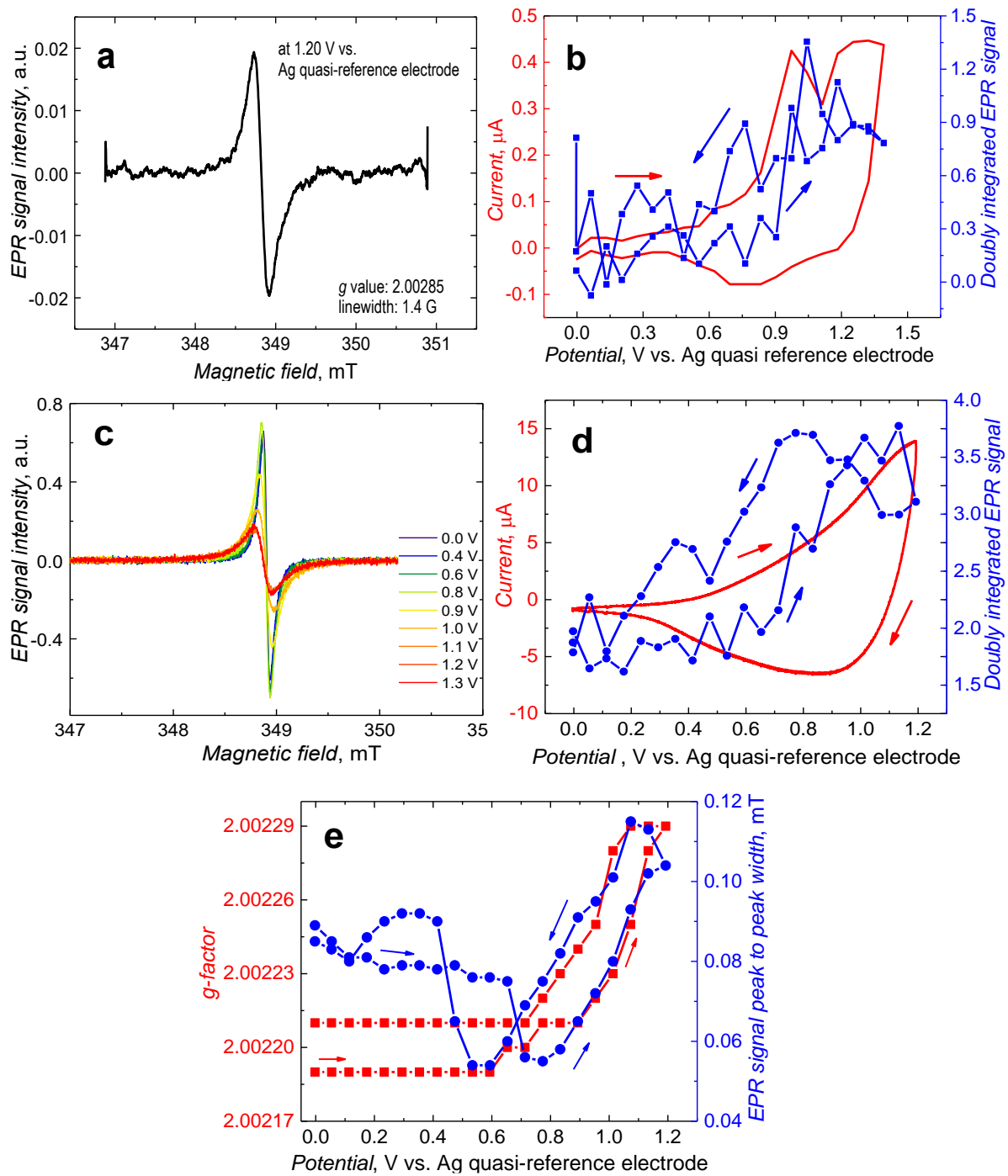


**Figure 3-10.** The EPR spectra for pCNZ1 deposited on the ITO-layered glass slide in a monomer-free solution (a) at 1.20 V vs. Ag/AgCl. (b) The (blue) spin concentration change with the potential curve during doping and dedoping, compared with the (red) CV curve. The EPR spectra for pFM3, deposited on ITO, during (c) potentiostatic electrochemical doping, (d) the (blue) spin concentration change during doping and dedoping, compared with the (red) CV curve. (e) (red) In-situ determined g-factor and the change in (blue) the EPR signal linewidth vs. potential for pFM3.

This observation may indicate some overlap of the redox processes when polaron and bipolaron are formed at relatively close potentials. Noteworthy, the *g*-factor of 2.00221 for the reduced polymer is higher than that initial of 2.00218, indicating slight changes in the polymer electronic structure during oxidation-reduction changes. From Figure 3-10e, the linewidth evolution with potential shows its gradual decrease from 0.085 mT until the potential of ca. 0.70 V when linewidth decreased sharply, reaching 0.055 mT. The decrease of the signal width indicates the formation of polarons during polymer oxidation up to ~0.70 V. Then, the linewidth increased substantially with the potential increase reaching 0.105 mT at 1.20 V and then decreased with the pFM3 reduction. The *g*-factor and linewidth evolution stipulates that doping proceeded through oxidation of neutral molecule to radical cations and dications located on carbon and sulphur atoms. The polymer reduction proceeds through the bipolaron to polaron, then to a neutral polymer, although the polymer is not fully de-doped in the experiment timescale. Interestingly, at potentials less positive than 0.50 V, the EPR signal width rapidly increased back to nearly its initial value. This behavior is consistent with the existence of more localized spin defects remaining after incomplete reduction of the polymer.

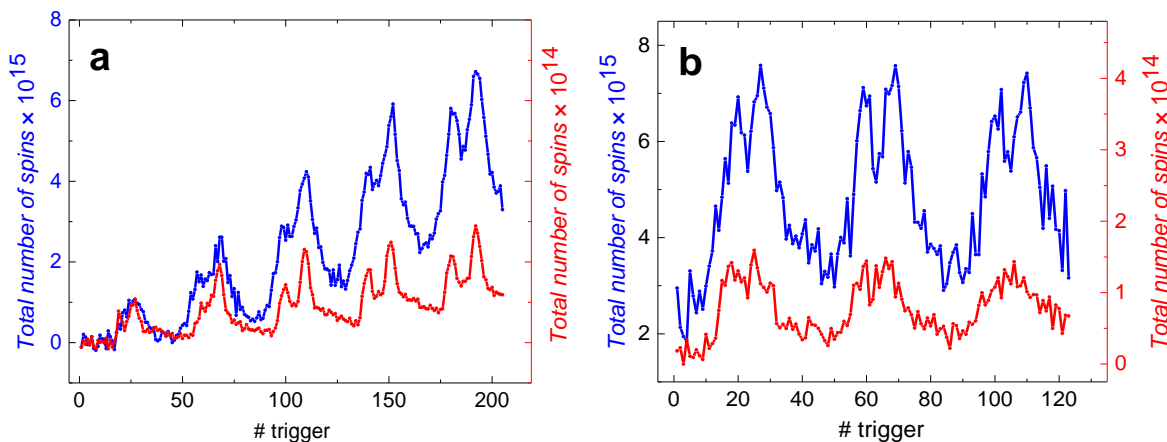


**Figure 3-11.** Comparison of the total number of spins formed (a) during (red) CNZ1 and (blue) FM3 potentiodynamic electropolymerization on ITO and (b) in the preliminarily formed (red) pCNZ1 and (blue) pFM3 in a monomer-free solution.

The total number of spins generated during multi-cyclic FM3 monomer oxidation in consecutive potential cycles rose much faster than during CNZ1 monomer oxidation, although the initially generated number of spins was quite similar for both monomers (Figure 3-11). However, the number of radicals formed in pCNZ1 were ~30 times lower than in pFM3, in

harmony with the much thinner polymer film formed (Figure 3-11). Nevertheless, the number of spins generated during each oxidation-reduction cycle was quite reproducible for both films.

These findings are supported by spin density maps (Figure 3-12) of radical cations for both monomers. The spin density in the CNZ1 radical cation (Figure 3-12a) is spread throughout the molecule. However, the spin density in the FM3 radical cation is mainly concentrated on the carbazole thiophene moiety (Figure 3-12b).

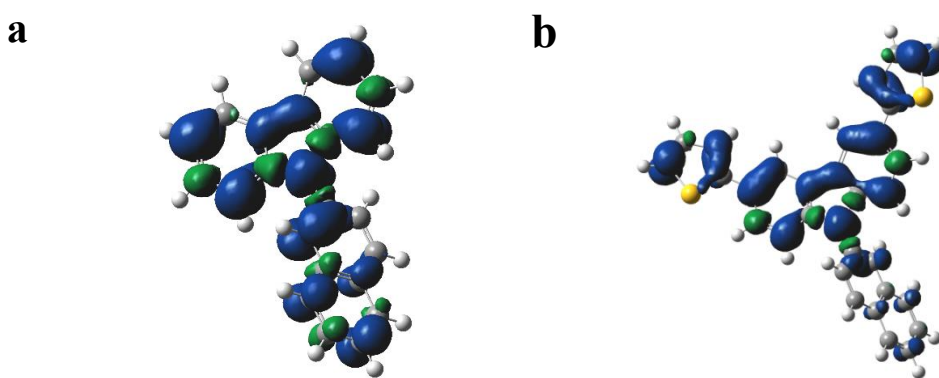


**Figure 3-12.** Spin density distribution in radical cations (isovalue = 0.001) of (a) CNZ1 and (b) FM3 monomers. Blue and green colors represent positive (spin-up) and negative (spin-down) spin polarization, respectively.

The experimental findings suggest that the effective polymerization in CNZ1 is lowered because the generated radical cation is delocalized over the entire molecule, including the naphthalene moiety. The electrostatic potential surface (EPS) calculations (Figure 3-13) for neutral molecules, radical cations, and dications of CNZ1 and FM3 support this finding. Generally, the EPS is derived from the electron density. It enables a better understanding of chemical reactivity. Figure 3-13 depicts the EPS around the CNZ1 and FM3 monomers, with red, blue, and green colors representing the highest negative, positive, and neutral electrostatic regions responsible for electrophilic or nucleophilic attack.<sup>354</sup> The positive (blue) electrostatic potential is propagated across all compounds, as seen in the ESP map of investigated compounds. However, the negative (red) electrostatic potential is located inside the carbazole moiety and on the thiophene rings for the neutral forms. The radical cation form produces an overall positive electrostatic potential, higher at the center. The thiophene rings feature the lowest positive ESP values ranging between +0.06 and +0.07 a.u. These findings demonstrate

that thiophene substituents at the carbazole ring alter the distribution of ESP around the monomers investigated and enhance the reactivity of their radical-cation forms. A similar ESP trend is seen for the CNZ1 and FM3 dimers.

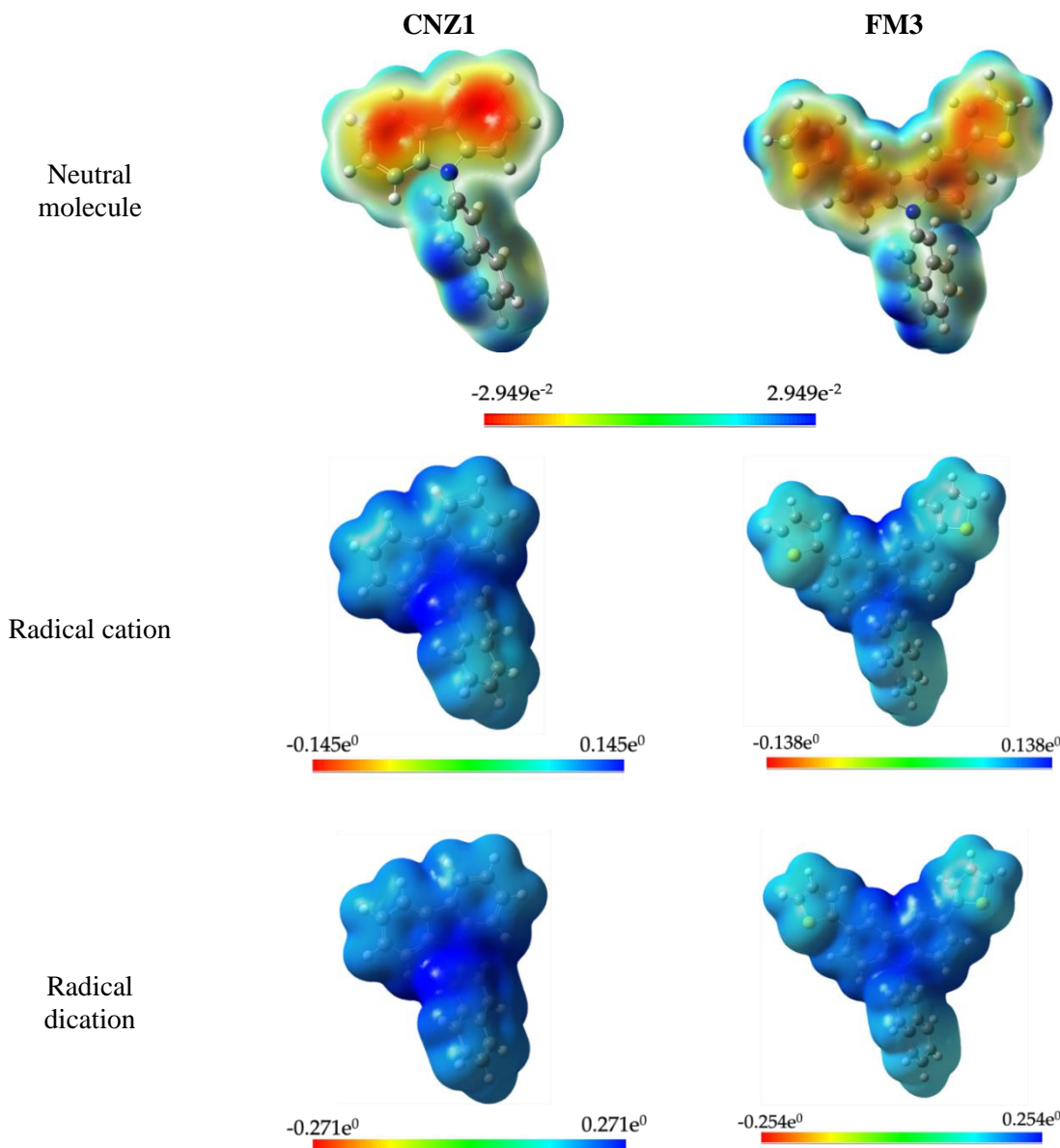


**Figure 3-13.** Visualization of the electrostatic potential (ESP) of CNZ1 and FM3 monomers in acetonitrile. The isodensity surface represents the molecules at 0.001 a.u. of an electron density function, colored according to the local ESP.

Electrochemical, UV-vis-NIR, and EPR spectroelectrochemical studies, combined with DFT calculations, confirmed that the studied CNZ1 and FM3 monomers undergo oxidation, forming radical cations. However, the CNZ1 radical cation is largely delocalized, making longer oligomers and polymers' initiation more difficult than in the case of the FM3 radical cation.

### 3.4 Conclusions

The results compare the photo- and electrochemical properties of the naphthalene-appended carbazole and thietyl-carbazole, as well as their polymers. Upon oxidative electropolymerization, CNZ1 forms a thin film. However, dominant products are short-chain oligomers that do not adhere to the electrode surface. For FM3, a thick conducting film is deposited on the electrode upon electropolymerization. The UV-vis-NIR and EPR spectroelectrochemical experiments combination with quantum chemistry calculations allowed understanding differences in mechanisms of the electropolymerization between those two monomers. Both polymer films were electroactive in an acetonitrile solution of the (TBA)PF<sub>6</sub> supporting electrolyte upon electro-oxidation. The UV-vis-NIR absorption of CNZ1 is linked with the formation of localized cation radicals consisting of oxidized monomers and dimers and weak EPR signals.

On the other hand, the FM3 showed a strong absorption band, indicating the formation of more extensively conjugated systems and a stable EPR signal. Moreover, reversible EPR and UV-vis-NIR spectroscopic features were revealed during polymers' doping and dedoping. The EPR spectroscopy study divulged that paramagnetic and diamagnetic species were formed at lower and higher oxidation potentials.

Comparison of the experimental results with the DFT calculated spin density maps, Mulliken charge distributions, and electrostatic potential surfaces for CNZ1 and FM3 in neutral, cation radical, and dication were made. For CNZ1, the radical delocalization was significant, lowering the chance of cation radical coupling reaction and preventing the formation of longer polymeric chains. However, in FM3, the radical delocalization was restricted to the carbazole-thiophene unit.

# **Chapter 4**

## **Molecularly imprinted polymer (MIP) nanoparticles-based electrochemical chemosensors for selective determination of cilostazol and its pharmacologically active primary metabolite in human plasma**

The research work described in Chapter 4 encompasses the study using MIP nanoparticles (Section 4.1) and MIP films (Section 4.2) for devising, fabricating, and testing chemosensors for selective cilostazol determination in human plasma.

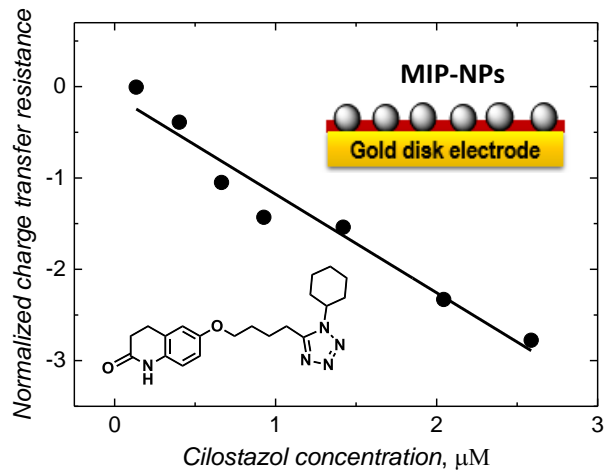
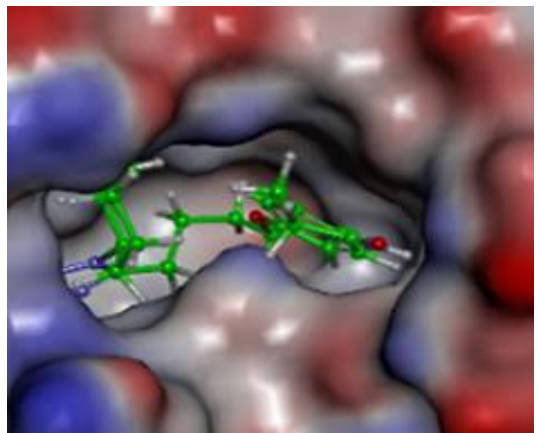
## **4.1 Molecularly imprinted polymer nanoparticles-based electrochemical chemosensors for selective determination of cilostazol and its pharmacologically active primary metabolite in human plasma**

The present Section 4.1 of Chapter 4 discusses the research work partially published in *Biosens. Bioelectron.*, **2021**, 193, 113542, <https://doi.org/10.1016/j.bios.2021.113542>

### **Abstract**

Molecularly imprinted polymer (MIP) nanoparticles-based differential pulse voltammetry (DPV) and electrochemical impedance spectroscopy (EIS) chemosensors for antiplatelet drug substance, cilostazol (CIL), and its pharmacologically active primary metabolite, 3,4-dehydrocilostazol (dhCIL), selective determination in human plasma were devised, prepared, and tested. Molecular mechanics (MM), molecular dynamics (MD), and density functional theory (DFT) simulations provided the optimum structure and predicted the stability of the pre-polymerization complex of the CIL template with the chosen functional acrylic monomers. Moreover, they accounted for the MIP selectivity manifested by the molecularly imprinted cavity with the CIL molecule complex stability higher than that for each interference. On this basis, a fast and reliable method for determining both compounds was developed to meet an essential requirement concerning the personalized drug dosage adjustment. The LOD at the signal-to-noise ratio of  $S/N = 3$  in DPV and EIS determinations using the ferrocene redox probe in a "gate effect" mode was  $93.5 (\pm 2.2)$  and  $86.5 (\pm 4.6)$  nM CIL, respectively, and the linear dynamic concentration range was 134 nM to 2.58  $\mu$ M in both techniques. The chemosensor was highly selective to common biological interferences, including cholesterol and glucose, and less selective to structurally similar dehydroaripiprazole. Advantageously, it responded to 3,4-dehydrocilostazol, thus allowing for the determination of CIL and dhCIL together. The EIS chemosensor appeared slightly superior to the DPV chemosensor concerning its selectivity to interferences. The CIL DPV sorption data were fitted with Langmuir, Freundlich, and Langmuir-Freundlich isotherms. The determined sorption parameters indicated that the imprinted cavities were relatively homogeneous and efficiently interacted with the CIL molecule.

## Graphical abstract



#### 4.1.1 Introduction

The study described in the present chapter provides a systematic approach to fabricate an electrochemical chemosensor for the selective determination of CIL. The simulations using MM, MD, and DFT established the stoichiometry and stability of both the pre-polymerization complex of CIL with the chosen functional and cross-linking monomers, as well as CIL and each interferent separately, with the molecular cavity imprinted with CIL in nanoMIPs, towards nanoMIP selectivity.

NanoMIPs with the highest CIL binding efficiency were then chosen to fabricate chemosensors to determine CIL and dhCIL. For that, the nanoMIPs were embedded in a polytyramine film, deposited by electropolymerization on Au disk electrodes (Figure 4.1-1). The nanoMIPs molecular cavities' binding CIL and dhCIL abilities were evaluated using the "gate effect."<sup>304,355</sup> Moreover, CIL was determined in human plasma. Because few earlier reported electrochemical chemosensors for CIL lack interferences studies confirming the chemosensor suitability for practical use,<sup>247,249</sup> we strongly believe that our present research provides unique detailed results on the electrochemical chemosensing in the human plasma of CIL and dhCIL, in which the matrix effect is considered. The prepared chemosensor is inexpensive, sensitive, easy to operate, and selectively determines CIL and dhCIL.

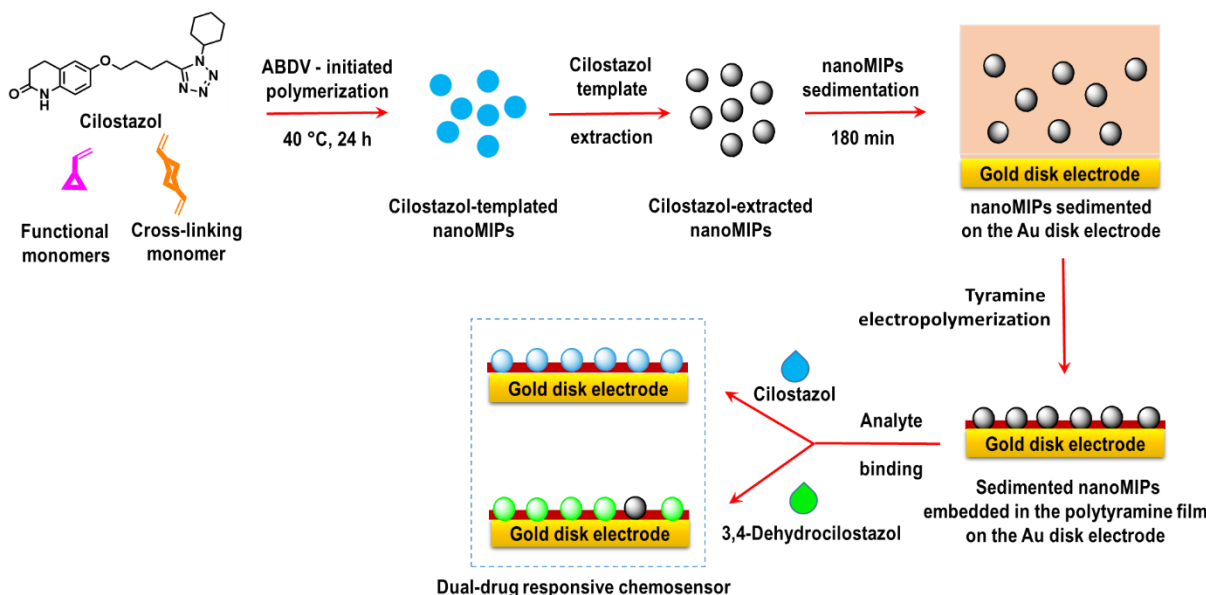


**Figure 4.1-1.** The flowchart of electrochemical chemosensor preparation.

## 4.1.2 Experimental and procedures

The procedure for synthesizing the CIL-templated MIP nanoparticles and their method of immobilization on an electrode with polytyramine has been discussed in Chapter 2. In the EIS experiments, an ac excitation signal of frequency in the range of 1 MHz to 100 mHz and 10-mV sinusoidal amplitude was used, and signals were measured at the constant potential of 0.20 V vs. Ag quasi-reference electrode applied. In DPV measurements, the potential step was 5 mV, and the amplitude of 50-ms pulses applied was 25 mV.

### 4.1.2.1 Samples preparing for the nanoMIPs or nanoNIPs binding cilostazol tests

A 100 µM CIL stock acetonitrile solution was prepared. Separately, suspensions of polymer NPs (1, 10, and 15 mg) in acetonitrile (500 µL) were prepared and then mixed with the CIL stock solution (100 µL). The final sample volume was next adjusted to 1 mL with acetonitrile. Subsequently, the polymer NPs were allowed to bind CIL overnight at room temperature on a homemade tube rotator. Afterward, they were centrifuged off (10 000 rpm, 30 min). Lastly, a supernatant solution (500 µL) was pipetted off and then filtered before HPLC determination of CIL in it. The amount of CIL bound to polymer NPs was calculated by subtracting the amount of unbound CIL from its initial amount.

### 4.1.2.2 Preparing cilostazol spiked plasma solutions

For CIL determination in a real sample, a human plasma sample (0.5 mL, with citrate as the anticoagulant) donated by healthy volunteers was ten times diluted with acetonitrile (4.5 mL) to prepare a stock solution. This dilution resulted in precipitation of a solid, centrifuged out at 10 000 rpm for 10 min at 25 °C. Next, ferrocene and (TBA)ClO<sub>4</sub> were added to the supernatant to reach 10 mM and 0.1 M concentrations, respectively. Then, measurements were performed at known CIL concentrations. Similarly, 100 times diluted artificial Nortrol serum solutions spiked with different concentrations of CIL were prepared following the procedure mentioned in the Appendix.

After chemosensor fabrication, a 1-ml sample of the above ferrocene redox probe solution was placed in an electrochemical cell, and the polytyramine (nanoMIP-A) or polytyramine (nanoNIP-A) film-coated electrode was immersed in this solution. Later, CIL of different

concentrations was added, and both DPV and EIS measurements were performed. The resulting changes in the detection signals were then used to construct the calibration plots.

#### **4.1.2.3 Cilostazol-induced protein precipitating in human plasma**

The UV-vis spectroscopy experiments were performed to evaluate possible CIL interaction with human plasma proteins. For that, a stock acetonitrile solution of CIL was prepared. Two separate CIL samples of this solution (2.7 mL each) were taken to study the possible loss of free CIL because of its interaction with the proteins, followed by their precipitation. Water (0.3 mL) was added to one sample while plasma (0.3 mL) was to the other. These solutions were vortexed at room temperature and then centrifuged at 10 000 rpm for 10 min. Finally, 1 mL of a supernatant sample was pipetted off for the UV spectroscopy measurements.

### **4.1.3 Results and discussion**

#### **4.1.3.1 Optimizing nanoMIPs composition**

To optimize the nanoMIPs composition, we synthesized nanoMIPs at different FM and CLM combinations and ratios by assessing their affinity for CIL by HPLC (Figure 4.1-2). Aiming at small, globular particles to interface with an electrode, we found nanoMIP synthesis by precipitation polymerization in acetonitrile as a promising opportunity. This porogenic solvent is often used for synthesizing sub-micrometer-sized MIP particles,<sup>356</sup> predominantly via noncovalent imprinting based on H-bonding. Thus, the presence of the lactam group on a CIL molecule is suitable for H-binding. High CIL solubility in acetonitrile prompted us to test some FMs, commonly used with this solvent, to imprint molecular cavities in nanoMIPs by incurring H-bonding. The tested FMs included MAA, 4-VP, and IA (Table 4.1-1). Among them, MAA is, perhaps, the most widely used to synthesize nanoMIPs. Moreover, IA is a common (carboxylic acid)-based FM, which can afford multiple interactions thanks to its dual functionality. Besides, 4-VP is used to raise  $\pi$ - $\pi$  stacking in aqueous solutions,<sup>357</sup> but it can also build a synergistic effect with MAA in the acetonitrile solvent.<sup>358</sup> Furthermore, the presence of aromatic moieties, such as a tetrazole and a 6-membered ring located close to the lactam moiety on a CIL molecule suggests that the application of 4-VP might be promising.

The nanoMIPs, prepared solely using the MAA functional monomer, bound CIL stronger than other synthesized nanoMIPs did (Figure 4.1-2a). Surprisingly, the exchange of IA for

MAA to serve as the FM did not improve the nanoMIPs properties. Instead, it slightly increased the non-specific binding on nanoNIPs despite twice as many available carboxyl groups on the MAA molecule. Further, replacing acetonitrile with octanenitrile, a lower-polarity solvent favoring H-bonding, appeared unsuccessful in improving the nanoMIP-C binding capacity (Figure 4.1-2c).

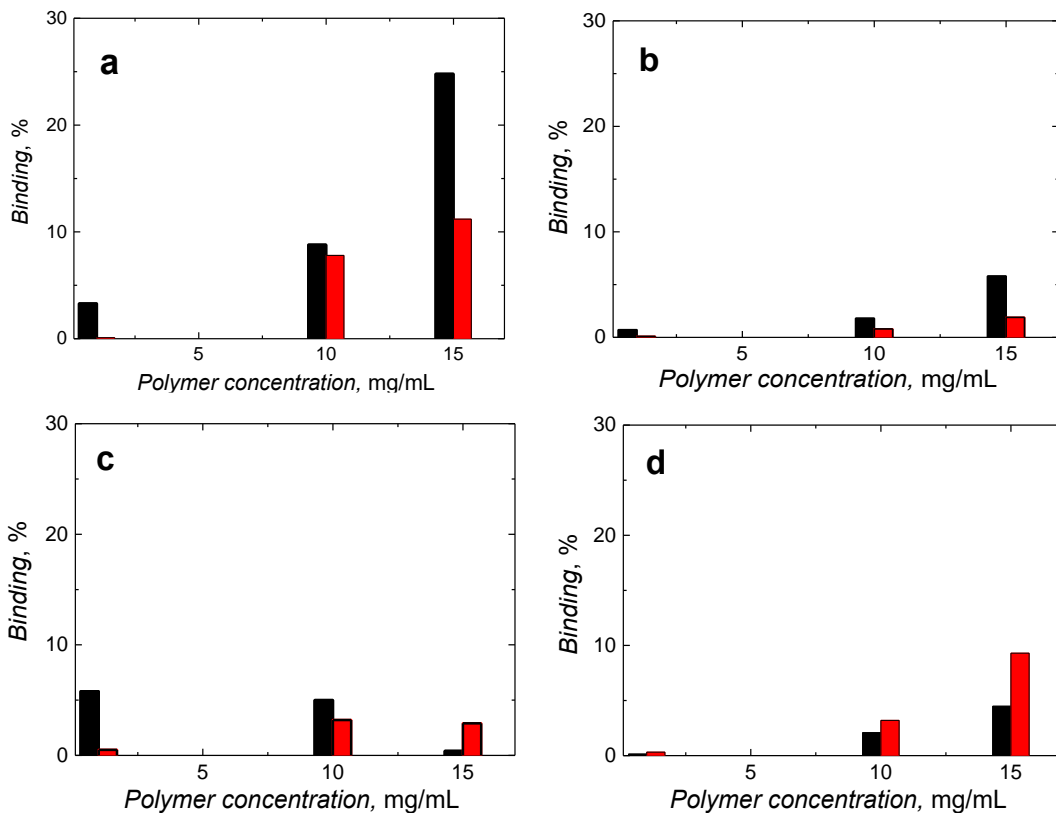


**Figure 4.1-2.** Histograms of 10  $\mu\text{M}$  CIL binding by (black) nanoMIPs and (red) nanoNIPs at different polymer NPs concentrations. The nanoMIPs and nanoNIPs were prepared using functional monomers of (a) methacrylic acid, (b) and (c) methacrylic acid, and 4-vinylpyridine as well as (d) itaconic acid. The solvent for polymerization was (a), (b), and (d) acetonitrile and (c) octanenitrile.

Next, for each monomer combination used to prepare nanoMIPs, the binding capacity of the nanoMIPs to CIL was determined (Table 4.1-1). Apparently, this capacity is the highest for nanoMIP-A. Therefore, this polymer was further used for chemosensor preparation. For different nanoMIPs, the order of the determined binding capacity was the same as that of the

calculated Gibbs free energy changes ( $\Delta G_{\text{complex}}$ ), i.e., predicted stability of the pre-polymerization complexes formed in solution.

Because of a normalized binding capacity to CIL relatively high, nanoMIP-B might be another candidate for chemosensor preparation. However, CIL template complete removal from the nanoMIP-B appeared difficult. Over 50 extraction rounds were needed for that. Therefore, nanoMIP-B was not used any further.

#### 4.1.3.2 Computer simulations procedures

The stability of the CIL : FM pre-polymerization complex formed in the solution for polymerization is crucial for successful molecular imprinting. The Gibbs free energy changes due to the formation of different complexes were calculated to ascertain this stability. Toward that, the boxes containing the CIL molecule were surrounded by sixteen FM molecules to obtain the initial complex structures. For the solution in which two different functional monomers were present, such as MAA (FM1) and 4-VP (FM2), the CIL template molecule was surrounded by a mixture of FMs in the 1 : 8 : 8 molar ratios. The monomer molecules were randomly located around the template molecule, and then the energy was minimized. Next, eight FM molecules were chosen by considering the strongest interactions with the CIL molecule and the molar ratios according to the synthesis procedure, namely, CIL : FM of 1 : 8 or CIL : FM1 : FM2 of 1 : 4 : 4. Then, the obtained complex structures were optimized again. Next, twenty-five molecules of CLM were added to the systems, reflecting the stoichiometry adopted in the synthetic procedure, and then the Gibbs free energy was minimized. Subsequently, the MD simulations for each system of the CIL : FM : CLM ratios of 1 : 8 : 25 and CIL : FM1 : FM2 : CLM of 1 : 4 : 4 : 25 were performed. Furthermore, CIL molecules were removed from the polymers, and the emptied spaces were proposed as theoretical models of molecular cavities imprinted in the nanoMIPs.

These cavities were then used for sorption and selectivity modeling. CIL was used in the binding efficacy examinations of nanoMIP-A through nanoMIP-D to rationalize the selection of the monomer (Figure 4.1-3). Theoretical selectivity studies were performed by inserting molecules of dhCIL, dehydroaripiprazole, cholesterol, or glucose interferences in the nanoMIP-A model cavity instead of the CIL analyte molecule. Those molecules' interactions with the cavity in an acetonitrile-water solution were simulated with MD, and the Gibbs free

energy change ( $\Delta G_{\text{bind}}$ ) accompanying the polymer matrix binding of the template, analyte, or interference molecules were calculated using Equation 2-2.

As expected, the Gibbs free energy changes due to cavity interactions with the CIL molecule ( $\Delta G_{\text{bind}}$ ) followed those of the experimental binding capacity of the nanoMIPs to CIL (Table 4.1-1), thus confirming the experimental results.

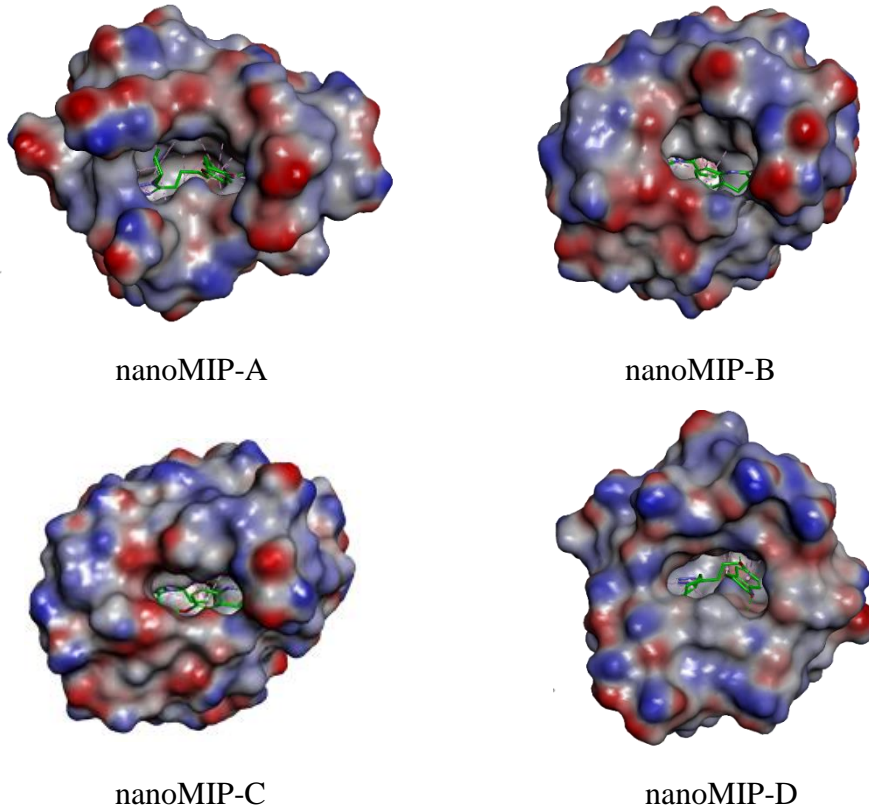


**Figure 4.1-3.** Simulated structures of the space-filling models of the (a) nanoMIP-A (CIL : MAA : EGDMA = 1 : 8 : 25 in the acetonitrile porogen), nanoMIP-B (CIL : MAA : 4-VP : EGDMA = 1 : 4 : 4 : 25 in acetonitrile porogen), nanoMIP-C (CIL : MAA : 4-VP : EGDMA = 1 : 4 : 4 : 25 in octanenitrile porogen), and nanoMIP-D (CIL : IA : EGDMA = 1 : 8 : 25 in acetonitrile porogen) with the CIL molecule embedded. The surface distribution of the molecular electrostatic potential (MEP) is colored according to the interpolated (blue) positive and (red) negative charge.

#### 4.1.3.3 DLS determining sizes of nanoMIPs and nanoNIPs

Dynamic light scattering (DLS) was used for the determination of solvodynamic sizes of nanoMIPs and nanoNIPs, which were 160 ( $\pm 20$ ) nm and 157 ( $\pm 19$ ) nm, respectively.

A relatively narrow range of nanoMIPs size distribution reached herein is crucial for attaining the high binding ability of nanoMIPs.<sup>289</sup>

**Table 4.1-1.** Composition of different CIL-templated nanoMIPs, NPs preparation conditions, the binding capacity determined, and the Gibbs free energy change due to the formation of a pre-polymerization complex in a solution using the EGDMA cross-linking monomer and the ABDV initiator at 40 °C ( $\Delta G_{\text{complex}}$ ), as well as the complex of the imprinted cavity with the CIL molecule ( $\Delta G_{\text{bind}}$ ).

Polymer	FM1	FM2	Molar ratio of CIL : FM1 : FM2	Solvent	Normalized binding capacity for 15 mg nanoMIPs per mL	$\Delta G_{\text{complex}}$ (kJ/mol)	$\Delta G_{\text{bind}}^e$ (kJ/mol)
nanoMIP-A	MAA	-	1 : 8 : 0	Acetonitrile	24.8	-323.79 <sup>a</sup>	-192.20
nanoMIP-B	MAA	4-VP	1 : 4 : 4	Acetonitrile	5.8	-256.12 <sup>b</sup>	-175.17
nanoMIP-C	MAA	4-VP	1 : 4 : 4	Octanenitrile	0.4	-46.45 <sup>b</sup>	-75.99
nanoMIP-D	IA	-	1 : 8 : 0	Acetonitrile	4.48	-128.14 <sup>a</sup>	-94.46

$$^a \Delta G_{\text{complex}} = \Delta G_{\text{system}} - \Delta G_{\text{CIL}} - 8\Delta G_{\text{FM1}} - 25\Delta G_{\text{CL}}$$

$$^b \Delta G_{\text{complex}} = \Delta G_{\text{system}} - \Delta G_{\text{CIL}} - 4\Delta G_{\text{FM1}} - 4\Delta G_{\text{FM2}} - 25\Delta G_{\text{CL}}$$

$\Delta G_{\text{complex}}$ ,  $\Delta G_{\text{system}}$ ,  $\Delta G_{\text{CIL}}$ ,  $\Delta G_{\text{FM1}}$ ,  $\Delta G_{\text{FM2}}$ , and  $\Delta G_{\text{CL}}$  stand for the Gibbs free energy change originating from forming a pre-polymerization complex, the whole system, cilostazol, FM1, FM2, and CL in acetonitrile or octanenitrile, respectively.

<sup>e</sup> Values of  $\Delta G_{\text{bind}}^e$  were calculated using Equation 2-2.

#### 4.1.3.4 Microscopic imaging of nanoMIPs immobilized in the polytyramine films on electrodes

For superior chemosensor performance, optimizing the electrode surface coverage with nanoMIPs, embedded in the polytyramine film is crucial. Accordingly, complete coverage of nanoMIPs can block the diffusion of analyte molecules to nanoMIP molecular cavities. Furthermore, an insufficient thickness of the film can affect the mechanical stability of the polymer NP layer on the other. The AFM determined average surface roughness and thickness of the film were 27 ( $\pm 4$ ) and 170 ( $\pm 30$ ) nm, respectively. The latter value is close to the DLS determined average solvodynamic nanoMIPs and nanoNIPs size of 160 ( $\pm 20$ ) and 157 ( $\pm 19$ ) nm, respectively. Apparently, the (polytyramine film)-embedded nanoparticles

were partially exposed. The SEM and AFM (Figure 4.1-4a and 4a') imaging confirmed the presence of the incompletely encapsulated nanoMIPs in this film.

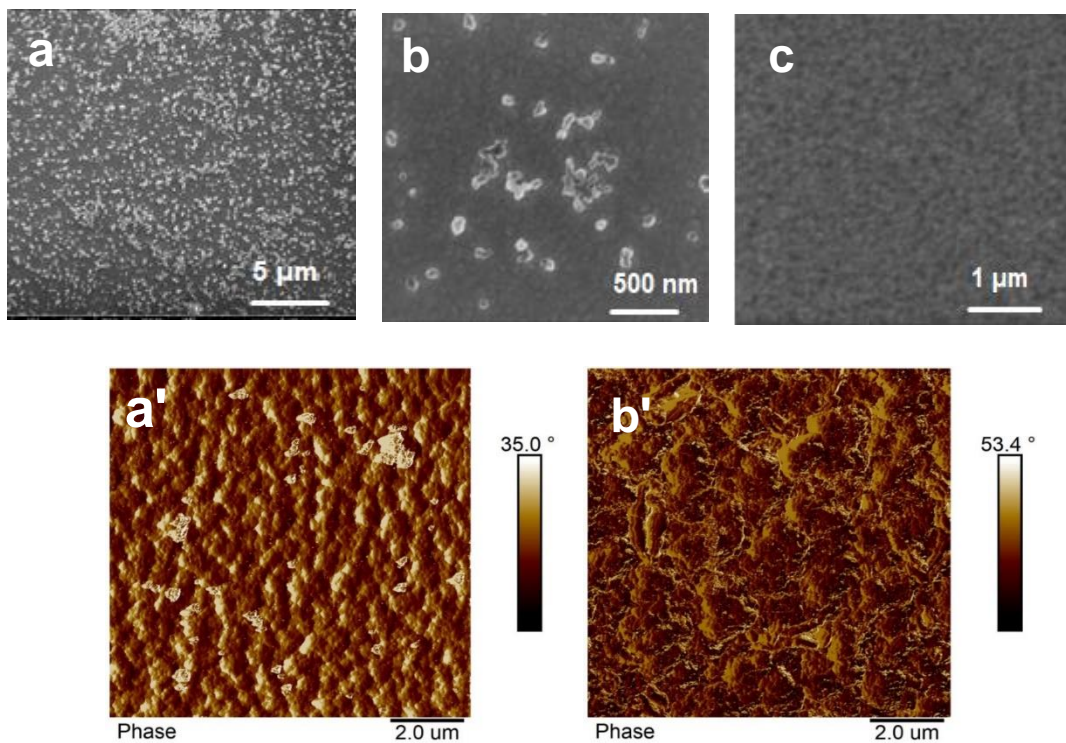


**Figure 4.1-4.** (a), (b), and (c) SEM as well as (a') and (b') AFM images of (a), (b), and (a') the nanoMIPs embedded in the polytyramine film, and (c) and (b') a plain polytyramine film deposited on the Au-layered glass slide electrode.

#### 4.1.3.5 Electrochemical characterizing nanoMIPs immobilized in polytyramine films on electrodes

Choosing the most appropriate nanoMIPs immobilization procedure is vital for effectively integrating them with a transducer surface, here on the electrode surface, to prepare an MIP chemosensor. Polymer film deposition by electropolymerization is an attractive alternative to chemical polymerization for the robust integration of an MIP recognition element with a conducting transducer.<sup>359,360</sup> Furthermore, compared to other immobilization procedures, the MIP attachment by electropolymerization has an intrinsic ability to control the film's morphology by adjusting the appropriate deposition conditions, including the deposition time and the potential applied. Therefore, it is used in various applications to integrate functional nanomaterials into deposited films.<sup>361,362</sup> Herein, we immobilized polymer NPs in a polytyramine film using a multi-cyclic potentiodynamic deposition (Figure 4.1-5b).

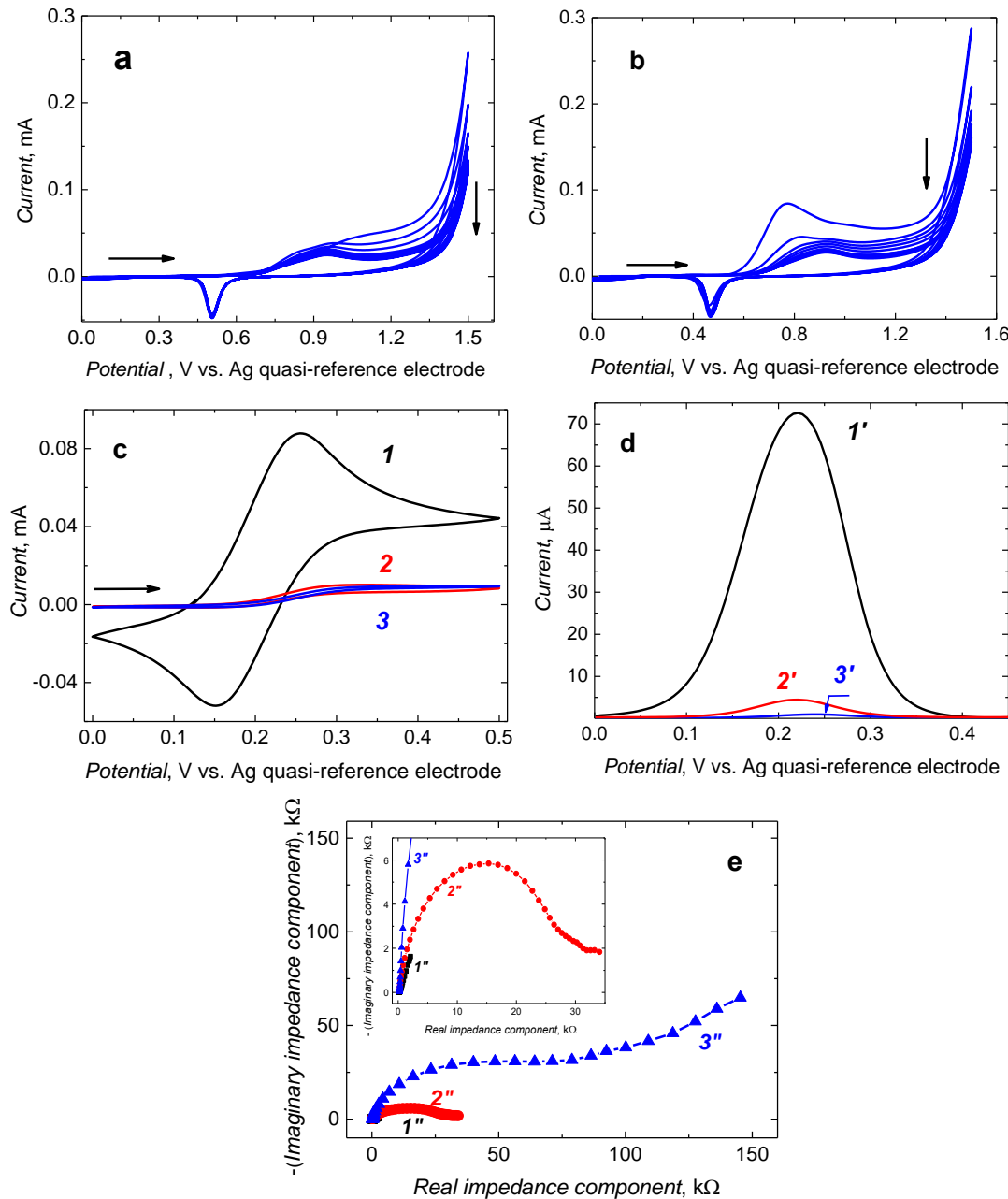


**Figure 4.1-5.** The multi-cyclic potentiodynamic curve for 10 mM tyramine in 25 mM  $\text{H}_2\text{SO}_4$  recorded with a 2-mm diameter Au disk electrode at a  $50\text{-mV s}^{-1}$  potential scan rate in the (a) absence and (b) presence of nanoMIPs sedimented on the electrode surface for 180 min. The curves of (a) CV, (b) DPV and (c) EIS at 0.20 V vs. Ag quasi-reference electrode, for 10 mM ferrocene and 0.1 (TBA) $\text{ClO}_4$  in acetonitrile recorded on (curves 1, 1', and 1'') the 2-mm diameter Au bare electrode and the electrode coated with (curves 2, 2', and 2'') the polytyramine film, and (curves 3, 3', and 3'') the polytyramine film with nanoMIPs embedded. Inset in (c) is a magnified part of the Nyquist plots in the low real impedance component range.

There is one anodic and one cathodic peak at 0.80 and 0.46 V vs. Ag quasi-reference electrode, respectively, in the potentiodynamic curve recorded. The anodic peak decreased in the initial few cycles, then increased, and, later, it became constant. This behavior was similar to that of polytyramine potentiodynamic deposition in the absence of NPs (Figure 4.1-5a), indicating polytyramine film deposition. However, there was no direct evidence of nanoMIPs immobilization in the polytyramine film.

The CV (curve 3 in Figure 4.1-5c) and DPV (curve 3' in Figure 4.1-5d) peak currents in the ferrocene solution of acetonitrile at the electrode coated with the polytyramine/nanoMIPs film, were suppressed. Moreover, the polytyramine film alone blocked electro-oxidation of ferrocene (curves 2 and 2' in Figure 4.1-5c and 5d, respectively). However, the diameter of the semicircle in the EIS Nyquist plot for the polytyramine/nanoMIPs of ~91 k $\Omega$  was much larger (curve 3'' in Figure 4.1-5e) than that of 8.4 k $\Omega$  for the polytyramine film alone (curve 2'' in Figure 4.1-5e). Thus, the polytyramine/nanoMIPs film blocked the electrode more extensively.

#### 4.1.3.6 Optimizing conditions of polymer NPs immobilization on electrodes

The nanoMIPs were allowed to sediment for four different time intervals, vis., 30, 150, 180 min, and 24 h (Figure 4.1-6a), followed by potentiodynamic polytyramine film deposition. For the firm holding of the polymer NPs, this electropolymerization was optimized using different tyramine concentrations (Figure 4.1-6b).

If nanoMIPs were sedimented for merely 30 min, the resulting chemosensor detectability of CIL (curve 2 in Figure 4.1-6a) was similar to that obtained using a genuine polytyramine film (curve 1 in Figure 4.1-6a). Evidently, an insufficient amount of nanoMIPs was immobilized during 30-min sedimentation. For 150-min (curve 3 in Figure 4.1-6a) and 180-min (curve 4 in Figure 4.1-6a) sedimentations, the normalized DPV peak currents were almost the same, substantiating the full settlement of the NPs. However, 24-h sedimentation deteriorated the chemosensor performance (curve 5 in Figure 4.1-6a). Therefore, 180-min sedimentation was used as optimized for subsequent experiments. If polytyramine was deposited from a solution of higher tyramine concentration, the chemosensor lost its selectivity. That is, the detectability of the CIL analyte and dehydroaripiprazole interference was similar (curves 1' and 2', respectively, in Figure 4.1-6b).

Presumably, that was because of the extensive coverage of the NPs with the polytyramine film. The film deposited in this case was thicker, and diffusion of both the analyte and the redox probe through the film was largely hindered, leading to a weak chemosensor response.

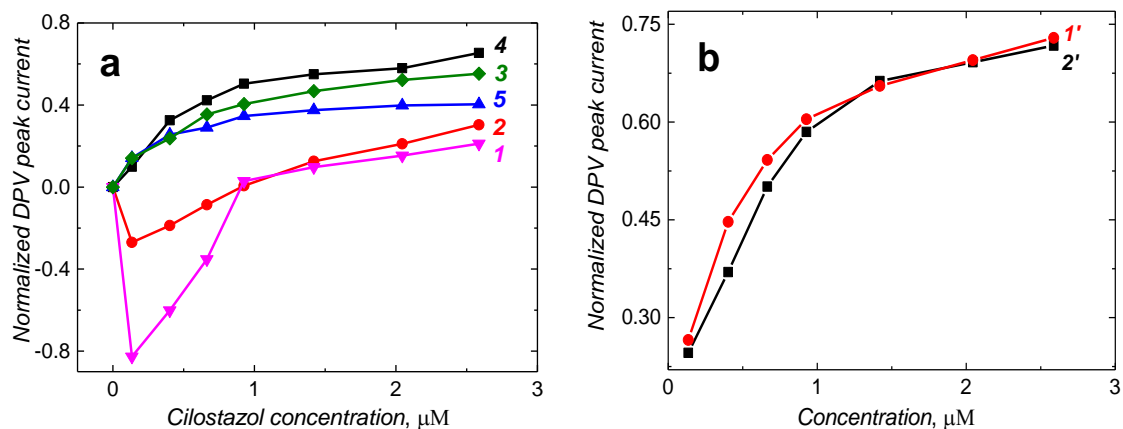


**Figure 4.1-6.** Plots of normalized DPV peak currents vs. CIL concentration in 10 mM ferrocene and 0.1 M (TBA)ClO<sub>4</sub> in acetonitrile (a) for the polytyramine film deposited on the Au disk electrodes (curve 1) without nanoMIPs and with nanoMIPs sedimented for (curve 2) 30 min, (curve 3) 150 min, (curve 4) 180 min, and (curve 5) 24 h as well as (b) for determination of (curve 1') CIL and (curve 2') dehydroaripiprazole at the 180-min nanoMIPs sedimentation time.

#### 4.1.3.7 CIL electrochemical determining with the polytyramine-(nanoMIP-A) and polytyramine-(nanoNIP) film-coated electrodes

When CIL was added to the acetonitrile solution of ferrocene, complementary cavities of the polytyramine-(nanoMIP-A) film, deposited on the electrode, bound CIL molecules. Being governed by the gate effect,<sup>304</sup> this binding decreased the DPV peak current of ferrocene with an increasing concentration of CIL (curves 1 – 8 in Figure 4.1-7a). It reached saturation at the CIL concentration exceeding 2.5 μM. The normalized DPV peak current ( $I_{DPV,0} - I_{DPV,s}$ )/ $I_{DPV,0}$ ), where  $I_{DPV,0}$  and  $I_{DPV,s}$  stand for the initial and actual DPV peak current, was linearly dependent on the logarithm of CIL concentration. The linear dynamic concentration range extended from 135 nM to 2.58 μM CIL with the calibration plot obeying a semilogarithmic linear regression equation of  $(I_{DPV,0} - I_{DPV,s})/I_{DPV,0} = 0.36 (\pm 0.01)/\log [\mu M] \times \log \{c_{cilostazol} [\mu M]\} + 0.450 (\pm 0.006)$  (curve 1'' in Figure 4.1-7c).

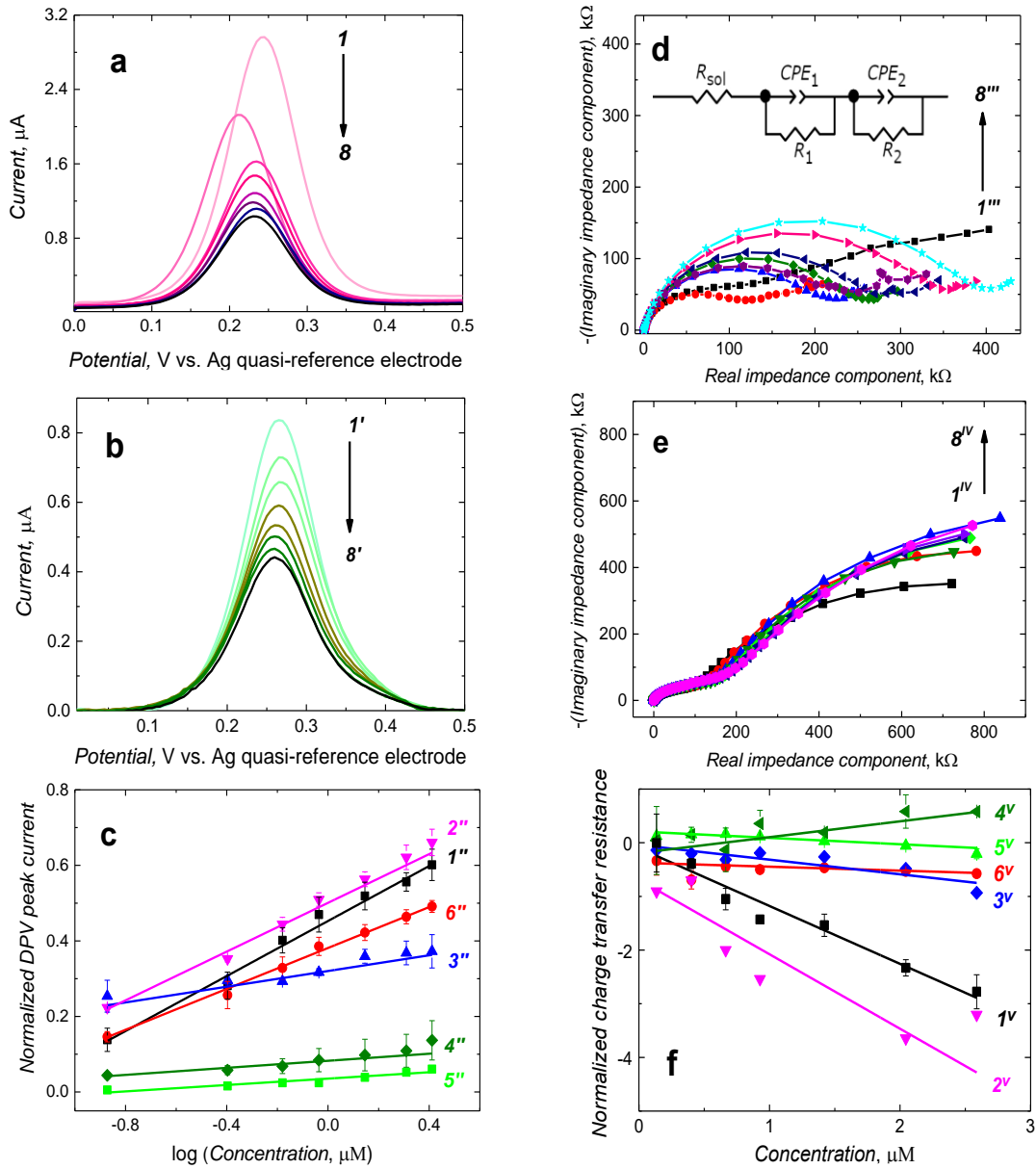


**Figure 4.1-7.** (a) – (c) DPV and (d) – (f) EIS at 0.20 V vs. Ag quasi-reference electrode curves, recorded at 2-mm diameter Au disk electrodes, coated with the polytyramine films containing (a) and (d) CIL-extracted nanoMIPs, and (b) and (e) nanoNIPs for (curves 1, 1', 1'', and 1<sup>IV</sup>) 0 nM (curves 2, 2', 2'', and 2<sup>IV</sup>) 134 nM, (curves 3, 3', 3'', and 3<sup>IV</sup>) 402 nM, (curves 4, 4', 4'', and 4<sup>IV</sup>) 664 nM, (curves 5, 5', 5'', and 5<sup>IV</sup>) 927 nM, (curves 6, 6', 6'', and 6<sup>IV</sup>) 1.42  $\mu\text{M}$ , (curves 7, 7', 7'', and 7<sup>IV</sup>) 2.04  $\mu\text{M}$ , and (curves 8, 8', and 8'', and 8<sup>IV</sup>) 2.58  $\mu\text{M}$  CIL in 10 mM ferrocene and 0.1 M (TBA) $\text{ClO}_4$  in acetonitrile. Calibration plots of (c) DPV normalized peak currents and (f) EIS determined normalized charge transfer resistance, constructed using electrodes coated with the polytyramine film containing (curves 1'' - 5'', and 1<sup>V</sup> - 5<sup>V</sup>) CIL-extracted nanoMIPs and (curves 6'' and 6<sup>V</sup>) nanoNIPs for (curves 1'', 6'', and 1<sup>V</sup>, 6<sup>V</sup>) CIL, (curves 2'' and 2<sup>V</sup>) dhCIL, (curves 3'' and 3<sup>V</sup>) dehydroaripiprazole, (curves 4'' and 4<sup>V</sup>) cholesterol, and (curves 5'' and 5<sup>V</sup>) glucose. Inset in (d) is the equivalent circuit scheme used for curve fitting where  $R_{\text{sol}}$ ,  $R_1$ , and  $R_2$  is the solution, charge transfer, and polymer film resistance, respectively.

The sensitivity and correlation coefficient were  $0.36 (\pm 0.01) / \log [\mu\text{M}]$ , and  $R^2 = 0.98$ , respectively. At the signal-to-noise ratio of  $S/N = 3$ , the LOD was  $93.5 (\pm 2.2) \text{ nM CIL}$ . For the solutions of the same composition, EIS spectra were recorded (Figure 4.1-7d) and the normalized ferrocene charge transfer resistance,  $(R_{ct,0} - R_{ct,s})/R_{ct,0}$  where  $R_{ct,0}$  and  $R_{ct,s}$  denotes the initial and actual charge transfer resistance, was determined. The following linear regression equation describes this resistance dependence on the CIL concentration.  $(R_{ct,0} - R_{ct,s})/R_{ct,0} = -1.07 (\pm 0.10) [1/\mu\text{M}] \times c_{cilostazol} [\mu\text{M}] - 0.09 (\pm 0.15)$ . The sensitivity and the regression coefficient were  $-1.07 (\pm 0.10) [1/\mu\text{M}]$  and  $R^2 = 0.94$ , respectively. At  $S/N = 3$ , the LOD was  $86.5 (\pm 4.6) \text{ nM CIL}$ .

Under the same solution conditions, the DPV peak current changes (Figure 4.1-7b and curve 6" in Figure 4.1-7c) and the charge transfer resistance changes (Figure 4.1-7e and curve 6<sup>V</sup> in Figure 4.1-7f) for the nanoNIPs immobilized in the polytyramine film were much smaller than those for the nanoMIPs yielding smaller apparent sensitivity of  $0.27 (\pm 0.004) 1/\log [\mu\text{M}]$  and  $-0.07 (\pm 0.02) [1/\mu\text{M}]$ , respectively. These results indirectly confirm the presence in nanoMIPs of imprinted cavities that enhance CIL binding. Furthermore, the apparent imprinting factor, estimated from the ratio of the slopes of CIL calibration plots for the nanoMIPs and nanoNIPs film-coated electrodes, was for DPV surprisingly low ( $IF = 1.34$ ) and for EIS appreciably high ( $IF = 15.28$ ). This discrepancy might arise from different effects contributing to the signals measured with each technique.

#### **4.1.3.8 Determining isotherm parameters of polytyramine-(nanoMIP-A) binding of cilostazol**

Efforts were extended to determine the parameters of CIL binding by CIL-extracted nanoMIPs embedded in the polytyramine film. Typically, the Langmuir, Freundlich, and Langmuir-Freundlich isotherms<sup>363–365</sup> most accurately describe this binding. Therefore, herein, these three isotherms were tested to describe the ferrocene normalized DPV peak current dependence on the CIL concentration in the ferrocene solution alone (Figure 4.1-8a) and the human plasma (Figure 4.1-8b). The Langmuir-Freundlich isotherm best fits the experimental data of CIL sorption on nanoMIPs (Tables 4.1-2 and 4.1-4), indicating that the imprinted cavities were

relatively homogeneously distributed in the polytyramine matrix, and the CIL analyte was chemisorbed in these cavities.

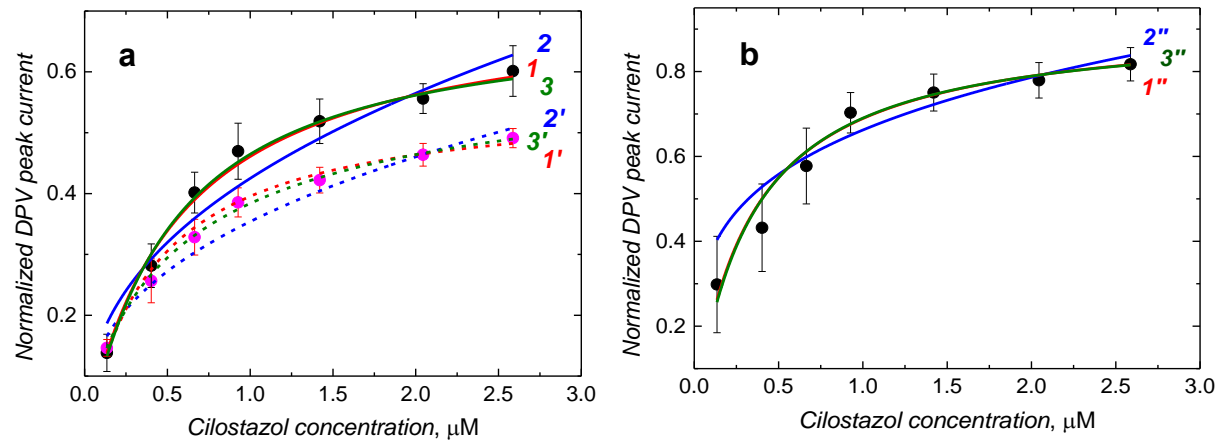


**Figure 4.1-8.** The (curves 1, 1', and 1'') Langmuir (red), (curves 2, 2', and 2'') Freundlich (blue), and (curves 3, 3', and 3'') Langmuir-Freudlich (green) isotherm fitting to the normalized DPV peak current change with the CIL concentration change (a) for (curves 1, 2, and 3) CIL-extracted nanoMIPs (solid curves) and (curves 1', 2', and 3') nanoNIPs (dash curves) in 10 mM ferrocene and 0.1 M (TBA)ClO<sub>4</sub> in acetonitrile, and (b) for (curves 1'', 2'', and 3'') CIL-extracted nanoMIPs in the ten times diluted human plasma in 10 mM ferrocene and 0.1 M (TBA)ClO<sub>4</sub> in acetonitrile. The nanoparticles were immobilized in polytyramine films, deposited on 2-mm diameter Au disk electrodes.

**Table 4.1-2.** Isotherms' parameters for the nanoMIP chemosensor fitted to the normalized DPV current vs. CIL concentration curves in acetonitrile (curves 1, 2, and 3 in Figure 4.1-8a).

Isotherm type	Isotherm equation	Isotherm fitting parameters			$R^2$
		$\Delta I_{\text{normalized DPV}}$ DPV,max	$K, \mu\text{M}^{-1}$	$n_h$	
Langmuir	$\Delta I_{\text{normalized DPV}} = \Delta I_{\text{normalized DPV,max}} \frac{K_L c_{\text{CIL}}}{1 + K c_{\text{CIL}}}$	0.72 ( $\pm 0.02$ )	1.77 ( $\pm 0.15$ ) <sup>a</sup>	-	0.993
Freundlich	$\Delta I_{\text{normalized DPV}} = K_F c_{\text{CIL}}^n$	-	0.42 ( $\pm 0.02$ ) <sup>b</sup>	2.43 ( $\pm 0.30$ ) <sup>d</sup>	0.946
Langmuir-Freudlich	$\Delta I_{\text{normalized DPV}} = \Delta I_{\text{normalized DPV,max}} \frac{(K_{LF} c_{\text{CIL}})^n}{1 + (K_{LF} c_{\text{CIL}})^n}$	0.69 ( $\pm 0.04$ )	1.94 ( $\pm 0.30$ ) <sup>c</sup>	1.07 ( $\pm 0.12$ ) <sup>e</sup>	0.993

$\Delta I_{\text{normalized DPV,max}}$  – maximum value of normalized DPV peak current, <sup>a</sup>  $K_L$  – Langmuir constant,

<sup>b</sup>  $K_F$  – Freundlich constant, <sup>c</sup>  $K_{LF}$  – Langmuir-Freudlich constant, <sup>d</sup> Sorption intensity, <sup>e</sup>  $n_h$  - Homogeneity factor.

Moreover, the cavities homogeneity was high. Interestingly, the homogeneity factor was substantially higher for nanoMIPs (1.07) than for nanoNIPs (0.80). Expectedly, this difference in factors indicates that CIL binding in nanoNIPs encompasses a broader range of non-equivalent binding sites.

#### **4.1.3.9 Polytyramine-(nanoMIP-A) chemosensor selectivity to dhCIL metabolite and common interferences**

The nanoMIP-A molecular cavity's selectivity to the dhCIL metabolite and common interferences in acetonitrile was estimated as the ratio of the slopes of the calibration plot for CIL to that of dhCIL or that of the interference. Notably, the selectivity to dhCIL (Table 4.1-3) was low (curves 1'' and 2'' in Figure 4.1-7c, and curves 1<sup>V</sup> and 2<sup>V</sup> in Figure 4.1-7f). Thus, the chemosensor is advantageous for determining the CIL analyte and its dhCIL metabolite together. The selectivity to cholesterol (curves 1'' and 4'' in Figure 4.1-7c, and curves 1<sup>V</sup> and 4<sup>V</sup> in Figure 4.1-7f) and glucose (curves 1'' and 5'' in Figure 4.1-7c, and curves 1<sup>V</sup> and 5<sup>V</sup> in Figure 4.1-7f) was relatively high (Table 4.1-3) whereas to dehydroaripiprazole (curves 1'' and 3'' in Figure 4.1-7c, and curves 1<sup>V</sup> and 3<sup>V</sup> in Figure 4.1-7f) it was moderate.

**Table 4.1-3.** The DPV and EIS determined nanoMIP-A cavity selectivity to metabolite dhCIL and interferences, the sorption constant ( $K_{LF}$ ) calculated from the Langmuir-Freundlich isotherm, and the calculated Gibbs free energy change ( $\Delta G_{bind}$ ) accompanying complexation of the nanoMIP-A model cavity with CIL, dhCIL, and the interferences.

Compound	Experimental selectivity		$\Delta G_{bind}$ (kJ/mol)	Sorption constant $K_{LF}$
	DPV	EIS		
CIL	-	-	-192.20	1.94 ( $\pm 0.29$ )
dhCIL	~1.13	0.8	-173.16	0.52 ( $\pm 0.34$ )
3,4-Dehydroaripiprazol	3.50	3.9	-104.15	$1.23 \times 10^{-6}$ ( $\pm 3.7 \times 10^{-4}$ )
Cholesterol	7.90	Very high	-111.98	$5.66 \times 10^{-7}$ ( $\pm 1.8 \times 10^{-4}$ )
Glucose	9.00	9.7	-117.70	$0.71 \times 10^{-3}$ ( $\pm 0.05$ )

Next, the CIL and dhCIL analyte and interference molecules' interactions with the nanoMIP-A cavity were compared theoretically to enlighten the properties of the prepared chemosensor. To sum up, the interferences' molecules were located in the nanoMIP-A cavity

in a way different from that of the CIL molecules because they were too large or too small. Therefore, their interactions with the cavity are much weaker than those of CIL molecules. Hence, the interferences would not disturb the CIL and dhCIL determination together.

#### 4.1.3.10 Polytyramine-(nanoMIP-A) chemosensor efficiency of CIL determination in real samples

It is crucial for chemosensors' clinical applications to determine their performance in body fluids, such as human plasma, to estimate the matrix's effect. Toward that, gold electrodes coated with polytyramine films embedding CIL-extracted nanoMIP-A were herein employed to determine CIL in plasma samples. Accordingly, a plasma sample (with citrate as the anticoagulant) was ten times diluted with the acetonitrile solution of 10 mM ferrocene. That resulted in the precipitation of proteins, which were then centrifuged off. Then, samples of this solution were spiked with solutions of CIL of different concentrations. The UV-vis spectra recorded for the supernatant solutions to estimate possible CIL interaction with the plasma proteins showed only a negligible CIL binding to the proteins, which then precipitated during the dilution (Figure 4.1-9). Thus, a significant amount of CIL remained in the diluted plasma solution.

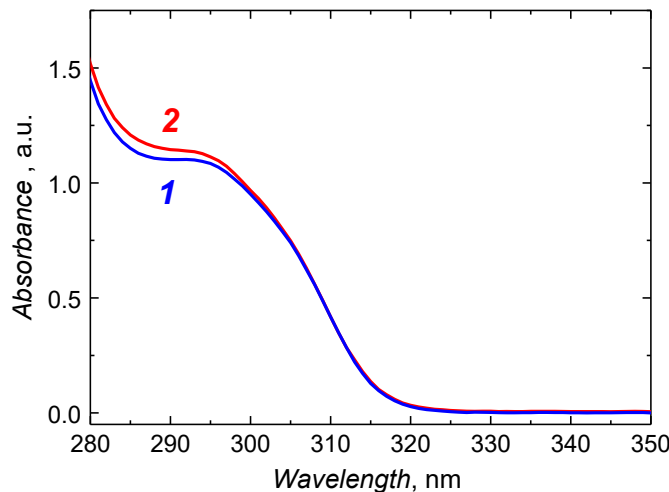


**Figure 4.1-9.** The UV spectrum of (curve 1) CIL in the supernatant solution after plasma dilution, and (curve 2) CIL in the supernatant in the acetonitrile : water (9 : 1, v/v) mixed-solvent solution.

Notably, the chemosensor appeared successful in determining CIL in diluted human plasma samples (curve *I* in Figure 4.1-10a and curve *I'* in Figure 4.1-10b). Moreover, the slope of 0.39 ( $\pm 0.04$ ) [1/log  $\mu\text{M}$ ] for the calibration plot constructed only slightly deviated from that of 0.33 ( $\pm 0.02$ ) [1/log  $\mu\text{M}$ ] in the acetonitrile-water mixture (9 : 1, *v/v*) (curve 2 in Figure 4.1-10a and curve 2' in Figure 4.1-10b), respectively.

**Table 4.1-4.** Isotherm parameters for the nanoMIP chemosensor fitted to the normalized DPV peak current vs. CIL concentration in human plasma depicted in curves *I''*, *2''*, and *3''* in Figure 4.1-8b.

Isotherm type	Isotherm equation	Isotherm fitting parameters			$R^2$
		$\Delta I_{\text{normalized}}$ DPV,max	$K, \mu\text{M}^{-1}$	$n$	
Langmuir	$\Delta I_{\text{normalized DPV}} = \Delta I_{\text{normalized DPV,max}} \frac{K_L c_{\text{CIL}}}{1 + K c_{\text{CIL}}}$	0.92 ( $\pm 0.03$ )	2.94 ( $\pm 0.48$ ) <sup>a</sup>	-	0.959
Freundlich	$\Delta I_{\text{normalized DPV}} = K_F c_{\text{CIL}}^{\frac{1}{n}}$	- ( $\pm 0.02$ ) <sup>b</sup>	0.66 ( $\pm 0.77$ ) <sup>d</sup>	4.03	0.86
Langmuir-Freundlich	$\Delta I_{\text{normalized DPV}} = \Delta I_{\text{normalized DPV,max}} \frac{(K_{\text{LF}} c_{\text{CIL}})^n}{1 + (K_{\text{LF}} c_{\text{CIL}})^n}$	0.91 ( $\pm 0.07$ )	2.96 ( $\pm 0.58$ ) <sup>c</sup>	1.02 ( $\pm 0.25$ ) <sup>e</sup>	0.949

$\Delta I_{\text{normalized DPV,max}}$  – maximum value of normalized DPV peak current,

<sup>a</sup>  $K_L$  – the Langmuir constant,

<sup>b</sup>  $K_F$  – the Freundlich constant,

<sup>c</sup>  $K_{\text{LF}}$  – the Langmuir-Freundlich constant,

<sup>d</sup> Sorption intensity,

<sup>e</sup>  $n_h$  - Homogeneity factor.

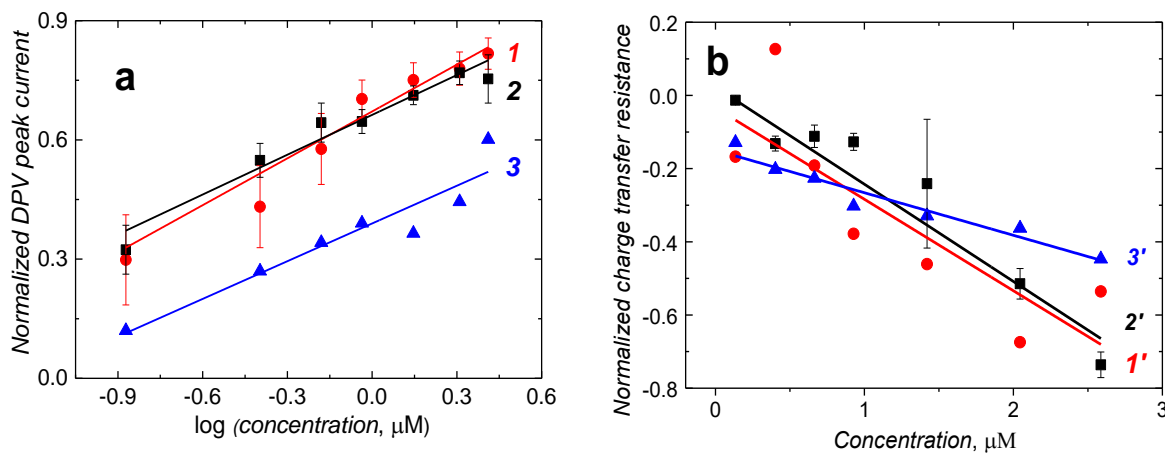


**Figure 4.1-10.** (a) DPV and (b) EIS calibration plots for CIL determination at Au electrodes coated with polytyramine films containing CIL-extracted nanoMIPs in 10 mM ferrocene and 0.1 M (TBA) $\text{ClO}_4$  in (curves 1 and 1') human plasma 10 times diluted with acetonitrile, (curves 2 and 2') the acetonitrile-water (9 : 1, v/v) solution, and (curves 3 and 3') for dhCIL determination in human plasma 10 times diluted with acetonitrile.

**Table 4.1-5.** Results of CIL determination in human plasma with the nanoMIP-A film-coated electrode from the DPV calibration plot.

Sample No.	Concentration of added cilostazol, $\mu\text{M}$	Normalized DPV peak current	Calculated cilostazol concentration, $\mu\text{M}$	Recovery, %
1	0.13	0.32 ( $\pm 0.11$ )	0.09 ( $\pm 3 \times 10^{-6}$ )	69.2 ( $\pm 22.1$ )
2	0.40	0.51 ( $\pm 0.10$ )	0.35 ( $\pm 1 \times 10^{-6}$ )	87.5 ( $\pm 21.7$ )
3	0.66	0.60 ( $\pm 0.09$ )	0.66 ( $\pm 0.001$ )	100.0 ( $\pm 19$ )
4	0.92	0.65 ( $\pm 0.05$ )	0.93 ( $\pm 0.003$ )	101.0 ( $\pm 19.9$ )
5	1.42	0.72 ( $\pm 0.04$ )	1.51 ( $\pm 1.20$ )	106.3 ( $\pm 15.8$ )
6	2.04	0.79 ( $\pm 0.04$ )	2.45 ( $\pm 1.13$ )	120.0 ( $\pm 13.4$ )
7	2.58	0.83 ( $\pm 0.04$ )	3.23 ( $\pm 1.06$ )	125.1 ( $\pm 11.4$ )

Average recovery: 101.4 ( $\pm 17.6$ )  
No. of repetitions,  $n = 3$

The calculated recovery (Table 4.1-5) was adequate for sensing CIL and dhCIL in human plasma samples by the prepared chemosensor. Similarly, chemosensor performance appeared

superior for cilostazol determination in the 100 times diluted synthetic Nortrol serum (Figure A-4).

#### **4.1.4 Summary and conclusions**

The DPV and EIS chemosensors for CIL and its dhCIL pharmacologically active primary metabolite determination, aided by molecular imprinting in polymers, were devised, fabricated, and compared. Four different types of molecularly imprinted with CIL polymer nanoparticles (nanoMIPs) were synthesized and examined at various functional monomers combinations. The CIL binding capacity was the highest if methacrylic acid was exclusively used as the functional monomer. The resulting nanoMIP-A particles were then successfully embedded by sedimentation, followed by tyramine electropolymerization, in a polytyramine film deposited on an Au electrode surface. Both DPV and EIS chemosensors appeared suitable for determining CIL and dhCIL with the LOD of 93.5 ( $\pm 2.2$ ) and 86.5 ( $\pm 4.6$ ) nM CIL, respectively, in the linear dynamic concentration range of 0.135 to 2.58  $\mu$ M, and appreciably high selectivity to common interferences including cholesterol, glucose, and moderate to dehydroaripiprazole. Remarkably, these relatively low LOD values for the CIL drug substance have not yet been reported for any electrochemical method of CIL determination.

Computer simulations permitted analyzing the interactions governed by the analytes' sorption at the molecular level. The Langmuir-Freundlich isotherm best fitted the experimental data of CIL sorption on nanoMIPs, indicating that the imprinted cavities were relatively homogeneously distributed in the MIP matrix with the CIL molecules chemisorbed in these cavities.

#### **4.1.5 Future prospective**

We have demonstrated that the chemosensors fabricated may help diagnostics within the CIL and dhCIL concentration ranges in body fluids required in the future clinical trials of CIL. Our future research will aim to make the chemosensors reusable and to cross-validate their performance with LC-MS, GC-MS, etc.

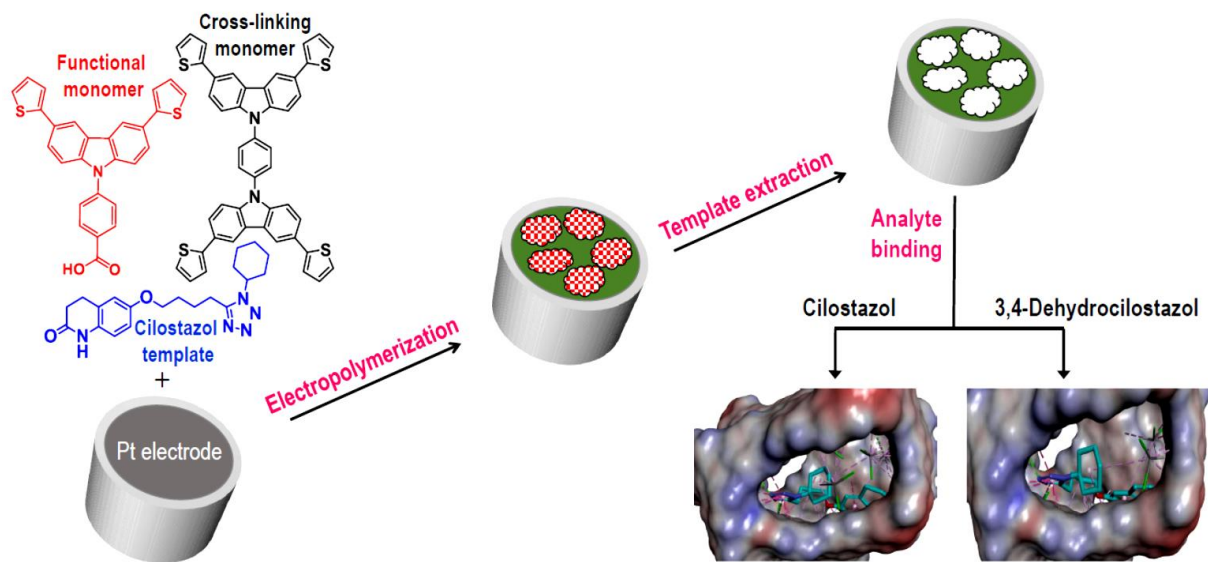
## **4.2 Cilostazol-imprinted polymer film-coated electrode as an electrochemical chemosensor for selective determination of cilostazol and its active primary metabolite**

The present Section 4.2 of Chapter 4 discusses the research work partially described in *J. Mater. Chem. B*, **2022**, advanced paper, DOI: [10.1039/d1tb02186a](https://doi.org/10.1039/d1tb02186a).

### **Abstract**

An electrochemical chemosensor for cilostazol (CIL) determination was devised, engineered, and tested. For that, a conducting film of the functionalized thiophene-appended carbazole-based polymer, molecularly imprinted with CIL (MIP-CIL), was potentiodynamically deposited on a Pt disk electrode by oxidative electropolymerization. Thanks to electro-oxidation potentials lower than that of CIL, the carbazole monomers outperformed pyrrole, thiophene, and phenol monomers, in this electropolymerization. The pre-polymerization complexes quantum-mechanical and molecular dynamics analyses allowed selecting the most appropriate monomer from the three thiophene-appended carbazoles examined. The MIP film-coated electrode was then used as a selective CIL chemosensor in the linear dynamic concentration range of 50 to 924 nM with a high apparent imprinting factor,  $IF = 10.6$ . The MIP-CIL responded similarly to CIL and CIL's pharmacologically active primary metabolite, 3,4-dehydrocilostazol (dhCIL), thus proving suitable for their determination together. Simulated models of the MIP cavities binding of the CIL, dhCIL, and interferences molecules allowed predicting chemosensor selectivity. The MIP film sorption of CIL and dhCIL was examined using DPV by peak current data fitting with the Langmuir (L), Freundlich (F), and Langmuir-Freundlich (LF) isotherms. The LF isotherm best described this sorption with the sorption equilibrium constant ( $K_{LF}$ ) for CIL and dhCIL of  $12.75 \times 10^{-6}$  and  $0.23 \times 10^{-6}$  M, respectively. Moreover, the chemosensor cross-reactivity to common interferences study resulted in the selectivity to cholesterol and dehydroaripiprazole of 1.52 and 8.0, respectively. The chemosensor proved useful for determining CIL and dhCIL in human plasma with appreciable recovery (99.3-134.1%) and the LOD of 15 nM.

## Graphical abstract



## 4.2.1 Introduction

Our present study aims at engineering an MIP electrochemical chemosensor suitable as a potential point-of-care (PoC) tool to determine the CIL concentration in human plasma. Accordingly, we have successfully imprinted CIL in a functionalized (thiophene-appended carbazole)-based conducting MIP and simultaneously deposited it on an electrode surface as a thin film via potentiodynamic electropolymerization. Being user-friendly, selective, sensitive, and allowing for the early detection of many disease symptoms,<sup>366,367</sup> electrochemical MIP-based chemosensors can serve as attractive PoC tools.

Potentiodynamic electropolymerization is a well-established technique providing a homogenous polymer film coating a transducer, i.e., an electrode in our study. Likewise, the deposited CIL-templated MIP (MIP-CIL) film was then used as a recognition unit of an electrochemical chemosensor. Here, we overcome challenges encountered in our previous work<sup>300</sup> by achieving a lower LOD, lower linear dynamic concentration range, ease of sensor preparation, and cross-validation of CIL and dhCIL in a test solution and the CIL and dhCIL spiked human plasma by LC-MS. The CIL-extracted MIP-CIL affinity to analytes and interferences was computationally modeled with the complexation and sorption processes' molecular dynamics (MD) simulations.

## 4.2.2 Experimental and procedures

Preparation of CIL-imprinted and non-imprinted polymer films and their deposition on the electrodes are discussed in Chapter 2. All CV and DPV measurements were performed at room temperature, 20 ( $\pm 1$ ) °C, using the electrochemical mini cell and 10-mM ferrocene redox probe in 0.1 M (TBA)ClO<sub>4</sub>, in DCM. In the DPV measurements, the potential was scanned from 0 to 0.70 V vs. Ag/AgCl with the potential step of 5 mV. The amplitude of 50-ms pulses applied was 25 mV.

### 4.2.2.1 Preparing human plasma samples

Stock solutions of 1.0 mg mL<sup>-1</sup> CIL and 0.1 mg mL<sup>-1</sup> dhCIL were prepared by dissolving weighed portions of the CIL and dhCIL reference standards in methanol. Working solutions were prepared by diluting stock solutions with the mixed methanol : 0.1% formic acid (1 : 1,

*v/v*) solution. Human plasma samples (with the citrate anticoagulant added) were prepared by spiking the blank plasma with the appropriate working solution at a volume ratio of 12.5 : 1. The CIL concentration ranged from 27.1 to 8120 nM in the human plasma sample, whereas the dhCIL concentration in this sample was 81.6 nM (Table 4.2-4). The samples were split into two parts for simultaneous CIL and dhCIL determining with the MIP-film electrochemical chemosensing and LC-MS.

#### **4.2.2.2 Cilostazol (CIL) and 3,4-dehydrocilostazol (dhCIL) determining in human plasma with LC-MS**

In human plasma, CIL and dhCIL were determined using LC-MS. The liquid-liquid extraction with a mixed solvent solution of 1-butanol : chloroform: *tert*-butyl methyl ether (3 : 20 : 77, *v/v/v*) was used for sample preparation. The sample components were separated using LC-MS on the Zorbax SB-C18 150 × 3.0 mm, 3.5 µm column (Agilent Technologies, USA) at 50 ( $\pm 2$ ) °C. A mixed solvent solution of 0.01% formic acid, methanol, and acetonitrile (50 : 25 : 25, *v/v/v*) served as the mobile phase. Positive electrospray ionization mass spectrometry was applied with a single-ion monitoring mode to determine CIL and dhCIL. Isotope-labeled CIL (cilostazol-d11) was used as the internal standard. CIL ions, the internal standard, and dhCIL were monitored at the respective *m/z* ratio of 370.1, 381.1, and 368.0. The complete analysis run time was 10 min. The method was validated, and the study was performed in compliance with the OECD Principles of Good Laboratory Practice.

#### **4.2.2.3 Cilostazol (CIL) and 3,4-dehydrocilostazol (dhCIL) determining in human plasma using MIP chemosensor**

The plasma samples of known CIL concentration, determined with LC-MS, were thawed in air and then diluted with DCM. Next, the resulting mixture was vortexed (3000 rpm) for a few minutes and then left to separate the organic and aqueous phases. Afterward, the organic phase was collected, then centrifuged for 10 min at 10,000  $g_g$  to separate the slug. The supernatant solution samples, 3518.6 and 8120 nM in CIL (Sample Nos. 4 and 5 in Table 4.2-4), were diluted 10 times. However, samples 27.1, 81.2, and 676.7 nM in CIL and 81.6 nM in dhCIL were not diluted at all. To each sample, (TBA)ClO<sub>4</sub> and the ferrocene redox probe were added to reach the 0.1 M and 10 mM concentrations, respectively. A 1-mL sample of the above ferrocene solution was placed in an electrochemical mini cell. The MIP-CIL film-coated

electrode was immersed in this solution, and the DPV current was measured. The resulting changes in the DPV peak currents were then used for constructing calibration plots and calculating recovery.

### 4.2.3 Results and discussion

#### 4.2.3.1 Selecting functional monomers

Chemosensors with an MIP film as the recognition unit should recognize the target analyte with sufficient selectivity, detectability, and sensitivity. That is only possible if the analyte appropriately interacts with the MIP. Interactions in the pre-polymerization complex solution can define MIP properties, and its components can already be selected at this stage. Toward that, three pre-polymerization complexes (PPCs) consisting of CIL, FM1, or FM2, or FM3, and CLM in DCM were constructed. The resulting PPC1 model containing FM1, of the highest negative energy ( $\Delta G_C = -400.99 \text{ kJ/mol}$ ) is shown in Figure 4.2-1, and the less favorable models of PPC2 and PPC3 containing FM2 and FM3 resulted in  $\Delta G_C$  of -376.48 and -384.13 kJ/mol, respectively. All functional monomers complexed CIL quite strongly, but that formed by FM1 was the most stable. Comparing intermolecular interactions in all systems helps explain favorable complex features. Furthermore, PPC1 was selected for modeling the polymer cavity and sorption of the analytes.

#### 4.2.3.2 Electrochemical characterizing of CIL as well as functional and cross-linking monomers

Before the electropolymerization, it is vital to determine the electro-oxidation potential of each of its components, vis., the CIL template, and the functional and cross-linking monomers. This information enables choosing monomers with electro-oxidation potential lower than that of the template to avoid CIL template electro-oxidation during electropolymerization. It transpired that CIL was electro-oxidized at 1.13 V vs. Ag quasi-reference electrode (Figure 4.2-2a), while the selected functional and cross-linking monomers were electroactive at 0.93 and 0.92 V vs. Ag quasi-reference electrode, respectively (Figure 4.2-2b and 2c).

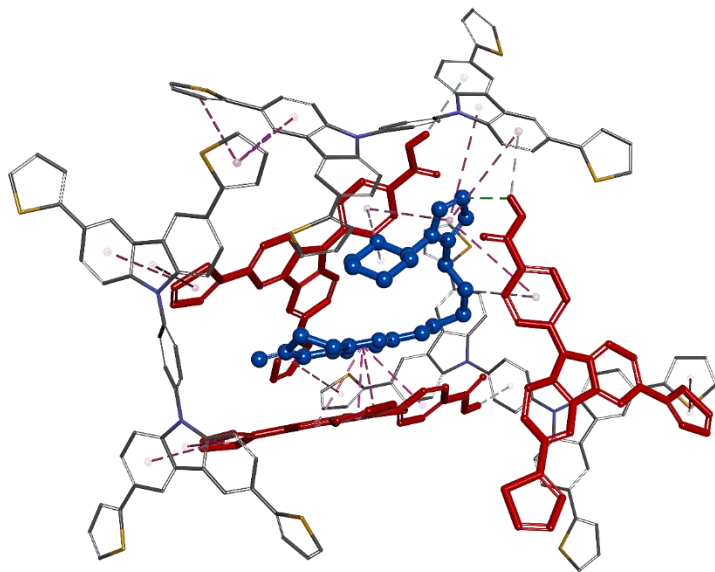


**Figure 4.2-1.** A computer-simulated PPC1 skeleton model of the pre-polymerization complex of CIL with FM1 and CLM at the molar ratio of 1 : 3 : 3 in DCM. Significant intermolecular interactions are indicated with dashed lines.

These monomers have scarcely been exploited in the MIP research despite their ability of facile derivatization. Because their electro-oxidation potentials are lower than the CIL electro-oxidation potential, they outperform pyrrole, thiophene, and phenol monomers in the electropolymerization studied.

#### 4.2.3.3 Simultaneous depositing and characterizing the MIP and NIP films

After preparing the pre-polymerization complexes in solutions, those were electropolymerized under potentiodynamic conditions to deposit MIP and NIP films on Pt electrodes. Two consecutive potential cycles in the range of 0 and 1.0 V vs. Ag quasi-reference electrode were executed to maintain the oxidation potential below that of CIL electro-oxidation (Figure 4.2-2d). During the first cycle, the anodic peak was formed at 0.90 V vs. Ag quasi-reference electrode. In the second cycle, one broad cathodic and one broad anodic peak emerged at potentials between 0.45 and 0.75 V and between 0.40 and 0.80 V vs. Ag quasi-reference electrode, respectively. The anodic peaks may arise from the formation of the cationic radicals of the deposited polymer films. Moreover, the current increase in each consecutive cycle indicates the deposition of the increasing amounts of the conducting polymer. Notably, it was necessary to roughen the electrode surface for enhancing polymer film adhesion. To this end,

the Pt electrode was matted with 1000 grit sandpaper. Films deposited on electrodes pre-treated that way were mechanically stable.

Furthermore, successful deposition of a stable MIP film was confirmed by changes in faradaic currents using the DCM solution of the ferrocene redox probe (Figure 4.2-2). That is, CV peak-to-peak potential separation for the polymer film-coated electrode (curve 2 in Figure 4.2-2e) was larger than that for the bare Pt electrode (curve 1 in Figure 4.2-2e) and, consequently, the DPV peak current for the polymer film-coated electrode (curve 2' in Figure 4.2-2f) was significantly smaller than that for the bare Pt electrode (curve 1' in Figure 4.2-2f).

#### 4.2.3.4 Characterizing deposited MIP and NIP films

Finally, CIL was extracted from the MIP-CIL film with 10 mM NaOH for 30 min. This extraction resulted in a significant decrease in the DPV peak current of the redox probe. The PM-IRRAS measurements were subsequently performed to confirm CIL template removal from the MIP (Figure 4.2-3). Weak bands at  $\sim 3065$ ,  $\sim 2965$   $\text{cm}^{-1}$ , and  $2877$   $\text{cm}^{-1}$  in the spectra of all deposited films may be assigned to C-H bond stretching vibration in aromatic and aliphatic moieties, respectively. Moreover, a well-pronounced band at  $1725$   $\text{cm}^{-1}$  was present in the spectra of all films. It originated from C=O bond stretching, confirming successful copolymerization and deposition of all monomers in the pre-polymerization complex solution. This inference is supported by the presence of the  $1515$   $\text{cm}^{-1}$  band corresponding to C-C aromatic ring stretching and a  $1604$   $\text{cm}^{-1}$  band characteristic for C-C stretching of the carbazole moiety. However, a low-intensity band in the  $620 - 700$   $\text{cm}^{-1}$  region was not evident in the MIP film's spectrum before extraction. The MIP film was relatively thin, and therefore, its CIL content was low compared to the monomers' contents. Therefore, presumably, this band is suppressed when CIL interacts with the polymer film.

However, it appeared in both the MIP and NIP film spectrum after CIL extraction. That confirms the template CIL presence in the deposited MIP film, then its successful extraction.

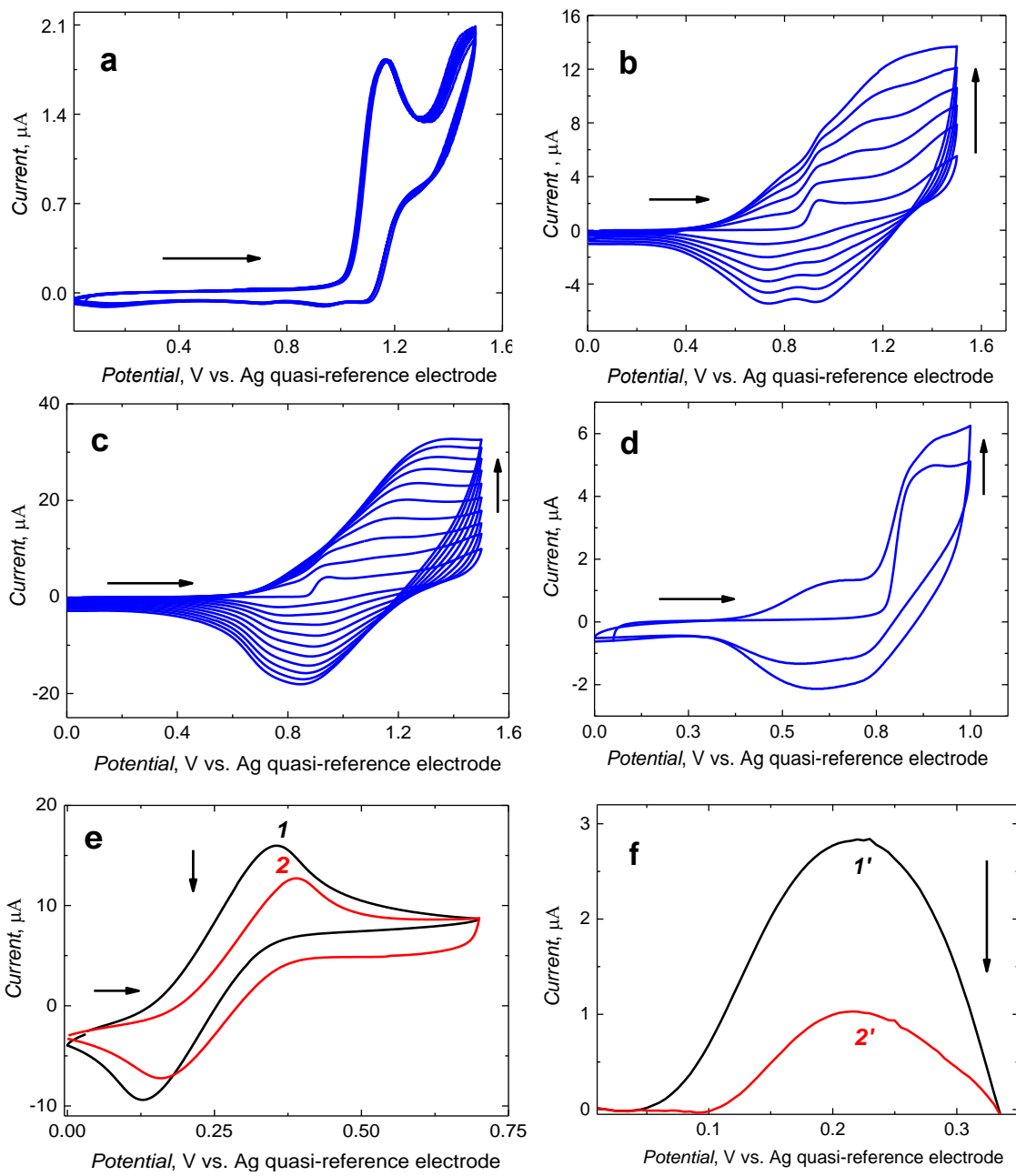


**Figure 4.2-2.** Multi-cyclic potentiodynamic curves recorded at the 0.75-mm diameter Pt disk electrode at a 100-mV s<sup>-1</sup> scan rate for (a) 1 mM CIL, (b) 1 mM FM1, (c) 1 mM CLM, and (d) the two-cycle potentiodynamic curve for MIP film deposition; a DCM solution of 0.1 mM CIL, 0.3 mM FM1, 0.3 mM CLM, and 0.1 M (TBA)ClO<sub>4</sub> was used for this deposition. The (e) CV and (f) background corrected DPV curves for 10 mM ferrocene and 0.1 M (TBA)ClO<sub>4</sub> in DCM on (curves 1 and 1') the bare electrode, and (curves 2 and 2') the MIP-CIL film-coated electrode.

The 2-D surface topography of the films deposited on Au film-layered glass slides was analyzed at different stages of the MIP and NIP films preparation, i.e., the electrode coated with (i) the CIL-templated MIP film, (ii) the MIP-CIL film, and (iii) the NIP film. The deposited films were homogeneous, being composed of triangular and rectangular grains. The AFM determined MIP film thickness and roughness were 96 ( $\pm 2$ ) and 12.7 ( $\pm 0.3$ ) nm, respectively. The CIL removal from the MIP further decreased film thickness to 69 ( $\pm 5$ ) nm while the roughness increased to 13.8 ( $\pm 1$ ) nm (Figure 4.2-4). Presumably, that may indicate either removal of the outermost film layer or film contraction upon CIL extraction.

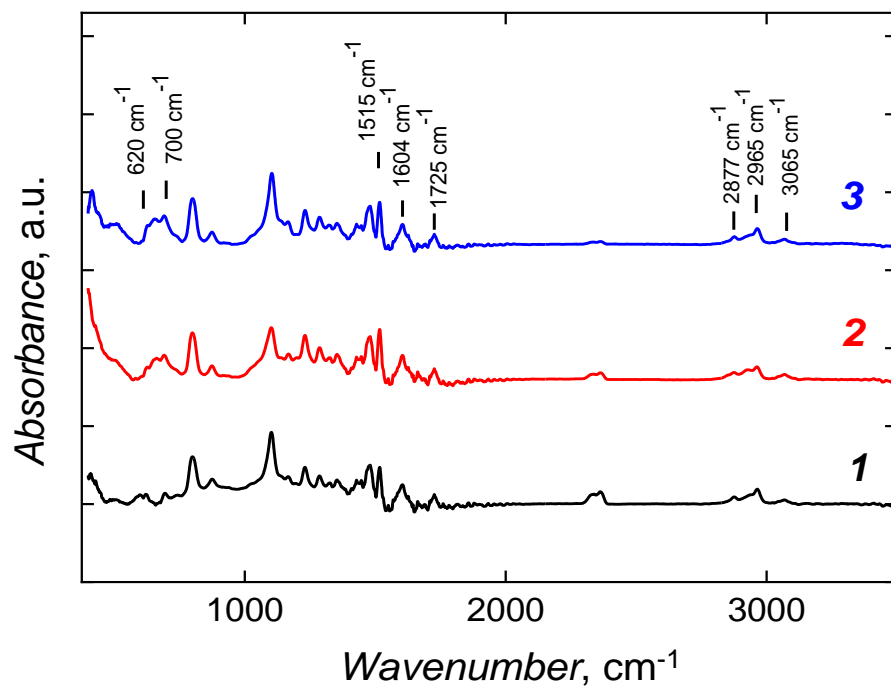


**Figure 4.2-3.** PM-IRRAS spectra for MIP film-coated electrodes (spectrum 1) before and (spectrum 2) after 30-min CIL extraction with 10 mM NaOH, and (spectrum 3) the NIP film-coated electrode.

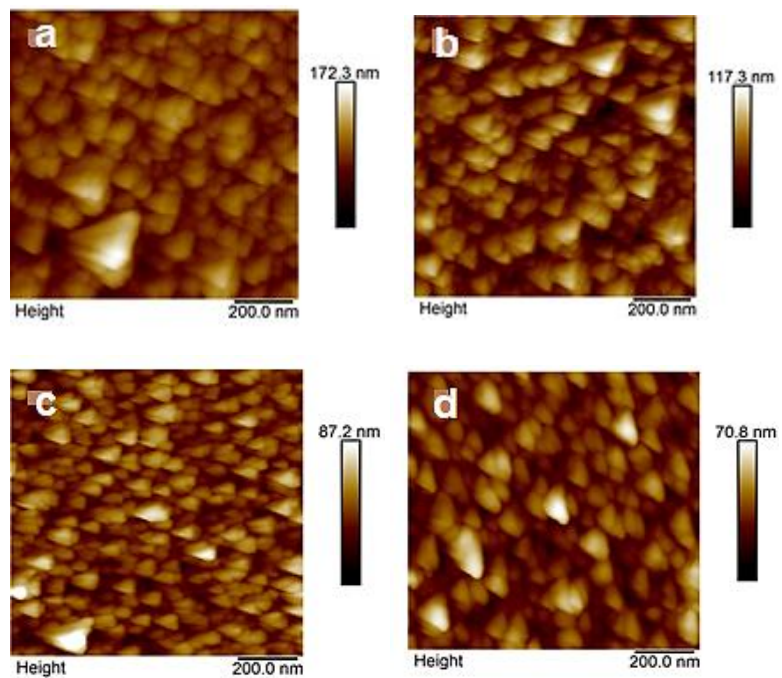


**Figure 4.2-4.** AFM images of (a) and (b) MIP and (c) and (d) NIP film-coated (glass slide)/Ti/Au electrodes (a) and (c) before, and (b) and (d) after 30-min CIL extraction with 10 mM NaOH.

The as-prepared NIP film thickness and roughness were 44 ( $\pm 6$ ) and 9.5 ( $\pm 0.1$ ) nm, respectively. Moreover, after CIL extraction, the roughness of the NIP film decreased to 7.6 ( $\pm 0.2$ ) nm, indicating the formation of a more uniform film. Generally, both MIP and NIP films were relatively uniform, being composed of irregularly shaped grains. The average sizes of the grains were quite similar for MIP and NIP films, amounting to 87 ( $\pm 24$ ) and 79 ( $\pm 20$ ) nm, respectively. CIL template extraction affected only negligibly the grain size, equaling 86 ( $\pm 24$ ) and 83 ( $\pm 22$ ) nm for the MIP and NIP film, respectively.

#### 4.2.3.5 Electrochemical determining of CIL using MIP-CIL film-coated electrodes

After CIL addition to the ferrocene DCM solution, CIL molecules interacted with complementary recognition cavities of the MIP-CIL film, thereby decreasing the DPV peak of ferrocene (Figure 3a), as a result of the so-called "gate effect".<sup>304,355</sup> This current decrease was more pronounced at higher CIL concentrations (Figure 4.2-5a, curves 1 - 7).

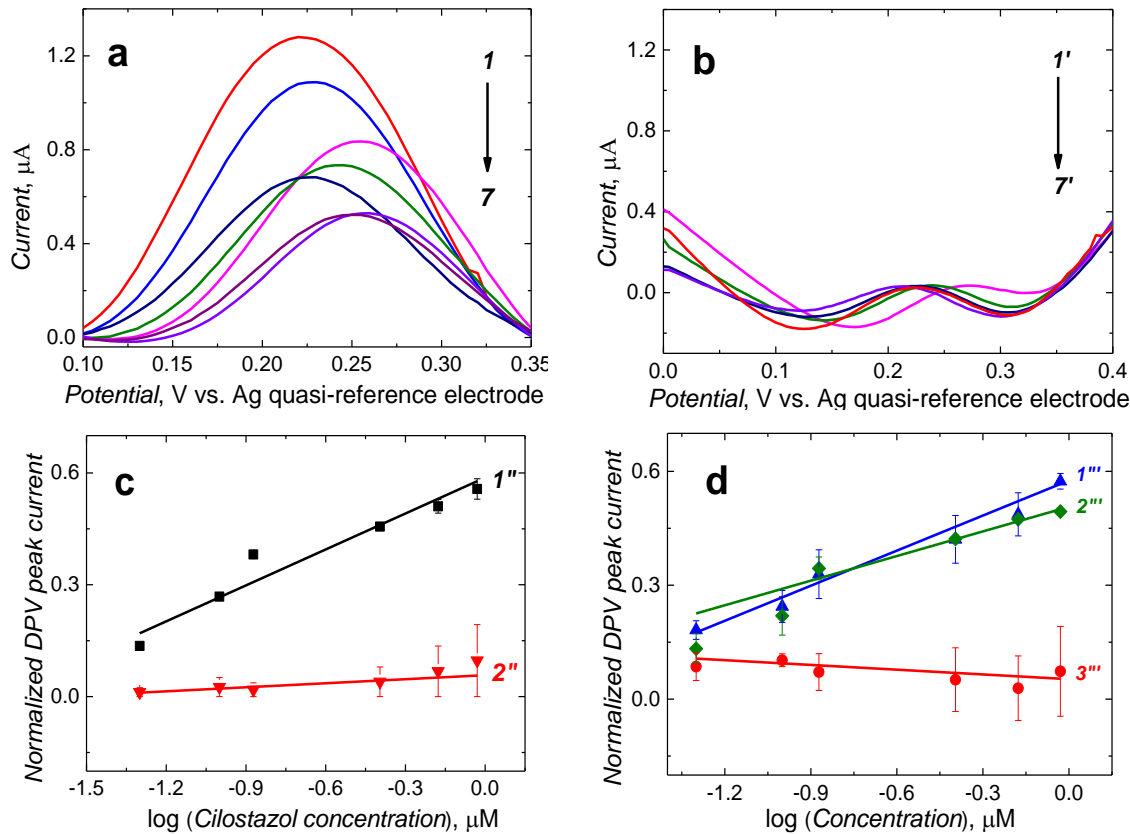


**Figure 4.2-5.** Background corrected DPV curves for the (a) MIP (curves 1 - 7) and (b) NIP (curves 1' - 7') film-coated 0.75-mm diameter Pt disk electrodes after CIL extraction, in (curves 2 and 2') 50, (curves 3 and 3') 99.8, (curves 4 and 4') 134, (curves 5 and 5') 402, (curves 6 and 6') 665.9, and (curves 7 and 7') 923.6 nM CIL in 10 mM ferrocene and 0.1 M (TBA) $\text{ClO}_4$  in DCM. (c) DPV calibration plots for the electrodes coated with the film of (curve 1'') MIP-CIL and (curve 2'') NIP. (d) DPV calibration plots for MIP-CIL film-coated electrode for (curve 1''') dhCIL, (curve 2''') cholesterol, (curve 3''') dehydroaripiprazole in 10 mM ferrocene and 0.1 M (TBA) $\text{ClO}_4$  in DCM.

However, the DPV peak for the NIP film did not differ much after CIL addition (Figure 4.2-5b, curves 1' - 7'). The normalized DPV peak current,  $[(I_{\text{DPV},0} - I_{\text{DPV},s})/I_{\text{DPV},0}]$ , where  $I_{\text{DPV},0}$  and  $I_{\text{DPV},s}$  stand for the initial and actual DPV peak current, respectively], was linearly dependent on the logarithm of CIL concentration throughout the considered concentration range. A semi-logarithmic linear regression equation of  $(I_{\text{DPV},0} - I_{\text{DPV},s})/I_{\text{DPV},0} = 0.32(\pm 0.03) [1/\log \mu\text{M}] \times c_{\text{cilostazol}} [\log \mu\text{M}] + 0.58(\pm 0.02)$  describes the calibration plot (Figure 4.2-5c, curve 1''). The correlation coefficient and sensitivity were  $R^2 = 0.927$  and  $0.32 (\pm 0.03) [1/\log \mu\text{M}]$ , respectively. A linear dynamic concentration range covered 50 to 923.6 nM CIL with the LOD of 15 nM.

In the case of the NIP film-coated electrode, the normalized DPV peak currents for CIL at similar concentrations were smaller (Figure 4.2-5c, curve 2''). The sensitivity was  $0.03 (\pm 0.01) [1/\log \mu\text{M}]$ . This result indirectly confirms the successful imprinting of molecular cavities in the MIP. Accordingly, the apparent imprinting factor was relatively high,  $IF = 10.6$ . It was calculated as the ratio of slopes of calibration plots for the MIP and NIP film-coated electrodes. Common interferences encountered in body fluids were used to perform the cross-reactivity studies for estimating the molecular recognition's selectivity of the MIPs. Experimental selectivity was determined as the ratio of the slope of the calibration plot of the MIP film chemosensor for CIL to that of dhCIL or that of any interference. Favorably, the selectivity for the dhCIL was very low, vis.,  $\sim 1.06$  (Figure 4.2-5d, curve 1'') indicating that the chemosensor is not selective to dhCIL and this metabolite is likely to be determined together with CIL. That is understandable because of the only minor difference in the CIL and dhCIL structures. Advantageously, the selectivity for structurally similar dehydroaripiprazole analog (Figure 4.2-5d, curve 3'') was high, equaling 8.0. However, a low selectivity of 1.52 for cholesterol (Figure 4.2-5d, curve 2'') indicates that the chemosensor is weakly selective to this interference, presumably, because its molecule is smaller than the CIL molecule. Therefore, it can easily penetrate the cavity.

Moreover, the MIP film repeatability for the determination of CIL was examined. Five MIP film-coated electrodes were inserted in identical solutions of 50 nM CIL to determine it. The current response with the RSD value was  $1.02 (\pm 0.10) \mu\text{A}$ . Evidently, the repeatability of the MIP film-coated electrodes towards CIL was high.

#### 4.2.3.6 Chemosensor analytical performance in determining CIL and dhCIL in human plasma

Estimating the matrix effect on the chemosensors' performance is crucial for analyte determination in real samples. With that respect, an MIP film-coated electrode was applied for CIL determination in human plasma. The plasma samples spiked with CIL of known concentration, determined with LC-MS, were thawed in air and then diluted with DCM.

Remarkably, the chemosensor determined CIL and dhCIL successfully in spiked human plasma, with high recovery (Table 4.2-4). Notably, the devised chemosensor analytical parameters favorably compared with already known chemosensors. The LOD is lower, but the linear dynamic concentration range is broader only for the luminescence-based sensor.

However, this sensor was devised for CIL determination in pharmaceutical formulations and was not tested for real plasma samples. Therefore, no biological matrix effect was studied. Moreover, the determination procedure described herein is less demanding than that needed for luminescence-based chemosensing. Furthermore, the efforts were extended here to determine the parameters of CIL binding by the MIP-CIL film. Typically, Langmuir (L), Freundlich (F), and Langmuir-Freundlich (LF) isotherms most accurately describe this binding.<sup>363</sup> Therefore, these three isotherms were tested herein to describe the normalized ferrocene DPV peak current dependence on the CIL concentration in the ferrocene DCM solution (Figure 4.2-6, and Tables 4.2-1a and 4.2-1b). The LF isotherm fit to the data acquired was the best, meaning that CIL molecules predominantly interact with the imprinted cavities and not mutually with themselves and that cavity distribution is to some extent heterogenic. The homogeneity factor ( $n_h$ ) exceeding 1, determined, indicates that the sorption is favorable (Table 4.2-2). Moreover, the binding constant ( $K_{LF}$ ) calculated is reasonably high.

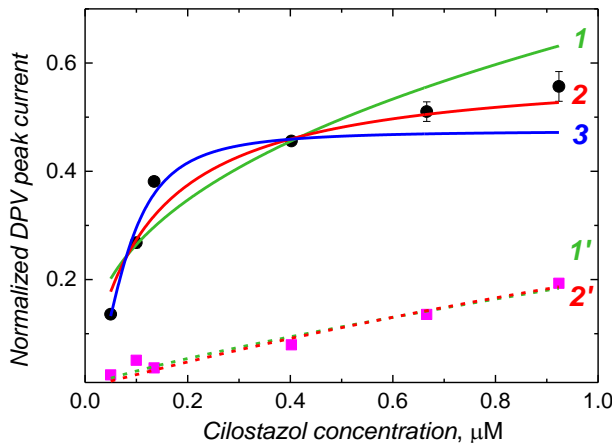


**Figure 4.2-6.** The normalized DPV peak current change with the CIL concentration change for 0.75-mm diameter Pt disk electrodes coated with the film of (curves 1, 2, and 3) CIL-extracted MIP (solid cures) and (curves 1', and 2') NIP (dash curves) in 10 mM ferrocene and 0.1 M (TBA) $\text{ClO}_4$  in DCM. The data points were fitted with the (curve 1) and (curve 1') Freundlich (green), (curve 2) and (curve 2') Langmuir (red), and (curve 3) Langmuir-Freudlich (blue) isotherms.

**Table 4.2-1a.** Parameters of isotherms fitted to the normalized DPV peak current dependence on the CIL concentration at the MIP film-coated electrode (Figure 4.2-6).

Isotherm type	Isotherm equation	Fitted isotherm parameters			
		$\Delta I_{\text{normalized}}$ DPV,max	$K, \mu\text{M}^{-1}$	$n$	$R^2$
Langmuir	$\Delta I_{\text{normalized DPV}} = \Delta I_{\text{normalized DPV,max}} \frac{K_L c_{\text{CIL}}}{1 + K_L c_{\text{CIL}}}$	0.59 ( $\pm 0.048$ )	8.53 ( $\pm 2.498$ ) <sup>a</sup>	-	0.935
Freundlich	$\Delta I_{\text{normalized DPV}} = K_F c_{\text{CIL}}^{\frac{1}{n}}$	-	0.65 ( $\pm 0.066$ ) <sup>b</sup>	2.55 ( $\pm 0.574$ ) <sup>d</sup>	0.865
Langmuir-Freundlich	$\Delta I_{\text{normalized DPV}} = \Delta I_{\text{normalized DPV,max}} \frac{(K_{LF} c_{\text{CIL}})^n}{1 + (K_{LF} c_{\text{CIL}})^n}$	0.47 ( $\pm 0.017$ )	12.72 ( $\pm 1.152$ ) <sup>c</sup>	2.09 ( $\pm 0.431$ ) <sup>e</sup>	0.971

**Table 4.2-1b.** Parameters of isotherms fitted to the normalized DPV peak current dependence on the CIL concentration at the NIP film-coated electrode (Figure 4.2-6).

Isotherm type	Isotherm equation	Fitted isotherm parameters			
		$\Delta I_{\text{normalized}}$ DPV,max	$K, \mu\text{M}^{-1}$	$n_h$ <sup>e</sup>	$R^2$
Langmuir	$\Delta I_{\text{normalized DPV}} = \Delta I_{\text{normalized DPV,max}} \frac{K_L c_{\text{CIL}}}{1 + K_L c_{\text{CIL}}}$	0.93 ( $\pm 1.181$ )	0.27 ( $\pm 0.411$ ) <sup>a</sup>	-	0.794
Freundlich	$\Delta I_{\text{normalized DPV}} = K_F c_{\text{CIL}}^{\frac{1}{n}}$	-	0.19 ( $\pm 0.013$ ) <sup>b</sup>	1.25 ( $\pm 0.177$ ) <sup>d</sup>	0.876
Langmuir-Freundlich	$\Delta I_{\text{normalized DPV}} = \Delta I_{\text{normalized DPV,max}} \frac{(K_{LF} c_{\text{CIL}})^n}{1 + (K_{LF} c_{\text{CIL}})^n}$	0.99	0.17	0.77	0.834

$\Delta I_{\text{normalized DPV}}$  – normalized DPV peak current

$\Delta I_{\text{normalized DPV,max}}$  – maximum value of normalized DPV peak current

<sup>a</sup>  $K_L$  – Langmuir constant

<sup>b</sup>  $K_F$  – Freundlich constant

<sup>c</sup>  $K_{LF}$  – Langmuir-Freundlich constant

<sup>d</sup> Sorption intensity

<sup>e</sup>  $n_h$  - Homogeneity factor

**Table 4.2-2.** Parameters of Langmuir-Freundlich isotherms, fitted to the normalized ferrocene DPV peak current dependence on the CIL, dhCIL, cholesterol, and dehydroaripiprazole concentration, for the CIL-extracted MIP film-coated electrode.

Compound	Fitted isotherm parameters			
	$\Delta I_{\text{normalized}}$ DPV,max	$K_{\text{LF}}^{\text{a}}$ , $\mu\text{M}^{-1}$	$n^{\text{b}}$	$R^2$
Cilostazol	0.47 ( $\pm 0.02$ )	12.72 ( $\pm 1.15$ )	2.09 ( $\pm 0.43$ )	0.97
3,4-Dehydrocilostazol	1.75 ( $\pm 0.25$ )	0.23 ( $\pm 0.19$ )	0.48 ( $\pm 0.19$ )	0.99
Cholesterol	0.57 ( $\pm 0.04$ )	7.29 ( $\pm 0.92$ )	0.47 ( $\pm 0.02$ )	0.97
Dehydroaripiprazole	0.19	0.0001	0.0004	No fit

<sup>a</sup>  $K_{\text{LF}}$  – Langmuir-Freundlich constant

<sup>b</sup>  $n_h$  – homogeneity factor

#### 4.2.3.7 Chemosensor selectivity calculated via simulations

The chemosensor application for analyte determination in real samples should be selective to the interferences. This issue can be modeled by simulating the analyte and interferences binding by the MIP. To this end, the cavity in the MIP-CIL model was simulated based on the PPC1 complex structure. In this model, the cavity was treated as the host for binding, separately, molecules of all guest compounds tested. The molecular structures of the cavity and the distribution of the MEP on its surface generated by the FM1 and CLM molecules are presented in Figures 4.2-7a and 4.2-7b. The neutral potential is located deep inside the cavity, while the regions with the negative (red) to positive (blue) potentials are close to the cavity edge, in heteroatoms proximity. The binding was simulated for CIL and dhCIL analytes, as well as cholesterol and dehydroaripiprazole interferences to assess the chemosensor selectivity. The optimized structures of the cavity interacting with the above guest molecules are presented in Figures 4.2-7c through 7f. The calculated Gibbs free energy change ( $\Delta G_{\text{bind}}$ ) and the experimental selectivity of the MIP-CIL to each guest compound studied are compared in Table 4.2-3. Apparently, the predicted MIP cavities affinities to CIL and dhCIL are high and similar, whereas affinities to dehydroaripiprazole and cholesterol, favorably, are much lower. The interactions within the cavity and localization of guest molecules can explain the differences in the affinities. CIL and dhCIL molecules are located in similar cavity regions,

and their conformations are almost identical. Hence, the intermolecular interactions are similar.

To sum up, the MIP-CIL can be proposed as the recognition unit of a chemosensor for selective CIL and dhCIL determination in the presence of the cholesterol and dehydroaripiprazole interferences. Moreover, the impact of solvent on the intermolecular interactions was explored. For a non-covalently imprinted polymer synthesizing, a porogen solvent is an essential factor affecting the pre-polymerization complex formation and then sorption of the analyte or interferences in the resulting MIP molecular cavities.<sup>368</sup> The herein adopted simulation strategy considering the solvent in imprinting revealed the DCM molecules' participation in intermolecular interactions with molecules of the CIL template, the FM1, and CLM monomers, and interferences.

**Table 4.2-3.** The determined MIP-CIL cavity selectivity to the dhCIL metabolite and interferences, and calculated Gibbs free energy ( $\Delta G_{\text{bind}}$ ) changes accompanying the MIP-CIL model cavity complexation of the dhCIL and the interferences.

Guest compound	DPV determined selectivity	Calculated $\Delta G_{\text{bind}}$ , kJ/mol
Cilostazol (CIL)	-	-159.29
3,4-Dehydrocilostazol (dhCIL)	~1.06	-153.77
Cholesterol	1.52	-140.75
Dehydroaripiprazole	8.00	-90.74

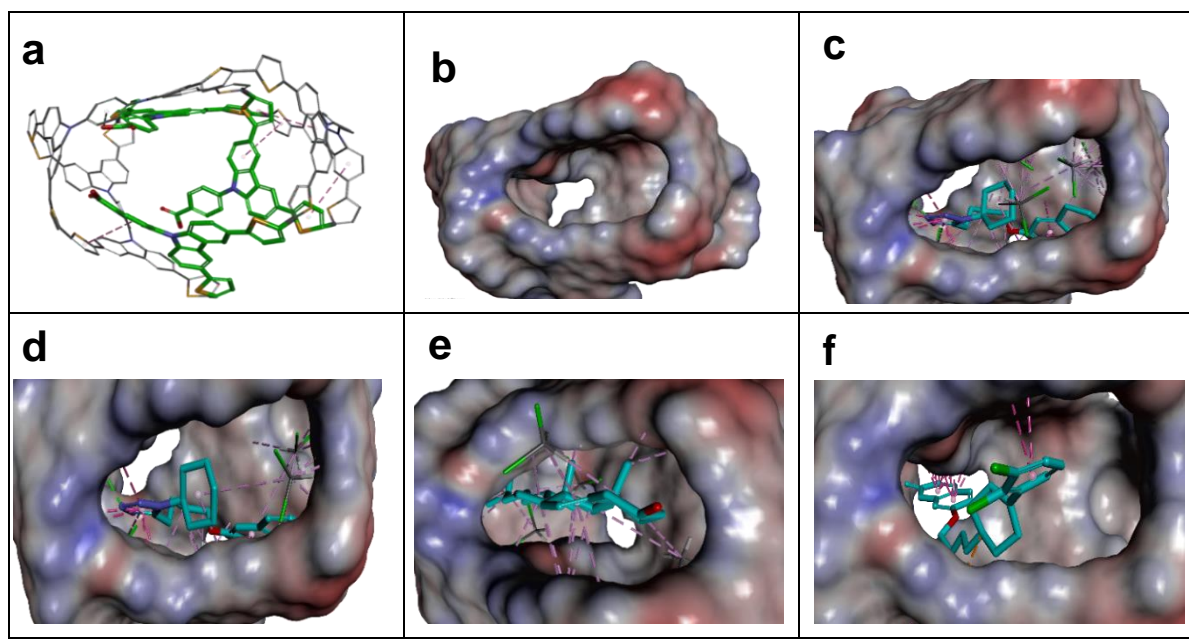


**Figure 4.2-7.** Computer simulated structures of the molecular cavity in MIP-CIL. (a) The skeleton model, (b) surface distribution of molecular electrostatic potential (MEP) colored according to the interpolated (blue) positive and (red) negative charge, (c) with CIL (d) dhCIL (e) dehydroaripiprazole, and (f) cholesterol molecule entrapped showing interactions with dichloromethane.

**Table 4.2-4.** Comparison of CIL and dhCIL methods of determination in the CIL-spiked human plasma and a test solution using LC-MS and the MIP-CIL chemosensor.

Sample No.	LC-MS determined CIL in the test solution, nM	LC-MS determined CIL in human plasma, nM <sup>a</sup>	Recovery, %	CIL concentration in the test solution, nM	MIP chemosensor determined CIL in the test solution, nM	Recovery, %
1	27.1	28.6	105.5	27.1	27.2 ( $\pm 4.5$ )	100.3 ( $\pm 16.6$ )
2	81.2	88.2	108.6	81.2	80.7 ( $\pm 3.9$ )	99.3 ( $\pm 4.8$ )
3	676.7	717.4	106.0	676.7	734.0 ( $\pm 3.1$ )	108.4 ( $\pm 0.4$ )
4	3518.6	3500	99.4	351.8	354.0 ( $\pm 4.5$ )	100.6 ( $\pm 1.3$ )
5	8120.0	7626.5	93.9	812.0	1088.9 ( $\pm 13.4$ )	134.1 ( $\pm 1.6$ )
dhCIL	81.6	89.8	110.0	81.6	89.5 ( $\pm 1.4$ )	109.6 ( $\pm 1.7$ )

#### 4.2.4 Conclusions

The chosen electroactive thiophene-appended carbazole functional and cross-linking monomers appeared effective in CIL molecular imprinting in a polymer. The prepared thin MIP film checked itself as the recognition unit of an electrochemical chemosensor for selective CIL determination in human plasma. Its apparent imprinting factor was as high as  $IF = 10.6$ , indicating efficient imprinting. The DPV normalized peak current for the ferrocene redox probe dependence on the logarithm of CIL concentration was linear between 50 and 924 nM CIL. The attained LOD of 15 nM in CIL was well below the cut-off 135 nM value adopted in clinical practice. Therefore, the chemosensor seems promising for use in clinical analysis.

Moreover, the electrochemical MIP chemosensor is an excellent candidate for point-of-care (PoC) applications because of the short ( $< 5$  min) time of CIL determination, disposability, operation simplicity, repeatability, and low cost, all essential in monitoring the patient's response to treatment at home. Furthermore, the chemosensor response to the dhCIL metabolite is nearly identical to that of the CIL analyte. Therefore, beneficially, they can be determined together. Advantageously, the chemosensor is highly selective to dehydroaripiprazole interference. However, it is not selective to cholesterol, presumably because its molecule is smaller than that of CIL. Hence, cholesterol molecules can readily become entrapped in the CIL-imprinted cavities. Therefore, cholesterol should be pre-removed from clinical samples. As a very lipophilic substance, it can readily be extracted with highly non-polar solvents, e.g., aliphatic hydrocarbons that do not dissolve polar CIL and dhCIL. Fitting the selected isotherms to the sorption data indicated the formation of molecular cavities imprinted in the MIP and these cavities' strong CIL binding. Binding sites distribution in the MIP is somewhat non-homogeneous. Notably, fitting the isotherms for the NIP revealed significantly weaker and relatively homogeneous binding of non-interacting molecules. Computational simulations allowed selecting the most appropriate monomers for the MIP synthesis. The theoretical binding model explained the differences in chemosensor selectivity and emphasized the DCM solvent role in the intermolecular interaction

# Chapter 5

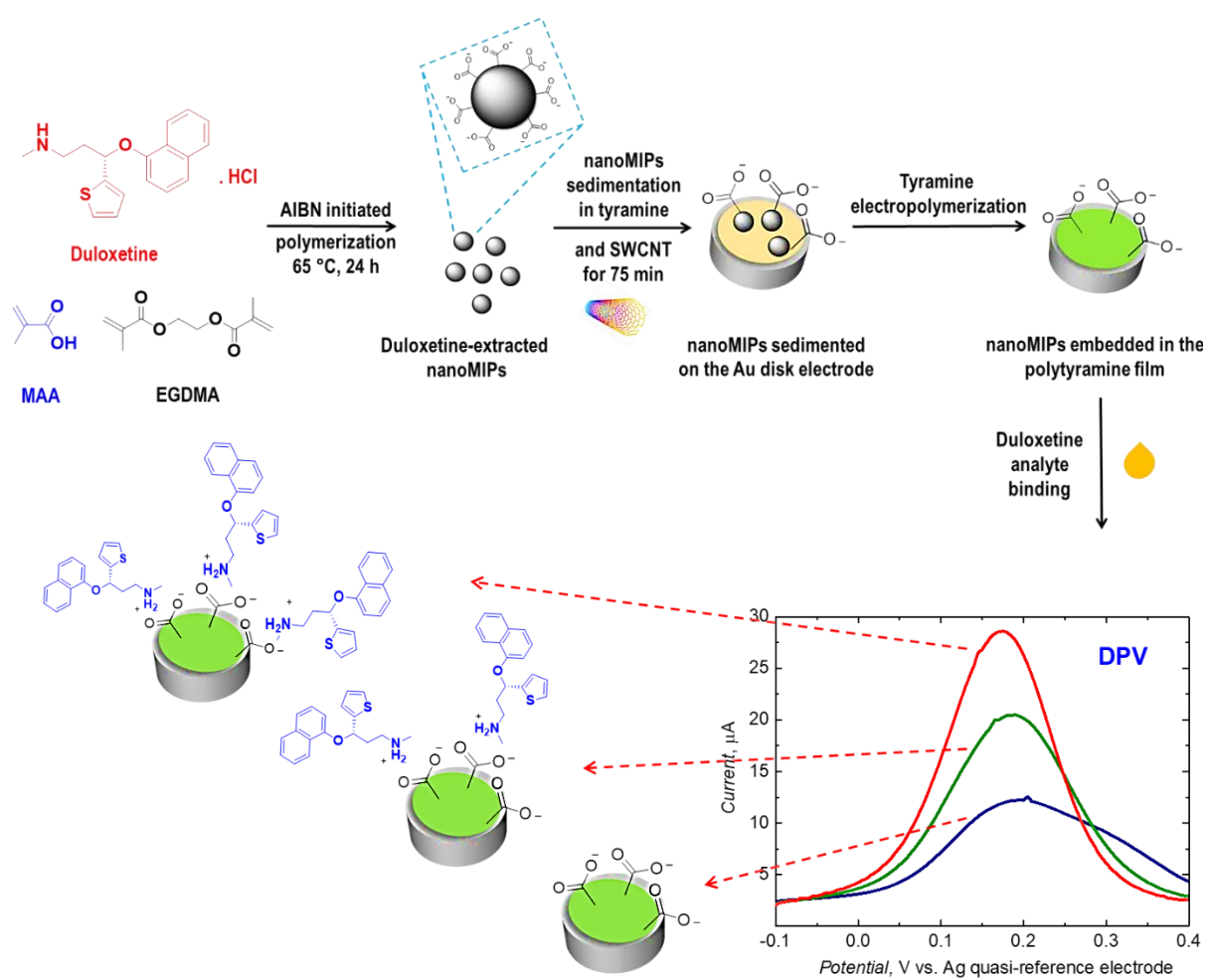
## Polytyramine film-coated single-walled carbon nanotube electrochemical chemosensor with molecularly imprinted polymer nanoparticles for duloxetine selective determination in human plasma

This chapter discusses the research work partially described in a manuscript submitted for publication, authored by *Jyoti, Teresa Żolek, Dorota Maciejewska, Edyta Gilant, Elżbieta Gniazdowska, Andrzej Kutner, Krzysztof R. Noworyta, and Włodzimierz Kutner*

### Abstract

We report on an electrochemical chemosensor for selective determination of a duloxetine (DUL) antidepressant. Polyacrylic nanoparticles, molecularly imprinted with DUL (DUL-nanoMIPs) and then uniformly embedded in a polytyramine film supported on single-walled carbon nanotubes (SWCNTs), i.e., a nanoMIPs-SWCNTs@(polytyramine film) surface construct, constituted a recognition unit of this chemosensor. DUL-nanoMIPs and non-imprinted (nanoNIPs) were immobilized on Au electrodes in SWCNTs supported polytyramine films, deposited by potentiodynamic electropolymerization. Computational design at the molecular dynamics (MD) level of DUL-nanoMIPs helped select the most appropriate functional and cross-linking monomers and analyze the selectivity of the chemosensor. These monomers contributed to synthesizing three different DUL-nanoMIPs and nanoNIPs types by precipitation polymerization. DUL-nanoMIPs, synthesized from respective methacrylic acid (MAA) and ethylene glycol dimethylacrylate (EGDMA) as the functional and cross-linking monomer, respectively, revealed the highest affinity to the DUL analyte. The chemosensor was successfully applied for DUL selective determination in human plasma. Linear dynamic concentration range extending from 10 pM to 676 nM DUL and the LOD equaling 1.6 pM in the plasma was determined by differential pulse voltammetry (DPV). The HPLC-UV measurements confirmed the DUL electrochemical chemosensing.

## Graphical abstract



## 5.1 Introduction

The objective of the present study was to prepare an electrochemical chemosensor for duloxetine (DUL) using DUL-templated MIP nanoparticles as the recognition unit. For that, we first prepared MIP nanoparticles imprinted with DUL (DUL-nanoMIPs) by precipitation polymerization. Next, the sedimentation deposited single-walled carbon nanotubes (SWCNTs) and DUL-nanoMIPs on the electrode surface. Then, we deposited a polytyramine film on this electrode by tyramine potentiodynamic electropolymerization. Due to the SWCNTs and polytyramine presence, the recognition unit of the MIP chemosensor thus fabricated resembled a network. NanoMIPs revealed a high affinity to DUL. SWCNTs served as "electrical bridges" for the electron transfer between nanoMIPs, and polytyramine was the layer binding these NPs. Therefore, the selectivity of the developed nanoMIPs chemosensor towards DUL was higher than that towards interferences. Moreover, the chemosensor sensitivity, durability, and determination repeatability were high. The chemosensor was successfully used for DUL determination in human plasma. The HPLC-UV determination confirmed the practical usefulness of the chemosensor.

## 5.2 Experimental section and procedures

All DPV and EIS measurements were performed using the electrochemical mini-vessel, described in Chapter 2 above, filled with the phosphate-buffered saline, PBS, (pH = 7.2) solution of the 10 mM  $K_3[Fe(CN)_6]$  and 10 mM  $K_4[Fe(CN)_6]$  redox probe. In the DPV measurements, the potential was scanned from -0.10 to 0.40 V vs. Ag/AgCl with the potential step of 5 mV, and the amplitude of 50-ms pulses applied of 25 mV. In the EIS experiments, an ac excitation signal of frequency in the range of 1 MHz to 100 mHz and a 10-mV sinusoidal amplitude was used at the applied potential of 0.15 V vs. Ag/AgCl.

### 5.2.1 Preparing human plasma samples for DUL determination

A 1.0-mg/mL DUL stock solution was prepared by dissolving a weighed DUL portion in methanol. Working solutions were then prepared by diluting the stock solution with 50% methanol. Human plasma samples (with citrate as the anticoagulant) were prepared by spiking the blank plasma with the appropriate working solution at a volume ratio of 20 : 1. Thus, the

DUL concentration in the human plasma samples ranged from 33.6 to 840.6 nM. Each sample was split into two parts for DUL determination using an electrochemical chemosensor with the nanoMIPs-SWCNTs@polytyramine film as the signal transduction unit and the HPLC-UV method.

### **5.2.2 DUL determining in human plasma using nanoMIPs-SWCNTs@polytyramine film-coated electrode**

The human plasma samples of known DUL concentrations were thawed in air and then ten times diluted with PBS ( $\text{pH} = 7.2$ ). These samples were made 10 mM in the  $\text{K}_3[\text{Fe}(\text{CN})_6]$  and 10 mM in the  $\text{K}_4[\text{Fe}(\text{CN})_6]$  redox probe. The 1-ml samples of the DUL-spiked human plasma solutions containing this redox probe were consecutively placed in the electrochemical mini-vessel. Then the nanoMIPs-SWCNTs@polytyramine film-coated electrode was immersed in these solutions, and the DPV current peak,  $I_{\text{DPV}}$ , values were measured for DUL of known concentrations. The resulting changes in the  $I_{\text{DPV}}$  detection signals were used for constructing the DUL calibration plot.

### **5.2.3 DUL determining in human plasma using HPLC-UV**

The DUL in human plasma was also determined using HPLC-UV to confirm the DUL chemosensing. The liquid-liquid extraction with the *tert*-butyl methyl ether was used for sample preparation. The sample components were separated using HPLC-UV on the Symmetry C18 150 × 3.0 mm, 3.5  $\mu\text{m}$  column (Waters, USA) at 25 ( $\pm 2$ ) °C. A mixture of 10 mM ammonium formate and acetonitrile (62.5 : 37.5,  $v/v$ ) served as the mobile phase. The UV light with a selected wavelength of 230 nm was applied for the DUL detection. Fluoxetine hydrochloride served as the internal standard. The complete analysis run time was 12 min. This determination was performed in compliance with the OECD Principles of Good Laboratory Practice (GLP).

## **5.3 Results and discussion**

First, the most appropriate functional and cross-linking monomers were selected by computer modeling. These monomers were used at different ratios to find the MIPs with the highest affinity towards the target DUL analyte. After complete characterization, the most promising nanoMIP particles were immobilized on gold electrodes. First, the affinity, cross-reactivity,

repeatability, and reproducibility were investigated using PBS samples. Then, DUL was determined in human plasma samples to validate the developed chemosensing system.

### 5.3.1 Functional and cross-linking monomers effect on the pre-polymerization complex stability

MIP properties were determined using the modeled structure of the pre-polymerization complex built of the DUL template with four different functional and two cross-linking monomers. For that, determining the most appropriate molecular composition of the complex was an essential part of the studies preceding nanoMIP synthesis. First, the complex systems of the DUL-to-MAA stoichiometric ratio of 1 : 3, 1 : 4, 1 : 5, and 1 : 6 were analyzed. The systems were generated by surrounding a DUL molecule with twelve MAA molecules. Then, after the energy optimization, the appropriate numbers of MAA molecules, i.e., 3, 4, 5, or 6, were selected to create the center of the pre-polymerization complexes. The main criteria for the selection involved the strongest interactions of DUL with the monomers of the hydrogen bond and  $\pi$ - $\pi$  interactions. Then structures of these complexes were optimized again, and, for preserving the internal geometry, an auxiliary restraining potential was applied to the monomers in subsequent computations. With the use of MM and MD, four models of the pre-polymerization complexes of DUL with MAA and EGDMA were constructed. The Gibbs free energy changes accompanying the complexation were defined by intermolecular interactions between the template and functional or cross-linking monomer. Using these calculations, we chose the most appropriate stoichiometric ratio for the nanoMIP synthesis. In subsequent computations, three different functional monomers vis., 4-VP, AA, and HPMA, as well as two cross-linking monomers, vis., EGDMA and BIS, were considered by simulating four pre-polymerization complex systems at the 1 : 5 : 20 molar ratios. The final stage of structural modeling consisted of creating the MIP molecular cavity. That used the most stable pre-polymerization complex structure of the DUL: MAA : EGDMA ratio of 1 : 5 : 20, predicted for the complex synthesis (Figure 5-1).

Next, the template was removed from the resulting MIP, and the space vacated was proposed as the theoretical model of the sorption cavity in the nanoMIP. The cavity model was used for analyzing analyte and interferences sorption from aqueous solutions. The DUL analyte and creatinine, urea, glucose, and cholesterol interferences were successively inserted

in the cavity, and then the MD simulated their sorption. The resulting values of the Gibbs free energy change,  $\Delta G_C$ , for all systems tested, are presented in Table 5-1.

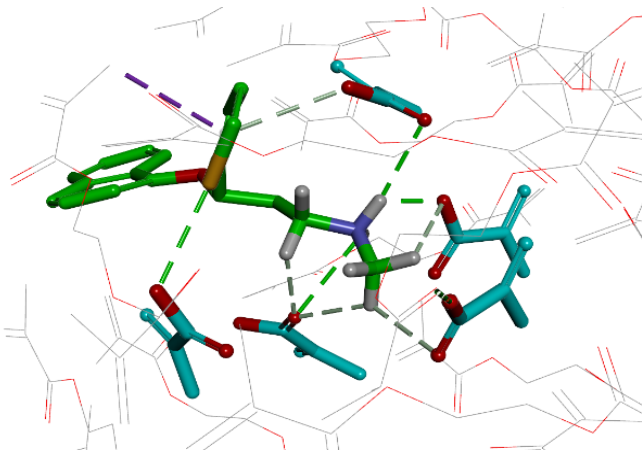


**Figure 5-1.** Simulated skeleton model of the pre-polymerization complex of DUL with MAA surrounded by EGDMA molecules at the 1 : 5: 20 molar ratios. Significant intermolecular interactions are indicated with dashed lines.

**Table 5-1.** Compositions of mixtures for preparation of pre-polymerization complexes and the Gibbs free energy changes,  $\Delta G_C$  ( $\Delta G_C = \Delta G_{\text{system}} - \Delta G_{\text{DUL}} - n \cdot \Delta G_{\text{FM}} - 20 \cdot \Delta G_{\text{CLM}}$ ), for eight complex systems simulated.

Complex system	$\Delta G_C$ kJ/mol
DUL : MAA : EGDMA, 3 : 20	-313.95
DUL : MAA : EGDMA, 4 : 20	-342.69
DUL : MAA : EGDMA, 5 : 20	-343.81
DUL : MAA : EGDMA, 6 : 20	-321.35
DUL : MAA : BIS, 5 : 20	-39.14
DUL : 4-VP : EGDMA, 5 : 20	-248.68
DUL : AA : BIS, 5 : 20	-11.96
DUL : HPMA : BIS, 5 : 20	-13.23

MAA – methacrylic acid, 4-VP – 4-vinylpyridine, AA – acrylamide, HPMA – *N*-(2-hydroxypropyl) methacrylamide, EGDMA – ethylene glycol dimethacrylate, BIS – *N,N'*-methylenebisacrylamide. The  $\Delta G_{\text{system}}$ ,  $\Delta G_{\text{DUL}}$ ,  $\Delta G_{\text{FM}}$ ,  $\Delta G_{\text{CLM}}$  and  $n$  symbols respectively stand for the Gibbs free energy change accompanying the formation of the system, DUL, functional and cross-linking monomers, and the number of functional monomer molecules in the complex.

### **5.3.2 NanoMIPs synthesizing by precipitation polymerization**

Once the functional monomer, cross-linking monomer, and their optimum stoichiometric ratios for stable pre-polymerization complex formation were selected through computational modeling, nanoMIPs, and their corresponding nanoNIPs were synthesized using the precipitation polymerization procedure discussed in Chapter 2 above.

### **5.3.3 NanoMIPs and nanoNIPs size and zeta potential determining**

Dynamic light scattering (DLS) determined the hydrodynamic size and zeta potential of the nanoMIPs and nanoNIPs. For DLS measurements, 1-mg mL<sup>-1</sup> nanoMIPs and nanoNIPs samples were ultrasonicated in deionized water. The average sizes of nanoMIPs and nanoNIPs were 157 ( $\pm 14$ ) and 529 ( $\pm 18$ ) nm, respectively. The zeta potential for the nanoMIPs and nanoNIPs was -9.6 and -46.3 mV, respectively. It revealed the net surface charge and long-term stability of the nanoparticles. Since the negative nanoMIPs' zeta potential was relatively low, they experienced rapid aggregation (Figure 5-4b); in contrast, nanoNIPs with relatively high negative zeta potential were very stable.

### **5.3.4 Experimental determining of the duloxetine analyte binding to nanoMIPs**

NanoMIPs should be placed as close as possible to the electrode surface so that after binding the DUL analyte, the transducer, here, the electrode, generated a well pronounced analytical signal. For that, herein, we used tyramine which, upon electropolymerization, forms a thin polymer film, widely applied for tissue repair and drug release, among others.<sup>369</sup>

Initially, nanoMIPs were immobilized in the polytyramine film using five potentiodynamic cycles (Figure 5-2a). Subsequently, three different sets of nanoMIPs and nanoNIPs chemosensors were devised to elucidate their sensitivity towards the DUL analyte. The nanoMIP chemosensor prepared using MAA and EGDMA as the functional and cross-linking monomer, respectively, was very sensitive to DUL (Figure 5-2b). However, the nanoMIPs chemosensor, fabricated using either AA (Figure 5-2c) or HPMA (Figure 5-2d) as the functional monomer, DUL binding was weak. Therefore, nanoMIPs embedded in the polytyramine film, synthesized using MAA and EGDMA, were applied in further studies.

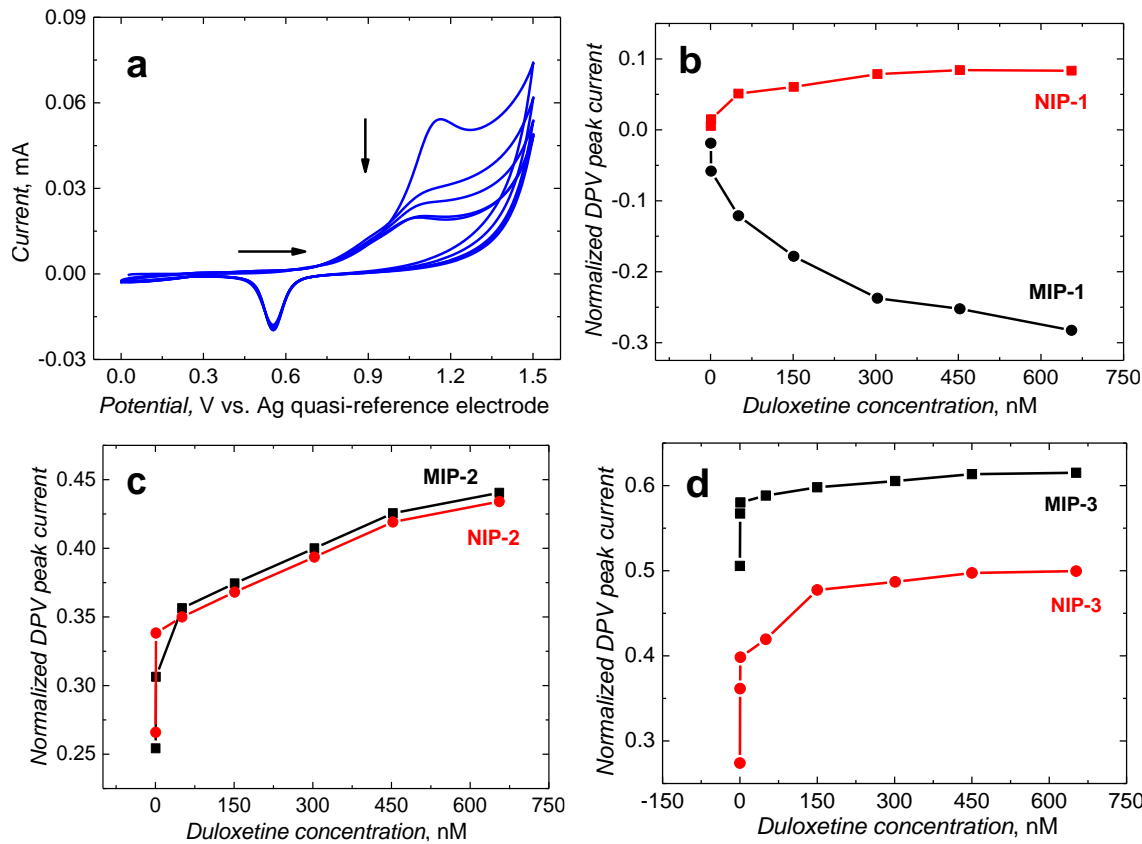


**Figure 5-2.** (a) The multi-cyclic potentiodynamic curve for a mixture of 10 mM tyramine in 25 mM  $\text{H}_2\text{SO}_4$  on a 2-mm diameter Au-disk electrode at a 50-mV  $\text{s}^{-1}$  potential scan rate in the presence of polymer NPs. Plots of normalized DPV peak currents vs. DUL concentration in 10 mM  $\text{K}_3[\text{Fe}(\text{CN})_6]$  and 10 mM  $\text{K}_4[\text{Fe}(\text{CN})_6]$  in 0.1 M PBS (pH = 7.2) for the nanoMIPs (black) and nanoNIPs (red) embedded in the polytyramine film and prepared using functional and cross-linking monomers of (b) MAA and EGDMA, (c) AA and BIS, and (d) HPMA and BIS.

### 5.3.5 Optimizing polymer NPs integration with electrodes for signal enhancement using SWCNTs

Choosing the most suitable polymer NPs immobilization method is crucial for their successful integration with a transducer surface, here, the electrode surface, to construct an MIP chemosensor. Three different ways were used to enhance the MIP/NIP chemosensor signal by incorporating single-walled carbon nanotubes. Moreover, another substituent was considered to increase the chemosensor signal. To this end, MWCNTs were used (Figure 5-3d). Their concentration was thrice higher than that of the SWCNTs. From Figure 5-3d, it is evident that the SWCNTs performed better than the MWCNTs.

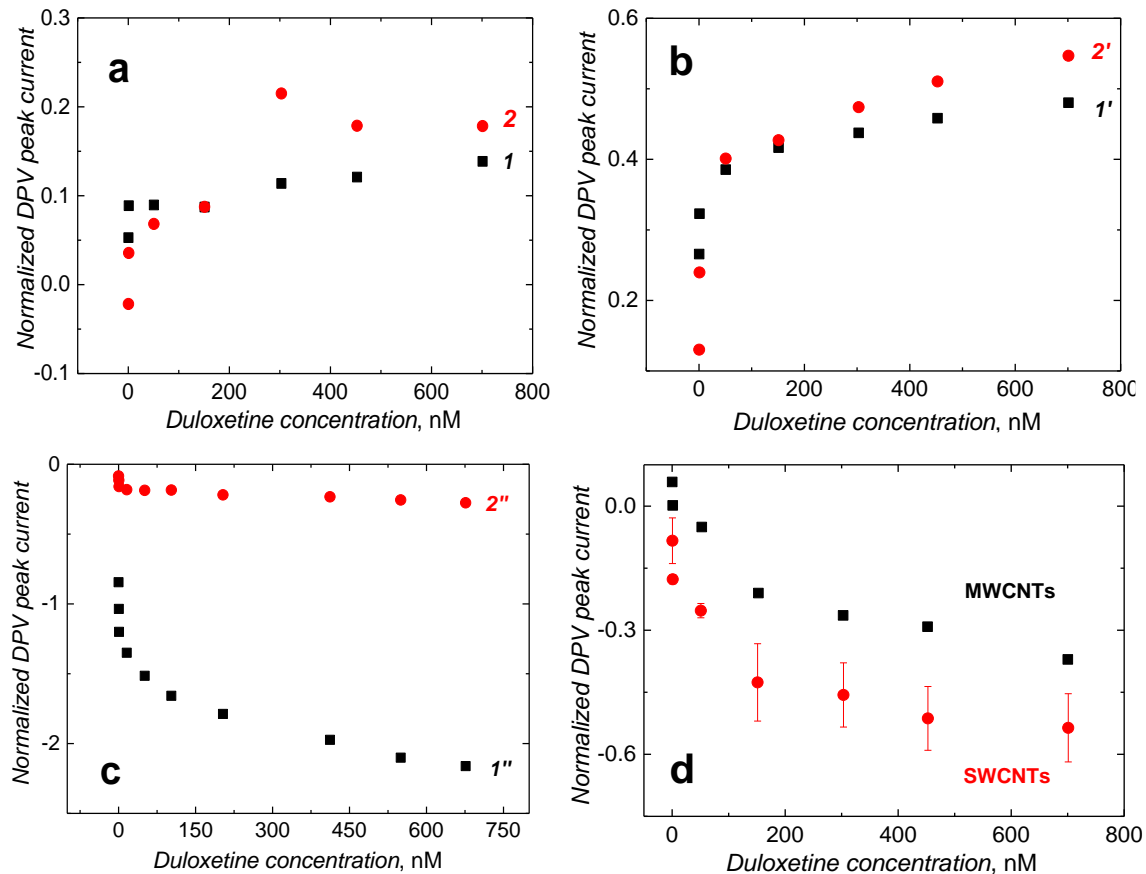


**Figure 5-3.** Plots of normalized DPV peak currents vs. DUL concentration in 10 mM  $\text{K}_3[\text{Fe}(\text{CN})_6]$  and 10 mM  $\text{K}_4[\text{Fe}(\text{CN})_6]$  in 0.1 M PBS ( $\text{pH} = 7.2$ ) recorded on the Au disk electrode for nanoMIPs (curves 1, 1', and 1'') or nanoNIPs (curves 2, 2', and 2'') chemosensor fabricated using (a) drop-coated SWCNTs (b) drop-coated functionalized SWCNT-COOH and (c) a mixture of SWCNTs with tyramine. (d) The normalized DPV peak current vs. DUL concentration plot for the nanoMIP chemosensor fabricated using SWCNTs and MWCNTs as signal enhancers.

Suppose electrodes were first to drop coated with the SWCNTs (Figure 5-3a) or functionalized SWCNTs-COOH (Figure 5-3b), followed by electropolymerization of tyramine in the presence of polymer NPs. In that case, the prepared imprinted NPs chemosensor could not selectively bind DUL. However, when SWCNTs, DUL-imprinted NPs, and tyramine solution were mixed and sedimented for 75 min followed by potentiodynamic electropolymerization, the resulting MIP chemosensor effectively bound DUL (Figure 5-3c), in contrast to the NIP NPs. Therefore, mixing together all three components instead of drop-coating was preferred for the fabrication of the chemosensor for subsequent experiments.

### 5.3.6 SEM and AFM imaging of nanoMIPs and nanoNIPs

The changes in morphology and structure of the electrode surface after (nanoMIPs-SWCNTs)@polytyramine film deposition in five potentiodynamic cycles were monitored by SEM imaging. This imaging confirmed the formation of a web-like structure where nanoMIPs were encapsulated in the SWCNTs-polytyramine film (Figure 5-4a and 4b), unlike the SWCNTs-polytyramine film (Figure 5-4c).

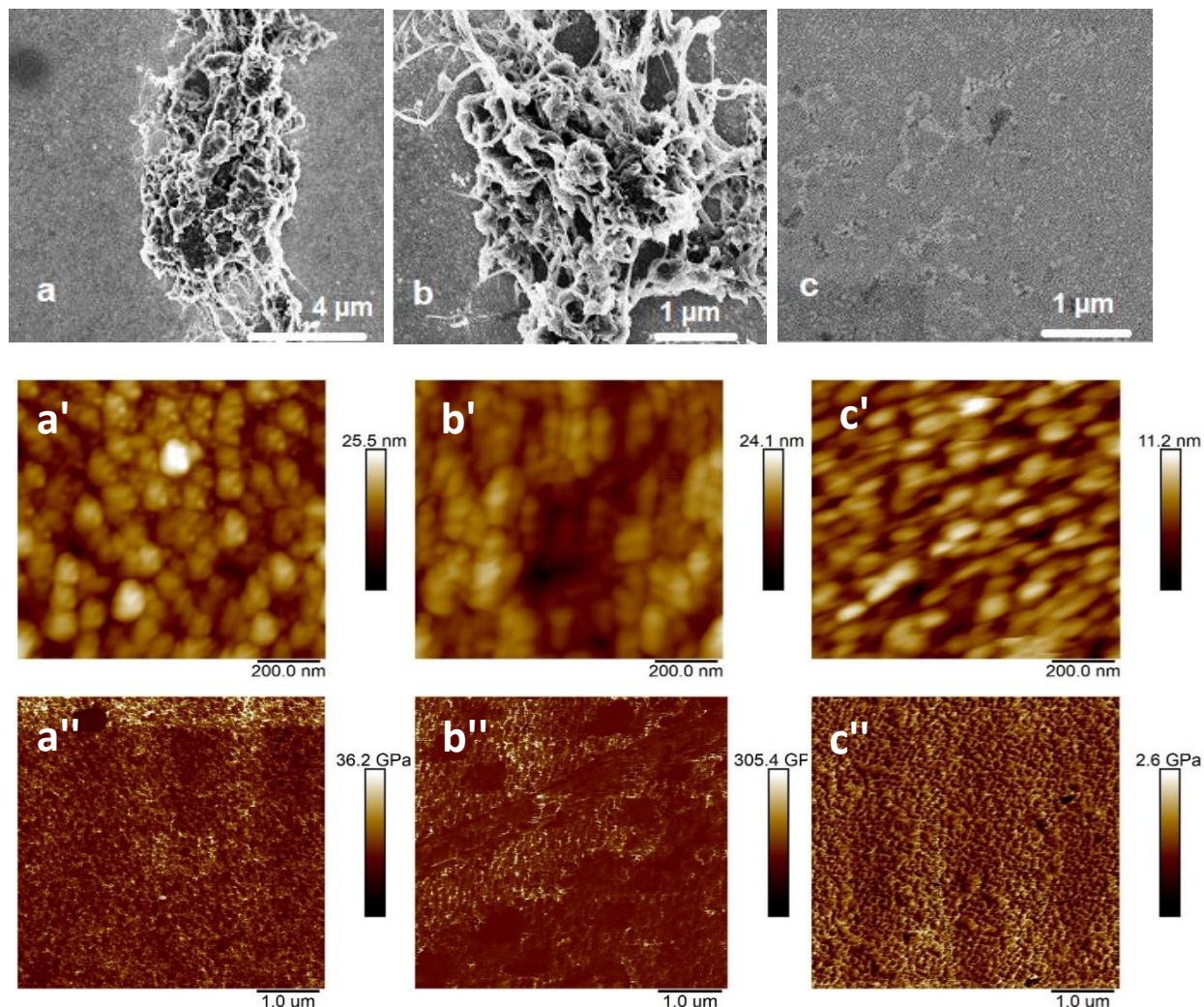


**Figure 5-4.** SEM images at different magnifications of (a) and (b) nanoMIPs embedded in the SWCNTs-polytyramine film, and (c) the SWCNTs-polytyramine film without nanoMIP. Both films were deposited on the Au-layered glass slide electrodes. AFM topography images and Young's module map (a''), (b'') and (c'') of the (a') and (a'') nanoMIPs and (b') and (b'') nanoNIPs embedded along with SWCNTs in the polytyramine film, and (c') and (c'') the polytyramine film with the SWCNTs in the absence of nanoMIPs and nanoNIPs. All of the films were deposited on the Au-layered glass slide electrodes.

AFM imaging correlated well with SEM imaging. It shows reticulated structures, composed of SWCNTs, nanoMIPs or nanoNIPs, and polytyramine, irregularly scattered on the film surface. The film between these structures is relatively uniform (Figure 5-4a', 4b', and 4c'). The (nanoMIPs-SWCNTs)@polytyramine film, (nanoNIPs-SWCNTs)@polytyramine film, and SWCNTs@polytramine film roughness ( $R_a$ ) was 3.3 ( $\pm 1.2$ ), 5.7 ( $\pm 1.2$ ), and 1.7 ( $\pm 0.3$ ) nm, respectively. The films are composed of rounded or elliptical 20 to 100 nm in size agglutinated grains. The (nanoMIPs-SWCNTs)@polytyramine, (nanoNIPs-SWCNTs)@polytyramine, and SWCNTs@polytyramine film thickness was 145 ( $\pm 6$ ), 69 ( $\pm 17$ ), and 81 ( $\pm 22$ ) nm, respectively. The examination of the nanomechanical properties of the films showed that the (nanoMIPs-SWCNTs)@polytyramine and SWCNTs@polytyramine are mechanically homogeneous (Figure 5-4a'', 4b'', and 4c'')). On the other hand, the (nanoNIPs-SWCNTs)@polytyramine film contained domains of different hardness (Figure 5-4b''). They had larger lumps of grains. The (nanoMIPs-SWCNTs)@polytyramine, (nanoNIPs-SWCNTs)@polytyramine, and SWCNTs@polytyramine film medium Young modulus was 6.0 ( $\pm 0.2$ ), 23.1 ( $\pm 3.9$ ), and 1.9 ( $\pm 0.3$ ) GPa, respectively.

### 5.3.7 Electrochemical characterizing of nanoMIP/nanoNIPs and SWCNTs immobilized in polytyramine films on electrodes

The sedimented nanoMIPs and SWCNTs were immobilized in a polytyramine film using five potentiodynamic cycles (Figure 5-5b). In the multi-cyclic potentiodynamic curve, two anodic peaks at  $\sim 0.99$ ,  $\sim 1.34$  V and one cathodic at  $\sim 0.61$  V vs. Ag quasi-reference electrode were present. In consecutive cycles, anodic currents decreased, indicating electrode coating with a thicker after each cycle non-conducting polymer film. This behavior resembled the SWCNTs@polytyramine film potentiodynamic deposition in the absence of nanoMIPs (Figure 5-5a), confirming polytyramine film deposition. When SWCNTs were embedded in the nanoMIPs@polytyramine film, the peak current was enhanced, demonstrating SWCNTs' vital role in the electron transfer. The slope of the calibration plot of the (nanoMIPs-SWCNTs)@polytyramine film-coated electrode was almost four times higher than the nanoMIPs@polytyramine film-coated electrode (Figure 5-5f).

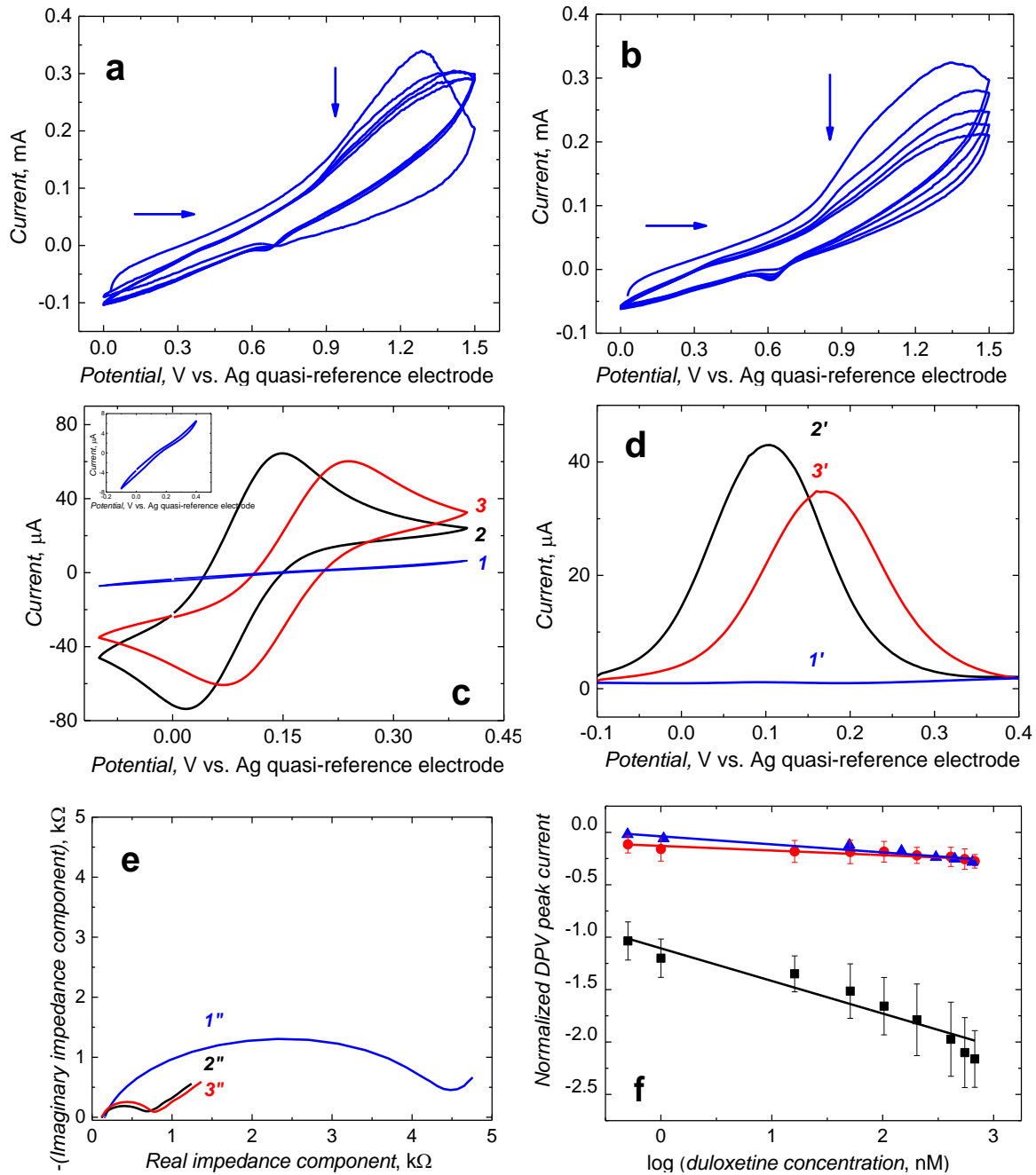


**Figure 5-5.** The multi-cyclic potentiodynamic curve for a mixture of 10 mM tyramine in 25 mM H<sub>2</sub>SO<sub>4</sub> and SWCNTs on a 2-mm diameter Au-disk electrode at a 50-mV s<sup>-1</sup> potential scan rate in the (a) absence and (b) presence of nanoMIPs sedimented on the electrode surface for 75 min. (c) CV and (d) DPV voltammograms, and (e) Nyquist curves at 0.15 V for 10 mM K<sub>3</sub>[Fe(CN)<sub>6</sub>] and 10 mM K<sub>4</sub>[Fe(CN)<sub>6</sub>] in 0.1 M PBS (pH = 7.2) recorded on the Au disk electrode coated with the film of (curves 1, 1', and 1'') nanoMIPs@polytyramine, (curves 2, 2', and 2'') SWCNTs@polytyramine, and (curves 3, 3', and 3'') nanoMIPs-SWCNTs@polytyramine. (f) Calibration plots of normalized DPV peak current constructed using electrodes coated with the (black) nanoMIPs-SWCNTs@polytyramine, (red) nanoNIPs-SWCNTs@polytyramine, (blue) nanoMIPs@polytyramine film.

Expectedly, the  $\text{K}_4[\text{Fe}(\text{CN})_6]/\text{K}_3[\text{Fe}(\text{CN})_6]$  in the PBS ( $\text{pH} = 7.2$ ) peaks in the CV (Figure 5-5c) and DPV (Figure 5-5d) curves for the (nanoMIPs-SWCNTs)@polytyramine film-coated electrode were lower than for the SWCNTs@polytyramine film-coated electrode. These peaks were exploited to confirm the successful immobilization of nanoMIPs in the SWCNTs@polytyramine film (Figure 5-5c - 5e). That is, both CV and DPV peaks for the (nanoMIPs-SWCNTs)@polytyramine film-coated electrode (curve 3 in Figure 5-5c and curve 3' in Figure 5-5d, respectively) were significantly smaller than those for the SWCNTs@polytyramine film-coated electrode (curve 2 in Figure 5-5c and curve 2' in Figure 5-5d, respectively).

Moreover, the semicircle diameter corresponding to the charge transfer resistance,  $R_{ct}$ , in the Nyquist plot for the (nanoMIPs-SWCNTs)@polytyramine film-coated electrode was larger than that for the SWCNTs@polytyramine film-coated electrode (curves 3'' and 2'', respectively, in Figure 5-5e), thus manifesting more extensive charge transfer blocking of the former electrode.

### 5.3.8 DPV and EIS determining of DUL with the (nanoMIPs-SWCNTs)@polytyramine film-coated electrode

(NanoMIPs-SWCNTs)@polytyramine film-coated Au-disk electrodes were used for the DUL determination with DPV (Figure 5-6a and 6b) and EIS (Figure 5-6c and 6d) in the presence of the  $\text{K}_4[\text{Fe}(\text{CN})_6]/\text{K}_3[\text{Fe}(\text{CN})_6]$  redox probe. The normalized DPV peak ( $I_{DPV,0} - I_{DPV,s}/I_{DPV,0}$ ), where  $I_{DPV,0}$ , and  $I_{DPV,s}$  stand for the initial and actual DPV peak, linearly depended on the logarithm of DUL concentration,  $c_{DUL}$  (Figure 5-6e). The linear dynamic concentration range was 10 pM to 676 nM DUL obeying the semi-logarithmic regression equation of  $(I_{DPV,0} - I_{DPV,s}/I_{DPV,0}) = -0.39 (\pm 0.021)/\log [\text{nM}] \times \log \{c_{DUL} [\text{nM}]\} - 1.00 (\pm 0.038)$  (Figure 5-6e, curve 1). The sensitivity and correlation coefficient were  $-0.39 (\pm 0.021)/\log [\text{nM}]$ , and 0.96, respectively. At the signal-to-noise ratio,  $S/N = 3$ , the chemosensor's LOD was 1.6 pM DUL being adequately low for the DUL determination in body fluids.

Moreover, the DPV signal for the nanoNIPs-SWCNTs@polytyramine film-coated electrode did not change much with the DUL concentration increase, thus indirectly confirming successful imprinting. This signal dependence on DUL concentration is described by the semi-logarithmic regression equation of  $(I_{DPV,0} - I_{DPV,s}/I_{DPV,0}) = -0.03 (\pm 0.003)/\log [\text{nM}] \times \log \{c_{DUL} [\text{nM}]\} - 0.14 (\pm 0.007)$  (Figure 5-6e, curve 6) for the

concentration range of 10 pM to 923  $\mu$ M DUL. The sensitivity and correlation coefficient were  $-0.03 (\pm 0.003)/\log [nM]$  and 0.89, respectively. The apparent imprinting factor was estimated from the ratio of the slopes of DUL calibration plots for the nanoMIPs-SWCNTs@polytyramine to nanoNIPs-SWCNTs@polytyramine film-coated electrodes as  $IF = 13.0$ .

Immediately after recording the DPV curves, the EIS spectra were recorded for the same solutions to gain insight into mechanistic aspects of the chemosensor response. In Nyquist plots, the semicircles' diameters correspond to the redox probe faradaic processes' charge transfer resistance,  $R_{ct}$ . Both for nanoMIPs and nanoNIPs, semicircles were well pronounced (Figure 5-6c and 6d). A modified Randles-Ershler equivalent circuit (Figure 5-6g) fitted well to these spectra. For (nanoMIPs-SWCNTs)@polytyramine, the  $R_{ct}$  linearly increased with the logarithm of DUL concentration (Figure 5-6f), fulfilling the following semi-logarithmic regression equation.  $(R_{ct,0} - R_{ct,s})/R_{ct,0} = 0.10 (\pm 0.003)/\log [nM] \times \log \{c_{DUL} [nM]\} + 0.29 (\pm 0.007)$ . The sensitivity and regression coefficient were  $0.10 (\pm 0.003)/\log [nM]$  and  $R^2 = 0.98$ , respectively. At  $S/N = 3$ , the LOD was 2.0 pM DUL.

However, for (nanoNIPs-SWCNTs)@polytyramine, the  $R_{ct}$  did not change much with the change of the logarithm of the DUL concentration (Figure 5-6f). The linear regression equation was  $(R_{ct,0} - R_{ct,s})/R_{ct,0} = 0.01 (\pm 0.004)/\log [nM] \times \log \{c_{DUL} [nM]\} + 0.02 (\pm 0.009)$ . The sensitivity at  $S/N = 3$  was  $0.01 (\pm 0.004)/\log [nM]$ . The apparent imprinting factor, calculated as the ratio of slopes of the EIS calibration plots for nanoMIPs and nanoNIPs, was 7.5.

Moreover, the selectivity coefficients ( $\alpha$ ) for glucose and creatinine were 15 and 1.4, respectively. Advantageously, the EIS chemosensor was irresponsive to cholesterol in the same concentration range.

Analytical parameters of the fabricated chemosensor, including the linear dynamic concentration range and LOD, were compared to those already reported in the literature and presented in Chapter 1, Section 1.3.2. Apparently, the present chemosensor outmatches all those previously reported.

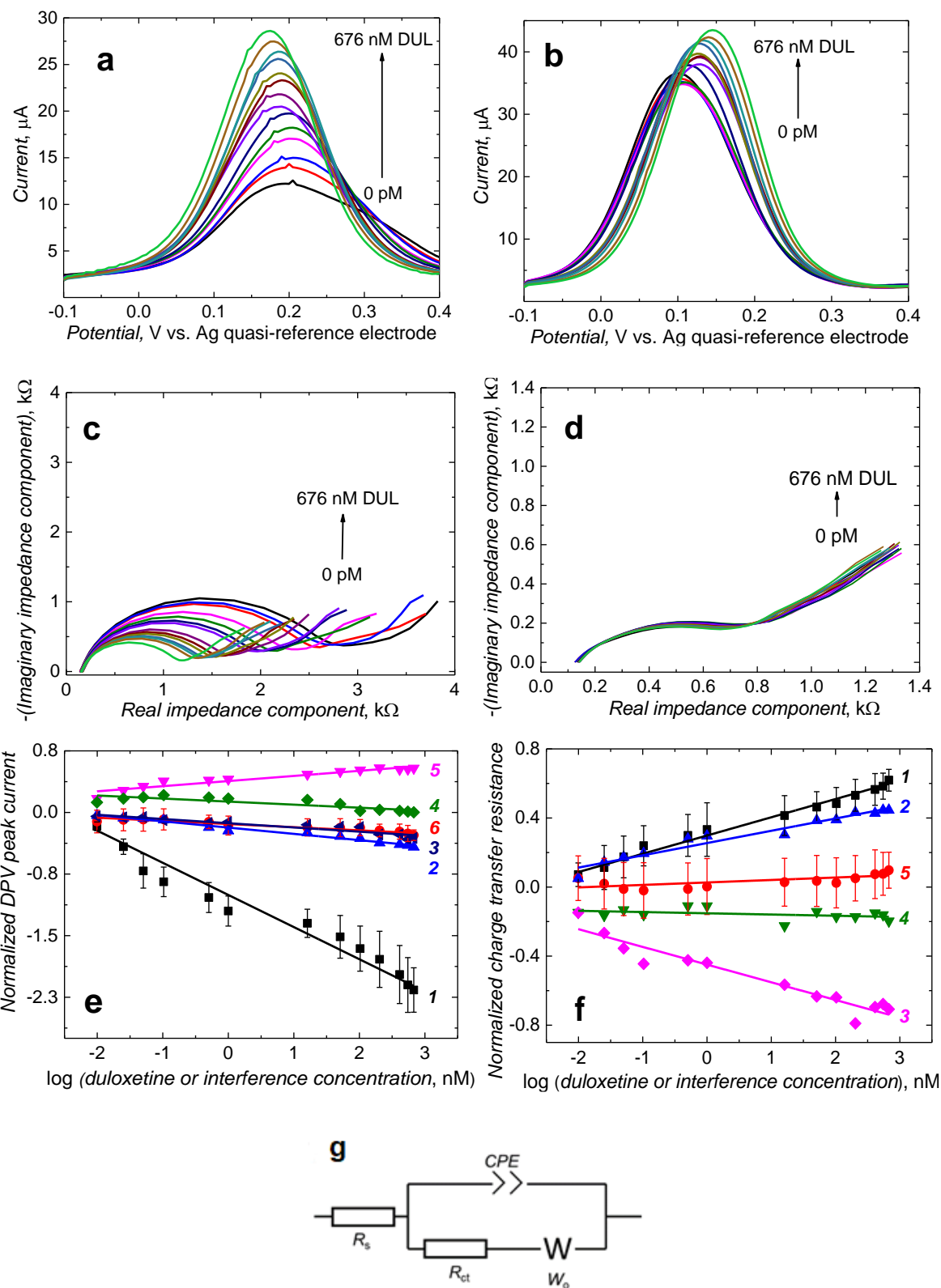


**Figure 5-6.** (a) and (b) DPV peaks current, and (c) and (d) Nyquist plots recorded using the SWCNTs-polytyramine film-coated 2-mm diameter Au disk electrodes with (a) and (c) nanoMIPs and (b) and (d) nanoNIPs in the presence of DUL of different concentrations in 10 mM K<sub>3</sub>[Fe(CN)<sub>6</sub>] and 10 mM K<sub>4</sub>[Fe(CN)<sub>6</sub>] in 0.1 M PBS (pH = 7.2) vs. Ag quasi-reference electrode. The semilogarithmic calibration plots of the (e) DPV currents normalized peaks constructed using electrodes coated with the (curves 1 - 5) nanoMIPs-SWCNTs@polytyramine and (curve 6) nanoNIPs-SWCNTs@polytyramine film. Curves 1, 2, 3, 4, and 5 are respective calibration plots for DUL, creatinine, urea, glucose, and cholesterol. (f) normalized charge transfer resistance against the DUL or interferences' concentration constructed using electrodes coated with the SWCNTs@polytyramine film containing (curves 1 - 4) nanoMIPs and (curve 5) nanoNIPs. Curves 1, 2, 3, and 4 are calibration plots for DUL, creatinine, cholesterol, and glucose, respectively. (g) A modified Randles-Ershler equivalent circuit used to fit the EIS spectra.

### 5.3.9 Cross-reactivity study

Although the chemosensor detectability of the target DUL analyte is adequate, it was necessary to test the chemosensor against common interferences encountered in human plasma (Figure 5-6e and 6f). Cross-reactivity experiments were performed with four common interferences, including urea, glucose, creatinine, and cholesterol, at concentrations of the same order as DUL to determine the selectivity coefficient ( $\alpha$ ) values (Figure 5-6e and 6f). For that, ratios of slopes of the DUL calibration plot to that of the interference were calculated. Advantageously, the chemosensor was unresponsive to cholesterol. In summary, after integrating the (nanoMIPs-SWCNTs)@polytyramine film with the electrode surface to devise a complete chemosensor, this was appreciably selective to common interferences.

### 5.3.10 NanoMIPs-SWCNTs@polytyramine stability and reusability

Two essential criteria required for any sensing device, on top of sensitivity and selectivity, are stability and reusability. Our chemosensor was stable for at least two months with a merely 4.0% signal decay (Figure 5-7) and was reused at least five times without significant DUL sensing ability loss. For its reuse, DUL was 30-min extracted with methanol after each determination.

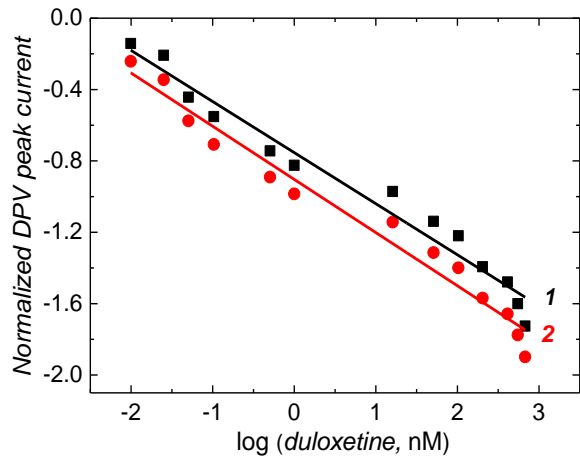


**Figure 5-7.** Calibration plots of normalized DPV peak current constructed using electrodes coated with the SWCNTs-polytyramine film containing nanoMIPs after addition of different concentrations of DUL in 10 mM  $\text{K}_3[\text{Fe}(\text{CN})_6]$  and 10 mM  $\text{K}_4[\text{Fe}(\text{CN})_6]$  in 0.1 PBS ( $\text{pH} = 7.2$ ) vs. Ag quasi-reference electrode. Curves 1 and 2 represent calibration plots for DUL at the two-month reused and newly prepared electrode, respectively.

### 5.3.11 Computational modeling of the nanoMIP cavity as well as simulating analyte and interferences sorption in this cavity

The model of the cavity imprinted in the MIP was set up based on the DUL : MAA : EGDMA, 1 : 5 : 20 complex described above. Figure 5-8a presents the MEP distribution on the cavity surface. The negative potential areas predominate at the back of the cavity in the proximity of oxygen atoms of carbonyls and carboxyls, while the positive potential areas are located close to the cavity edge. The positive potential areas are near hydrogen atoms of the hydroxyls.

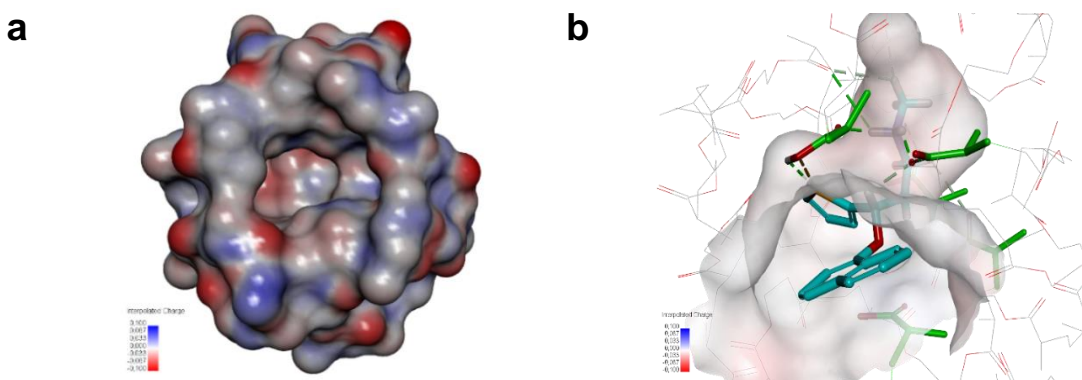


**Figure 5-8.** (a) Surface distribution of molecular electrostatic potential (MEP) colored according to the interpolated (blue) positive and (red) negative charge of a computationally modeled structure of the molecular cavity imprinted in DUL-nanoMIP and (b) simulated visualization of the DUL analyte in the theoretically generated DUL-nanoMIP cavity.

The computed values of the Gibbs free energy change due to nanoMIPs binding of the analyte or interferences ( $\Delta G_{\text{bind}}$ ) are presented in Table 5-2. Clearly, the nanoMIPs strongest interactions are predicted for DUL, corresponding well to a high experimental imprinting factor. The free energy changes computed for the creatinine, urea, glucose, and cholesterol interferences are much lower. Hence, those should not interfere with the DUL determination. The experimental selectivity coefficient ( $\alpha$ ) values correlated similarly, confirming computational predictions.

**Table 5-2.** Calculated changes of the Gibbs free energy ( $\Delta G_{\text{bind}}$ ) due to nanoMIP binding of the DUL analyte and selected interferences, DPV experimental values of the imprinting factor ( $IF$ ), and the selectivity coefficient ( $\alpha$ ).

Compound	Experimental selectivity coefficient $\alpha$	Calculated $\Delta G_{\text{bind}}$ (kJ/mol)
Duloxetine (DUL)	-	-201.96
Creatinine/tautomer of creatinine	5.5	-55.54/-100.75
Cholesterol	-	-24.45
Urea	7.8	-68.20
Glucose	13.0	-36.30

### 5.3.12 DUL determining in human plasma with the (nanoMIPs- SWCNTs) @polytyramine chemosensor

The practical usability of a newly fabricated chemosensor should be evaluated with real samples to estimate the matrix effect. With that in mind, the present chemosensor performance was investigated for DUL-spiked human plasma samples (Table 5-3). These samples, anticoagulated with citrate, were then ten times diluted with PBS (pH = 7.2). Significantly, the chemosensor determined DUL using DPV in plasma samples. Hence, the chemosensor is suitable for DUL determination in plasma.

**Table 5-3.** Comparison of DUL methods of determination in human plasma and a test solution using HPLC-UV and the MIP-DUL chemosensor.

Sample No.	LC-MS determined DUL concentration in the test solution, nM	LC-MS determined DUL concentration in human plasma, nM <sup>a</sup>	Recovery, %	DUL concentration in the test solution, nM	MIP-chemosensor determined DUL concentration in the test solution, nM	Recovery, %
1	33.6	33.2	98.8	3.3	4.0 ( $\pm 1.25$ )	121.2 ( $\pm 39.0$ )
2	100.8	100.5	99.7	10.0	10.6 ( $\pm 2.47$ )	106.0 ( $\pm 24.7$ )
3	336.2	332.2	98.8	33.6	30.2 ( $\pm 8.75$ )	89.8 ( $\pm 26.0$ )
4	571.6	577.0	100.9	57.1	59.5 ( $\pm 12.8$ )	104.2 ( $\pm 22.5$ )
5	840.6	802.6	95.4	84.0	89.4 ( $\pm 11.0$ )	106.4 ( $\pm 13.1$ )

<sup>a</sup> Arithmetic average ( $n = 6$ )

## 5.4 Conclusions

The present research was devoted to developing a sensitive and selective method for duloxetine (DUL) determination in human plasma. For that, we devised, fabricated, and tested a new nanoMIPs-based electrochemical chemosensor. The DUL-imprinted nanoMIPs and SWCNTs were sedimented on a transducer (electrode) surface and then immobilized in a polytyramine film deposited by electropolymerization. The functional and cross-linking monomers most appropriate to obtain nanoMIPs of a high affinity to the target DUL analyte were selected based on the computational simulations performed. Recognizing properties and stability of the nanoMIPs are high. The linear dynamic concentration range extended from 10 pM to 676 nM DUL, outmatching all those previously reported by several orders of magnitude. The DPV and EIS chemosensors engineered herein are suitable for determining DUL at S/N = 3 with the LOD of 1.6 and 2.0 pM, respectively, which is well below the limit adopted in clinical practice (33 nM). Nevertheless, the DPV chemosensor outperforms the EIS chemosensor in all aspects of DUL chemosensing. The DPV peaks for the DUL analyte in the presence of interferences,

commonly encountered in human plasma, were at least five times smaller than for this analyte in blank PBS (pH = 7.2). The chemosensor durability (at least two months), reusability (at least five times), and repeatability are appreciably high. Hence, the chemosensor is beneficial for clinical analysis in health protection due to the possibility of DUL monitoring in human plasma.

# Chapter 6

## Research summary and future perspectives

Over the years, the quantification of pharmaceutical drugs has gained researchers' attention as it is vital for diagnosis and the pharmaceutical industry. For quantifying drugs, chemosensors have been successfully used so far. However, being multi-parametric systems, their fabrication was challenging. Moreover, in this case, the "one optimization, fits all" strategy does not work well, and every individual target demands its design. Therefore, understanding the mechanism of interactions between the template molecule and the functional moieties plays an important role. In this regard, huge efforts are made. Nowadays, the composition of the most stable pre-polymerization complexes is determined using quantum-chemical calculations for designing molecular cavities.

The present research used molecularly imprinted acrylate and carbazole polymers as the recognition units to build sensitive and selective chemosensors for quantifying chosen drugs. As the first step, fifteen monomers of carbazole moiety were synthesized, out of which three of thiophene-appended carbazole monomers were newly designed. Later, three DPV and/or EIS chemosensors were successfully designed, fabricated, and tested for CIL and DUL drugs. Two separate CIL electrochemical chemosensors were prepared based on two different molecularly imprinted polymer recognition units, i.e., MIP nanoparticles (nanoMIPs) and MIP films. Relatively high values of apparent imprinting factors confirmed the formation of selective molecular cavities in the imprinted polymers.

CIL imprinted nanoMIPs were prepared using functional acrylic-based monomers, immobilized on the surface of the transducers in polytyramine film. Interactions of the MIP cavities, formed by functional acrylic or thiophene appended carbazole monomers, with CIL were simulated with MM, MD, and DFT. The LOD at the signal-to-noise ratio of  $S/N = 3$  in DPV and EIS determinations using the ferrocene redox probe in a "gate effect" mode was  $93.5 (\pm 2.2)$  and  $86.5 (\pm 4.6)$  nM CIL, respectively, and the linear dynamic concentration range stretched from 134 nM to 2.58  $\mu$ M CIL in both techniques. That is, the detectability of the CIL EIS chemosensor was higher than that of the DPV chemosensor. The chemosensor response to CIL and dhCIL was tested using voltammetric and EIS techniques. Those revealed

appreciable selectivities to the interferences, including cholesterol and glucose, and structurally similar dehydroaripiprazole in human plasma. Thiophene-appended carbazole monomers were used as functional and cross-linking monomers to prepare MIP films. Chemosensors were exhaustively characterized spectroscopically using PM-IRRAS spectroscopy and microscopically using AFM and SEM. In this case, short (<5 min) time of CIL determination, operation simplicity, repeatability, low cost, lower LODs were achieved. Moreover, CIL and dhCIL cross-validation in spiked human plasma by LC-MS confirmed the MIP chemosensing.

For DUL chemosensing, nanoMIPs imprinted with DUL were prepared by precipitation polymerization of chosen functional acrylic monomers. Those nanoMIPs were then uniformly embedded in a polytyramine film supported on the SWCNTs nanoarchitecture. The MM and MD simulations, followed by DFT calculations, selected the functional and cross-linking monomers best-suited to reach the highest nanoMIPs affinity and sensitivity to the DUL analyte. Both the DPV and EIS chemosensors were suitable for determining DUL with the LOD of 1.6 and 2.0 pM, respectively, i.e., it is well below the 33 nM limit adopted in clinical practice. DPV peaks measured after injecting interfering compounds, commonly present in human plasma, were at least five times smaller than those for DUL. The chemosensor was highly stable (at least two months) and reusable (at least 5 times).

Interestingly, from the synthesis point of view, some of the monomers studied did not form polymer films upon electro-oxidation while remaining electrochemically active. Spectroelectrochemical studies of the selected monomers' electro-oxidation using UV-vis-NIR and EPR spectroscopy were conducted to understand the reasons for this behavior. Comparative studies of the monomers undergoing electro-oxidative polymerization and those undergoing electro-oxidation without polymerization allowed rationalizing the observed behavior. The subsequent quantum-chemistry modeling of the selected monomers capable and incapable of electropolymerization provided insight into the radical formation and electronic structure of the cation radicals formed.

MIPs have tremendous potential for applications as chemosensors and increasing need in the field of chemistry, as well as for biotechnology. Lastly, their applications to the chemosensing of pharmaceuticals provide exciting prospects for industries and great benefits for society.

The present thesis covers essential information from exploiting the conducting films to depositing the nanoMIPs on different substrates using various components to prepare the sensing platforms. Therefore, it is envisioned that the information provided by this thesis will assist future research in developing a hybrid sensor platform capable of detecting other medications of interest with higher selectivity, stability, and repeatability. Moreover, additional issues arise due to the acquired knowledge, which may be addressed in future research.

### **Challenges to overcome in future**

1. All human plasma samples were ten times diluted before analyte determination. The analyte concentrations in spiked plasma samples were known. However, measuring the undiluted plasma containing an unknown analyte concentration would be impressive. For that, future collaborations with the hospitals and other medical institutions would be valuable.
2. What is the likelihood of the existing model being commercialized and evolved into a point-of-care device? For that, several improvements should be made in terms of practical design. The concentration of each component used for chemosensor fabrication, its sample volume, nanoMIPs and SWCNTs sedimentation time on the electrode surface, and post-measurement disposal procedure are pivotal. The precision and cost of the hand-held equipment are also relevant. However, if money and research skills are not limited, it is possible to rapidly develop miniaturization and large-scale quality control.

## Appendix

### A1. Spectral characterization of FM1 and FM2 monomer and their polymer

The normalized absorption and emission spectrum maxima for FM1 in dichloromethane was recorded at  $\lambda_{\text{abs, max}} = 317 \text{ nm}$ ,  $345 \text{ nm}$ ,  $\lambda_{\text{em, max}} = 484 \text{ nm}$ , and whereas for FM2 appeared at  $\lambda_{\text{abs, max}} = 267, 312, 341 \text{ nm}$ , and  $\lambda_{\text{em, max}} = 386 \text{ nm}$  and  $406 \text{ nm}$  (Figure A-1(a,b)). However, 1 mM monomers in 0.1 M TBA( $\text{PF}_6$ ) anhydrous dichloromethane solution were electrochemically oxidized utilizing ten potentiodynamic cycles on the ITO electrode vs. Ag pseudo-reference electrode at a scan rate of  $50 \text{ mV s}^{-1}$  to deposit the polymeric films of FM1 and FM2. The normalized absorption for FM1 and FM2 polymer films were observed at  $\lambda_{\text{abs, max, polymer}} = 270, 398 \text{ nm}$  and  $\lambda_{\text{abs, max, polymer}} = 250, 324, 393 \text{ nm}$ , respectively. It can be concluded that polymer shows a bathochromic shift.

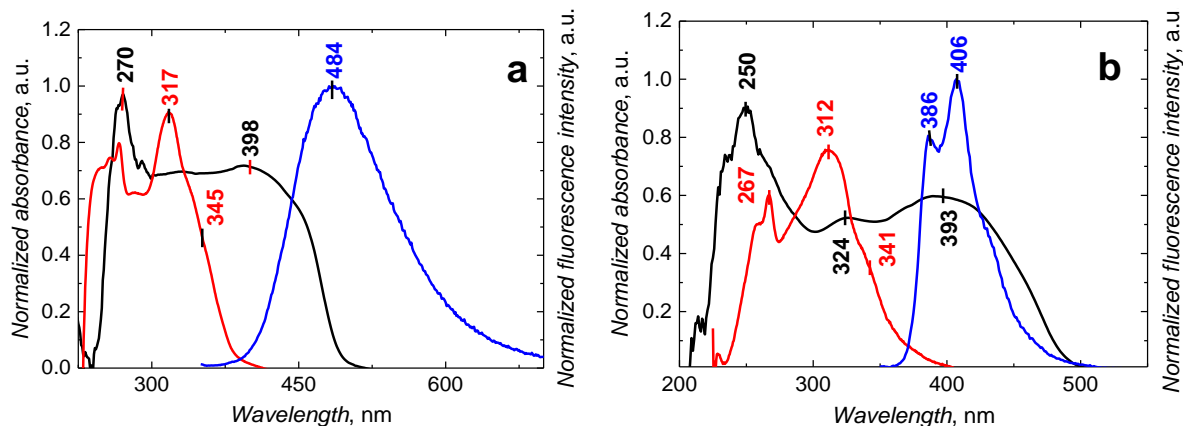
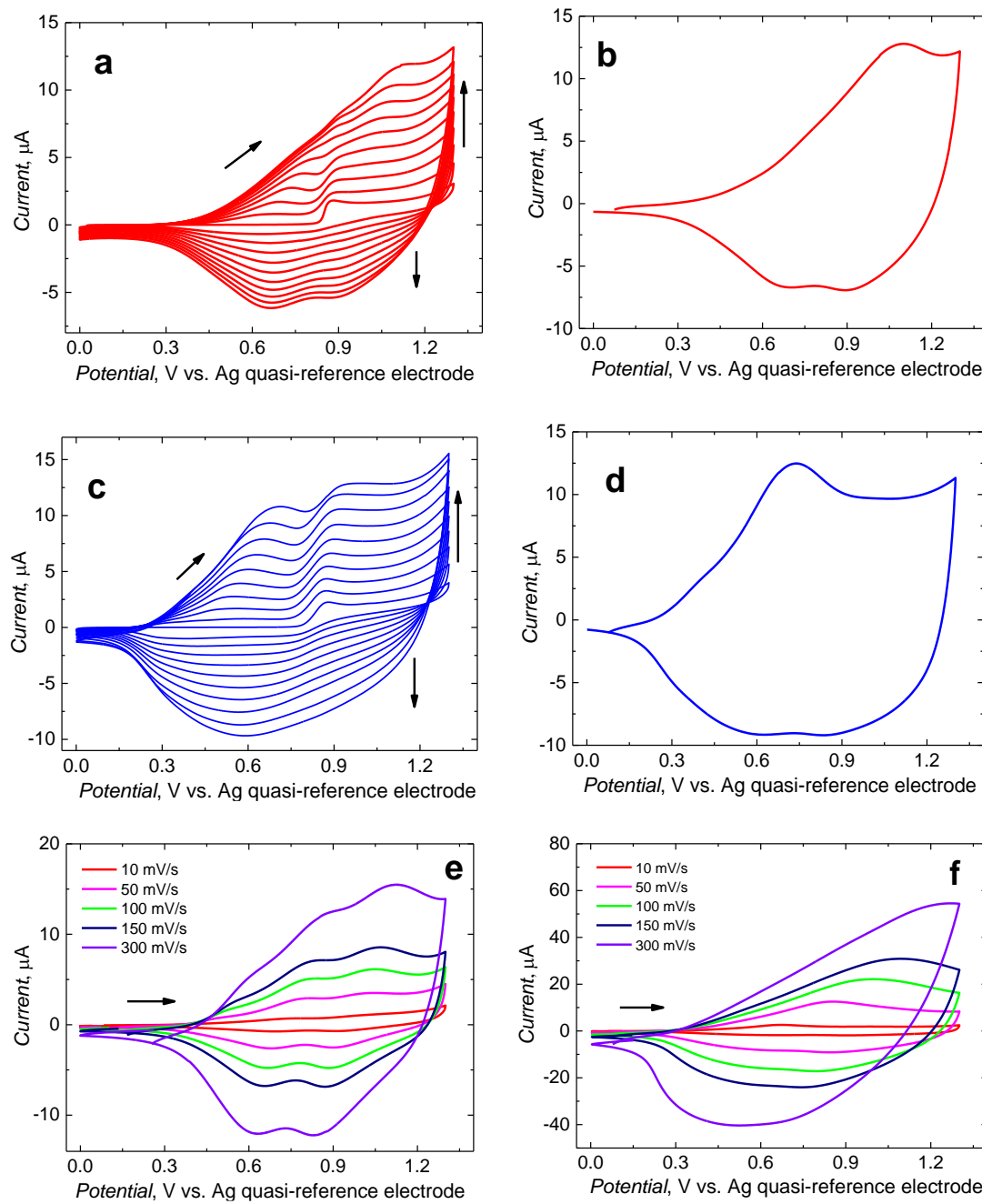


Figure A-1. Normalized absorption of monomers (red) and its polymer films (black) and their normalized emission spectra (blue) recorded for 0.5 mM (a) FM1 and (b) FM2 in dichloromethane. Polymer films were deposited on the ITO electrode potentiodynamically using five cycles in 0.1 M (TBA) $\text{PF}_6$  in DCM at  $50 \text{ mV s}^{-1}$ .

### A2. Simultaneous electrochemical depositing and characterizing the FM1 and FM2 polymer films

The FM1 and FM2 monomers' potentiodynamic electro-oxidation utilizing ten potentiodynamic cycles is demonstrated in Figures A-2a and 2c. Both FM1 and FM2 showed irreversible anodic peaks at the same potentials, 0.87 V and 0.87 V vs. Ag quasi-reference electrode, respectively, in the first anodic scan. In the second cycle, one broad cathodic and

one broad anodic peak emerged both for FM1 and FM2. Moreover, with each subsequent cycle, the peaks for both monomers increased, confirming conducting film deposition.



**Figure A-2.** Multi-cyclic potentiodynamic curves for (a) electropolymerization of 1 mM FM1 (b) doping-dedoping of the polymerized FM1, (c) electropolymerization of 1 mM FM2, and (d) doping-dedoping of polymerized FM2, recorded at the Pt disk electrode in 0.1 M (TBA)PF<sub>6</sub> in DCM at 50 mV s<sup>-1</sup>. (e) and (f) CV curves for the polymerized FM1 and FM2 in 0.1 M (TBA)PF<sub>6</sub>, in DCM, for different potential scan rates.

Then, the electrochemical activity of the deposited polymerized FM1 and FM2 films was examined by performing CV measurements in the monomers' absence. The film-coated electrodes were rinsed with DCM between the potential cycling in solutions containing then not containing the monomers. The polymer films showed broad cathodic and anodic peaks (Figures A-2b and 1d), characteristic of doping-dedoping of highly conductive polymers. This feature was more pronounced for the polymerized FM2 film. Furthermore, one ill-defined peak at 1.10 V and two cathodic peaks at 0.69 and 0.89 V were seen for the polymerized FM1 (Figure A-2b). For the polymerized FM2, the anodic peak at 0.75 V and two cathodic peaks at 0.62 and 0.83 V were seen (Figure A-2d).

Moreover, the potential scan rate dependence of the peaks was examined for 300, 150, 100, 50, 10 mV s<sup>-1</sup> (Figures A-2e and 2f).

#### *A3. SEM imaging of the deposited polymer films of FM1 and FM2*

The SEM served to carry out morphological studies of polymer films of thiophene-appended carbazole samples. The SEM images were taken at different magnifications (Figure A-3). Top-view SEM images (Figure A-3a' and 3b') reveal a polymerized FM2 film homogeneously deposited on the ITO-layered glass slide. The film of polymerized FM1 presents a characteristic cauliflower-like morphological structure (Figures A-3a and 3b), while FM2 exhibits a globular structure (Figures A-3a' and 3b'). Moreover, higher magnification images of globules of the FM2 film display more effective plentiful ion diffusion pathways into and out of the polymer films during the redox process. Furthermore, the functional monomers' structures were DFT optimized (Figures A-3c and 3c').

#### *A4. Preparing an artificial Nortrol serum solution*

For the artificial serum sample study, 0.5 mL of commercial Nortrol serum was diluted with 4.5 mL of deionized water to prepare a stock solution. A 500-µL sample of this solution was then diluted with 4.5 mL of acetonitrile, resulting in solid precipitation. This solid was then centrifuged off at 10 000 rpm for 10 min at 25 °C. The supernatant, i.e., 100 times diluted artificial serum, was made 10 mM in ferrocene and 0.1 M in (TBA)ClO<sub>4</sub>. Similarly, 200, 500, and 1000 times diluted artificial serum samples were prepared. Then, CIL added at predefined concentrations was determined.

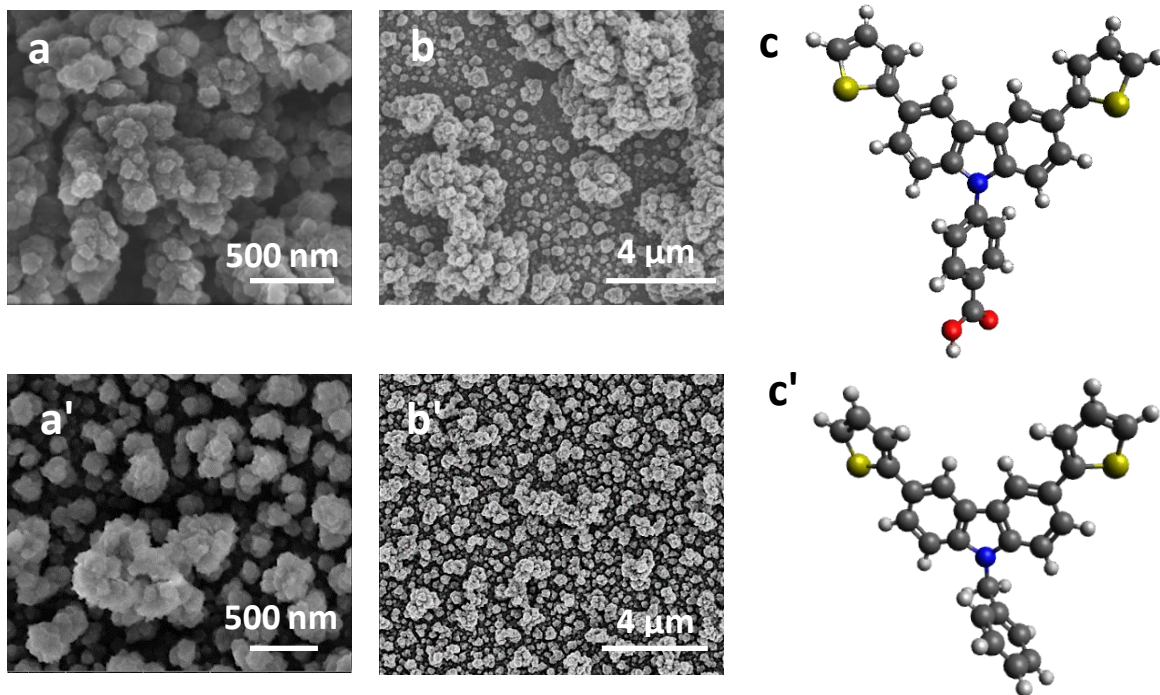


**Figure A-3.** (a) and (a') High, and (b) and (b'), and (a') and (b'), and FM2 polymer film deposited on the ITO electrode. (c) and (c') the FM1 and FM2 structures optimized with the DFT method at the B3LYP 6-311G (d, p) level of approximation.

#### A5. NanoMIPs chemosensor performance towards CIL determination in diluted artificial serum

For practical applications of chemosensors, their performance in real samples should be measured to estimate the matrix's effect. Toward that, the nanoMIP-immobilized polytyramine film was employed to determine CIL in an artificial Nortrol serum sample at different dilutions (Figure A-4a). The slope of the constructed calibration curve for CIL determination in 1000, 500, 200, and 100 times diluted serum with a 10 mM ferrocene and 0.1 M (TBA) $\text{ClO}_4$  were found to be 0.15 ( $\pm 0.01$ ), 0.25 ( $\pm 0.05$ ), 0.16 ( $\pm 0.02$ ), and 0.33 ( $\pm 0.01$ )  $\mu\text{A}/\log \mu\text{M}$  (Figure A-4a). The best CIL quantification results were obtained in 100 times diluted artificial serum. For comparison, solutions of different CIL concentrations were added to the acetonitrile-water (9 : 1,  $v : v$ ) mixture of 10 mM ferrocene and 0.1 M (TBA) $\text{ClO}_4$ . The constructed calibration curve slope of 0.33 ( $\pm 0.01$ )  $\mu\text{A}/\log \mu\text{M}$  for CIL determination in the diluted serum samples (curve  $I'$  in Figure A-4b) was very close to that of the calibration curve of 0.33 ( $\pm 0.02$ )  $\mu\text{A}/\log \mu\text{M}$  for CIL determination in an acetonitrile-water

(9 : 1,  $v : v$ ) solution (Figure A-4b, curve 2'). However, the normalized DPV peak current was higher for each concentration because of the matrix effect.

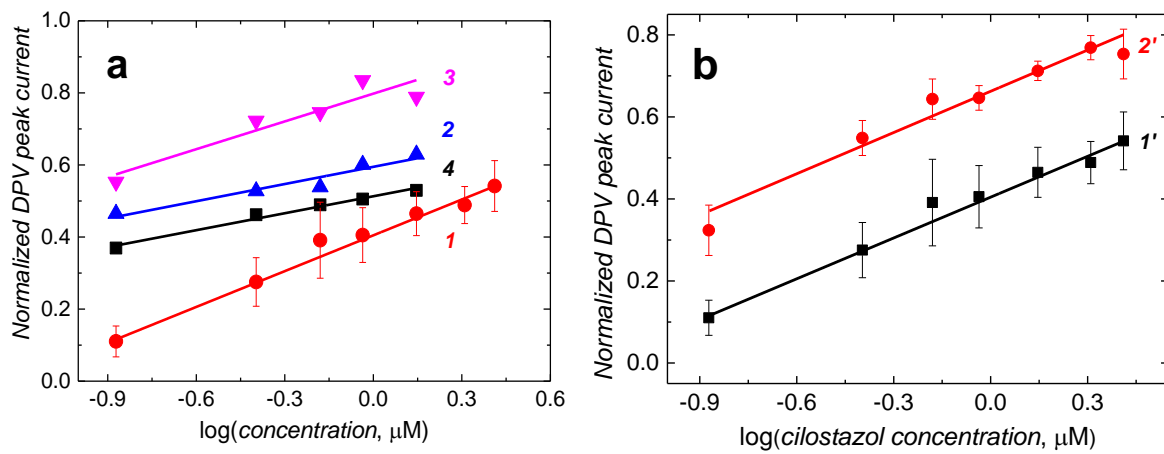


**Figure A-4.** Semilogarithmic DPV calibration plots for CIL at electrodes coated with the polytyramine film with immobilized nanoMIPs in 10 mM ferrocene and 0.1 M (TBA) $\text{ClO}_4$  (a) at different artificial serum dilutions (b) 100 times diluted artificial Nortrol serum (1') and in an acetonitrile-water (9 : 1,  $v : v$ ) solution (2'). Calibration curves 1, 2, 3, and 4 represent 100, 200, 500, and 1000 times diluted artificial serum.

**Table A1.** Theoretical electronic absorption spectra of CNZ1 and FM2 monomers in acetonitrile calculated at the TD-DFT level of theory.

Compound	Molecular charge	Electronic state transition	$\lambda_{\max}$ , nm	Excitation energy, eV	Oscillator strength, a.u.	Electronic transition
CNZ1	0	S1: 77→78	354.21	3.50	0.125	HOMO→LUMO
		S2: 77→79	327.20	3.79	0.049	HOMO→LUMO+1
	+1	S2: 76B→77B	1494.17	0.83	0.1062	HOMO-1→HOMO
		S3: 75B→77B	710.64	1.74	0.1938	HOMO-1→HOMO
	+2	S2: 75→77	1594.72	0.778	0.062	HOMO-1→LUMO
		S3: 74→77	703.74	1.762	0.480	HOMO-2→LUMO
		S4: 73→77	660.28	1.878	0.138	HOMO-3→LUMO
	+3	S5: 72→77	541.35	2.290	0.061	HOMO-4→LUMO
		S6: 71→77	472.96	2.622	0.025	HOMO-5→LUMO
		S1: 119→120	365.90	3.389	0.126	HOMO→LUMO
FM3	0	S3: 119→122	336.27	3.687	0.504	HOMO→LUMO+2
		S4: 118→120	315.23	3.933	0.060	HOMO-1→LUMO
		S5: 119→123	313.31	3.957	0.289	HOMO→LUMO+3
		S6: 118→121	306.04	4.051	0.505	HOMO-1→LUMO+1
		S1: 118B→119B	1878.27	0.660	0.113	HOMO-1→HOMO
		S2: 117B→119B	1374.66	0.902	0.071	HOMO-2→HOMO
	+1	S3: 116B→119B	1030.26	1.203	0.198	HOMO-3→HOMO
		S4: 115B→119B	840.57	1.475	0.193	HOMO-4→HOMO
		S6: 113B→119B	762.28	1.626	0.0055	HOMO-6→HOMO
	+2	S1: 118→119	2028.08	0.6114	0.0880	HOMO→LUMO
		S2: 117→119	1799.76	0.6888	0.0802	HOMO-1→LUMO
		S3: 116→119	950.89	1.3038	0.2921	HOMO-2→LUMO
		S4: 114→119	920.54	1.3470	0.0145	HOMO-4→LUMO
		S5: 113→119	919.06	1.3491	0.0260	HOMO-5→LUMO
		S6: 115→119	877.09	1.4136	0.539	HOMO-3→LUMO

**Table A2.** Theoretical electronic absorption spectra of CNZ1a and FM3a dimers in acetonitrile calculated at the TD-DFT level of theory.

Compound	Molecular charge	Electronic state transition	$\lambda_{\text{max}}$ , nm	Excitation energy, eV	Oscillator strength, a.u.	Electronic transition
CNZ1a	0	S1: 153→154	386.07	3.2115	0.5412	HOMO→LUMO
		S2: 153→155	378.55	3.2752	0.0114	HOMO→LUMO+1
		S3: 153→156	369.50	3.3554	0.0026	HOMO→LUMO+2
		S4: 153→158	341.49	3.6307	0.0700	HOMO-3→LUMO+4
		S5: 153→157	338.16	3.6664	0.9231	HOMO-4→LUMO+3
		S6: 152→154	329.36	3.7644	0.0183	HOMO-1→LUMO
	+1	S1: 152B→153B	1998.88	0.6203	0.4606	HOMO-1→HOMO
		S2: 151B→153B	1403.93	0.8831	0.0015	HOMO-2→HOMO
		S3: 150B→153B	1311.23	0.9456	0.1123	HOMO-3→HOMO
		S4: 149B→153B	1212.55	1.0225	0.0010	HOMO-4→HOMO
		S5: 148B→153B	1051.12	1.1795	0.1589	HOMO-5→HOMO
		S6: 147B→153B	728.91	1.7010	0.0001	HOMO-6→HOMO
FM3a	+2	S1: 152→153	1753.99	0.7069	0.4436	HOMO→LUMO
		S2: 151→153	1505.85	0.8234	0.0160	HOMO-1→LUMO
		S3: 150→153	1498.12	0.8276	0.1385	HOMO-2→LUMO
		S4: 149→153	1396.70	0.8877	0.0013	HOMO-3→LUMO
		S5: 148→153	1015.91	1.2204	0.8282	HOMO-4→LUMO
		S6: 147→153	716.09	1.7314	0.0044	HOMO-5→LUMO
	0	S1: 237→238	520.96	2.3799	2.0854	HOMO→LUMO
		S2: 237→239	430.95	2.8770	0.0067	HOMO→LUMO+1
		S3: 237→240	429.21	2.8886	0.1781	HOMO→LUMO+2
		S4: 236→238	422.36	2.9355	0.0079	HOMO-1→LUMO
		S5: 237→241	408.12	3.0379	0.019	HOMO→LUMO+3
		S6: 237→242	407.54	3.0423	0.0012	HOMO→LUMO+4
+1	0	S1: 236B→237B	2022.54	0.6130	0.7481	HOMO-1→HOMO
		S2: 235B→237B	1582.96	0.7832	0.0030	HOMO-2→HOMO
		S3: 234B→237B	1024.29	1.2104	0.2670	HOMO-3→HOMO
	+1	S4: 233B→237B	945.82	1.3109	0.0009	HOMO-4→HOMO
		S5: 232B→237B	872.82	1.4205	0.0730	HOMO-5→HOMO

	S6: 231B→237B	760.26	1.6308	0.0011	HOMO-6→HOMO
	S1: 236→237	2827.68	0.4385	1.7597	HOMO→LUMO
	S2: 235→237	1760.78	0.7041	0.0097	HOMO-1→LUMO
+2	S3: 234→237	1317.82	0.9408	0.4044	HOMO-2→LUMO
	S4: 233→237	1274.27	0.9730	0.0009	HOMO-3→LUMO
	S5: 232→237	995.30	1.2457	0.4764	HOMO-4→LUMO
	S6: 231→237	816.67	1.5182	0.0070	HOMO-5→LUMO

## References

- (1) Qian, L.; Durairaj, S.; Prins, S.; Chen, A. Nanomaterial-Based Electrochemical Sensors and Biosensors for the Detection of Pharmaceutical Compounds. *Biosens. Bioelectron.* **2021**, *175*, 112836.
- (2) Holthoff, E. L.; Bright, F. V. Molecularly Tempered Materials in Chemical Sensing. *Anal. Chim. Acta* **2007**, *594*, 147–161.
- (3) Hedegaard, H.; Miniño, A. M.; Warner, M. Drug Overdose Deaths in the United States, 1999–2019. *NCHS Data Brief* **2020**, No. 394, 1–8.
- (4) Doggui, R.; Adib, K.; Baldacchino, A. Understanding Fatal and Non-Fatal Drug Overdose Risk Factors: Overdose Risk Questionnaire Pilot Study—Validation. *Front. Pharmacol.* **2021**, *12* (September), 1–8.
- (5) European Monitoring Centre for Drugs and Drug Addiction. *Drug-Related Deaths and Mortality in Europe*; 2019.
- (6) Yamamoto, J. Recent Trends of Drug Abuse in Japan. *Ann. N. Y. Acad. Sci.* **2004**, *1025* (1), 430–438.
- (7) Jones, C. M.; Houry, D.; Han, B.; Baldwin, G.; Vivolo-Kantor, A.; Compton, W. M. Methamphetamine Use in the United States: Epidemiological Update and Implications for Prevention, Treatment, and Harm Reduction. *Ann. N. Y. Acad. Sci.* **2021**.
- (8) Tucker, G. T. Personalized Drug Dosage – Closing the Loop. *Pharm. Res.* **2017**, *34* (8), 1539–1543.
- (9) Hulanicki, A.; Glab, S.; Ingman, F. Chemical Sensors: Definitions and Classification. *Pure Appl. Chem.*, **1991**, *63*, 1247. **1991**, *63* (9), 1247–1250.
- (10) Thevenot, D. R.; Tóth, K.; Durst, R. A.; Wilson, S. G. Electrochemical Biosensors: Recommended Definitions and Classification. *Pure Appl. Chem.* **1999**, *71* (12), 2333–2348.
- (11) Shaw, L.; Dennany, L. Applications of Electrochemical Sensors: Forensic Drug Analysis. *Curr. Opin. Electrochem.* **2017**, *3* (1), 23–28.
- (12) Yang, A.; Yan, F. Flexible Electrochemical Biosensors for Health Monitoring. *ACS Appl. Electron. Mater.* **2021**, *3* (1), 53–67.
- (13) Srivastava, A. K.; Upadhyay, S. S.; Rawool, C. R.; Punde, N. S.; Rajpurohit, A. S. Voltammetric Techniques for the Analysis of Drugs Using Nanomaterials Based Chemically Modified Electrodes. *Curr. Anal. Chem.* **2019**, *15* (3), 249–276.
- (14) Hammarling, K.; Engholm, M.; Andersson, H.; Sandberg, M.; Nilsson, H. E. Broad-Range Hydrogel-Based PH Sensor with Capacitive Readout Manufactured on a Flexible Substrate. *Chemosensors* **2018**, *6* (30), 1–15.
- (15) Choodum, A.; Kanatharana, P.; Wongniramaikul, W.; NicDaeid, N. A Sol-Gel Colorimetric Sensor for Methamphetamine Detection. *Sensors Actuators, B Chem.* **2015**, *215*, 553–560.
- (16) Helwig, A.; Müller, G.; Paul, S. Health Monitoring of Aviation Hydraulic Fluids Using

- Opto-Chemical Sensor Technologies. *Chemosensors* **2020**, *8* (131), 1–20.
- (17) Scarpa, E.; Mastronardi, V. M.; Guido, F.; Algieri, L.; Qualtieri, A.; Fiammengo, R.; Rizzi, F.; De Vittorio, M. Wearable Piezoelectric Mass Sensor Based on PH Sensitive Hydrogels for Sweat PH Monitoring. *Sci. Rep.* **2020**, *10* (1), 1–10.
  - (18) Pinet, É.; Hamel, C.; Glišić, B.; Inaudi, D.; Miron, N. Health Monitoring with Optical Fiber Sensors: From Human Body to Civil Structures. In *Proc.SPIE*; 2007; Vol. 6532.
  - (19) Guan, X.; Wang, Z.; Zhao, W.; Huang, H.; Wang, S.; Zhang, Q.; Zhong, D.; Lin, W.; Ding, N.; Peng, Z. Flexible Piezoresistive Sensors with Wide-Range Pressure Measurements Based on a Graded Nest-like Architecture. *ACS Appl. Mater. Interfaces* **2020**, *12* (23), 26137–26144.
  - (20) Ballard, Z. S.; Joung, H. A.; Goncharov, A.; Liang, J.; Nugroho, K.; Di Carlo, D.; Garner, O. B.; Ozcan, A. Deep Learning-Enabled Point-of-Care Sensing Using Multiplexed Paper-Based Sensors. *NPJ Digit. Med.* **2020**, *3* (66), 1–8.
  - (21) Manmana, Y.; Kubo, T.; Otsuka, K. Recent Developments of Point-of-Care (POC) Testing Platform for Biomolecules. *TrAC - Trends Anal. Chem.* **2021**, *135*, 116160.
  - (22) Canals, J.; Franch, N.; Alonso, O.; Vilà, A.; Diéguez, A. A Point-of-Care Device for Molecular Diagnosis Based on CMOS SPAD Detectors with Integrated Microfluidics. *Sensors (Switzerland)* **2019**, *19* (3), 445.
  - (23) Kosack, C. S.; Page, A. L.; Klatser, P. R. A Guide to Aid the Selection of Diagnostic Tests. *Bull. World Heal. Organ.* **2017**, *95* (9), 639–645.
  - (24) Amalfitano, E.; Karlikow, M.; Norouzi, M.; Jaenes, K.; Cicek, S.; Masum, F.; Sadat Mousavi, P.; Guo, Y.; Tang, L.; Sydor, A.; Ma, D.; Pearson, J. D.; Trcka, D.; Pinette, M.; Ambagala, A.; Babiuk, S.; Pickering, B.; Wrana, J.; Bremner, R.; Mazzulli, T.; Sinton, D.; Brumell, J. H.; Green, A. A.; Pardee, K. A Glucose Meter Interface for Point-of-Care Gene Circuit-Based Diagnostics. *Nat. Commun.* **2021**, *12* (1), 1–10.
  - (25) Luppa, P. B. Point-of-Care Testing at the Interface of Emerging Technologies and New Clinical Applications. *J. Lab. Med.* **2020**, *44* (2), 59–61.
  - (26) Saylan, Y.; Denizli, A. Fundamentals and Applications of Molecularly Imprinted Systems. In *Molecular Imprinting for Nanosensors and Other Sensing Applications*; Denizli, A., Ed.; Elsevier: Ankara, 2021; pp 1–17.
  - (27) Belbruno, J. J. Molecularly Imprinted Polymers. *Chem. Rev.* **2019**, *119*, 94–119.
  - (28) Haupt, K.; Mosbach, K. Molecularly Imprinted Polymers and Their Use in Biomimetic Sensors. *Chem. Rev.* **2000**, *100* (3), 2495–2504.
  - (29) Adumitrăchioaie, A.; Tertiş, M.; Cernat, A.; Săndulescu, R.; Cristea, C. Electrochemical Methods Based on Molecularly Imprinted Polymers for Drug Detection. A Review. *Int. J. Electrochem. Sci.* **2018**, *13* (3), 2556–2576.
  - (30) Wang, L.; Zhi, K.; Zhang, Y.; Liu, Y.; Zhang, L.; Yasin, A.; Lin, Q. Molecularly Imprinted Polymers for Gossypol via Sol-Gel, Bulk, and Surface Layer Imprinting-A Comparative Study. *Polymers (Basel)*. **2019**, *11* (602).
  - (31) Mayes, A. G.; Whitcombe, M. J. Synthetic Strategies for the Generation of Molecularly Imprinted Organic Polymers. *Adv. Drug Deliv. Rev.* **2005**, *57* (12), 1742–1778.

- (32) Whitcombe, M. J.; Rodriguez, M. E.; Villar, P.; Vulfson, E. N. A New Method for the Introduction of Recognition Site Functionality into Polymers Prepared by Molecular Imprinting: Synthesis and Characterization of Polymeric Receptors for Cholesterol. *J. Am. Chem. Soc.* **1995**, *117* (27), 7105–7111.
- (33) Ramanavicius, S.; Ramanavicius, A. Conducting Polymers in the Design of Biosensors and Biofuel Cells. *Polymers (Basel)*. **2021**, *13* (1), 1–19.
- (34) Ramanavicius, S.; Jagminas, A.; Ramanavicius, A. Advances in Molecularly Imprinted Polymers Based Affinity Sensors (Review). *Polymers (Basel)*. **2021**, *13* (6), 974.
- (35) Rutkowska, M.; Płotka-Wasylka, J.; Morrison, C.; Wieczorek, P. P.; Namieśnik, J.; Marć, M. Application of Molecularly Imprinted Polymers in Analytical Chiral Separations and Analysis. *TrAC - Trends Anal. Chem.* **2018**, *102*, 91–102.
- (36) Ndunda, E. N.; Mizaikoff, B. Molecularly Imprinted Polymers for the Analysis and Removal of Polychlorinated Aromatic Compounds in the Environment: A Review. *Analyst* **2016**, *141* (11), 3141–3156.
- (37) Azizi, A.; Bottaro, C. S. A Critical Review of Molecularly Imprinted Polymers for the Analysis of Organic Pollutants in Environmental Water Samples. *J. Chromatogr. A*. **2020**, *1614*, 460603.
- (38) Liu, X.; Wang, X.; Tan, F.; Zhao, H.; Quan, X.; Chen, J.; Li, L. An Electrochemically Enhanced Solid-Phase Microextraction Approach Based on Molecularly Imprinted Polypyrrole/Multi-Walled Carbon Nanotubes Composite Coating for Selective Extraction of Fluoroquinolones in Aqueous Samples. *Anal. Chim. Acta* **2012**, *727*, 26–33.
- (39) Gao, R.; Su, X.; He, X.; Chen, L.; Zhang, Y. Preparation and Characterisation of Core-Shell CNTs@MIPs Nanocomposites and Selective Removal of Estrone from Water Samples. *Talanta* **2011**, *83* (3), 757–764.
- (40) Ahmad, O. S.; Bedwell, T. S.; Esen, C.; Garcia-Cruz, A.; Piletsky, S. A. Molecularly Imprinted Polymers in Electrochemical and Optical Sensors. *Trends Biotechnol.* **2019**, *37* (3), 294–309.
- (41) Puoci, F.; Cirillo, G.; Curcio, M.; Parisi, O. I.; Iemma, F.; Picci, N. Molecularly Imprinted Polymers in Drug Delivery: State of Art and Future Perspectives. *Expert Opin. Drug Deliv.* **2011**, *8* (10), 1379–1393.
- (42) Sharma, P. S.; Iskierko, Z.; Noworyta, K.; Cieplak, M.; Borowicz, P.; Lisowski, W.; D’Souza, F.; Kutner, W. Synthesis and Application of a “Plastic Antibody” in Electrochemical Microfluidic Platform for Oxytocin Determination. *Biosens. Bioelectron.* **2018**, *100*, 251–258.
- (43) Wulff, G. Enzyme-like Catalysis by Molecularly Imprinted Polymers. *Chem. Rev.* **2002**, *102* (1), 1–28.
- (44) Peeters, M.; Eersels, K.; Junkers, T.; Wagner, P. Molecularly Imprinted Polymers: Synthetic Receptors for Diagnostic Medical Devices. In *Molecularly Imprinted Catalysts - Principles, Syntheses, and Applications*; Li, S., Cao, S., Piletsky, S. A., Turner, A. P. F., Eds.; Elsevier: Amsterdam, 2016; pp 253–271.
- (45) Zaidi, S. A. Molecular Imprinted Polymers as Drug Delivery Vehicles. *Drug Deliv.*

**2016**, **23** (7), 2262–2271.

- (46) Xie, X.; Bu, Y.; Wang, S. Molecularly Imprinting: A Tool of Modern Chemistry for Analysis and Monitoring of Phenolic Environmental Estrogens. *Rev. Anal. Chem.* **2016**, **35** (2), 87–97.
- (47) Bedwell, T. S.; Whitcombe, M. J. Analytical Applications of MIPs in Diagnostic Assays: Future Perspectives. *Anal. Bioanal. Chem.* **2016**, **408** (7), 1735–1751.
- (48) Goud, K. Y.; Reddy, K. K.; Khorshed, A.; Kumar, V. S.; Mishra, R. K.; Oraby, M.; Ibrahim, A. H.; Kim, H.; Gobi, K. V. Electrochemical Diagnostics of Infectious Viral Diseases: Trends and Challenges. *Biosens. Bioelectron.* **2021**, **180** (February), 113112.
- (49) Yang, H. H.; Zhang, S. Q.; Tan, F.; Zhuang, Z. X.; Wang, X. R. Surface Molecularly Imprinted Nanowires for Biorecognition. *J. Am. Chem. Soc.* **2005**, **127** (5), 1378–1379.
- (50) Haupt, K.; Rangel, P. X. M.; Tse, B. B. S. Molecularly Imprinted Polymers : Antibody Mimics for Bioimaging and Therapy. *Chem. Rev.* **2020**, **120**, 9554–9582.
- (51) Vlatakis, G.; Andersson, L. I.; Müller, R.; Mosbach, K. Drug Assay Using Antibody Mimics Made by Molecular Imprinting. *Nature* **1993**, **361** (6413), 645–647.
- (52) Yarman, A.; Kurbanoglu, S.; Zebger, I.; Scheller, F. W. Simple and Robust: The Claims of Protein Sensing by Molecularly Imprinted Polymers. *Sens. Actuators, B* **2021**, **330**, 129369.
- (53) Denmark, D. J.; Mohapatra, S.; Mohapatra, S. S. Point-of-Care Diagnostics: Molecularly Imprinted Polymers and Nanomaterials for Enhanced Biosensor Selectivity and Transduction. *EuroBiotech J.* **2020**, **4** (4), 184–206.
- (54) Cui, F.; Zhou, Z.; Zhou, H. S. Molecularly Imprinted Polymers and Surface Imprinted Polymers Based Electrochemical Biosensor for Infectious Diseases. *Sensors* **2020**, **20** (4), 996.
- (55) Arshady, R.; Mosbach, K. Synthesis of Substrate-Selective Polymers by Host-Guest Polymerization. *Makromol. Chem.* **1981**, **182**, 687–692.
- (56) Andersson, L.; Sellergren, B.; Mosbach, K. Imprinting of Amino Acid Derivatives in Macroporous Polymers. *Tetrahedron Lett.* **1984**, **25** (45), 5211–5214.
- (57) Fresco-Cala, B.; Batista, A. D.; Cárdenas, S. Molecularly Imprinted Polymer Micro-And Nano-Particles: A Review. *Molecules*. 2020, pp 1–23.
- (58) Dong, C.; Shi, H.; Han, Y.; Yang, Y.; Wang, R.; Men, J. Molecularly Imprinted Polymers by the Surface Imprinting Technique. *Eur. Polym. J.* **2021**, **145**, 110231.
- (59) Poma, A.; Guerreiro, A.; Whitcombe, M. J.; Elena, V. Solid-Phase Synthesis of Molecularly Imprinted Polymer Nanoparticles with a Reusable Template – “ Plastic Antibodies .” *Adv Funct Mater.* **2013**, **23** (22), 2821–2827.
- (60) Yilmaz, E.; Mosbach, K.; Haupt, K. Influence of Functional and Cross-Linking Monomers and the Amount of Template on the Performance of Molecularly Imprinted Polymers in Binding Assays. *Anal. Commun.* **1999**, **36** (5), 167–170.
- (61) Cummins, W.; Duggan, P.; McLoughlin, P. Systematic Cross-Selectivity Study of the Factors Influencing Template Receptor Interactions in Molecularly Imprinted Nitrogen Heterocycles. *Biosens. Bioelectron.* **2006**, **22** (3), 372–380.

- (62) Tunc, Y.; Hasirci, N.; Yesilada, A.; Ulubayram, K. Comonomer Effects on Binding Performances and Morphology of Acrylate-Based Imprinted Polymers. *Polymer (Guildf)*. **2006**, *47* (20), 6931–6940.
- (63) Karlsson, J. G.; Karlsson, B.; Andersson, L. I.; Nicholls, I. A. The Roles of Template Complexation and Ligand Binding Conditions on Recognition in Bupivacaine Molecularly Imprinted Polymers. *Analyst* **2004**, *129* (5), 456–462.
- (64) Pérez-Moral, N.; Mayes, A. G. Noncovalent Imprinting in the Shell of Core-Shell Nanoparticles. *Langmuir* **2004**, *20* (9), 3775–3779.
- (65) Mijangos, I.; Navarro-Villoslada, F.; Guerreiro, A.; Piletska, E.; Chianella, I.; Karim, K.; Turner, A.; Piletsky, S. Influence of Initiator and Different Polymerisation Conditions on Performance of Molecularly Imprinted Polymers. *Biosens. Bioelectron.* **2006**, *22* (3), 381–387.
- (66) Vaughan, A. D.; Sizemore, S. P.; Byrne, M. E. Enhancing Molecularly Imprinted Polymer Binding Properties via Controlled/Living Radical Polymerization and Reaction Analysis. *Polymer (Guildf)*. **2007**, *48* (1), 74–81.
- (67) O'Shannessy, D. J.; Ekberg, B.; Mosbach, K. Molecular Imprinting of Amino Acid Derivatives at Low Temperature (0°C) Using Photolytic Homolysis of Azobisnitriles. *Anal. Biochem.* **1989**, *177* (1), 144–149.
- (68) Khumsap, T.; Corpuz, A.; Nguyen, L. T. Epitope-Imprinted Polymers: Applications in Protein Recognition and Separation. *RSC Adv.* **2021**, *11* (19), 11403–11414.
- (69) Wu, D.; Baaziz, W.; Gu, B.; Marinova, M.; Hernández, W. Y.; Zhou, W.; Vovk, E. I.; Ersen, O.; Safonova, O. V.; Addad, A.; Nuns, N.; Khodakov, A. Y.; Ordomsky, V. V. Surface Molecular Imprinting over Supported Metal Catalysts for Size-Dependent Selective Hydrogenation Reactions. *Nat. Catal.* **2021**, *4* (7), 595–606.
- (70) Lach, P.; Sharma, P. S.; Golebiewska, K.; Cieplak, M.; D’Souza, F.; Kutner, W. Molecularly Imprinted Polymer Chemosensor for Selective Determination of an N-Nitroso-l-Proline Food Toxin. *Chem. - A Eur. J.* **2017**, *23* (8), 1942–1949.
- (71) Wackerlig, J.; Lieberzeit, P. A. Molecularly Imprinted Polymer Nanoparticles in Chemical Sensing - Synthesis, Characterisation and Application. *Sens. Actuators B Chem.* **2015**, *207* (Part A), 144–157.
- (72) Rico-Yuste, A.; Carrasco, S. Molecularly Imprinted Polymer-Based Hybrid Materials for the Development of Optical Sensors. *Polymers (Basel)*. **2019**, *11* (7).
- (73) Blanco-López, M. C.; Lobo-Castañón, M. J.; Miranda-Ordieres, A. J.; Tuñón-Blanco, P. Electrochemical Sensors Based on Molecularly Imprinted Polymers. *TRAC - Trends Anal. Chem.* **2004**, *23* (1), 36–48.
- (74) Sharma, P. S.; Iskierko, Z.; Pietrzyk-Le, A.; D’Souza, F.; Kutner, W. Bioinspired Intelligent Molecularly Imprinted Polymers for Chemosensing: A Mini-Review. *Electrochim. Commun.* **2015**, *50*, 81–87.
- (75) Panahi, Y.; Motaharian, A.; Hosseini, M. R. M.; Mehrpour, O. High Sensitive and Selective Nano-Molecularly Imprinted Polymer Based Electrochemical Sensor for Midazolam Drug Detection in Pharmaceutical Formulation and Human Urine Samples. *Sensors Actuators, B Chem.* **2018**, *273* (June), 1579–1586.

- (76) Ye, L.; Mosbach, K. Polymers Recognizing Biomolecules Based on a Combination of Molecular Imprinting and Proximity Scintillation: A New Sensor Concept. *J. Am. Chem. Soc.* **2001**, *123* (12), 2901–2902.
- (77) Wang, J.; Cheng, Y.; Peng, R.; Cui, Q.; Luo, Y.; Li, L. Co-Precipitation Method to Prepare Molecularly Imprinted Fluorescent Polymer Nanoparticles for Paracetamol Sensing. *Colloids Surf. A Physicochem. Eng. Asp.* **2020**, *587* (November 2019), 124342.
- (78) Huang, J.; Tong, J.; Luo, J.; Zhu, Y.; Gu, Y.; Liu, X. Green Synthesis of Water-Compatible Fluorescent Molecularly Imprinted Polymeric Nanoparticles for Efficient Detection of Paracetamol. *ACS Sustain. Chem. Eng.* **2018**, *6* (8), 9760–9770.
- (79) Tan, S.; Jiang, J.; Yan, B.; Shen, G.; Yu, R. Preparation of a Novel Fluorescence Probe Based on Covalent Immobilization by Emulsion Polymerization and Its Application to the Determination of Metronidazole. *Anal. Chim. Acta* **2006**, *560* (1–2), 191–196.
- (80) Belmont, A. S.; Jaeger, S.; Knopp, D.; Niessner, R.; Gauglitz, G.; Haupt, K. Molecularly Imprinted Polymer Films for Reflectometric Interference Spectroscopic Sensors. *Biosens. Bioelectron.* **2007**, *22* (12), 3267–3272.
- (81) Motaharian, A.; Hosseini, M. R. M.; Naseri, K. Determination of Psychotropic Drug Chlorpromazine Using Screen-Printed Carbon Electrodes Modified with Novel MIP-MWCNTs Nano-Composite Prepared by Suspension Polymerization Method. *Sensors Actuators, B Chem.* **2019**, *288* (January), 356–362.
- (82) Li, Y.; Fu, Q.; Zhang, Q.; He, L. Preparation and Evaluation of Uniform-Size (-)-Ephedrineimprinted Polymeric Microspheres by Multi-Step Swelling and Suspension Polymerization. *Anal. Sci.* **2006**, *22* (10), 1355–1360.
- (83) Anderson, R. A.; Ariffin, M. M.; Cormack, P. A. G.; Miller, E. I. Comparison of Molecularly Imprinted Solid-Phase Extraction (MISPE) with Classical Solid-Phase Extraction (SPE) for the Detection of Benzodiazepines in Post-Mortem Hair Samples. *Forensic Sci. Int.* **2008**, *174* (1), 40–46.
- (84) Alanazi, K.; Garcia Cruz, A.; Di Masi, S.; Voorhaar, A.; Ahmad, O. S.; Cowen, T.; Piletska, E.; Langford, N.; Coats, T. J.; Sims, M. R.; Piletsky, S. A. Disposable Paracetamol Sensor Based on Electroactive Molecularly Imprinted Polymer Nanoparticles for Plasma Monitoring. *Sens. Actuators, B Chem.* **2021**, *329*, 129128.
- (85) Altintas, Z.; Guerreiro, A.; Piletsky, S. A.; Tothill, I. E. NanoMIP Based Optical Sensor for Pharmaceuticals Monitoring. *Sens. Actuators B Chem.* **2015**, *213*, 305–313.
- (86) Afzali, M.; Mostafavi, A.; Shamsipur, T. A Novel Electrochemical Sensor Based on Magnetic Core@shell Molecularly Imprinted Nanocomposite (Fe<sub>3</sub>O<sub>4</sub>@graphene Oxide@MIP) for Sensitive and Selective Determination of Anticancer Drug Capecitabine. *Arab. J. Chem.* **2020**, *13* (8), 6626–6638.
- (87) Mutharani, B.; Ranganathan, P.; Chen, S. M.; Tsai, H. C. Temperature-responsive Voltammetric Sensor Based on Stimuli-Sensitive Semi-Interpenetrating Polymer Network Conductive Microgels for Reversible Switch Detection of Nitrogen Mustard Analog Chlorambucil (Leukeran<sup>TM</sup>). *Electrochim. Acta* **2021**, *374*, 137866.
- (88) Alizadeh, T.; Ganjali, M. R.; Rafiei, F.; Akhoundian, M. Synthesis of Nano-Sized Timolol-Imprinted Polymer via Ultrasonication Assisted Suspension Polymerization in

Silicon Oil and Its Use for the Fabrication of Timolol Voltammetric Sensor. *Mater. Sci. Eng. C* **2017**, *77*, 300–307.

- (89) Khosrokhavar, R.; Motaharian, A.; Milani Hosseini, M. R.; Mohammadsadegh, S. Screen-Printed Carbon Electrode (SPCE) Modified by Molecularly Imprinted Polymer (MIP) Nanoparticles and Graphene Nanosheets for Determination of Sertraline Antidepressant Drug. *Microchem. J.* **2020**, *159* (April), 105348.
- (90) Menon, S.; Jesny, S.; Girish Kumar, K. A Voltammetric Sensor for Acetaminophen Based on Electropolymerized-Molecularly Imprinted Poly(o-Aminophenol) Modified Gold Electrode. *Talanta* **2018**, *179* (September 2017), 668–675.
- (91) Teng, Y.; Fan, L.; Dai, Y.; Zhong, M.; Lu, X.; Kan, X. Electrochemical Sensor for Paracetamol Recognition and Detection Based on Catalytic and Imprinted Composite Film. *Biosens. Bioelectron.* **2015**, *71*, 137–142.
- (92) El-Naby, E. H.; Kamel, A. H. Potential Transducers Based Man-Tailored Biomimetic Sensors for Selective Recognition of Dextromethorphan as an Antitussive Drug. *Mater. Sci. Eng. C* **2015**, *54*, 217–224.
- (93) Paquin, F.; Rivnay, J.; Salleo, A.; Stingelin, N.; Silva, C. Multi-Phase Semicrystalline Microstructures Drive Exciton Dissociation in Neat Plastic Semiconductors. *J. Mater. Chem. C* **2015**, *3*, 10715–10722.
- (94) Veith, C.; Diot-Néant, F.; Miller, S. A.; Allais, F. Synthesis and Polymerization of Bio-Based Acrylates: A Review. *Polym. Chem.* **2020**, *11* (47), 7452–7470.
- (95) Wang, S.; Shuai, L.; Saha, B.; Vlachos, D. G.; Epps, T. H. From Tree to Tape: Direct Synthesis of Pressure Sensitive Adhesives from Depolymerized Raw Lignocellulosic Biomass. *ACS Cent. Sci.* **2018**, *4* (6), 701–708.
- (96) He, F.; Jin, K.; Sun, J.; Fang, Q. Biobased Anethole/Polyacrylate Cross-Linked Materials with Good Transparency and High Thermostability. *ACS Sustain. Chem. Eng.* **2018**, *6* (3), 3575–3579.
- (97) Sellergren, B. Imprinted Chiral Stationary Phases in High-Performance Liquid Chromatography. *J. Chromatogr. A* **2001**, *906* (1–2), 227–252.
- (98) Chaves, A. R.; Chiericato Júnior, G.; Queiroz, M. E. C. Solid-Phase Microextraction Using Poly(Pyrrole) Film and Liquid Chromatography with UV Detection for Analysis of Antidepressants in Plasma Samples. *J. Chromatogr., B Anal. Technol. Biomed. Life Sci.* **2009**, *877* (7), 587–593.
- (99) Karnka, R.; Chaiyasat, P.; Chaiyasat, A. Synthesis of Uniform and Stable Molecularly Imprinted Polymer Particles by Precipitation Polymerization. *Orient. J. Chem.* **2017**, *33* (5), 2370–2376.
- (100) Korposh, S.; Chianella, I.; Guerreiro, A.; Caygill, S.; Piletsky, S.; James, S. W.; Tatam, R. P. Selective Vancomycin Detection Using Optical Fibre Long Period Gratings Functionalised with Molecularly Imprinted Polymer Nanoparticles. *Analyst* **2014**, *139* (9), 2229–2236.
- (101) Mazzotta, E.; Turco, A.; Chianella, I.; Guerreiro, A.; Piletsky, S. A.; Malitestà, C. Solid-Phase Synthesis of Electroactive Nanoparticles of Molecularly Imprinted Polymers. A Novel Platform for Indirect Electrochemical Sensing Applications. *Sensors Actuators,*

*B Chem.* **2016**, *229*, 174–180.

- (102) Ye, L.; A. G. Cormack, P.; Mosbach, K. Molecularly Imprinted Monodisperse Microspheres for Competitive Radioassay. *Anal. Commun.* **1999**, *36* (2), 35–38.
- (103) Li, K.; Stöver, H. D. H. Synthesis of Monodisperse Poly(Divinylbenzene) Microspheres. *J. Polym. Sci. Part A Polym. Chem.* **1993**, *31* (13), 3257–3263.
- (104) Li, W.-H.; Stöver, H. D. H. Monodisperse Cross-Linked Core–Shell Polymer Microspheres by Precipitation Polymerization. *Macromolecules* **2000**, *33* (12), 4354–4360.
- (105) Yang, S.; Shim, S. E.; Lee, H.; Kim, G. P.; Choe, S. Size and Uniformity Variation of Poly(MMA-Co-DVB) Particles upon Precipitation Polymerization. *Macromol. Res.* **2004**, *12* (5), 519–527.
- (106) Eun Shim, S.; Yang, S.; Choe, S. Mechanism of the Formation of Stable Microspheres by Precipitation Copolymerization of Styrene and Divinylbenzene. *J. Polym. Sci., Part A Polym. Chem.* **2004**, *42* (16), 3967–3974.
- (107) Li, W.-H.; Stöver, H. D. H. Mono- or Narrow Disperse Poly(Methacrylate-Co-Divinylbenzene) Microspheres by Precipitation Polymerization. *J. Polym. Sci., Part A Polym. Chem.* **1999**, *37* (15), 2899–2907.
- (108) Takekoh, R.; Li, W.-H.; Burke, N. A. D.; Stöver, H. D. H. Multilayered Polymer Microspheres by Thermal Imprinting during Microsphere Growth. *J. Am. Chem. Soc.* **2006**, *128* (1), 240–244.
- (109) Zhang, H. Controlled/"living" Radical Precipitation Polymerization: A Versatile Polymerization Technique for Advanced Functional Polymers. *Eur. Polym. J.* **2013**, *49* (3), 579–600.
- (110) Ye, L.; Weiss, R.; Mosbach, K. Synthesis and Characterization of Molecularly Imprinted Microspheres. *Macromolecules* **2000**, *33* (22), 8239–8245.
- (111) Chaitidou, S.; Kotrotsiou, O.; Kotti, K.; Kammona, O.; Bukhari, M.; Kiparissides, C. Precipitation Polymerization for the Synthesis of Nanostructured Particles. *Mater. Sci. Eng. B Solid-State Mater. Adv. Technol.* **2008**, *152* (1–3), 55–59.
- (112) Liu, X.; Ren, J.; Su, L.; Gao, X.; Tang, Y.; Ma, T.; Zhu, L.; Li, J. Novel Hybrid Probe Based on Double Recognition of Aptamer-Molecularly Imprinted Polymer Grafted on Upconversion Nanoparticles for Enrofloxacin Sensing. *Biosens. Bioelectron.* **2017**, *87*, 203–208.
- (113) Niu, H.; Yang, Y.; Zhang, H. Efficient One-Pot Synthesis of Hydrophilic and Fluorescent Molecularly Imprinted Polymer Nanoparticles for Direct Drug Quantification in Real Biological Samples. *Biosens. Bioelectron.* **2015**, *74*, 440–446.
- (114) Zouaoui, F.; Bourouina-Bacha, S.; Bourouina, M.; Jaffrezic-Renault, N.; Zine, N.; Errachid, A. Electrochemical Sensors Based on Molecularly Imprinted Chitosan: A Review. *TrAC - Trends Anal. Chem.* **2020**, *130*, 115982.
- (115) Karrat, A.; Lamaoui, A.; Amine, A.; Palacios-Santander, J. M.; Cubillana-Aguilera, L. Applications of Chitosan in Molecularly and Ion Imprinted Polymers. *Chem. Africa* **2020**, *3* (3), 513–533.

- (116) Yarahmadi, S.; Azadbakht, A.; Derikvand, R. M. Hybrid Synthetic Receptor Composed of Molecularly Imprinted Polydopamine and Aptamers for Impedimetric Biosensing of Urea. *Microchim. Acta* **2019**, *186* (2).
- (117) Baleviciute, I.; Ratautaitė, V.; Ramanaviciene, A.; Balevičius, Z.; Broeders, J.; Croux, D.; McDonald, M.; Vahidpour, F.; Thoelen, R.; Ceuninck, W. De; Haenen, K.; Nesladek, M.; Reza, A.; Ramanavicius, A. Evaluation of Theophylline Imprinted Polypyrrole Film. *Synth. Met.* **2015**, *209*, 206–211.
- (118) Elfadil, D.; Lamaoui, A.; Pelle, F. Della; Amine, A. Molecularly Imprinted Polymers Combined with Electrochemical Sensors for Food Contaminants Analysis. *Molecules* **2021**, *26*, 1–40.
- (119) Hutchins, R. S.; Bachas, L. G. Nitrate-Selective Electrode Developed by Electrochemically Mediated Imprinting/Doping of Polypyrrole. *Anal. Chem.* **1995**, *67* (10), 1654–1660.
- (120) Malitesta, C.; Mazzotta, E.; Picca, R. A.; Poma, A.; Chianella, I.; Piletsky, S. A. MIP Sensors - The Electrochemical Approach. *Anal. Bioanal. Chem.* **2012**, *402* (5), 1827–1846.
- (121) Mohsen, A.; Rzaij, J. M. A Review on : Molecularly Imprinting Polymers by Ion-Selective Electrodes for Determination Drugs. *J. Chem. Rev.* **2020**, *2* (3), 148–156.
- (122) Hussain, K. K.; Moon, J. M.; Park, D. S.; Shim, Y. B. Electrochemical Detection of Hemoglobin: A Review. *Electroanalysis* **2017**, *29* (10), 2190–2199.
- (123) Rebelo, P.; Costa-Rama, E.; Seguro, I.; Pacheco, J. G.; Nouws, H. P. A.; Cordeiro, M. N. D. S.; Delerue-Matos, C. Molecularly Imprinted Polymer-Based Electrochemical Sensors for Environmental Analysis. *Biosens. Bioelectron.* **2021**, *172* (2021), 112719.
- (124) Hui, Y.; Bian, C.; Xia, S.; Tong, J.; Wang, J. Synthesis and Electrochemical Sensing Application of Poly(3,4-Ethylenedioxythiophene)-Based Materials: A Review. *Anal. Chim. Acta* **2018**, *1022*, 1–19.
- (125) Barclay, T. G.; Hegab, H. M.; Clarke, S. R.; Ginic-Markovic, M. Versatile Surface Modification Using Polydopamine and Related Polycatecholamines: Chemistry, Structure, and Applications. *Adv. Mater. Interfaces* **2017**, *4* (19), 1601192.
- (126) Palladino, P.; Bettazzi, F.; Scarano, S. Polydopamine: Surface Coating, Molecular Imprinting, and Electrochemistry—Successful Applications and Future Perspectives in (Bio)Analysis. *Anal. Bioanal. Chem.* **2019**, *411* (19), 4327–4338.
- (127) Liu, K.; Wei, W. Z.; Zeng, J. X.; Liu, X. Y.; Gao, Y. P. Application of a Novel Electrosynthesized Polydopamine-Imprinted Film to the Capacitive Sensing of Nicotine. *Anal. Bioanal. Chem.* **2006**, *385* (4), 724–729.
- (128) Prabhu, A.; Crapnell, R. D.; Eersels, K.; van Grinsven, B.; Kunhiraman, A. K.; Singla, P.; McClements, J.; Banks, C. E.; Novakovic, K.; Peeters, M. Reviewing the Use of Chitosan and Polydopamine for Electrochemical Sensing. *Curr. Opin. Electrochem.* **2021**, *100885*.
- (129) Cooper, S. E.; Venton, B. J. Fast-Scan Cyclic Voltammetry for the Detection of Tyramine and Octopamine. *Anal. Bioanal. Chem.* **2009**, *394* (1), 329–336.

- (130) Tran, L. D.; Piro, B.; Pham, M. C.; Ledoan, T.; Angiari, C.; Dao, L. H.; Teston, F. A Polytyramine Film for Covalent Immobilization of Oligonucleotides and Hybridization. *Synth. Met.* **2003**, *139* (2), 251–262.
- (131) Miao, Y.; Chen, J.; Hu, Y. Electrodeposited Nonconducting Polytyramine for the Development of Glucose Biosensors. *Anal. Biochem.* **2005**, *339* (1), 41–45.
- (132) Liu, M. Q.; Jiang, J. H.; Feng, Y. L.; Shen, G. L.; Yu, R. Q. Glucose Biosensor Based on Immobilization of Glucose Oxidase in Electrochemically Polymerized Polytyramine Film and Overoxidised Polypyrrole Film on Platinized Carbon Paste Electrode. *Chinese J. Anal. Chem.* **2007**, *35* (10), 1435–1438.
- (133) Sztandera, K.; Marcinkowska, M.; Gorzkiewicz, M.; Janaszewska, A.; Laurent, R.; Zabłocka, M.; Mignani, S.; Majoral, J. P.; Klajnert-Maculewicz, B. In Search of a Phosphorus Dendrimer-Based Carrier of Rose Bengal: Tyramine Linker Limits Fluorescent and Phototoxic Properties of a Photosensitizer. *Int. J. Mol. Sci.* **2020**, *21* (12), 1–20.
- (134) Situmorang, M.; Justin Gooding, J.; Brynn Hibbert, D.; Barnett, D. Development of Potentiometric Biosensors Using Electrodeposited Polytyramine as the Enzyme Immobilization Matrix. *Electroanalysis* **2001**, *13* (18), 1469–1474.
- (135) Loprasert, S.; Hedström, M.; Thavarungkul, P.; Kanatharana, P.; Mattiasson, B. Sub-Attomolar Detection of Cholera Toxin Using a Label-Free Capacitive Immunosensor. *Biosens. Bioelectron.* **2010**, *25* (8), 1977–1983.
- (136) Ismail, F.; Adelaju, S. B. Galvanostatic Entrapment of Penicillinase into Polytyramine Films and Its Utilization for the Potentiometric Determination of Penicillin. *Sensors* **2010**, *10* (4), 2851–2868.
- (137) Zhou, L.; Sluing, F.; Pravda, M.; Glennon, J. D.; Luong, J. H. T. Selective Detection of Dopamine Using Glassy Carbon Electrode Modified by a Combined Electropolymerized Permselective Film of Polytyramine and Polypyrrole-1-Propionic Acid. *Electroanalysis* **2009**, *21* (7), 797–803.
- (138) Frasco, M. F.; Truta, L. A. A. N. A.; Sales, M. G. F.; Moreira, F. T. C. Imprinting Technology in Electrochemical Biomimetic Sensors. *Sensors* **2017**, *17* (523), 1–29.
- (139) Shang, F.; Liu, Y.; Hrapovic, S.; Glennona, J. D.; Luong, J. H. T. Selective Detection of Dopamine Using a Combined Permselective Film of Electropolymerized (Poly-Tyramine and Poly-Pyrrole-1-Propionic Acid) on a Boron-Doped Diamond Electrode. *Analyst* **2009**, *134*, 519–527.
- (140) Yuqing, M.; Jianrong, C.; Xiaohua, W. Using Electropolymerized Non-Conducting Polymers to Develop Enzyme Amperometric Biosensors. *Trends Biotechnol.* **2004**, *22* (5), 227–231.
- (141) De Rycke, E.; Trynda, A.; Jaworowicz, M.; Dubruel, P.; De Saeger, S.; Beloglazova, N. Capacitive Sensing of an Amphetamine Drug Precursor in Aqueous Samples: Application of Novel Molecularly Imprinted Polymers for Benzyl Methyl Ketone Detection. *Biosens. Bioelectron.* **2021**, *172* (November 2020), 112773.
- (142) El-Akaad, S.; Mohamed, M. A.; Abdelwahab, N. S.; Abdelaleem, E. A.; De Saeger, S.; Beloglazova, N. Capacitive Sensor Based on Molecularly Imprinted Polymers for

- Detection of the Insecticide Imidacloprid in Water. *Sci. Rep.* **2020**, *10* (1), 1–10.
- (143) Namsheer, K.; Rout, C. S. Conducting Polymers: A Comprehensive Review on Recent Advances in Synthesis, Properties and Applications. *RSC Adv.* **2021**, *11* (10), 5659–5697.
- (144) Ibanez, J. G.; Rincón, M. E.; Gutierrez-Granados, S.; Chahma, M.; Jaramillo-Quintero, O. A.; Frontana-Uribe, B. A. Conducting Polymers in the Fields of Energy, Environmental Remediation, and Chemical-Chiral Sensors. *Chem. Rev.* **2018**, *118* (9), 4731–4816.
- (145) Lu, H.; Li, X.; Lei, Q. Conjugated Conductive Polymer Materials and Its Applications: A Mini-Review. *Front. Chem.* **2021**, *9* (September), 6–11.
- (146) Das, T. K.; Prusty, S. Review on Conducting Polymers and Their Applications. *Polym. - Plast. Technol. Eng.* **2012**, *51* (14), 1487–1500.
- (147) Agobi, A. U.; Louis, H.; Magu, T. O.; Dass, P. M. A Review on Conducting Polymers-Based Composites for Energy Storage Application. *J. Chem. Rev.* **2019**, *1* (1), 19–34.
- (148) Ates, M. A Review on Conducting Polymer Coatings for Corrosion Protection. *J. Adhes. Sci. Technol.* **2016**, *30* (14), 1510–1536.
- (149) Pirhady Tavandashti, N.; Ghorbani, M.; Shojaei, A.; Mol, J. M. C.; Terryn, H.; Baert, K.; Gonzalez-Garcia, Y. Inhibitor-Loaded Conducting Polymer Capsules for Active Corrosion Protection of Coating Defects. *Corros. Sci.* **2016**, *112*, 138–149.
- (150) Tan, C. K.; Blackwood, D. J. Corrosion Protection by Multilayered Conducting Polymer Coatings. *Corros. Sci.* **2003**, *45* (3), 545–557.
- (151) Maziz, A.; Özgür, E.; Bergaud, C.; Uzun, L. Progress in Conducting Polymers for Biointerfacing and Biorecognition Applications. *Sensors and Actuators Reports* **2021**, *3* (2021), 100035.
- (152) Wang, Y.; Liu, A.; Han, Y.; Li, T. Sensors Based on Conductive Polymers and Their Composites: A Review. *Polym. Int.* **2020**, *69* (1), 7–17.
- (153) Ravichandran, R.; Sundarrajan, S.; Venugopal, J. R.; Mukherjee, S.; Ramakrishna, S. Applications of Conducting Polymers and Their Issues in Biomedical Engineering. *J. R. Soc. Interface* **2010**, *7* (SUPPL. 5), S559–S579.
- (154) Zeng, Q.; Zhang, L.; Li, Z.; Qin, J.; Tang, B. Z. New Polyacetylene-Based Chemosensory Materials for the “Turn-on” Sensing of  $\alpha$ -Amino Acids. *Polymer (Guildf.)* **2009**, *50* (2), 434–440.
- (155) Liu, Y.; Mills, R. C.; Boncella, J. M.; Schanze, K. S. Fluorescent Polyacetylene Thin Film Sensor for Nitroaromatics. *Langmuir* **2001**, *17* (24), 7452–7455.
- (156) Maeda, K.; Hirose, D.; Okoshi, N.; Shimomura, K.; Wada, Y.; Ikai, T.; Kanoh, S.; Yashima, E. Direct Detection of Hardly Detectable Hidden Chirality of Hydrocarbons and Deuterated Isotopomers by a Helical Polyacetylene through Chiral Amplification and Memory. *J. Am. Chem. Soc.* **2018**, *140* (9), 3270–3276.
- (157) Wang, F.; Zhu, L.; Zhang, J. Electrochemical Sensor for Levofloxacin Based on Molecularly Imprinted Polypyrrole-Graphene-Gold Nanoparticles Modified Electrode. *Sensors Actuators, B Chem.* **2014**, *192*, 642–647.

- (158) Waffo, A. F. T.; Yesildag, C.; Caserta, G.; Katz, S.; Zebger, I.; Lensen, M. C.; Wollenberger, U.; Scheller, F. W.; Altintas, Z. Fully Electrochemical MIP Sensor for Artemisinin. *Sensors Actuators, B Chem.* **2018**, 275 (August), 163–173.
- (159) Li, C.; Shi, G. Polythiophene-Based Optical Sensors for Small Molecules. *ACS Appl. Mater. Interfaces* **2013**, 5 (11), 4503–4510.
- (160) Mathiyarasu, J.; Senthilkumar, S.; Phani, K. L. N.; Yegnaraman, V. PEDOT-Au Nanocomposite Film for Electrochemical Sensing. *Mater. Lett.* **2008**, 62 (4–5), 571–573.
- (161) Wen, Y.; Xu, J. Scientific Importance of Water-Processable PEDOT-PSS and Preparation, Challenge and New Application in Sensors of Its Film Electrode: A Review. *J. Polym. Sci. A Polym. Chem.* **2017**, 55 (7), 1121–1150.
- (162) Xu, G.; Jarjes, Z. A.; Desprez, V.; Kilmartin, P. A.; Travas-Sejdic, J. Sensitive, Selective, Disposable Electrochemical Dopamine Sensor Based on PEDOT-Modified Laser Scribed Graphene. *Biosens. Bioelectron.* **2018**, 107 (November 2017), 184–191.
- (163) Nayana, V.; Kandasubramanian, B. Polycarbazole and Its Derivatives: Progress, Synthesis, and Applications. *Polymers (Basel)*. **2020**, 12 (9), 1–33.
- (164) Prakash, R.; Srivastava, R. C.; Seth, P. K. Polycarbazole Modified Electrode; Nitric Oxide Sensor. *Polym. Bull.* **2001**, 46 (6), 487–490.
- (165) Soganci, T.; Baygu, Y.; Kabay, N.; Gök, Y.; Ak, M. Comparative Investigation of Peripheral and Nonperipheral Zinc Phthalocyanine-Based Polycarbazoles in Terms of Optical, Electrical, and Sensing Properties. *ACS Appl. Mater. Interfaces* **2018**, 10 (25), 21654–21665.
- (166) Kumar Konidena, R.; Justin Thomas, K. R.; Kumar Dubey, D.; Sahoo, S.; Jou, J. H. A New Molecular Design Based on Hybridized Local and Charge Transfer Fluorescence for Highly Efficient (>6%) Deep-Blue Organic Light Emitting Diodes. *Chem. Commun.* **2017**, 53 (86), 11802–11805.
- (167) Ambrose, J. F.; Carpenter, L. L.; Nelson, R. F. Electrochemical and Spectroscopic Properties of Cation Radicals: III. Reaction Pathways of Carbazolium Radical Ions. *J. Electrochem. Soc.* **1975**, 122 (7), 876–894.
- (168) Diamant, Y.; Furmanovich, E.; Landau, A.; Lellouche, J. P.; Zaban, A. Electrochemical Polymerization and Characterization of a Functional Dicarbazole Conducting Polymer. *Electrochim. Acta* **2003**, 48 (5), 507–512.
- (169) Inzelt, G. Formation and Redox Behaviour of Polycarbazole Prepared by Electropolymerization of Solid Carbazole Crystals Immobilized on an Electrode Surface. *J. Solid State Electrochem.* **2003**, 7 (8), 503–510.
- (170) Venkateswararao, A.; Thomas, K. R. J. Carbazole-Based Organic Dyes for Dye-Sensitized Solar Cells: Role of Carbazole as Donor, Auxiliary Donor and  $\pi$ -Linker. In *Solar Cell Nanotechnology*; John Wiley & Sons, Ltd, 2013; pp 41–96.
- (171) Lee, K.; Kim, D. A Theoretical Study of Carbazole Dimers: Does Carbazole Form an Excimer That Undermines the Performance of Organic Light Emitting Diodes? *Int. J. Quantum Chem.* **2020**, 120 (19), 21–24.

- (172) Venkateswararao, A.; Thomas, K. R. J.; Lee, C.-P.; Li, C.-T.; Ho, K.-C. Organic Dyes Containing Carbazole as Donor and  $\pi$ -Linker: Optical, Electrochemical, and Photovoltaic Properties. *ACS Appl. Mater. Interfaces* **2014**, *6* (4), 2528–2539.
- (173) Park, J. H.; Kim, E. K.; El-Deeb, I. M.; Jung, S. J.; Choi, D. H.; Kim, D. H.; Yoo, K. H.; Kwon, J. H.; Lee, S. H. New Bipolar Green Host Materials Containing Benzimidazole-Carbazole Moiety in Phosphorescent OLEDs. *Bull. Korean Chem. Soc.* **2011**, *32* (3), 841–846.
- (174) Kumar, V.; Choudhury, N.; Kumar, A.; De, P.; Satapathi, S. Poly-Tryptophan/Carbazole Based FRET-System for Sensitive Detection of Nitroaromatic Explosives. *Opt. Mater. (Amst.)* **2020**, *100* (September 2019), 109710.
- (175) Issa, S.; Prandina, A.; Bedel, N.; Rongved, P.; Yous, S.; Le Borgne, M.; Bouaziz, Z. Carbazole Scaffolds in Cancer Therapy: A Review from 2012 to 2018. *J. Enzym. Inhib. Med. Chem.* **2019**, *34* (1), 1321–1346.
- (176) Caruso, A.; Ceramella, J.; Iacopetta, D.; Saturnino, C.; Mauro, M. V.; Bruno, R.; Aquaro, S.; Sinicropi, M. S. Carbazole Derivatives as Antiviral Agents: An Overview. *Molecules* **2019**, *24* (10).
- (177) Le, T. H.; Kim, Y.; Yoon, H. Electrical and Electrochemical Properties of Conducting Polymers. *Polymers (Basel)* **2017**, *9* (4).
- (178) Meana-Esteban, B.; Petr, A.; Kvarnström, C.; Ivaska, A.; Dunsch, L. Poly(2-Methoxynaphthalene): A Spectroelectrochemical Study on a Fused Ring Conducting Polymer. *Electrochim. Acta* **2014**, *115*, 10–15.
- (179) Ambrose, J. F.; Nelson, R. F. Anodic Oxidation Pathways of Carbazoles I. Carbazole and N-Substituted Derivatives. *J. Electrochem. Soc.* **1968**, *115* (11), 1159–1163.
- (180) Sharma, P. S.; Pietrzyk-le, A. Electrochemically Synthesized Polymers in Molecular Imprinting for Chemical Sensing. *Anal. Bioanal. Chem.* **2012**, *402*, 3177–3204.
- (181) Karon, K.; Lapkowski, M. Carbazole Electrochemistry: A Short Review. *J. Solid State Electrochem.* **2015**, *19* (9), 2601–2610.
- (182) Ayrancı, R.; Vargun, E.; Ak, M. Conjugated and Fluorescent Polymer Based on Dansyl-Substituted Carbazole : Investigation of Electrochromic and Ion Sensitivity. *ECS J. Solid State Sci. Technol* **2017**, *6* (5), 211–216.
- (183) Vedarajan, R.; Hosono, Y.; Matsumi, N.  $\pi$ -Conjugated Polycarbazole – Boron Complex as a Colorimetric Fl Uoride Ion Sensor. *Solid State Ion.* **2014**, *262*, 795–800.
- (184) Maslowska-jarzyna, K.; Korczak, M. L.; Wagner, J. A.; Chmielewski, M. J. Carbazole-Based Colorimetric Anion Sensors. *Molecules* **2021**, *26* (3025), 1–16.
- (185) Nie, H.; Sun, G.; Zhang, M.; Klaus, M. Fluorescent Conjugated Polycarbazoles for Explosives Detection : Side Chain Effects on TNT Sensor Sensitivity. *J. Mater. Chem.* **2012**, *22*, 2129–2132.
- (186) Synthesis, T.; Hollow, T. Template-Free Synthesis of Tunable Hollow Microspheres of Aniline and Aminocarbazole Copolymers Emitting Colorful Fluorescence for Ultrasensitive Sensors. *Chem. Eng. J.* **2019**, *357*, 776–786.
- (187) Ates, M.; Castillo, J.; Sarac, A. S.; Schuhmann, W. Carbon Fiber Microelectrodes

Electrocoated with Polycarbazole and Poly(Carbazole-Co-p-Tolylsulfonyl Pyrrole) Films for the Detection of Dopamine in Presence of Ascorbic Acid. *Microchim. Acta* **2008**, *160*, 247–251.

- (188) Zhang, Y.; Wu, L.; Lei, W.; Xia, X.; Xia, M.; Hao, Q. Electrochemical Determination of 4-Nitrophenol at Polycarbazole/N-Doped Graphene Modified Glassy Carbon Electrode. *Electrochim. Acta* **2014**, *146*, 568–576.
- (189) Cywinski, P. J.; Idzik, K. R.; Cranfield, C. G.; Beckert, R.; Mohr, G. J.; Cywinski, P. J.; Idzik, K. R.; Cranfield, C. G. Synthesis and Sensing Properties of a New Carbazole Fluorosensor for Detection of Abacavir. *Supramol. Chem.* **2010**, *22* (10), 598–602.
- (190) Pernites, R.; Ponnappati, R.; Felipe, M. J.; Advincula, R. Electropolymerization Molecularly Imprinted Polymer (E-MIP) SPR Sensing of Drug Molecules: Pre-Polymerization Complexed Terthiophene and Carbazole Electroactive Monomers. *Biosens. Bioelectron.* **2011**, *26* (5), 2766–2771.
- (191) Yang, L.; Zhang, B.; Xu, B.; Zhao, F.; Zeng, B. Ionic Liquid Functionalized 3D Graphene-Carbon Nanotubes–AuPd Nanoparticles–Molecularly Imprinted Copolymer Based Paracetamol Electrochemical Sensor: Preparation, Characterization and Application. *Talanta* **2021**, *224* (August 2020), 121845.
- (192) Gajda, M.; Rybakiewicz, R.; Cieplak, M.; Źołek, T.; Maciejewska, D.; Gilant, E.; Rudzki, P. J.; Grab, K.; Kutner, A.; Borowicz, P.; Kutner, W.; Noworyta, K. R. Low-Oxidation-Potential Thiophene-Carbazole Monomers for Electro-Oxidative Molecular Imprinting: Selective Chemosensing of Aripiprazole. *Biosens. Bioelectron.* **2020**, *169* (August), 112589.
- (193) Luo, J.; Wei, W.; Zhu, Y.; Liu, R.; Liu, X. Synthesis of Water-Dispersible Molecularly Imprinted Electroactive Nanoparticles for the Sensitive and Selective Paracetamol Detection. *ACS Appl. Mater. Interfaces* **2016**, *8*, 21028–21038.
- (194) Zhong, C.; Yang, B.; Jiang, X.; Li, J. Current Progress of Nanomaterials in Molecularly Imprinted Electrochemical Sensing. *Crit. Rev. Anal. Chem.* **2018**, *48* (1), 15–32.
- (195) Jolly, P.; Tamboli, V.; Harniman, R. L.; Estrela, P.; Allender, C. J.; Bowen, J. L. Aptamer-MIP Hybrid Receptor for Highly Sensitive Electrochemical Detection of Prostate Specific Antigen. *Biosens. Bioelectron.* **2016**, *75*, 188–195.
- (196) Maduraiveeran, G.; Sasidharan, M.; Ganesan, V. Electrochemical Sensor and Biosensor Platforms Based on Advanced Nanomaterials for Biological and Biomedical Applications. *Biosens. Bioelectron.* **2018**, *103* (December 2017), 113–129.
- (197) Cuniberto, E.; Alharbi, A.; Wu, T.; Huang, Z.; Sardashti, K.; You, K. D.; Kisslinger, K.; Taniguchi, T.; Watanabe, K.; Kiani, R.; Shahrijerdi, D. Nano-Engineering the Material Structure of Preferentially Oriented Nano-Graphitic Carbon for Making High-Performance Electrochemical Micro-Sensors. *Sci. Rep.* **2020**, *10* (1), 1–11.
- (198) Xu, S.; Lin, G.; Zhao, W.; Wu, Q.; Luo, J.; Wei, W.; Liu, X.; Zhu, Y. Necklace-like Molecularly Imprinted Nanohybrids Based on Polymeric Nanoparticles Decorated Multiwalled Carbon Nanotubes for Highly Sensitive and Selective Melamine Detection. *ACS Appl. Mater. Interfaces* **2018**, *10* (29), 24850–24859.
- (199) Kirchner, E. M.; Hirsch, T. Recent Developments in Carbon-Based Two-Dimensional

Materials: Synthesis and Modification Aspects for Electrochemical Sensors. *Microchim. Acta* **2020**, *187* (8), 441.

- (200) Bezzon, V. D. N.; Montanheiro, T. L. A.; De Menezes, B. R. C.; Ribas, R. G.; Righetti, V. A. N.; Rodrigues, K. F.; Thim, G. P. Carbon Nanostructure-Based Sensors: A Brief Review on Recent Advances. *Adv. Mater. Sci. Eng.* **2019**, *2019*, 4293073.
- (201) Pan, M.; Yin, Z.; Liu, K.; Du, X.; Liu, H.; Wang, S. Carbon-Based Nanomaterials in Sensors for Food Safety. *Nanomaterials* **2019**, *9* (9), 1–23.
- (202) Beluomini, M. A.; Silva, J. L. da; Sá, A. C. de; Buffon, E.; Pereira, T. C.; Stradiotto, N. R. Electrochemical Sensors Based on Molecularly Imprinted Polymer on Nanostructured Carbon Materials: A Review. *J. Electroanal. Chem.* **2019**, *840* (September 2018), 343–366.
- (203) Ansari, S.; Karimi, M. Recent Configurations and Progressive Uses of Magnetic Molecularly Imprinted Polymers for Drug Analysis. *Talanta* **2017**, *167* (February), 470–485.
- (204) Gholivand, M. B.; Karimian, N. Chemical Fabrication of a Highly Selective and Sensitive Voltammetric Ganciclovir Sensor Based on Electropolymerized Molecularly Imprinted Polymer and Gold Nanoparticles on Multiwall Carbon Nanotubes / Glassy Carbon Electrode. *Sens. Actuators B Chem.* **2015**, *215*, 471–479.
- (205) Torkashvand, M.; Gholivand, M. B.; Malekzadeh, G. Construction of a New Electrochemical Sensor Based on Molecular Imprinting Recognition Sites on Multiwall Carbon Nanotube Surface for Analysis of Ceftazidime in Real Samples. *Sens. Actuators B Chem.* **2016**, *231*, 759–767.
- (206) Wang, Z.; Wang, K.; Zhao, L.; Chai, S.; Zhang, J.; Zhang, X.; Zou, Q. A Novel Sensor Made of Antimony Doped Tin Oxide-Silica Composite Sol on a Glassy Carbon Electrode Modified by Single-Walled Carbon Nanotubes for Detection of Norepinephrine. *Mater. Sci. Eng. C* **2017**, *80*, 180–186.
- (207) Long, F.; Zhang, Z.; Yang, Z.; Zeng, J.; Jiang, Y. Imprinted Electrochemical Sensor Based on Magnetic Multi-Walled Carbon Nanotube for Sensitive Determination of Kanamycin. *J. Electroanal. Chem.* **2015**, *755*, 7–14.
- (208) Bagheri, H.; Khoshhsafar, H.; Amidi, S.; Ardakani, Y. Analytical Methods. *Anal. Methods* **2016**, *8*, 3383–3390.
- (209) Wei, S.; Liu, Y.; Hua, T.; Liu, L.; Wang, H. Molecularly Imprinted Electrochemical Sensor for the Determination of Ampicillin Based on a Gold Nanoparticle and Multiwalled Carbon Nanotube-Coated Pt Electrode. *J. Appl. Polym. Sci.* **2014**, *131* (16).
- (210) Deiminiat, B.; Rounaghi, G. H. Fabrication of a New Electrochemical Imprinted Sensor for Determination of Ketamine Based on Modified Polytyramine/Sol-Gel/f-MWCNTs@AuNPs Nanocomposite/Pencil Graphite Electrode. *Sensors Actuators, B Chem.* **2018**, *259*, 133–141.
- (211) Fu, K.; Zhang, R.; He, J.; Bai, H.; Zhang, G. Sensitive Detection of Ketamine with an Electrochemical Sensor Based on UV-Induced Polymerized Molecularly Imprinted Membranes at Graphene and MOFs Modified Electrode. *Biosens. Bioelectron.* **2019**, *143* (August), 111636.

- (212) Florea, A.; Guo, Z.; Cristea, C.; Bessueille, F.; Vocanson, F.; Goutaland, F.; Dzyadevych, S.; Săndulescu, R.; Jaffrezic-Renault, N. Anticancer Drug Detection Using a Highly Sensitive Molecularly Imprinted Electrochemical Sensor Based on an Electropolymerized Microporous Metal-Organic Framework. *Talanta* **2015**, *138*, 71–76.
- (213) Seguro, I.; Pacheco, J. G.; Delerue-Matos, C. Low Cost, Easy to Prepare and Disposable Electrochemical Molecularly Imprinted Sensor for Diclofenac Detection. *Sensors* **2021**, *21* (6), 1–11.
- (214) Blanco-López, M. C.; Fernández-Llano, L.; Lobo-Castañón, M. J.; Miranda-Ordieres, A. J.; Tuñón-Blanco, P. Voltammetry of Diclofenac at Graphite, Carbon Composites, and Molecularly Imprinted Polymer-Composite Electrodes. *Anal. Lett.* **2004**, *37* (5), 915–927.
- (215) Mueller, T.; Hinterreiter, F.; Luft, C.; Poelz, W.; Haltmayer, M.; Dieplinger, B. Mortality Rates and Mortality Predictors in Patients with Symptomatic Peripheral Artery Disease Stratified According to Age and Diabetes. *J. Vasc. Surg.* **2014**, *59* (5), 1291–1299.
- (216) Shu, J.; Santulli, G. Update on Peripheral Artery Disease: Epidemiology and Evidence-Based Facts. *Atherosclerosis* **2018**, *275*, 379–381.
- (217) Zhao, J.; Harada, N.; Kurihara, H.; Nakagata, N.; Okajima, K. Cilostazol Improves Cognitive Function in Mice by Increasing the Production of Insulin-like Growth Factor-I in the Hippocampus. *Neuropharmacology* **2010**, *58* (4–5), 774–783.
- (218) Douglas, J. S.; Holmes, D. R.; Kereiakes, D. J.; Grines, C. L.; Block, E.; Ghazzal, Z. M. B.; Morris, D. C.; Liberman, H.; Parker, K.; Jurkovitz, C.; Murrah, N.; Foster, J.; Hyde, P.; Mancini, G. B. J.; Weintraub, W. S. Coronary Stent Restenosis in Patients Treated with Cilostazol. *Circulation* **2005**, *112* (18), 2826–2832.
- (219) Bramer, S. L.; Forbes, W. P.; Mallikaarjun, S. Cilostazol Pharmacokinetics after Single and Multiple Oral Doses in Healthy Males and Patients with Intermittent Claudication Resulting from Peripheral Arterial Disease. *Clin. Pharmacokinet.* **1999**, *37* (SUPPL. 2), 1–11.
- (220) Saitoh, S.; Saito, T.; Otake, A.; Owada, T.; Mitsugi, M.; Hashimoto, H.; Maruyama, Y. Cilostazol, a Novel Cyclic AMP Phosphodiesterase Inhibitor, Prevents Reocclusion after Coronary Arterial Thrombolysis with Recombinant Tissue-Type Plasminogen Activator. *Arterioscler. Thromb. Vasc. Biol.* **1993**, *13* (4), 563–570.
- (221) Ikeda, Y.; Sudo, T.; Kimura, Y. Cilostazol. In *Cilostazol, in Platelets*; Alan D. Michelson, Ed.; Massachusetts, USA, 2013; pp 1171–1183.
- (222) Kim, J.-R.; Jung, J. A.; Kim, S.; Huh, W.; Ghim, J.-L.; Shin, J.-G.; Ko, J.-W. Effect of Cilostazol on the Pharmacokinetics of Simvastatin in Healthy Subjects. *Biomed Res. Int.* **2019**, *2019*, 1–6.
- (223) Take, S.; Matsutani, M.; Ueda, H.; Hamaguchi, H.; Konishi, H.; Baba, Y.; Kawaratani, H.; Sugiura, T.; Iwasaka, T.; Inada, M. Effect of Cilostazol in Preventing Restenosis After Percutaneous Transluminal Coronary Angioplasty. *Am. J. Card.* **1997**, *79* (8), 1097–1099.

- (224) Motta, N. A. V.; Autran, L. J.; Brazão, S. C.; Lopes, R. de O.; Scaramello, C. B. V.; Lima, G. F.; Brito, F. C. F. de. Could Cilostazol Be Beneficial in COVID-19 Treatment? Thinking about Phosphodiesterase-3 as a Therapeutic Target. *Int. Immunopharmacol.* **2021**, *92* (November 2020), 107336.
- (225) Lee, S. W.; Park, S. W.; Kim, Y. H.; Yun, S. C.; Park, D. W.; Lee, C. W.; Hong, M. K.; Kim, H. S.; Ko, J. K.; Park, J. H.; Lee, J. H.; Choi, S. W.; Seong, I. W.; Cho, Y. H.; Lee, N. H.; Kim, J. H.; Chun, K. J.; Park, S. J. Drug-Eluting Stenting Followed by Cilostazol Treatment Reduces Late Restenosis in Patients With Diabetes Mellitus. The DECLARE-DIABETES Trial (A Randomized Comparison of Triple Antiplatelet Therapy With Dual Antiplatelet Therapy After Drug-Eluting Stent I. *J. Am. Coll. Cardiol.* **2008**, *51* (12), 1181–1187.
- (226) Saito, S.; Ihara, M. New Therapeutic Approaches for Alzheimer’s Disease and Cerebral Amyloid Angiopathy. *Front. Aging Neurosci.* **2014**, *6* (OCT), 1–11.
- (227) Hishikawa, N.; Fukui, Y.; Sato, K.; Ohta, Y.; Yamashita, T.; Abe, K. Comprehensive Effects of Galantamine and Cilostazol Combination Therapy on Patients with Alzheimer’s Disease with Asymptomatic Lacunar Infarction. *Geriatr. Gerontol. Int.* **2017**, *17* (10), 1384–1391.
- (228) Sakurai, H.; Hanyu, H.; Sato, T.; Kume, K.; Hirao, K.; Kanetaka, H.; Iwamoto, T. Effects of Cilostazol on Cognition and Regional Cerebral Blood Flow in Patients with Alzheimer’s Disease and Cerebrovascular Disease: A Pilot Study. *Geriatr. Gerontol. Int.* **2013**, *13* (1), 90–97.
- (229) Park, S. H.; Kim, J. H.; Bae, S. S.; Hong, K. W.; Lee, D. S.; Leem, J. Y.; Choi, B. T.; Shin, H. K. Protective Effect of the Phosphodiesterase III Inhibitor Cilostazol on Amyloid  $\beta$ -Induced Cognitive Deficits Associated with Decreased Amyloid  $\beta$  Accumulation. *Biochem. Biophys. Res. Commun.* **2011**, *408* (4), 602–608.
- (230) Hiramatsu, M.; Takiguchi, O.; Nishiyama, A. Cilostazol Prevents Amyloid  $\beta$  Peptide 25–35 -Induced Memory Impairment and Oxidative Stress in Mice. *Br. J. Pharmacol.* **2010**, *161*, 1899–1912.
- (231) Di Napoli, M.; Singh, P.; Lattanzi, S.; Divani, A. A. The Use of Cilostazol for Secondary Stroke Prevention: Isn’t Time to Be Evaluated in Western Countries? *Expert Opin. Pharmacother.* **2020**, *21* (4), 381–387.
- (232) Sahin, M.; Alizade, E.; Pala, S.; Alici, G.; Ozkan, B.; Akgun, T.; Emiroglu, Y.; Demir, S.; Yazicioglu, M. V.; Turkmen, M. M. The Effect of Cilostazol on Right Heart Function and Pulmonary Pressure. *Cardiovasc. Ther.* **2013**, *31* (6), e88–e93.
- (233) Dawson, D. L.; Cutler, B. S.; Hiatt, W. R.; Hobson, R. W.; Martin, J. D.; Bortey, E. B.; Forbes, W. P.; Strandness, D. E. A Comparison of Cilostazol and Pentoxifylline for Treating Intermittent Claudication. *Am. J. Med.* **2000**, *109* (7), 523–530.
- (234) O’Donnell, M. E.; Badger, S. A.; Sharif, M. A.; Young, I. S.; Lee, B.; Soong, C. V. The Vascular and Biochemical Effects of Cilostazol in Patients with Peripheral Arterial Disease. *J. Vasc. Surg.* **2009**, *49* (5), 1226–1234.
- (235) Taguchi, A.; Takata, Y.; Ihara, M.; Kasahara, Y.; Tsuji, M.; Nishino, M.; Stern, D.; Okada, M. Cilostazol Improves Cognitive Function in Patients with Mild Cognitive

Impairment: A Retrospective Analysis. *Psychogeriatrics* **2013**, *13* (3), 164–169.

- (236) <https://clinicaltrials.gov/ct2/results?recrs=&cond=combined+treatment&term=cilostazol&cntry=&state=&city=&dist=> (accessed 2021 -06 -06).
- (237) Akiyama, H.; Kudo, S.; Shimizu, T. The Absorption, Distribution and Excretion of a New Antithrombotic and Vasodilating Agent, Cilostazol, in Rat, Rabbit, Dog and Man. *Arzneimittelforschung*. **1985**, *35* (7A), 1124–1132.
- (238) Bramer, S. L.; Tata, P. N. V.; Mallikaarjun, S. Disposition of 14 C-Cilostazol after Single Dose Administration to Healthy Human Subjects. *Pharm. Res.* **1997**, *14*, S612.
- (239) Nirogi, R. V. S.; Kandikere, V. N.; Shukla, M.; Mudigonda, K.; Shrivastava, W.; Datla, P. V.; Yerramilli, A. Simultaneous Quantification of Cilostazol and Its Primary Metabolite 3,4-Dehydrocilostazol in Human Plasma by Rapid Liquid Chromatography/Tandem Mass Spectrometry. *Anal. Bioanal. Chem.* **2006**, *384* (3), 780–790.
- (240) Bhatt, N. M.; Chavada, V. D.; Patel, D. P.; Sharma, P.; Sanyal, M.; Shrivastav, P. S. Determination of Cilostazol and Its Active Metabolite 3,4-Dehydro Cilostazol from Small Plasma Volume by UPLC-MS/MS. *J. Pharm. Anal.* **2015**, *5* (1), 1–11.
- (241) Bramer, S. L.; Tata, P. N. V.; Vengurlekar, S. S.; Brisson, J. H. Method for the Quantitative Analysis of Cilostazol and Its Metabolites in Human Plasma Using LC / MS / MS. *J. Pharm. Biomed. Anal.* **2001**, *26*, 637–650.
- (242) Pareek, D.; Jain, S.; Basniwal, P.; Jain, D. RP-HPLC Determination of Cilostazol in Human Plasma: Application to Pharmacokinetic Study in Male Albino Rabbit. *Acta Chromatogr.* **2014**, *26* (2), 283–296.
- (243) Yeon, K. J.; Park, Y. J.; Park, K. M.; Park, J. S.; Ban, E.; Kim, M. K.; Kim, Y. B.; Kim, C. K. High-Performance Liquid Chromatographic Analysis of Cilostazol in Human Plasma with On-Line Column Switching. *J. Liq. Chromatogr. Relat. Technol.* **2005**, *28*, 109–120.
- (244) Gomes, M. L. S.; Klein, T.; Simionatto, M.; Nadal, J. M.; Zanin, S. M. W.; Borsato, D. M.; Farago, P. V. A Simple RP-HPLC/UV Method for Determination of Cilostazol in Polymeric Nanoparticles Suspensions: Development and Validation. *Lat. Am. J. Pharm.* **2015**, *34* (4), 803–809.
- (245) Ibrahim, F.; El-Din, M. S.; El-Aziz, H. A. New Validated Fluorescence Quenching Based Procedure for the Determination of Cilostazol and Clopidogrel in Bulk, Tablets and Biological Fluids, With Application of Stern-Volmer Equation. *Br. J. Pharm. Res.* **2016**, *12* (6), 1–15.
- (246) Saleh, M. A.; Taha, M. M.; Mohamed, M. A.; Allam, N. K. A Novel and Ultrasensitive Electrochemical Biosensor Based on MnO<sub>2</sub>-V<sub>2</sub>O<sub>5</sub> Nanorods for the Detection of the Antiplatelet Prodrug Agent Cilostazol in Pharmaceutical Formulations. *Microchem. J.* **2021**, *164* (January), 105946.
- (247) Jain, R.; Sharma, R. Novel Bismuth/Multi-Walled Carbon Nanotubes-Based Electrochemical Sensor for the Determination of Neuroprotective Drug Cilostazol. *J. Appl. Electrochem.* **2012**, *42*, 341–348.

- (248) Wassel, A.; Amin, A.; Ahmed, I.; Dessouki, H.; Hendawy, H. Electrochemical Behavior and Determination of Cilostazol in Pure, Urine and in Pharmaceutical Formulations. *Anal. Bioanal. Electrochem.* **2012**, *4* (2), 197–211.
- (249) Attia, M. S.; Mahmoud, W. H.; Youssef, A. O.; Mostafa, M. S. Cilostazol Determination by the Enhancement of the Green Emission of Tb<sup>3+</sup> Optical Sensor. *J. Fluoresc.* **2011**, *21* (6), 2229–2235.
- (250) Detke, M. J.; Ph, D.; Lu, Y.; Ph, D.; Watkin, J. G.; Phil, D.; Tran, P. V. Duloxetine: A New Treatment for the Emotional and Physical Symptoms of Depression. *Prim. Care Companion J. Clin. Psychiatry* **2003**, *5* (1), 19–28.
- (251) Bymaster, F. P.; Beedle, E. E.; Findlay, J.; Gallagher, P. T.; Krushinski, J. H.; Mitchell, S.; Robertson, D. W.; Thompson, D. C.; Wallace, L.; Wong, D. T. Duloxetine (Cymbalta<sup>TM</sup>), a Dual Inhibitor of Serotonin and Norepinephrine Reuptake. *Bioorg. Med. Chem. Lett.* **2003**, *13* (24), 4477–4480.
- (252) Sindhu, P.; Kumar, S.; Iqbal, B.; Ali, J.; Baboota, S. Duloxetine Loaded-Microemulsion System to Improve Behavioral Activities by Upregulating Serotonin and Norepinephrine in Brain for the Treatment of Depression. *J. Psychiatr. Res.* **2018**, *99* (January), 83–95.
- (253) Hu, B. Duloxetine Usage in Depression. In *The Neuroscience of Depression*; Martin, C. R., Hunter, L.-A., Patel, V. B., Preedy, V. R., Rajendram, R., Eds.; Elsevier, 2021; pp 357–368.
- (254) [Https://Blogpsychology.Wordpress.Com/A2-Psychology/Abnormality/Abnormal-Affect/](https://Blogpsychology.Wordpress.Com/A2-Psychology/Abnormality/Abnormal-Affect/).
- (255) Bansal, R.; Hellerstein, D. J.; Sawardekar, S.; O'Neill, J.; Peterson, B. S. Effects of the Antidepressant Medication Duloxetine on Brain Metabolites in Persistent Depressive Disorder: A Randomized, Controlled Trial. *PLoS One* **2019**, *14* (7), 1–25.
- (256) De Berardis, D.; Serroni, N.; Carano, A.; Scali, M.; Valchera, A.; Campanella, D.; D'Albenzio, A.; Di Giuseppe, B.; Saverio Moschetta, F.; Maria Salerno, R.; Maria Ferro, F. The Role of Duoxetine in the Treatment of Anxiety Disorders. *Neuropsychiatr. Dis. Treat.* **2018**, *4* (5), 929–935.
- (257) Schukro, R. P.; Oehmke, M. J.; Geroldinger, A.; Heinze, G.; Kress, H.; Pramhas, S. Efficacy of Duloxetine in Chronic Low Back Pain with a Neuropathic Component. *Anesthesiology* **2016**, *124* (1), 150–158.
- (258) Meagher, D.; Hannan, N.; Leonard, M. Duloxetine-Mirtazapine Combination in Depressive Illness: The Case for Limerick ‘Rocket Fuel.’ *Ir. J. Psych. Med.* **2006**, *23* (3), 116–118.
- (259) Menezes, H. S.; Bueno, B. B. M.; Ciulla, L.; Schuh, A.; Luz, F. D. F.; Alves, R. J. V.; Abegg, M. P.; Cirino, S. L. M. B. Antidepressant Behavioral Effects of Duloxetine and Amitriptyline in the Rat Forced Swimming Test. *Acta Cir. Bras.* **2008**, *23* (5), 447–450.
- (260) Bymaster, F. P.; Dreshfield-Ahmad, L. J.; Threlkeld, P. G.; Shaw, J. L.; Thompson, L.; Nelson, D. L.; Hemrick-Luecke, S. K.; Wong, D. T. Comparative Affinity of Duloxetine and Venlafaxine for Serotonin and Norepinephrine Transporters in Vitro and in Vivo, Human Serotonin Receptor Subtypes, and Other Neuronal Receptors.

*Neuropsychopharmacology* **2001**, *25* (6), 871–880.

- (261) Lisinski, A.; Hieronymus, F.; Näslund, J.; Nilsson, S.; Eriksson, E. Item-Based Analysis of the Effects of Duloxetine in Depression: A Patient-Level Post Hoc Study. *Neuropsychopharmacology* **2020**, *45* (3), 553–560.
- (262) Al-Qahtani, S. D. Potentiometric Determination of Duloxetine Hydrochloride Using Coated Wire Electrode in Pure and Pharmaceutical Preparations. *Asian J. Pharm.* **2017**, *11* (4), S854–S857.
- (263) Ammar, R. A.; Otaif, H.; Al-Warthan, A. Quantitative Determination of Duloxetine Hydrochloride in Pharmaceuticals and Urine Using Prepared Ion-Selective Membrane Electrode. *Int. J. Electrochem. Sci.* **2012**, *7* (5), 4369–4380.
- (264) Hassanein, A. M.; Moharram, Y. I.; Oraiby, N. F.; Ebied, S. E. Trace Determination of Duloxetine HCl in Formulation and Spiked Human Serum at a Carbon Paste Electrode. *Am. J. Anal. Chem.* **2017**, *08* (11), 708–725.
- (265) Attia, A. K.; Rashed, N. S.; Mohamed, O. A.; Kamal Attia, A. Voltammetric Assay of Duloxetine Hydrochloride at Carbon-Based Electrode Modified by Titanium Dioxide Nanoparticles Enriched with Multi-Walled Carbon Nanotubes. *TrAC - Trends Anal. Res.* **2018**, *1* (1), 1–6.
- (266) Alarfaj, N. A.; Ammar, R. A.; El-tohamy, M. F. Disposable Screen-Printed Sensors for Determination of Duloxetine Hydrochloride. *Chem. Cent. J.* **2012**, *6* (72), 1–13.
- (267) Prabu, S. L.; Shahnawaz, S.; Dinesh Kumar, C.; Shirwaikar, A. Spectrofluorimetric Method for Determination of Duloxetine Hydrochloride in Bulk and Pharmaceutical Dosage Forms. *Indian J. Pharm. Sci.* **2008**, *70* (4), 502–503.
- (268) Datar, P. A.; Waghmare, R. U. Development and Validation of an Analytical Method for the Stability of Duloxetine Hydrochloride. *J. Taibah Univ. Sci.* **2014**, *8* (4), 357–363.
- (269) Patel, S. K.; Patel, N. J.; Patel, K. M.; Patel, P. U.; Patel, B. H. Estimation of Duloxetine Hydrochloride in Pharmaceutical Formulations by RP-HPLC Method. *Indian J. Pharm. Sci.* **2008**, *70* (6), 825–827.
- (270) Bhimanadhuni, C. N.; Garikapati, D. R.; Srinivas, C. Development and Validation of RP-HPLC Method for Determination of Duloxetine Hydrochloride in Bulk and Dosage Form. *Int. Curr. Pharm. J.* **2012**, *1* (5), 98–102.
- (271) Afrouzi, H.; Amoli-diva, M. Sensitive HPLC Determination of Duloxetine after Extraction Using Magnetic Multi-Walled Carbon Nanotubes. *Curr. Anal. Chem.* **2017**, *13* (5), 417–424.
- (272) Ulu, S. T. Determination and Validation of Duloxetine Hydrochloride in Capsules by HPLC with Pre-Column Derivatization and Fluorescence Detection. *J. Chromatogr. Sci.* **2012**, *50* (6), 494–498.
- (273) Liu, X.; Du, Y.; Wu, X. Study on Fluorescence Characteristics of Duloxetine Hydrochloride. *Spectrochim. Acta A Mol. Biomol. Spectrosc.* **2008**, *71* (3), 915–920.
- (274) Ulu, S. T.; Elmali, F. T. Validated Spectrophotometric Method for the Determination, Spectroscopic Characterization and Thermal Structural Analysis of Duloxetine with 1,2-

Naphthoquinone-4-Sulphonate. *Opt. Spectrosc.* **2012**, *112* (3), 431–437.

- (275) Ito, C.; Okahana, N.; Wu, T.-S.; Wang, M.-L.; Lai, J.-S.; Kuoh, C.-S.; Furukawa, H. New Carbazole Alkaloids from *Murraya Euchrestifolia*. *Chem. Pharm. Bull.* **1992**, *40* (1), 230–232.
- (276) Lee, H. Y.; Jung, Y.; Kim, W.; Kim, J. H.; Suh, M. S.; Shin, S. K.; Yoon, H. J. Structure-Activity Relationship Studies of the Chromosome Segregation Inhibitor, Incentrom A. *Bioorg. Med. Chem. Lett.* **2008**, *18* (16), 4670–4674.
- (277) Zhang, T.; Gao, H.; Lv, A.; Wang, Z.; Gong, Y.; Ding, D.; Ma, H.; Zhang, Y.; Yuan, W. Z. Hydrogen Bonding Boosted the Persistent Room Temperature Phosphorescence of Pure Organic Compounds for Multiple Applications. *J. Mater. Chem. C* **2019**, *7* (29), 9095–9101.
- (278) Liu, Y.; Zhan, G.; Fang, P.; Liu, Z.; Bian, Z.; Huang, C. Manipulating Organic Triplet Harvesting in Regiosomeric Microcrystals. *J. Mater. Chem. C* **2017**, *5* (47), 12547–12552.
- (279) Hsiao, S. H.; Chen, Y. Z. Electrosynthesis of Redox-Active and Electrochromic Polymer Films from Triphenylamine-Cored Star-Shaped Molecules End-Capped with Arylamine Groups. *Eur. Polym. J.* **2018**, *99* (September 2017), 422–436.
- (280) Zhang, T.; Wang, X.; An, Z.; Fang, Z.; Zhang, Y.; Yuan, W. Z. Pure Organic Persistent Room-Temperature Phosphorescence at Both Crystalline and Amorphous States. *ChemPhysChem* **2018**, *19* (18), 2389–2396.
- (281) Hu, Y.; Zhang, J.; Li, Z.; Wang, X.; Yin, J.; Liu, S. H. Novel Scorpion-like Carbazole Derivatives: Synthesis, Characterization, Mechanochromism and Aggregation-Induced Emission. *Dye. Pigment.* **2018**, *151* (December 2017), 165–172.
- (282) Lee, D.-W.; Hong, S.-K.; Park, T.-Y.; Kim, Y.-H.; Kim, S.-S. NOVEL COMPOUND AND ORGANIC DEVICE USING SAME, 2009.
- (283) Kaafarani, B. R.; El-Ballouli, A. O.; Trattning, R.; Fonari, A.; Sax, S.; Wex, B.; Risko, C.; Khnayzer, R. S.; Barlow, S.; Patra, D.; Timofeeva, T. V.; List, E. J. W.; Brédas, J. L.; Marder, S. R. Bis(Carbazolyl) Derivatives of Pyrene and Tetrahydropyrene: Synthesis, Structures, Optical Properties, Electrochemistry, and Electroluminescence. *J. Mater. Chem. C* **2013**, *1* (8), 1638–1650.
- (284) Damit, E. F.; Nordin, N.; Ariffin, A.; Sulaiman, K. Synthesis of Novel Derivatives of Carbazole-Thiophene, Their Electronic Properties, and Computational Studies. *J. Chem.* **2016**, *2016*, 1–14.
- (285) Koene, B. E.; Loy, D. E.; Thompson, M. E. Asymmetric Triaryldiamines as Thermally Stable Hole Transporting Layers for Organic Light-Emitting Devices. *Chem. Mater.* **1998**, *10* (8), 2235–2250.
- (286) Bele, A. A.; Khale, A. An Overview on Thin Layer Chromatography. *Int. J. Pharm. Sci. Res.* **2011**, *2* (2), 256–267.
- (287) Srivastava, N.; Singh, A.; Kumari, P.; Nishad, J. H.; Gautam, V. S.; Yadav, M.; Bharti, R.; Kumar, D.; Kharwar, R. N. Advances in Extraction Technologies: Isolation and Purification of Bioactive Compounds from Biological Materials. In *Natural Bioactive Compounds*; Elsevier Inc., 2021; pp 409–433.

- (288) [Https://microbenotes.com/column-chromatography/..](Https://microbenotes.com/column-chromatography/)
- (289) Yoshimatsu, K.; Reimhult, K.; Krozer, A.; Mosbach, K.; Sode, K.; Ye, L. Uniform Molecularly Imprinted Microspheres and Nanoparticles Prepared by Precipitation Polymerization: The Control of Particle Size Suitable for Different Analytical Applications. *Anal. Chim. Acta* **2007**, *584* (1), 112–121.
- (290) Tenreiro, A.; Cordas, C. M.; Abrantes, L. M. Oligonucleotide Immobilisation on Polytyramine-Modified Electrodes Suitable for Electrochemical DNA Biosensors. *Port. Electrochim. Acta* **2003**, *21* (4), 361–370.
- (291) De Rycke, E.; Trynda, A.; Jaworowicz, M.; Dubruel, P.; De Saeger, S.; Beloglazova, N. Capacitive Sensing of an Amphetamine Drug Precursor in Aqueous Samples: Application of Novel Molecularly Imprinted Polymers for Benzyl Methyl Ketone Detection. *Biosens. Bioelectron.* **2021**, *172* (September 2020), 112773.
- (292) *BIOVIA, Dassault Systèmes Discovery Studio Modeling Environment., Release 2017.*; San Diego: Dassault Systèmes, 2016.
- (293) Frisch, M. J.; Trucks, G. W.; Schlegel, H. B.; Scuseria, G. E.; Robb, M. A.; Cheeseman, J. R.; Scalmani, G.; Barone, V.; Petersson, G. a.; Nakatsuji, H.; Li, X.; Caricato, M.; Marenich, A. V.; Bloino, J.; Janesko, B. G.; Gomperts, R.; Mennucci, B.; Hratchian, H. P.; Ortiz, J. V.; Izmaylov, A. F.; Sonnenberg, J. L.; Williams; Ding, F.; Lipparini, F.; Egidi, F.; Goings, J.; Peng, B.; Petrone, A.; Henderson, T.; Ranasinghe, D.; Zakrzewski, V. G.; Gao, J.; Rega, N.; Zheng, G.; Liang, W.; Hada, M.; Ehara, M.; Toyota, K.; Fukuda, R.; Hasegawa, J.; Ishida, M.; Nakajima, T.; Honda, Y.; Kitao, O.; Nakai, H.; Vreven, T.; Throssell, K.; Montgomery Jr., J. a.; Peralta, J. E.; Ogliaro, F.; Bearpark, M. J.; Heyd, J. J.; Brothers, E. N.; Kudin, K. N.; Staroverov, V. N.; Keith, T. a.; Kobayashi, R.; Normand, J.; Raghavachari, K.; Rendell, a. P.; Burant, J. C.; Iyengar, S. S.; Tomasi, J.; Cossi, M.; Millam, J. M.; Klene, M.; Adamo, C.; Cammi, R.; Ochterski, J. W.; Martin, R. L.; Morokuma, K.; Farkas, O.; Foresman, J. B.; Fox, D. J. *Gaussian 16, Inc.*; Wallingford CT, USA, 2016.
- (294) Breneman, C.; Wiberg, K. Determining Atom-Centered Monopoles from Molecular Electrostatic Potentials. The Need for High Sampling Density in Formamide Conformational Analysis. *J. Comput. Chem.* **1990**, *11* (3), 361–373.
- (295) Brooks, B. R.; Bruccoleri, R. E.; Olafson, B. D.; States, D. J.; Swaminathan, S.; Karplus, M. CHARMM: A Program for Macromolecular Energy, Minimization, and Dynamics Calculations. *J. Comput. Chem.* **1983**, *4* (2), 187–217.
- (296) Ryckaert, J.-P.; Ciccotti, G.; Berendsen, H. J. C. Numerical Integration of the Cartesian Equations of Motion of a System with Constraints: Molecular Dynamics of n-Alkanes. *J. Comput. Phys.* **1977**, *23* (3), 327–341.
- (297) Martinez, L.; Andrade, R.; Birgin, E. G.; Martinez, J. M. Packmol: A Package for Building Initial Configurations for Molecular Dynamics Simulations. *J. Comput. Chem.* **2009**, *30* (13), 2157–2164.
- (298) Wijeratne, K. Conducting Polymer Electrodes for Thermogalvanic Cells, 2018.
- (299) Chen, Y.; Chen, L.; Bi, R.; Xu, L.; Liu, Y. A Potentiometric Chiral Sensor for L-Phenylalanine Based on Crosslinked Polymethylacrylic Acid-Polycarbazole Hybrid

Molecularly Imprinted Polymer. *Anal. Chim. Acta* **2012**, *754*, 83–90.

- (300) Jyoti; Gonzato, C.; Żołek, T.; Maciejewska, D.; Kutner, A.; Merlier, F.; Haupt, K.; Sharma, P. S.; Noworyta, K. R.; Kutner, W. Molecularly Imprinted Polymer Nanoparticles-Based Electrochemical Chemosensors for Selective Determination of Cilostazol and Its Pharmacologically Active Primary Metabolite in Human Plasma. *Biosens. Bioelectron.* **2021**, *193*, 113542.
- (301) Ye, C.; Chen, X.; Zhang, D.; Xu, J.; Xi, H.; Wu, T.; Deng, D.; Xiong, C.; Zhang, J.; Huang, G. Study on the Properties and Reaction Mechanism of Polypyrrole@norfloxacin Molecularly Imprinted Electrochemical Sensor Based on Three-Dimensional CoFe-MOFs/AuNPs. *Electrochim. Acta* **2021**, *379*, 138174.
- (302) Gliga, L. E.; Iacob, B. C.; Cheșcheș, B.; Florea, A.; Barbu-Tudoran, L.; Bodoki, E.; Oprean, R. Electrochemical Platform for the Detection of Adenosine Using a Sandwich-Structured Molecularly Imprinted Polymer-Based Sensor. *Electrochim. Acta* **2020**, *354*.
- (303) Wang, J. *Analytical Electrochemistry*, 2nd Ed.; John Wiley & Sons, Inc.: New York, USA, 2000.
- (304) Yoshimi, Y.; Ohdaira, R.; Iiyama, C.; Sakai, K. ‘Gate Effect’ of Thin Layer of Molecularly-Imprinted Poly(Methacrylic Acid-Co-Ethyleneglycol Dimethacrylate). *Sens. Actuators, B* **2001**, *73* (1), 49–53.
- (305) Khalifa, M. E.; Abdallah, A. B. Molecular Imprinted Polymer Based Sensor for Recognition and Determination of Profenofos Organophosphorous Insecticide. *Biosens. Bioelectron.* **2019**, *2*, 100027.
- (306) Telegdi, J.; Shaban, A.; Vastag, G. Biocorrosion-Steel. In *Encyclopedia of Interfacial Chemistry: Surface Science and Electrochemistry*; 2018; pp 28–42.
- (307) Iskierko, Z.; Sharma, P. S.; Bartold, K.; Pietrzyk-Le, A.; Noworyta, K.; Kutner, W. Molecularly Imprinted Polymers for Separating and Sensing of Macromolecular Compounds and Microorganisms. *Biotechnol. Adv.* **2016**, *34* (1), 30–46.
- (308) Gamry. <https://www.gamry.com/application-notes/EIS/total-harmonic-distortion/>.
- (309) Wang, J. *Analytical Electrochemistry*, 3rd Ed.; John Wiley & Sons, Inc.: New Jersey, USA, 2006.
- (310) Petr, A.; Dunsch, L.; Neudeck, A. In Situ UV-Vis ESR Spectroelectrochemistry. *J. Electroanal. Chem.* **1996**, *412* (1–2), 153–158.
- (311) Rapta, P.; Dunsch, L. Dimerisation of Organic Radical Ions and Redox Reactions of Dimers as Studied by Temperature-Dependent in Situ ESR/UV-Vis-NIR Spectroelectrochemistry. *J. Electroanal. Chem.* **2001**, *507* (1–2), 287–292.
- (312) <https://commons.wikimedia.org/w/index.php?curid=2974242>.
- (313) <https://www.wpiinc.com/blog/post/ca-sup-2-sup-detection-in-muscle-tissue-using-fluorescence-spectroscopy>.
- (314) Monyoncho, E. A.; Zamlynny, V.; Woo, T. K.; Baranova, E. A. The Utility of Polarization Modulation Infrared Reflection Absorption Spectroscopy (PM-IRRAS) in Surface and: In Situ Studies: New Data Processing and Presentation Approach. *Analyst* **2018**, *143* (11), 2563–2573.

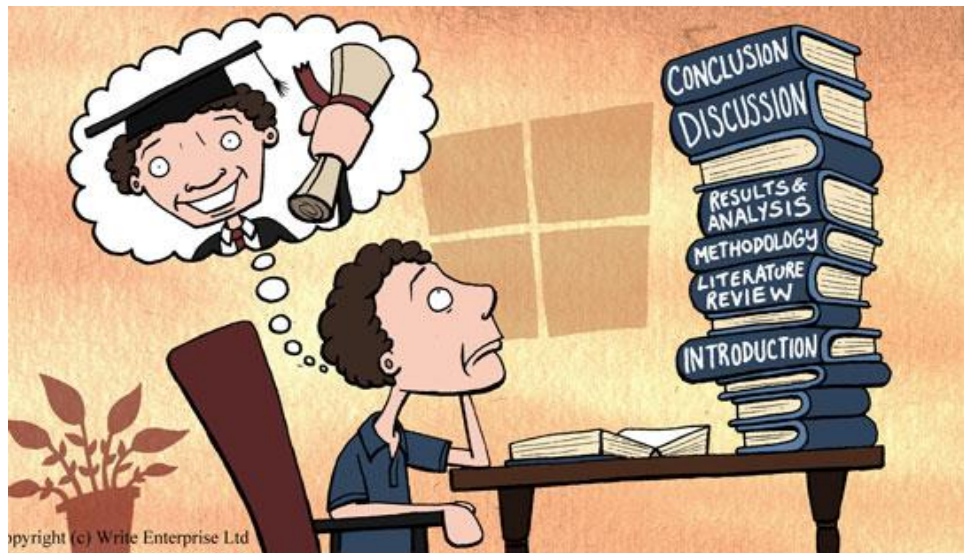
- (315) Kycia, A. H.; Su, Z. F.; Brosseau, C. L.; Lipkowski, J. In Situ PM-IRRAS Studies of Biomimetic Membranes Supported at Gold Electrode Surfaces. In *Vibrational Spectroscopy at Electrified Interfaces*; Wieckowski, A., Korzeniewski, C., Braunschweig., B., Eds.; John Wiley & Sons, Inc., 2013; pp 345–417.
- (316) Kaim, W.; Fiedler, J. Spectroelectrochemistry: The Best of Two Worlds. *Chem. Soc. Rev.* **2009**, *38* (12), 3373–3382.
- (317) Yin, J.; Ma, Y.; Li, G.; Peng, M.; Lin, W. A Versatile Small-Molecule Fluorescence Scaffold: Carbazole Derivatives for Bioimaging. *Coord. Chem. Rev.* **2020**, *412*, 213257.
- (318) <https://warwick.ac.uk/fac/sci/chemistry/research/stavros/stavrosgroup/overview/spectroelectrochemistry/>.
- (319) Tarábek, J.; Raptá, P.; Kalbáć, M.; Dunsch, L. In Situ Spectroelectrochemistry of Poly(N,N'-Ethylenebis(Salicylideneiminato)Cu(II)). *Anal. Chem.* **2004**, *76* (19), 5918–5923.
- (320) Bard, A. J.; Faulkner, L. R. *Electrochemical Methods. Fundamentals and Applications*, 2nd Ed.; John Wiley & Sons, Inc.: New York, USA, 2001; Vol. 2.
- (321) [Https://en.wikipedia.org/wiki/Electron\\_paramagnetic\\_resonance](Https://en.wikipedia.org/wiki/Electron_paramagnetic_resonance) ..
- (322) Chiesa, M.; Giamello, E.; Che, M. EPR Characterization and Reactivity of Surface-Localized Inorganic Radicals and Radical Ions. *Chem. Rev.* **2010**, *110* (3), 1320–1347.
- (323) <https://easyspin.org/easyspin/documentation/broadenings.html>
- (324) Dunsch, L. Recent Advances in in Situ Multi-Spectroelectrochemistry. *J. Solid State Electrochem.* **2011**, *15* (7–8), 1631–1646.
- (325) Zalibera, M.; Raptá, P.; Dunsch, L. In Situ ESR-UV/VIS/NIR Spectroelectrochemistry of an Empty Fullerene Anion and Cation: The C<sub>82</sub>:3 Isomer. *Electrochim. Commun.* **2007**, *9* (12), 2843–2847.
- (326) Gerber, F.; Krummen, M.; Potgeter, H.; Roth, A.; Siffrin, C.; Spoendlin, C. Practical Aspects of Fast Reversed-Phase High-Performance Liquid Chromatography Using 3 Mm Particle Packed Columns and Monolithic Columns in Pharmaceutical Development and Production Working under Current Good Manufacturing Practice. *J. Chromatogr. A* **2004**, *1036* (2), 127–133.
- (327) *Handbook of Instrumental Techniques for Analytical Chemistry*; Settle, F. A., Ed.; New Jersey, USA, 1997.
- (328) Zotou, A. An Overview of Recent Advances in HPLC Instrumentation. *Cent. Eur. J. Chem.* **2012**, *10* (3), 554–569.
- (329) Darwish, H. W.; Ali, N. A.; Naguib, I. A.; El Ghobashy, M. R.; Al-Hossaini, A. M.; Abdelrahman, M. M. Development and Validation of a Stability Indicating RP-HPLC-DAD Method for the Determination of Bromazepam. *PLoS One* **2021**, *16* (3 March), 1–12.
- (330) Lakshmi, S. A Review on Chromatography with High-Performance Liquid Chromatography (HPLC) and Its Functions. *J. Pharm. Anal.* **2015**, *4* (1), 1–15.
- (331) [https://commons.wikimedia.org/wiki/File:Preparative\\_HPLC.svg](https://commons.wikimedia.org/wiki/File:Preparative_HPLC.svg).

- (332) Stetefeld, J.; McKenna, S. A.; Patel, T. R. Dynamic Light Scattering: A Practical Guide and Applications in Biomedical Sciences. *Biophys. Rev.* **2016**, *8* (4), 409–427.
- (333) Cansu-Ergun, E. G.; Önal, A. M. Carbazole Based Electrochromic Polymers Bearing Ethylenedioxy and Propylenedioxy Scaffolds. *J. Electroanal. Chem.* **2018**, *815* (March), 158–165.
- (334) Kaleeswaran, D.; Vishnoi, P.; Kumar, S.; Chithiravel, S.; Walawalkar, M. G.; Krishnamoorthy, K.; Murugavel, R. Alkyl-Chain-Separated Triphenylbenzene - Carbazole Conjugates and Their Derived Polymers: Candidates for Sensory, Electrical and Optical Materials. *ChemistrySelect* **2016**, *1* (21), 6649–6657.
- (335) Data, P.; Zassowski, P.; Łapkowski, M.; Domagala, W.; Krompiec, S.; Flak, T.; Penkala, M.; Swist, A.; Soloducho, J.; Danikiewicz, W. Electrochemical and Spectroelectrochemical Comparison of Alternated Monomers and Their Copolymers Based on Carbazole and Thiophene Derivatives. *Electrochim. Acta* **2014**, *122*, 118–129.
- (336) Łapkowski, M.; Data, P.; Nowakowska-Oleksy, A.; Sołoducho, J.; Roszak, S. Electrochemical Characterization of Alternate Conducting Carbazole-Bisthiophene Units. *Mater. Chem. Phys.* **2012**, *131* (3), 757–763.
- (337) Hsiao, S. H.; Lin, S. W. Electrochemical Synthesis of Electrochromic Polycarbazole Films from N-Phenyl-3,6-Bis(N-Carbazolyl)Carbazoles. *Polym. Chem.* **2016**, *7* (1), 198–211.
- (338) Witker, D.; Reynolds, J. R. Soluble Variable Color Carbazole-Containing Electrochromic Polymers. *Macromolecules* **2005**, *38* (18), 7636–7644.
- (339) Chiu, S. K.; Chung, Y. C.; Liou, G. S.; Su, Y. O. Electrochemical and Spectral Characterizations of 9-Phenylcarbazoles. *J. Chin. Chem. Soc.* **2012**, *59* (3), 331–337.
- (340) Contal, E.; Sougueh, C. M.; Lakard, S.; Et Taouil, A.; Magnenet, C.; Lakard, B. Investigation of Polycarbazoles Thin Films Prepared by Electrochemical Oxidation of Synthesized Carbazole Derivatives. *Front. Mater.* **2019**, *6* (June).
- (341) Lakard, S.; Contal, E.; Mougin, K.; Magnenet, C.; Lakard, B. Electrochemical Preparation and Physicochemical Study of Polymers Obtained from Carbazole and N-((Methoxycarbonyl)Methyl)Carbazole. *Synth. Met.* **2020**, *270* (September), 116584.
- (342) Dennington, R.; Keith, T. A.; Millam, J. M. GaussView, Version 6.1, Semichem Inc., Shawnee Mission, KS. 2016.
- (343) Becke, A. D. Density-Functional Thermochemistry. III. The Role of Exact Exchange. *J. Chem. Phys.* **1993**, *98* (7), 5648–5652.
- (344) Kohn, W.; Sham, L. J. Self-Consistent Equations Including Exchange and Correlation Effects. *Phys. Rev. A* **1965**, *140* (5), 1133–1138.
- (345) Bauernschmitt, R.; Ahlrichs, R. Treatment of Electronic Excitations within the Adiabatic Approximation of Time-Dependent Density Functional Theory. *Chem. Phys. Lett.* **1996**, *256* (4–5), 454–464.
- (346) Wang, J. L.; Li, X.; Shreiner, C. D.; Lu, X.; Moorefield, C. N.; Tummalaapalli, S. R.; Medvetz, D. A.; Panzner, M. J.; Fronczek, F. R.; Wesdemiotis, C.; Newkome, G. R. Shape-Persistent, Ruthenium(II)- and Iron(II)-Bisterpyridine Metalloendrimers:

- Synthesis, Traveling-Wave Ion-Mobility Mass Spectrometry, and Photophysical Properties. *New J. Chem.* **2012**, *36* (2), 484–491.
- (347) Davies, A. G.; McGuchan, D. C. Electron Spin Resonance Spectra of Triptycene Radical Cations. *Organometallics* **1991**, *10*, 329–336.
- (348) Karon, K.; Lapkowski, M.; Dabuliene, A.; Tomkeviciene, A.; Kostiv, N.; Grazulevicius, J. V. Spectroelectrochemical Characterization of Conducting Polymers from Star-Shaped Carbazole-Triphenylamine Compounds. *Electrochim. Acta* **2015**, *154*, 119–127.
- (349) Joshi, M. V.; Hemler, C.; Cava, M. P.; Cain, J. L.; Bakker, M. G.; McKinley, A. J.; Metzger, R. M. Synthesis, Electrical Conductivity and Electron Paramagnetic Resonance Spectroscopy of Polymers Derived from NOPF<sub>6</sub>-Doped XYZ-Triheterocycles Based on Pyrrole, Furan, and Thiophene. *J. Chem Soc. Perk. Trans 2* **1993**, No. 6, 1081–1086.
- (350) Karon, K.; Lapkowski, M.; Juozas, G. Electrochemical and UV-Vis/ESR Spectroelectrochemical Properties of Polymers Obtained from Isomeric 2,7- and 3,6-Linked Carbazole Trimmers; Influence of the Linking Topology on Polymers Properties. *Electrochim. Acta* **2014**, *123*, 176–182.
- (351) Wang, Z.; Ma, W.; Chen, C.; Ji, H.; Zhao, J. Probing Paramagnetic Species in Titania-Based Heterogeneous Photocatalysis by Electron Spin Resonance (ESR) Spectroscopy — A Mini-Review. *Chem. Eng. J.* **2011**, *170* (2–3), 353–362.
- (352) Higginbotham, H. F.; Czichy, M.; Sharma, B. K.; Shaikh, A. M.; Kamble, R. M.; Data, P. Electrochemically Synthesised Xanthone-Cored Conjugated Polymers as Materials for Electrochromic Windows. *Electrochim. Acta* **2018**, *273*, 264–272.
- (353) Pander, P.; Swist, A.; Zassowski, P.; Soloducho, J.; Lapkowski, M.; Data, P. Electrochemistry and Spectroelectrochemistry of Polymers Based on D-A-D and D-D-D Bis(N-Carbazolyl) Monomers, Effect of the Donor/Acceptor Core on Their Properties. *Electrochim. Acta* **2017**, *257*, 192–202.
- (354) Nataraj, A.; Balachandran, V.; Karthick, T. Molecular Orbital Studies (Hardness, Chemical Potential, Electrophilicity, and First Electron Excitation), Vibrational Investigation and Theoretical NBO Analysis of 2-Hydroxy-5-Bromobenzaldehyde by Density Functional Method. *J. Mol. Struct.* **2013**, *1031*, 221–233.
- (355) Sharma, P. S.; Garcia-Cruz, A.; Cieplak, M.; Noworyta, K. R.; Kutner, W. ‘Gate Effect’ in Molecularly Imprinted Polymers: The Current State of Understanding. *Curr. Opin. Electrochem.* **2019**, *16*, 50–56.
- (356) Alexander, C.; Andersson, H. S.; Andersson, L. I.; Ansell, R. J.; Kirsch, N.; Nicholls, I. A.; O’Mahony, J.; Whitcombe, M. J. Molecular Imprinting Science and Technology: A Survey of the Literature for the Years up to and Including 2003. *J. Mol. Recognit.* **2006**, *19* (2), 106–180.
- (357) Haupt, K.; Dzgoev, A.; Mosbach, K. Assay System for the Herbicide 2,4-Dichlorophenoxyacetic Acid Using a Molecularly Imprinted Polymer as an Artificial Recognition Element. *Anal. Chem.* **1998**, *70* (3), 628–631.
- (358) Fuchs, Y.; Linares, A. V.; Mayes, A. G.; Haupt, K.; Soppera, O. Ultrathin Selective Molecularly Imprinted Polymer Microdots Obtained by Evanescent Wave

Photopolymerization. *Chem. Mater.* **2011**, *23* (16), 3645–3651.

- (359) Zhao, W.; Zhang, R.; Xu, S.; Cai, J.; Zhu, X.; Zhu, Y.; Wei, W.; Liu, X. Molecularly Imprinted Polymeric Nanoparticles Decorated with Au NPs for Highly Sensitive and Selective Glucose Detection. *Biosens. Bioelectron.* **2018**, *100*, 497–503.
- (360) Chen, L.; Wang, X.; Lu, W.; Wu, X.; Li, J. Molecular Imprinting : Perspectives and Applications. *Chem. Soc. Rev.* **2016**, *45* (21275158), 2137–2211.
- (361) Ezoji, H.; Rahimnejad, M. Nanoparticles-Based Electrochemical Sensors and Biosensors. In *Nanoparticle Design and Characterization for Catalytic Applications in Sustainable Chemistry*; Luque, R., Prinsen, P., Eds.; The Royal Society of Chemistry: Cambridge, 2019; pp 329–345.
- (362) Tonelli, D.; Scavetta, E.; Gualandi, I. Electrochemical Deposition of Nanomaterials for Electrochemical Sensing. *Sensors (Switzerland)* **2019**, *19* (5), 1186.
- (363) Umpleby, R. J.; Baxter, S. C.; Rampey, A. M.; Rushton, G. T.; Chen, Y.; Shimizu, K. D. Characterization of the Heterogeneous Binding Site Affinity Distributions in Molecularly Imprinted Polymers. *J. Chromatogr. B* **2004**, *804* (1), 141–149.
- (364) Rampey, A. M.; Umpleby, R. J.; Rushton, G. T.; Iseman, J. C.; Shah, R. N.; Shimizu, K. D. Characterization of the Imprint Effect and the Influence of Imprinting Conditions on Affinity, Capacity, and Heterogeneity in Molecularly Imprinted Polymers Using the Freundlich Isotherm-Affinity Distribution Analysis. *Anal. Chem.* **2004**, *76* (4), 1123–1133.
- (365) Umpleby, R. J.; Baxter, S. C.; Chen, Y.; Shah, R. N.; Shimizu, K. D. Characterization of Molecularly Imprinted Polymers with the Langmuir - Freundlich Isotherm. *Anal. Chem.* **2001**, *73* (19), 4584–4591.
- (366) Kidakova, A.; Reut, J.; Boroznjak, R.; Öpik, A.; Syritski, V. Advanced Sensing Materials Based on Molecularly Imprinted Polymers towards Developing Point-of-Care Diagnostics Devices. *Proc. Est. Acad. Sci.* **2019**, *68* (2), 158–167.
- (367) Afsarimanesh, N.; Mukhopadhyay, S. C.; Kruger, M. *Electrochemical Biosensor: Point-of-Care for Early Detection of Bone Loss*, 1st ed.; Subhas Chandra Mukhopadhyay, Ed.; Springer Nature Switzerland, 2019; Vol. 30.
- (368) Zhang, B.; Fan, X.; Zhao, D. Computer-Aided Design of Molecularly Imprinted Polymers for Simultaneous Detection of Clenbuterol and Its Metabolites. *Polymers (Basel)*. **2019**, *11* (1), 17.
- (369) Chen, M.; He, X.; Guo, Y.; Hu, J.; Liang, B.; Zeng, K.; Yang, G. A New Molecular Design Platform for High-Performance Polymers from Versatile Bio-Based Tyramine: A Case Study of Tyramine-Derived Phthalonitrile Resin. *Polym. Chem.* **2021**, *12* (3), 408–422.



**Exam time**